

**MODELLING AND CHARACTERIZATION OF MECHANICALLY REGULATED
TISSUE FORMATION AROUND BONE-INTERFACING IMPLANTS**

by

Craig Alexander Simmons

A thesis submitted in conformity with the requirements
for the degree of Doctor of Philosophy
Graduate Department of Mechanical and Industrial Engineering
University of Toronto

© Copyright by Craig A. Simmons 2000



National Library
of Canada

Acquisitions and
Bibliographic Services

395 Wellington Street
Ottawa ON K1A 0N4
Canada

Bibliothèque nationale
du Canada

Acquisitions et
services bibliographiques

395, rue Wellington
Ottawa ON K1A 0N4
Canada

Your file Votre référence

Our file Notre référence

The author has granted a non-exclusive licence allowing the National Library of Canada to reproduce, loan, distribute or sell copies of this thesis in microform, paper or electronic formats.

The author retains ownership of the copyright in this thesis. Neither the thesis nor substantial extracts from it may be printed or otherwise reproduced without the author's permission.

L'auteur a accordé une licence non exclusive permettant à la Bibliothèque nationale du Canada de reproduire, prêter, distribuer ou vendre des copies de cette thèse sous la forme de microfiche/film, de reproduction sur papier ou sur format électronique.

L'auteur conserve la propriété du droit d'auteur qui protège cette thèse. Ni la thèse ni des extraits substantiels de celle-ci ne doivent être imprimés ou autrement reproduits sans son autorisation.

0-612-49943-X

Canada

MODELLING AND CHARACTERIZATION OF MECHANICALLY REGULATED TISSUE FORMATION AROUND BONE-INTERFACING IMPLANTS

Doctorate of Philosophy, 2000

Craig Alexander Simmons

Graduate Department of Mechanical and Industrial Engineering
University of Toronto

Abstract

In many cases, orthopaedic and dental implants can restore function to diseased or damaged joints and edentulous jaws. However, in several challenging clinical situations, it is difficult to achieve adequate fixation (osseointegration) between the implant and bone. Since osseointegration is necessary for clinical success, implant failure rates in these cases are unacceptably high. Understanding the factors that allow bone-interfacing implants to osseointegrate rapidly and reliably should lead to improvements in their use and design.

With this being our goal, we investigated the influence of implant surface geometry and local tissue strains on peri-implant tissue formation. Using a rabbit model, we evaluated the histological and mechanical characteristics of the early healing tissues around nonfunctional implants with Ti6Al4V sintered porous surfaces and Ti plasma-sprayed surfaces. We found that the early healing tissues integrated with the three-dimensional interconnected structure of the sintered porous surface and mineralized more rapidly than the tissues around the irregular geometry of the plasma-sprayed surface. Consequently, the stiffness and strength of attachment was greater for the porous-surfaced implants. These results demonstrate that implant surface geometry influences early peri-implant tissue formation and, as a result, the early mechanical stability of implants.

To investigate the relationship between implant surface geometry, the local mechanical environment, and peri-implant tissue formation, we developed a computational micromechanical model based on homogenization methods to describe the effective and local properties of the porous-surfaced and plasma-sprayed peri-implant regions. In validation tests, we showed that the model provided reasonably accurate initial predictions of the properties of the peri-implant regions. Using the computational model, we compared the local mechanical environments around porous-surfaced and plasma-sprayed implants. In cases with minimal implant loading, the model predicted local tissue strains that permitted localized *and* appositional bone formation around porous-surfaced implants, but only appositional bone formation for plasma-sprayed implants. Based on the model predictions and experimental data from earlier studies, we proposed a quantitative model for the mechanical regulation of peri-implant tissue formation. The mechanoregulatory model is consistent with observations of tissue formation around porous-surfaced and plasma-sprayed implants, and provides initial criteria to evaluate the osseointegration potential of bone-interfacing implants.

Acknowledgements

Almost five years ago, I really struggled with my decision about where to go to pursue a doctorate. Had I been able to anticipate all the positive experiences and opportunities to grow professionally I would have at the University of Toronto, my decision would have been a lot easier. The nurturing environment here is due in large part to my thesis supervisors, Dr. Bob Pilliar and Prof. Shaker Meguid. Dr. Pilliar has always treated me more as a colleague than a student, allowing me to explore and shape my research independently, but providing guidance when it was necessary. This approach, coupled with his continuous encouragement, infectious enthusiasm and constant support, is responsible in large part for my maturation as a researcher and academic. His example as a mentor is one that I hope I can emulate one day.

Similarly, Prof. Meguid's contributions to my thesis work and education have been invaluable. His guidance and rigorous approach contributed significantly to the success and quality of this work. Through his perseverance, my confidence as a researcher and engineer has grown substantially. I am particularly grateful for his commitment to my interests and his concern for my well-being and success; his efforts in this regard were extraordinary.

I would also like to thank the various faculty members who served on my examination committees: Dr. John Davies, Dr. Marc Grynepas, Dr. Nigel Shrive, and Dr. Jan Spelt. In particular, I thank Dr. Ross Ethier, who not only served as a committee member, but also discussed with me the realities, both good and bad, of life as an academic.

Certainly this work would not have been possible without the help of a number of fantastic people. The efforts of Nancy Valiquette and Susan Carter were critical to the success of the rabbit surgeries; they also made them fun. Nancy also did all the histology and dug up old slides and data whenever I needed them. I am grateful for the technical wizardry of David Abdulla almost as much as I am for his post-golf barbeques. Thanks also to Chris Pereira and Bob Chernecky for technical assistance with the Instron and SEM. Henry Xue gave a lot of his time to help me with the photoelastic studies, and I thank him for that.

I am grateful for the financial support provided by a number of sources, including the Medical Research Council, University of Toronto Open Fellowships, an Ontario Graduate Scholarship in Science and Technology, and, at times, Mom and Dad.

Of course, lab wasn't all work, and there are a number of people who made lab exciting, stimulating, and fun – special thanks to GJ, Mark, Debbie, Jason, Peter, Chantal, and many more. Thanks also to the members of the EMDL, who despite the weirdness of my research project,

always made me feel welcome and part of the team. In particular, thanks to John, Mamdouh, and Nagi, who were always willing to help.

I am so thankful for my family and friends. Because of them, coming back to Toronto was much more than that – it was returning home. Thank you Mom, Dad, Louvain, and Art. Your support, advice, and love keep me going and inspire me. The cookies, cash, and use of the cars don't hurt either. Thanks to Kathleen, Scott, Emma, and Chris for keeping me laughing and being there when I need you. This thesis is dedicated to Gramps, not only the greatest mechanical engineer I know, but also the most generous and loving person I know. Finally, I am hugely indebted to Deb. She had enough faith in me to leave her motherland, had enough strength in her to withstand four years of American bashing, centigrade, and no Ann Taylor, and enough love in her to support me always. Thanks bud.

Table of Contents

Abstract	ii
Acknowledgements	iv
Table of Contents	vi
List of Tables	ix
List of Figures	xii
Nomenclature and Abbreviations	xx
Chapter 1 Introduction	1
1.1 Background and motivation.....	1
1.2 Bone-interfacing implants and surface design.....	2
1.3 Research objectives.....	4
1.4 Method of approach.....	4
1.5 Scope and format of the thesis.....	5
Chapter 2 Implant surface geometry and peri-implant tissue formation: Review of the literature	7
2.1 Introduction and scope.....	7
2.2 Overview of implant surface geometries.....	7
2.2.1 Subtractive processes to alter implant surface texture.....	8
2.2.2 Additive processes to form implant surface structures.....	9
2.3 The effect of surface geometry on peri-implant tissue formation.....	13
2.2.3 In vivo studies.....	13
2.2.4 In vitro studies.....	22
2.4 Summary.....	24
Chapter 3 Mechanical regulation of tissue formation: Review of the literature	25
3.1 Introduction and scope.....	25
3.2 Experimental studies of mechanically regulated tissue formation.....	25
3.2.1 Fracture healing and distraction osteogenesis.....	26
3.2.2 Skeletal development.....	28

3.2.3	Peri-implant tissue formation.....	28
3.2.4	Cell culture studies.....	32
3.3	Computational studies of mechanically regulated tissue formation	32
3.3.1	Fracture healing	33
3.3.2	Distraction osteogenesis.....	38
3.3.3	Skeletal development.....	39
3.3.4	Implant interface mechanics and tissue formation.....	41
3.4	Summary	47

Chapter 4 Animal model study of the influence of implant surface geometry on early post-implantation healing response 50

Summary..	50
4.1	Introduction and motivation.....	50
4.2	Specific research objectives.....	51
4.3	Materials and methods	52
4.3.1	Implants.....	52
4.3.2	Surgical procedure	54
4.3.3	Histological examination	55
4.3.4	Mechanical testing	57
4.3.5	Scanning electron microscopy examination	57
4.4	Results.....	58
4.4.1	Immediately post-implantation	58
4.4.2	Four days post-implantation	60
4.4.3	Eight days post-implantation	60
4.4.4	Sixteen days post-implantation.....	63
4.5	Discussion.....	65
4.6	Conclusions.....	69

Chapter 5 Development and validation of a computational model of the interface zone 70

Summary	70	
5.1	Introduction and motivation.....	71
5.2	Specific research objectives.....	72

5.3	Theoretical formulation of homogenization theory	73
5.4	Numerical implementation of homogenization theory	78
5.5	Additional comments on homogenization theory	80
5.6	Verification of the code	81
5.6.1	Methods.....	81
5.6.2	Results and discussion	82
5.7	Idealized geometry unit cell models of the porous-surfaced and plasma-sprayed interface zones	84
5.7.1	Features of the unit cell models	84
5.7.2	Effective and local properties of the idealized geometry unit cell models.....	85
5.8	Validation of computational model	89
5.8.1	Validation of the effective properties of the porous-surfaced interface zone.....	89
5.8.2	Validation of the effective properties of the plasma-sprayed interface zone.....	93
5.8.3	Validation of the local properties of the interface zones	94
5.9	Parametric investigations of implant surface pore size.....	100
5.9.1	Methods.....	101
5.9.2	Results and discussion	102
5.10	Development and analysis of geometrically accurate unit cell models	106
5.10.1	Methods.....	106
5.10.2	Results and discussion	108
5.11	Conclusions regarding the computational model.....	113

Chapter 6 Biomechanical analysis of the effect of implant surface geometry on early peri-implant tissue formation **115**

Summary.....	115
6.1 Introduction and motivation.....	115
6.2 Specific research objectives.....	116
6.3 Methods.....	117
6.4 Results.....	119
6.5 Discussion.....	124
6.5.1 Significance and implications of the results	125
6.5.2 Assumptions in the analysis.....	126
6.6 Conclusions.....	130

Chapter 7	Biomechanical investigation of implant micromovement and mechanically regulated peri-implant tissue formation	131
Summary.....		131
7.1	Introduction and motivation.....	132
7.2	Specific research objectives.....	133
7.3	Methods.....	134
7.3.1	Review of the canine micromovement experiments.....	134
7.3.2	Estimation of the early interface zone tissue material properties	136
7.3.3	Computational modelling of the micromovement experiments.....	137
7.4	Results.....	140
7.4.1	Estimation of early, pre-mineralized tissue material properties	140
7.4.2	Prediction of local tissue strains due to implant micromovement	141
7.5	Discussion	148
7.5.1	Threshold tissue strain for bone formation	148
7.5.2	Effect of implant surface geometry on local tissue strains	151
7.5.3	Assumptions in the analysis.....	153
7.6	A quantitative mechanoregulatory model of peri-implant tissue formation.....	157
7.6.1	Description of the model.....	158
7.6.2	Clinical implications.....	161
7.7	Conclusions.....	162
Chapter 8	Conclusions and recommendations for future work	163
8.1	Motivation.....	163
8.2	Research objectives and conclusions	163
8.3	Contributions of this research	166
8.4	Recommendations for future work	167
References		169

List of Tables

Table 2.1. Summary of in vivo studies on the effect of the surface geometry of non-functional screw-shaped implants on tissue formation and mechanical stability.	17
Table 2.2. Summary of in vivo studies on the effect of the surface geometry of non-functional press-fit implants on tissue formation and mechanical stability.	18
Table 2.3. Summary of in vivo studies on the effect of the surface geometry of functional implants on tissue formation and mechanical stability.	21
Table 5.1. Elastic properties of the materials in the unit cell finite element models used to validate the code (from Ghosh et al., 1995; Lukkassen et al., 1995).	82
Table 5.2. Comparison of the effective material properties predicted using HOMOOG with those published by Ghosh et al. (1995) for unit cell models A and B.	83
Table 5.3. Comparison of the effective material properties predicted using HOMOOG with those published by Lukkassen et al. (1995) for unit cell model C.	83
Table 5.4. Elastic constants used in the unit cell finite element models.	86
Table 5.5. Effective elastic constants of the homogenized interface zones predicted by the computational model.	87
Table 5.6. Elastic constants of the constituent materials of the experimental test specimens (Ko et al., 1996).	90
Table 5.7. Mechanical and optical constants of the constituent materials of the photoelastic test specimens (provided by the supplier).	96
Table 5.8. Dimensions (in μm) of unit cells used to investigate the effect of pore size (w) on the effective and local properties. Refer to Figure 5.5 and Figure 5.6 for definitions of dimension labels. An asterisk indicates baseline model geometry.	101
Table 6.1. Elastic properties used in the finite element models.	119
Table 7.1. Elastic properties used in the unit cell model. An asterisk indicates the baseline tissue material property.	137

Table 7.2. Linear elastic properties used in the global finite element model. An asterisk indicates the baseline Young's modulus for bone. 138

List of Figures

Figure 1.1. Examples of orthopaedic and dental implants used to restore joint and tooth function.	2
Figure 1.2. Histological sections demonstrating osseointegration of implants with (from left to right) a sintered porous surface (from Pilliar, 1991), a plasma-spray coated surface (from Vercaigne et al., 1998b), and a threaded surface (from Wennerberg et al., 1996c).	3
Figure 1.3. Schematic of the method of approach.	5
Figure 2.1. Summary of microscopic and macroscopic implant surface geometries.	8
Figure 2.2. Schematic demonstrating that textured surfaces can resist only shear forces, whereas structured surfaces can resist both shear and tensile forces.	10
Figure 2.3. (A) Scanning electron micrograph of the surface of a titanium plasma-sprayed implant, and (B) a back-scattered electron micrograph of a longitudinal section of a plasma-sprayed surface that has been applied to a grit-blasted substrate. Original magnifications: (A) $\times 500$; (B) $\times 800$	11
Figure 2.4. Scanning electron micrographs of a Ti6Al4V sintered porous surface demonstrating the 3D interconnected porosity (A) and the submicron-sized thermal etch lines on the sintered particles (B) (from Smith et al., 1989). Original magnifications: (A) $\times 200$; (B) $\times 1000$	12
Figure 3.1. Schematic of Carter’s tissue differentiation hypothesis (adapted from Carter et al., 1998).	34
Figure 3.2. Schematic of the quantitative mechanoregulatory hypothesis proposed by Claes and Heigele (1999) for fracture healing (adapted from Claes and Heigele, 1999).	38
Figure 3.3. Schematic of the mechanoregulatory relationship proposed by Prendergast et al. (1997) (adapted from Prendergast et al., 1997).	44
Figure 4.1. The implants used in this study were fabricated with a Ti6Al4V sintered porous surface (left) or a Ti plasma-sprayed surface (right).	53

Figure 4.2. Scanning electron micrographs of the (A) Ti6Al4V sintered porous-structured surface and (B) the Ti plasma-sprayed surface. Original magnifications: (A) $\times 200$; (B) $\times 500$.	53
Figure 4.3. Contact radiograph showing the implant location in rabbit femoral condyle.	54
Figure 4.4. Summary of the experimental design for the rabbit study.	55
Figure 4.5. Method for quantifying the mineralized area fraction (MAF) of the interface zone tissue.	56
Figure 4.6. Mechanical test fixture used to perform the pull-out tests.	57
Figure 4.7. Back-scattered electron micrographs demonstrating contact between the bone (BT) and implant (I) immediately after surgery for the porous-surfaced (A) and plasma-sprayed (B) implants. Original magnifications: (A) $\times 40$; (B) $\times 40$.	58
Figure 4.8. Pull-out strength (A) and maximum interface stiffness (B) measured for the two implant surface designs at each healing period. Data are presented as mean \pm standard error. An asterisk indicates a significant difference between implant designs ($p < 0.05$).	59
Figure 4.9. Histologic sections demonstrating a well-defined interface zone filled with healing tissue (HT) adjacent to both the porous-surfaced (A) and plasma-sprayed (B) implants after 4 days of healing. Original magnifications: (A) $\times 30$; (B) $\times 30$.	61
Figure 4.10. Scanning electron micrographs demonstrating more extensive coverage and interdigitation of the healing tissue matrix (indicated by arrows) with the sintered porous surface (A) than with the plasma-sprayed surface (B) four days post-implantation. Original magnifications: (A) $\times 100$; (B) $\times 100$.	61
Figure 4.11. Scanning electron micrographs taken 8 days after implantation demonstrating more extensive tissue interdigitation and maturation (indicated by arrows) with the sintered porous surface (A) than with the plasma-sprayed surface (B). Original magnifications: (A) $\times 600$; (B) $\times 500$.	62

Figure 4.12. Back-scattered electron micrographs of the porous-surfaced (A) and plasma-sprayed (B) interface zones 8 days post-implantation. Areas with matrix mineralization (indicated by arrows) are evident throughout the porous-surfaced interface zone. The same degree of mineralization was not evident in the plasma-sprayed interface zone. Original magnifications: (A) $\times 40$; (B) $\times 40$ 63

Figure 4.13. Mineralized area fraction (MAF) of the interface zone tissue at Days 8 and 16 post-implantation expressed relative to the average baseline value determined at Day 4 for each design. The data are presented as mean \pm standard error. Refer to the text for details on the Day 8 results. 64

Figure 4.14. Scanning electron micrographs taken 16 days after implantation showing extensive coverage and interdigitation of the sintered porous (A) and plasma-sprayed (B) surfaces with mineralized tissue and dense matrix. Numerous active osteoblasts (indicated by arrows) were observed on both surfaces. Original magnifications: (A) $\times 200$; (B) $\times 500$ 65

Figure 4.15. Back-scattered electron micrographs of the porous-surfaced (A) and plasma-sprayed (B) interface zones 16 days post-implantation. Both implant designs were osseointegrated by this point, with close apposition of bone to the implant surfaces. Original magnifications: (A) $\times 40$; (B) $\times 40$ 65

Figure 5.1. Schematic of the method of approach used in the development and validation of the computational model of the porous-surfaced and plasma-sprayed interface zones..... 74

Figure 5.2. A composite body comprised of repeating unit cells, which are representative of the microstructure. 75

Figure 5.3. Numerical implementation of the homogenization method using custom software (HOMOG) and a commercial finite element package (ANSYS). 80

Figure 5.4. Unit cell models used to verify the homogenization code. (A) A longitudinal section of a short fibre composite; (B) a longitudinal section of a long fibre composite (from Ghosh et al., 1995); and (C) a cross-section of a fibre-reinforced composite (from Lukkassen et al., 1995). 82

Figure 5.5. Idealized unit cell model of the porous-surfaced interface zone (baseline model). The displacements of the metal particles were constrained to one another in the model using the penalty method..... 85

Figure 5.6. Idealized unit cell model of the plasma-sprayed interface zone (baseline model)... 85

Figure 5.7. Field plots of the local structure tensor (M_{ijkl}) components for the plasma-sprayed interface zone tissue (left) and porous-surfaced interface zone tissue (right). Higher values of M_{ijkl} occur in regions with strain concentrations, whereas lower values of M_{ijkl} occur in strain-protected regions..... 87

Figure 5.8. Histograms of the local structure tensor (M_{ijkl}) components for the porous-surfaced and plasma-sprayed interface zone tissues. 88

Figure 5.9. Schematic of the “tissue-implant” interface of the experimental test specimens used by Ko et al. (1996) to measure the effective elastic constants of a porous-surfaced titanium/epoxy composite (adapted from Ko et al., 1996). 90

Figure 5.10. Idealized unit cell model used to predict the effective elastic constants of the porous-surfaced interface zone. 90

Figure 5.11. Effective elastic constants of the composite of porous-surfaced titanium and epoxy I (A) and epoxy II (B) predicted by the homogenization method for the current UC and the UC of Ko et al. (1996), and measured experimentally (Ko et al., 1996). The experimental data are presented as mean \pm standard deviation. An asterisk indicates a statistically significant difference between the theoretical and experimental values ($p < 0.01$)..... 92

Figure 5.12. Effective elastic constants of the plasma-sprayed interface zone predicted by the Hashin-Shtrikman and homogenization methods for the baseline idealized unit cell model. 94

Figure 5.13. Schematics of the photoelastic test specimens used to model the porous-surfaced (left) and plasma-sprayed (right) interface zones. 96

Figure 5.14. A comparison of the isochromatic fringe patterns obtained by the photoelastic method (top half) and the computational model (bottom half) for transverse loading of the porous-surfaced interface zone models. Numbers indicate corresponding regions in the two models (refer to text for an explanation)..... 98

Figure 5.15. A comparison of the isochromatic fringe patterns obtained by the photoelastic method (top half) and the computational model (bottom half) for transverse loading of the plasma-sprayed interface zone models. Numbers indicate corresponding regions in the two models (refer to text for an explanation)..... 98

Figure 5.16. A comparison of the isochromatic fringe patterns for the two interface zone models, and the fully bonded and non-bonded interface conditions. A 454 N load was applied transverse to the interface in these cases.....	100
Figure 5.17. The effect of pore size (w , in μm) on the effective elastic moduli predicted by the homogenization method for the porous-surfaced interface zone.....	103
Figure 5.18. The effect of pore size (w , in μm) on the effective elastic moduli predicted by the homogenization method for the plasma-sprayed interface zone.....	103
Figure 5.19. Box plots of the distributions of the local structure components for the porous-surfaced interface zone tissue for different implant surface pore sizes. The horizontal line within the box represents the median value, the upper and lower limits of the box represent the quartiles above and below the median, and the error bars indicate the full range of the local structure component.....	104
Figure 5.20. Box plots of the distributions of the local structure components for the plasma-sprayed interface zone tissue for different implant surface pore sizes.	105
Figure 5.21. Examples of geometrically accurate unit cell solid models for the porous-surfaced (top) and plasma-sprayed (bottom) interface zones. The scales for the two models are different.....	107
Figure 5.22. The effective moduli predicted by homogenization theory for the porous-surfaced geometrically accurate (GAUC) and idealized geometry unit cell models. The GAUC data are presented as mean \pm standard error of the mean. An asterisk indicates a statistically significant difference between the GAUC and idealized geometry values ($p < 0.05$).	110
Figure 5.23. The effective moduli predicted by homogenization theory for the plasma-sprayed geometrically accurate (GAUC) and idealized geometry unit cell models. The GAUC data are presented as mean \pm standard error of the mean. An asterisk indicates a statistically significant difference between the GAUC and idealized geometry values ($p < 0.05$).	110
Figure 5.24. Box plots of the distributions of the local structure components for the porous-surfaced interface zone tissue predicted with the geometrically accurate (GAUC) and idealized geometry unit cell models. The horizontal line within the box represents the median value, the upper and lower limits of the box represent the quartiles above and below the median, and the error bars indicate the full range of the local structure component....	111

Figure 5.25. Box plots of the distributions of the local structure components for the plasma-sprayed interface zone tissue predicted with the geometrically accurate (GAUC) and idealized geometry unit cell models.	112
Figure 5.26. Transverse local structure components (M_{1111}) of the interface zone tissue for portions of typical geometrically accurate unit cell models of the plasma-sprayed and sintered porous surfaces. The scales for the two models are different.	113
Figure 6.1. Two-dimensional plane stress finite element models of the implant and baseline unit cells with idealized geometries representing the porous-surfaced (top) and plasma-sprayed (bottom) designs.....	119
Figure 6.2. Field plots of the global equivalent interface zone strains for the two surface geometries.	121
Figure 6.3. Field plots of the local distortional and volumetric tissue strains for the two surface geometries at a mid-length location on the implants.	121
Figure 6.4. Histograms of the area fraction of tissue experiencing various levels of distortional and volumetric strain for the two implant surface designs at a mid-length location on the implants.....	122
Figure 6.5. Box plots of the distortional and volumetric tissue strains for porous-surfaced implants with different pore sizes. The horizontal line within the box represents the median strain value, the upper and lower limits of the box represent the quartiles above and below the median, and the error bars indicate the full range of the strain data.	123
Figure 6.6. Box plots of the distortional and volumetric tissue strains for plasma-sprayed implants with different pore sizes.	123
Figure 6.7. Histograms of the area fraction of tissue experiencing various levels of distortional and volumetric strain for the geometrically accurate unit cell models of the two surface designs at a mid-length location on the implants.....	124
Figure 7.1. Bone ingrowth (quantified as contact length fraction) into the mesial aspect of the surface structure of porous-surfaced implants for various levels of applied shear displacement (data from Pilliar et al., 1996). Data are presented as mean \pm standard error.	135

Figure 7.2. The global finite element model representing the transverse cross-section of the test implants used in the canine micromovement experiments (Pilliar et al., 1995).	137
Figure 7.3. The local strain components and hydrostatic stress were calculated along the tissue-bone interface, with the normalized path length, s , originating at the bottom of the unit cell.	140
Figure 7.4. Pull-out stiffnesses predicted by the finite element simulation for various values of the Young's modulus and the Poisson's ratio of the early, pre-mineralized interface zone tissue (i.e., four days post-implantation in the rabbit model).	141
Figure 7.5. Equivalent strain across the porous-surfaced interface zone with an applied shear displacement of 45 μm	143
Figure 7.6. Histograms of the local distortional and volumetric tissue strains in the porous-surfaced interface zone for an applied shear displacement of 45 μm	143
Figure 7.7. Field plots of the local distortional and volumetric tissue strains in the porous-surfaced interface zone for an applied shear displacement of 45 μm	144
Figure 7.8. Local transverse strain, longitudinal strain, and hydrostatic pressure at the tissue-bone interface for a porous-surfaced implant with an applied shear displacement of 45 μm . The distance along the bone surface was measured from the bottom to the top of the unit cell (refer to Figure 7.3).	144
Figure 7.9. Equivalent strain across the porous-surfaced and plasma-sprayed interface zones with an applied shear displacement of 10 μm	146
Figure 7.10. Local distortional and volumetric tissue strains in the porous-surfaced and plasma-sprayed interface zones for an applied shear displacement of 10 μm	146
Figure 7.11. Field plots of the local distortional and volumetric tissue strains in the porous-surfaced and plasma-sprayed interface zones for an applied shear displacement of 10 μm	147
Figure 7.12. Local transverse and longitudinal strain components at the tissue-bone interface for porous-surfaced and plasma-sprayed implants with an applied shear displacement of 10 μm	147

Figure 7.13. Local hydrostatic pressure at the tissue-bone interface for porous-surfaced and plasma-sprayed implants with an applied shear displacement of 10 μm	148
Figure 7.14. Model proposed to describe the mechanical regulation of peri-implant tissue formation around porous-surfaced and plasma-sprayed implants.	159

Nomenclature and Abbreviations

B	Strain-displacement matrix
BT	Bone tissue
C_{ijkl}^n	Local or microscopic stiffness (constitutive) tensor
\bar{C}_{ijkl}	Effective stiffness (constitutive) tensor
D	Element elasticity matrix
E	Young's modulus (isotropic material)
E_1	Effective transverse Young's modulus (i.e., normal to the implant interface)
E_2	Effective longitudinal Young's modulus (i.e., parallel to the implant interface)
f_σ	Stress-optic coefficient
$\mathbf{f}^{(e)}$	Element load vector
G_{12}	Effective shear modulus
H	Unit cell height
HT	Healing (interface zone) tissue
I	Implant
$\mathbf{K}^{(e)}$	Element stiffness matrix
L	Unit cell width
M_{ijkl}	Local structure tensor, which relates the local and average strains
M_{1111}	Transverse component of the local structure tensor
M_{2222}	Longitudinal component of the local structure tensor
M_{1212}	Shear component of the local structure tensor
MAF	Mineralized area fraction (%)
$N^{(e)}$	Number of elements
p	Statistical probability
r^2	Coefficient of determination
s	Tissue-bone interface path coordinate
t_i	Tractions applied to boundary of macroscopic domain
t_{sub}	Substrate layer width
t_{surf}	Surface structure layer width
t_{tissue}	Tissue layer width

\mathbf{u}	Nodal displacement vector
\mathbf{u}^n	Exact displacement vector
\mathbf{u}^0	Average or macroscopic displacement vector
$\mathbf{u}^1, \mathbf{u}^2, \text{ etc.}$	Perturbations in displacement vector
$V^{(e)}$	Element volume
V_{UC}	Unit cell volume
\mathbf{v}	Virtual displacement vector
w	Pore size
\mathbf{x}	Macroscopic scale position vector
\mathbf{y}	Microscopic scale position vector
α	Significance level
δ_{ij}	Kronecker delta
ϵ_{ij}	Small deformation strain tensor
ϵ_{ij}^n	Local or microscopic strain tensor
$\bar{\epsilon}_{ij}$	Average or macroscopic strain tensor
ϵ_{ij}^*	Fluctuating (periodic) strain tensor
ϵ_{dist}	Local distortional tissue strain
ϵ_{vol}	Local volumetric tissue strain
$\epsilon_1, \epsilon_2, \epsilon_3$	Local principal tissue strains
Γ	Boundary of macroscopic domain
η	Characteristic dimension; ratio of macroscopic to microscopic scales
λ	Penalty parameter
ν	Poisson's ratio (isotropic material)
ν_{12}	Effective major Poisson's ratio
ν_{21}	Effective minor Poisson's ratio
Ω^n	Total macroscopic and microscopic domains

Superscript T denotes matrix transpose

Chapter 1

Introduction

1.1 Background and motivation

The loss of joint and tooth function from disease and trauma is a significant health care problem, and one that will become more devastating as the population ages. A successful treatment strategy to restore function to diseased or damaged joints and edentulous jaws is the use of orthopaedic and dental implants (Figure 1.1). Dental implant use has tripled since 1986 (American Association of Oral and Maxillofacial Surgeons, 1999), and is expected to continue to rise rapidly. Currently, well over 300,000 dental implants are placed annually in the United States (National Institutes of Health, 1988). Survival rates of dental implants are as high as 91% after 9 years and in some cases, healthy functioning can be achieved even 15 years after implantation (Adell et al., 1981). Similarly, over 120,000 hip implants are placed annually in the U.S. (National Institutes of Health, 1994). In Canada, over 38,000 hip and knee joint replacements were performed in 1996/97, and the number of surgeries is rising (Canadian Institute for Health Information, 1999). Furthermore, these implants are successful, as evidenced by 16-year survival rates of over 95% reported for cemented femoral components (Kobayashi et al., 1997). Clearly, the use of implants is an important and effective treatment strategy in many cases.

However, in certain clinical situations, implant failure rates are unacceptably high. For instance, dental implant failure rates of greater than 35% have been reported 5 years after implantation in the maxilla and posterior mandible (Jaffin and Berman, 1991). Poor results have also been reported in regions with low bone density (Bryant, 1998; Jaffin and Berman, 1991; Jemt, 1993; Sennerby and Roos, 1998) and with limited bone volume (Bryant, 1998; Sennerby and Roos, 1998). Similarly, cementless orthopaedic implants are contraindicated for elderly people because of concerns about insufficient bone stock and ingrowth potential. Furthermore, current rehabilitation protocols require dental implants to remain non-functional for periods of up to 6 months, and rehabilitation periods after hip or knee replacement surgery prevent the patient

from full load-bearing for periods of months. Therefore, the challenge in orthopaedic and dental implantology is to establish implant designs, surgical procedures, and rehabilitation protocols that will restore function to patients more reliably and rapidly.

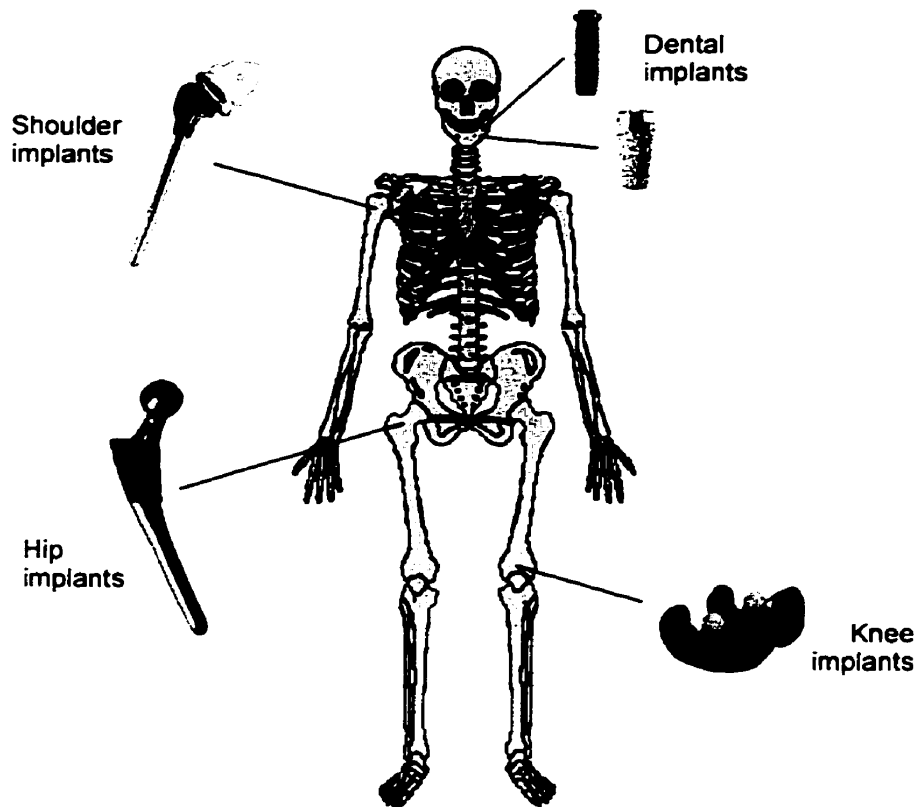


Figure 1.1. Examples of orthopaedic and dental implants used to restore joint and tooth function.

1.2 Bone-interfacing implants and surface design

All orthopaedic and dental implants are intended to be rigidly fixed within the host bone site. Firm fixation is necessary to withstand the functional loads to which these implants are subjected during normal daily activities, such as standing, walking, and in the case of dental implants, mastication. For cementless orthopaedic and press-fit dental implants, rigid fixation is achieved by mechanical interlock between the surface features of the implant and ingrown bone tissue (Figure 1.2). This condition is known as functional osseointegration, and is required for clinical success. Thus, the implant surface design plays an important role in determining clinical success, and as a result is an active area of research.

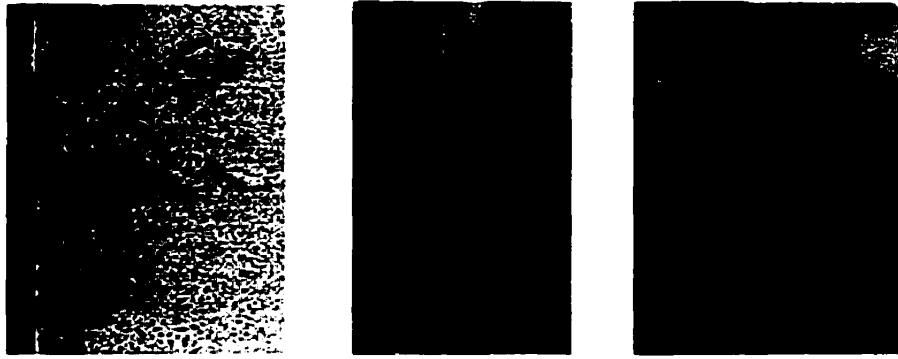


Figure 1.2. Histological sections demonstrating osseointegration of implants with (from left to right) a sintered porous surface (from Pilliar, 1991), a plasma-spray coated surface (from Vercaigne et al., 1998b), and a threaded surface (from Wennerberg et al., 1996c).

Implant surface design encompasses several characteristics, including surface chemistry, surface energy, and surface geometry. Implant surface geometry, including surface roughness and topography, is particularly important because experimental evidence indicates that surface geometry influences peri-implant tissue formation and ultimately, the clinical success of an implant. However, there is considerable debate, due in part to lack of experimental evidence, whether certain geometries are preferable to others in terms of rate and reliability of osseointegration. Furthermore, the mechanisms by which surface geometry affects tissue formation remain unknown. A possible mechanism has been suggested by earlier studies that showed the local mechanical environment in the healing tissue in the peri-implant region (the tissue-implant interface zone) regulates in part whether an implant becomes osseointegrated or anchored by fibrous tissue (Maniatopoulos et al., 1986; Pilliar et al., 1995; Szmukler-Moncler et al., 1998). However, the relationship between implant surface geometry and local mechanical environment and its role in regulating early interface zone tissue formation have not been investigated previously.

Identifying surface geometries that promote more rapid and reliable osseointegration will improve the design and use of orthopaedic and dental implants by simplifying surgical procedures, shortening patient rehabilitation times, and reducing the number of revision surgeries required to correct failed implants. Consequently, patient care will be improved and health care expenditures will be reduced. Additionally, identifying the mechanisms by which implant surface designs influence peri-implant tissue formation has important implications not only to

orthopaedic and dental implant design, but also to the design of fracture repair devices and engineered skeletal tissues.

1.3 Research objectives

Based on the motivation provided above, the objectives of this thesis were:

- (1) to investigate the effect of implant surface geometry on early tissue formation by determining the histological and mechanical characteristics of the tissue-implant interface zone for porous-surfaced and plasma-sprayed implants, two designs which are used clinically in orthopaedic and dental implant systems;
- (2) to develop a micromechanical model to describe accurately the effective and local properties of the porous-surfaced and plasma-sprayed interface zones;
- (3) to validate the numerical model experimentally and analytically; and
- (4) to apply the validated model:
 - a) to investigate the effect of surface geometry and local mechanical environment on peri-implant tissue formation; and
 - b) to propose a quantitative model of mechanical regulation of peri-implant tissue formation.

1.4 Method of approach

The approach used to meet the research objectives is outlined in Figure 1.3. The current work was divided into three components: an animal model study, the development and validation of the computational model, and the application of the computational model. The animal model study, described in Chapter 4, addressed Research Objective 1. The development and validation of the computational model involved development of code to implement the theoretical formulation numerically and validation of the predictions experimentally using mechanical and photoelastic testing. This component of the research addressed Objectives 2 and 3 and is summarized in Chapter 5. The final component of the research, described in Chapters 6 and 7, was the application of the animal model results and the computational model to investigate issues concerning mechanically regulated peri-implant tissue formation (Objective 4).

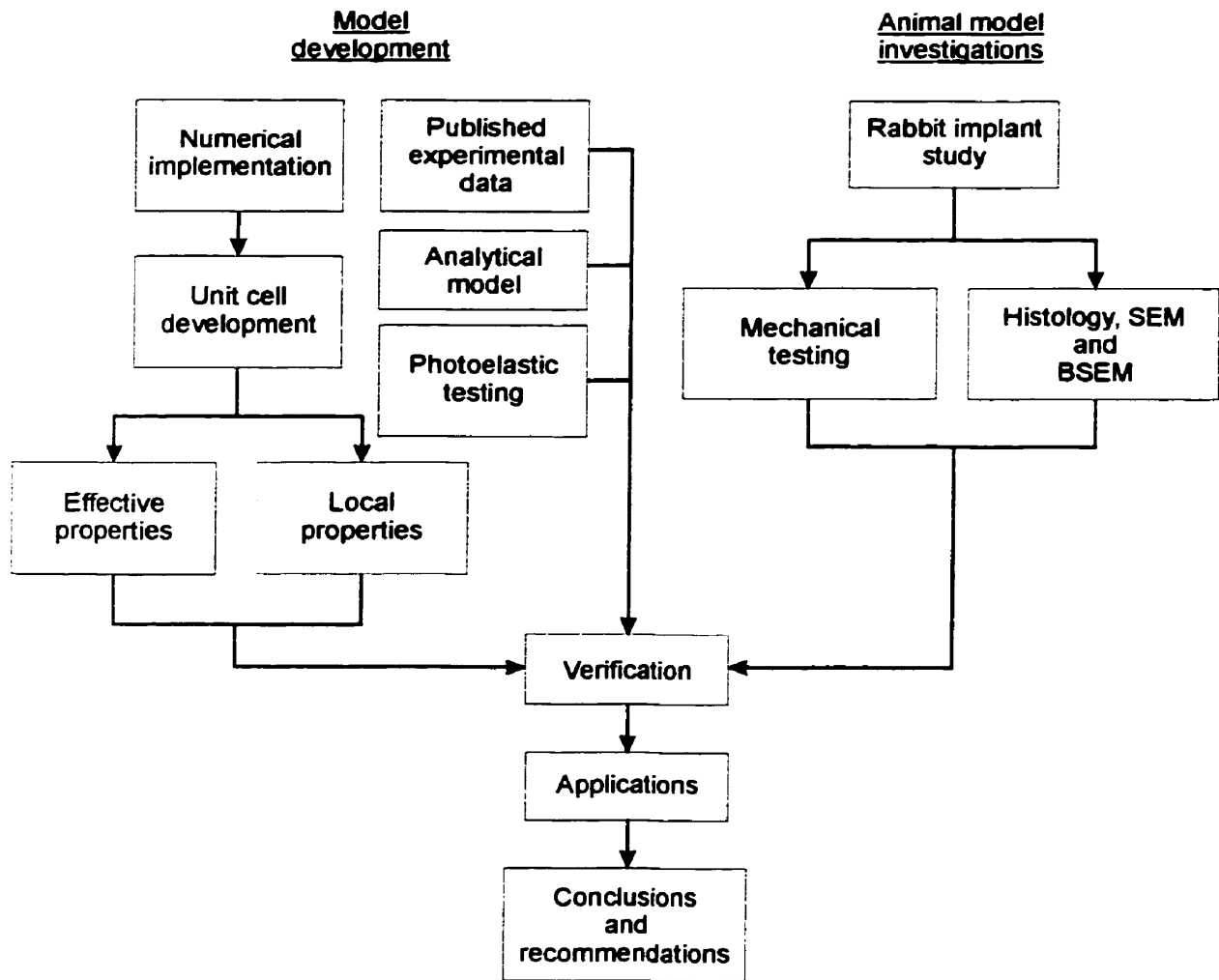


Figure 1.3. Schematic of the method of approach.

1.5 Scope and format of the thesis

The focus of this thesis is the effect of implant surface geometry on early peri-implant tissue formation, with particular emphasis on the regulation of tissue formation by local mechanical factors. Following this introductory chapter, Chapter 2 provides a critical review of the literature related to implant surface geometry and its influence on peri-implant tissue formation. Chapter 3 reviews experimental and computational studies on mechanical regulation of bone formation. The reviews of the literature demonstrate limitations and gaps in our understanding of the role of implant surface geometry and mechanical regulation of peri-implant tissue formation. In Chapter 4, we present the results of an animal model study that

demonstrates implant surface geometry influences early tissue formation. In order to investigate the role of the local mechanical environment in early tissue formation, we developed and validated a computational model to predict the local strains in the healing tissue around bone-interfacing implants. The model is presented in Chapter 5, along with additional investigations related to implant surface design. The computational model is applied in Chapter 6 to explain our observations from the animal experiments and again in Chapter 7 to investigate a quantitative mechanoregulatory model for peri-implant tissue formation. Finally, Chapter 8 summarizes the conclusions and contributions of this thesis, and provides recommendations for future work.

Chapter 2

Implant surface geometry and peri-implant tissue formation: Review of the literature

2.1 Introduction and scope

Various geometric surface designs have been used successfully in bone-interfacing orthopaedic and dental implants. In this chapter, the surface designs and characteristics of currently available cementless orthopaedic and endosseous dental implants are reviewed briefly. Since the focus of this thesis is *geometric* surface designs, implant surfaces formed with ceramic or other coatings that may be “bioactive” are not considered. Investigations on the effect of implant surface geometry on tissue formation and osseointegration, both in vivo and in vitro, are also reviewed.

2.2 Overview of implant surface geometries

The surface geometric features of bone-interfacing implants can be characterized as either macroscopic or microscopic (Pilliar, 1998) (Figure 2.1). Macroscopic features typically have dimensions measured in millimetres or greater, whereas microscopic surface features have dimensions ranging from submicrons to hundreds of microns (but less than a millimetre). Although macroscopic features, such as the threads on screw-shaped dental implants, may play an important role in initial implant stability and subsequent bone remodelling (leading to crestal bone loss for instance (Ko et al., 1992; Pilliar et al., 1991b; Rieger et al., 1990)), significant effects of variations in macroscopic thread design on initial tissue formation have not been demonstrated. Conversely, microscopic surface features have been shown to influence tissue formation and implant osseointegration in a number of in vivo experimental and cell culture studies (see Section 2.3), and therefore are the focus of this review.

The microscopic surface geometries used in cementless orthopaedic and endosseous dental implants and their characteristics are summarized in Figure 2.1 and the sections below. Microscopic features are produced either by subtractive processes, where material is removed from the implant surface resulting in alterations to the *surface texture*, or by additive processes, where material is deposited onto the implant substrate to form a *surface structure*.

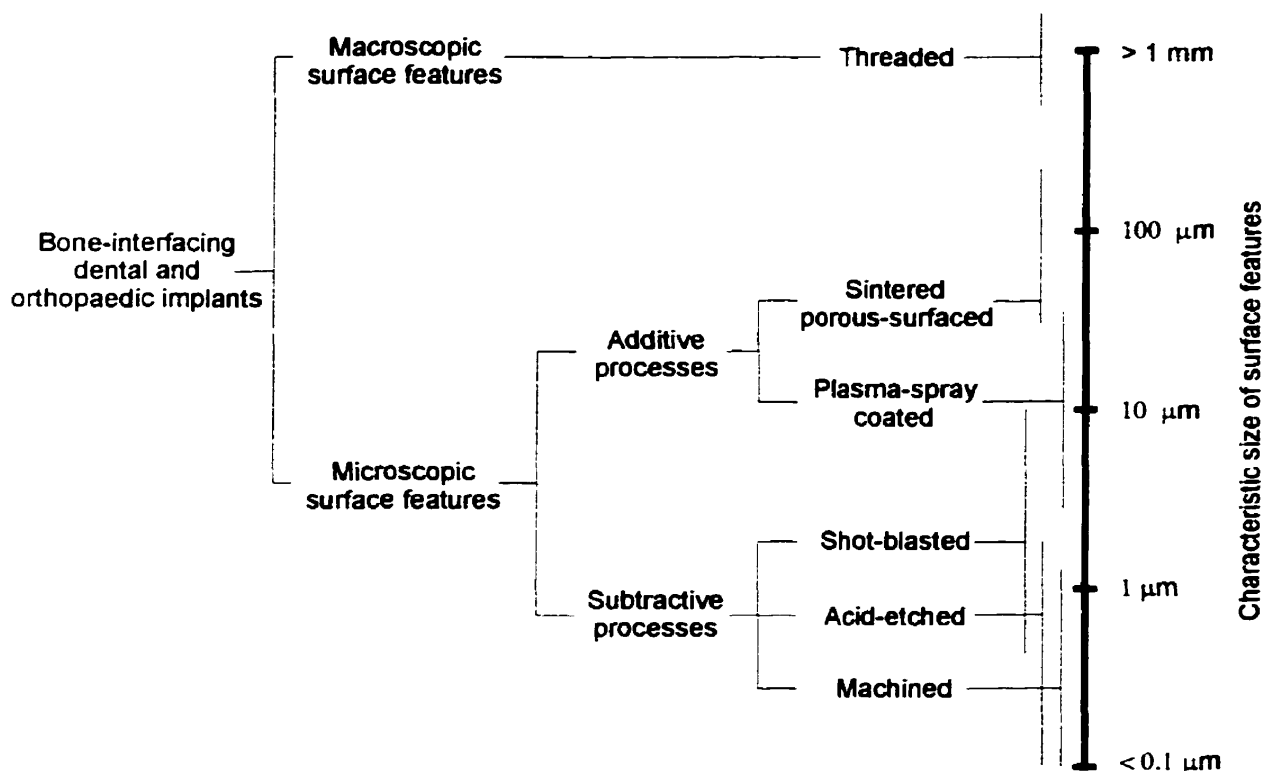


Figure 2.1. Summary of microscopic and macroscopic implant surface geometries.

2.2.1 Subtractive processes to alter implant surface texture

Subtractive processes are those in which material is removed from the implant surface resulting in alterations to the *surface texture*. Machining, shot-blasting, and chemical-etching are examples of subtractive processes that produce surface textures with features ranging in size from submicrons to approximately ten microns.

Machined surfaces

Machining operations to form threaded dental implants, for instance, result in alterations to the surface texture, such as machining lines, pits, gouges and some zones where metallic debris has been “cold-welded” to the implant surface inadvertently (Pilliar, 1998). Thus, implants with macroscopic surface features typically have superimposed microscopic surface textures. The sizes of these features are in the range of microns to sub-microns. Although differences in appearance due to variations in machining exist (Wennerberg et al., 1993), the differences in average surface roughness are minimal (see Section 2.3.1). Furthermore, a

significant effect of these minor surface variations on clinical performance has yet to be demonstrated.

Grit-blasted surfaces

The grit- or shot-blasting process is used to introduce intentionally surface irregularities and textures into which bone can grow, with the purpose of achieving implant fixation by mechanical interlock. The surface features are formed by eroding the substrate with SiC, Al₂O₃, glass, or TiO₂ particles as the blasting medium. This process results in irregular surface pits and depressions ranging in size from submicron to ten microns, depending on the blasting conditions (Pilliar, 1998). A cleaning process is required following blasting to remove any potentially toxic blasting medium that may be deposited onto the implant surface. A typical cleaning process includes dry-blasting with air to remove weakly adhered particles, followed by ultrasonic cleaning in acid and alkali solutions to dissolve particles that are more strongly attached. Post-blasting acid treatments can produce additional textural alterations to the surface by introducing etch pits. The acid treatment may also affect the chemical composition of the implant surface by assisting in the formation of a passive oxide layer.

Chemically-etched surfaces

As with shot-blasting, chemical-etching is used to produce textured implant surfaces for enhancing mechanical interlock between the bone and implant. Chemical-etching involves exposing the implant surface to controlled attack with acid solutions, thereby forming small pits over the surface in a fairly regular array. These pits are typically micron to sub-micron sized, and this treatment results in an approximate doubling of the implant surface area. Chemical-etching of threaded, press-fit, and cementless implants has been used not only on its own, but also in conjunction with shot-blasting to produce textured implant surfaces (Buser et al., 1998; Buser et al., 1991; Cochran et al., 1998).

2.2.2 Additive processes to form implant surface structures

Additive processes are those in which material is deposited onto the implant substrate to form a *surface structure*. As with surface textures, the purpose of surface structures is to provide a surface that will promote secure implant fixation by mechanical interlock between ingrown bone and the surface features. An important distinction between *surface structures* and *surface textures* with regard to bone ingrowth is that a surface structure provides regions into which bone can grow and mechanically interlock such that it can resist shear and tensile (i.e., normal to the

implant surface) forces. Textured surfaces can provide resistance to shear, but because of the surface topography of these designs, they are unable to provide significant resistance in tension (Figure 2.2). Typically, surface structures have features that may be as large as tens to hundreds of microns. In many cases, however, implants with microscopic surface structures (or macroscopic features) may have superimposed surface textures, as discussed below. Implant surfaces formed by additive processes include plasma-sprayed coatings and sintered porous surfaces.

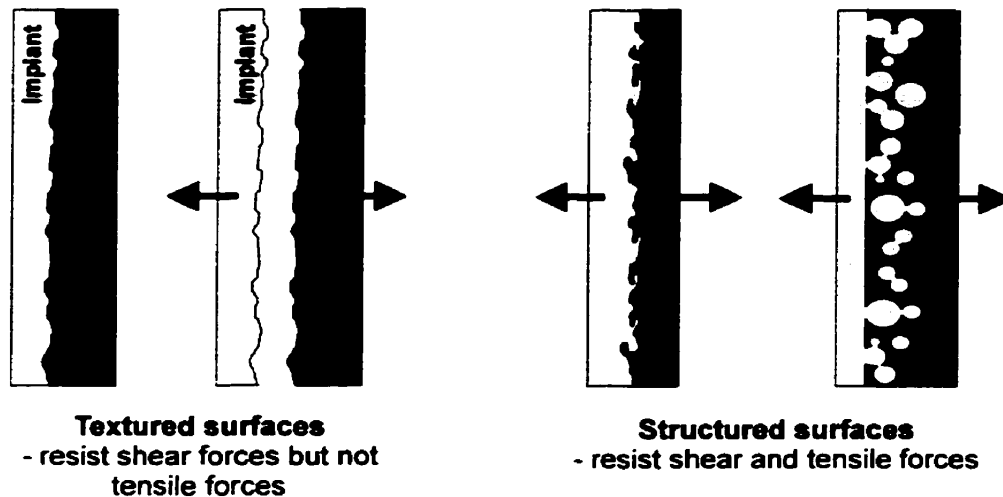


Figure 2.2. Schematic demonstrating that textured surfaces can resist only shear forces, whereas structured surfaces can resist both shear and tensile forces.

Plasma-sprayed surfaces

In the plasma-spraying process, powder particles are fully or partially melted in a hot plasma flame and then accelerated via a carrier gas and the action of an applied electrical potential to the implant surface. When the molten or partially molten material is deposited on the substrate surface, it solidifies rapidly. In some cases, post-plasma spraying anneals are used to improve bonding of the coating to the substrate and to blunt any sharp asperities that may have developed as a result of the high cooling rate (Pilliar, 1987; Pilliar, 1998). The resulting surface structure has an irregular geometry with some porosity (approximately 5% by volume) (Figure 2.3A). The pores are more or less isolated, in contrast to the interconnected network of pores and channels observed with sintered porous surfaces. However, plasma-sprayed surfaces do possess regions with undercuts and intrusions that permit interdigitation and mechanical interlock with tissue (Figure 2.3B).

Typically, metallic (commercially pure titanium (cpTi) and Ti alloy (Ti6Al4V)) and ceramic (so-called calcium hydroxyapatite) plasma-sprayed coatings are used. Similarly, stainless steel and Co alloy coatings can be formed by plasma-spraying. Metallic plasma-sprayed layers form a strong metallic bond with the substrate and typically have a thickness of 10-20 μm . Ceramic coatings are weakly bonded to the substrate, relying primarily on mechanical interlock of the deposited layer with the roughened surface of the metal substrate for attachment (Filiaggi et al., 1991), and typically have a thickness of 50 μm (de Groot et al., 1987).

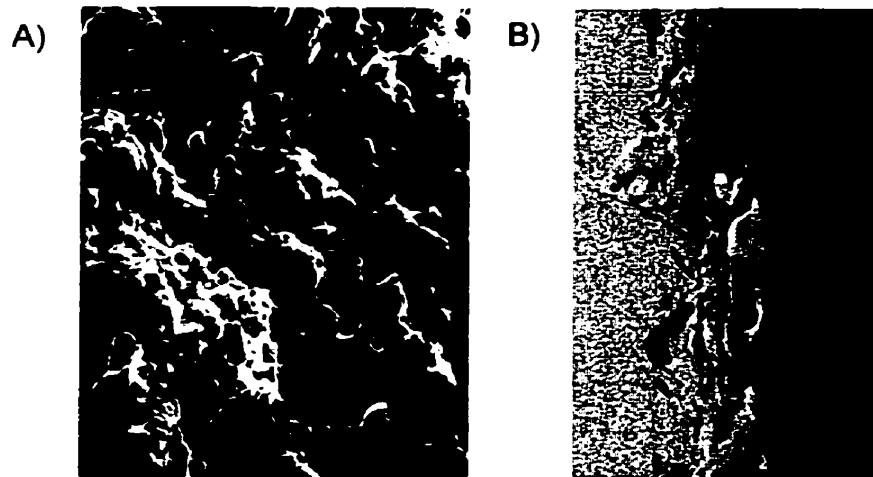


Figure 2.3. (A) Scanning electron micrograph of the surface of a titanium plasma-sprayed implant, and (B) a back-scattered electron micrograph of a longitudinal section of a plasma-sprayed surface that has been applied to a grit-blasted substrate. Original magnifications: (A) $\times 500$; (B) $\times 800$.

Sintered porous surfaces

Another additive process used to form implant surface structures is to sinter metal (cpTi, Ti6Al4V, CoCrMo) powders or fibres to a machined alloy (Ti6Al4V, CoCrMo) substrate to produce a porous surface. The sintering procedure is a high temperature annealing process that causes the powder particles or fibres to bond to each other and the solid substrate, with only minimal changes in particle or fibre shape. Good bonding is achieved by sintering in a high vacuum ($<10^{-5}$ torr), controlled atmosphere furnace at a high temperature. For cpTi and Ti6Al4V powders, sintering at a temperature of 1250°C for approximately one hour produces effective bonding (Pilliar, 1987). Cobalt alloy powders are sintered at slightly higher temperatures for longer times, typically 1300°C for 3 hours (Smith et al., 1989). For some

sintered fibre surface coatings, pressure is also applied to facilitate bonding to the substrate and between fibres (Pilliar, 1987).

The resulting surface structure is dependent on not only the sintering conditions, but also the particle or fibre size range. For orthopaedic implants, powders ranging in size from 50-1000 μm in diameter and fibres ranging in size from 190-300 μm in diameter have been used (Pilliar, 1987). For dental implants, a powder size range of 45-150 μm in diameter (-100/+325 mesh) has been used to produce a porous surface structure that is approximately 250-300 μm thick and consists of two to three particle layers bonded to each other and the implant substrate (Deporter et al., 1990). This surface structure has pore sizes in the range of 50-200 μm , a volume porosity of 35-40%, and a surface region with a three-dimensional interconnected porosity (Figure 2.4A). The combination of large pore size and pore interconnectivity allows ingrowth of bone and three-dimensional interdigitation of the bone with the surface structure. A side effect of the high temperature vacuum sintering treatment is the formation of regular submicron (0.1 μm) thermal etch lines on the surface of the sintered powders and solid substrate, thus superimposing a regular surface texture on the porous surface structure (Smith et al., 1989) (Figure 2.4B).

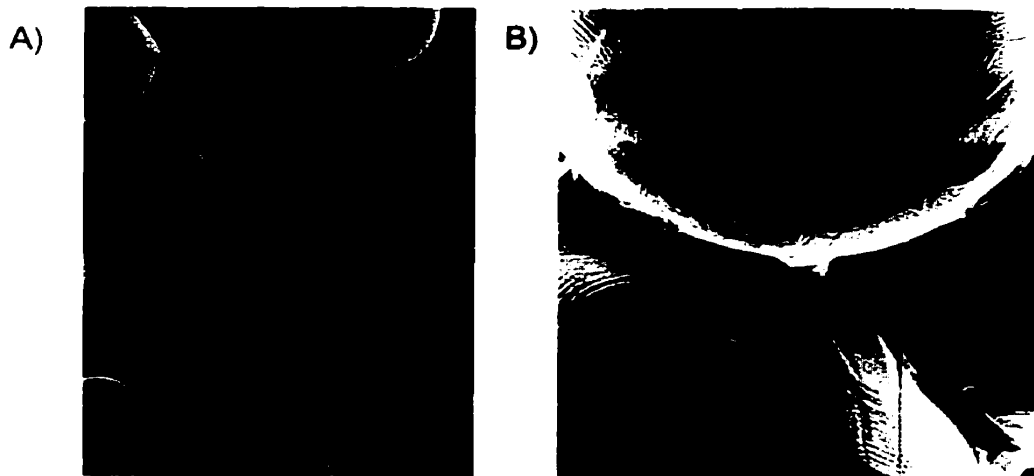


Figure 2.4. Scanning electron micrographs of a Ti6Al4V sintered porous surface demonstrating the 3D interconnected porosity (A) and the submicron-sized thermal etch lines on the sintered particles (B) (from Smith et al., 1989). Original magnifications: (A) $\times 200$; (B) $\times 1000$.

2.3 The effect of surface geometry on peri-implant tissue formation

Historically, the impetus for exploring various implant surface designs was to find surface geometries that facilitated rigid implant fixation by mechanical interlock between ingrown bone and the implant surface features. Numerous studies have demonstrated that several implant surface designs can achieve osseointegration. However, these studies have also demonstrated that some surface geometries may be preferable to others in terms of their ability to osseointegrate more rapidly and reliably. In this section, *in vivo* studies on the effect of surface geometry on peri-implant tissue formation are reviewed, for both non-functional and functional implants. Because of the focus of this thesis, only studies that examined the effect of surface geometry (as opposed to surface chemistry, for instance) are reviewed. General reviews considering other implant characteristics can be found in Cooper et al. (1998), Glantz (1998), Masuda et al. (1998), Schwartz, et al. (1997), and Wen et al. (1996). In addition to *in vivo* studies, several investigators have examined the effect of surface geometry on tissue formation *in vitro*, with the goal of determining the mechanism by which surface geometry influences tissue formation; those studies are reviewed here as well.

2.2.3 In vivo studies

Several experimental studies have examined the effect of implant surface geometry on bone formation by comparison of implant performance *in vivo*. Typically, implant performance is evaluated several weeks post-implantation once osseointegration, and in some cases bone remodelling, has occurred. Usually, the implants investigated are non-functional (i.e., not subjected to direct loading). Several relevant studies of this type are reviewed in this section. Relatively few studies have considered the effect of surface geometry on bone formation for implants subjected to early loading. Because of their relevance to implant osseointegration potential and the timing of post-operative loading, the results of these studies are reviewed as well.

Studies of non-functional implants in vivo

The effect of surface geometry on bone formation around non-functional implants is usually studied by placing the implants transversely in the tibiae or femora of various animal models, such that the implants are not subjected to direct loading. Evaluation of the bone response is made by determining the apposition of bone to the implant interface and measuring the failure strength by push-out, pull-out, or torsional testing.

Using these methods, Carlsson et al. (1988) measured removal torques six weeks post-implantation in rabbit femoral condyles. They found cpTi screws with surface features on the order of 1 μm in size had removal torques that were over 50% higher than the removal torques of screws that were electropolished (with surface irregularities of only 10 nm in size) (Table 2.1). Wilke et al. (1990) implanted titanium cortical screws with textures ranging from smooth (produced by electropolishing) to very rough. The roughest surfaces were produced by plasma-spraying and by sand-blasting with large grit (0.25-0.5 mm) followed by acid attack with HCl/H₂SO₄. They found that the implants with the rougher surfaces had removal torques that were up to seven times greater than those of the implants with the smoother surfaces nine weeks post-implantation. However, there were no differences two weeks post-implantation (Table 2.1). Buser et al. (1998) placed screw-type cpTi implants that were either sand-blasted or machined prior to acid-etching with HCl/H₂SO₄ in the maxillae of miniature pigs, and measured removal torques 4 to 12 weeks post-implantation. They found that the implants that were sand-blasted prior to chemical-etching had removal torques that were 75% to 125% higher than those of implants that were machined prior to etching at all time points (Table 2.1).

Wennerberg and her colleagues have investigated how modifications to the surface texture of screw-shaped cpTi implants by shot-blasting influenced bone response in rabbit femoral and tibial sites four to 52 weeks post-implantation. The results from several studies (Wennerberg et al., 1996a; Wennerberg et al., 1996b; Wennerberg et al., 1996c; Wennerberg et al., 1997) demonstrated that implants with shot-blasted surfaces had greater bone apposition and higher removal torques than those with machined surfaces (Table 2.1). Surfaces shot-blasted with 75 μm particles had slightly greater bone apposition than the surfaces shot-blasted with 25 μm particles (Table 2.1), and implants shot-blasted with 250 μm particles showed no functional differences from those shot-blasted with 25 μm particles. It is notable that the range of average surface roughness (i.e., the arithmetic mean deviation) varied between only 1.16 μm and 1.94 μm for shot sizes ranging between 25 μm and 250 μm .

Similar results have been obtained for press-fit implants with various surface textures. Using a transcortical canine femur model, Thomas and Cook (1985) compared press-fit implants with grit-blasted and polished surfaces and demonstrated greater bone apposition and push-out strength for the grit-blasted implants 32 weeks post-implantation (Table 2.2). Buser et al. (1991) also found a positive correlation between increasing surface roughness (6-50 μm) and bone-implant contact 3 and 6 weeks post-implantation for press-fit implants placed in the tibial and

femoral metaphyses of miniature pigs (Table 2.2). Using a canine mandible model, the same group demonstrated that sand-blasted, acid-etched titanium implants had 38% greater bone apposition than titanium plasma-sprayed implants 3 months post-implantation (Cochran et al., 1998) (Table 2.2). The authors concluded that sandblasted, acid-etched implants were more “osteophilic” and therefore promoted greater osseous contact at earlier time points compared to plasma-sprayed implants. Wong et al. (1995) observed no significant differences in bone apposition between fine sand-blasted, rough sand-blasted, and rough sand-blasted, acid etched implants after 12 weeks in the femoral condyles and tibial diaphyses of miniature pigs. However, the pull-out strengths were dependent on the surface treatment, with the sand-blasted, acid etched implants having the highest strengths (Table 2.2). Steinemann et al. (1986) investigated the mechanical integrity of the bone-implant interface for two surface geometries using a different approach. They compared the “tear-off” forces for sand-blasted and plasma-sprayed titanium implants placed in sites on the surface of the ulnas of monkeys. The “tear-off” force is the tensile force required to detach the implant from the bone. They found this force for the sand-blasted implants to be over twice that for the plasma-sprayed implants (Table 2.2). Given the surface geometries of typical sand-blasted and plasma-sprayed surfaces, these results are surprising and difficult to interpret, particularly because the authors failed to provide any details of the surface geometries or of the integrity of the plasma-sprayed coating after testing.

Dziedzic (1995) investigated bone healing for different implant surface designs using a bone chamber model. She found more extensive bone growth into the chambers with a sintered porous surface than those with an electropolished surface. The author hypothesized that the interconnected porosity of the porous-surfaced implants provided anchorage for the early healing tissue, which not only provided stability for the implant, but also guided bone formation (i.e., osseointegration).

Long-term comparisons of implants with surface *structures* have been limited to studies reported by Luckey et al. (1992) and Friedman et al. (1996). Luckey et al. (1992) found CoCr porous-surfaced implants had higher interface shear strengths on average than CoCr plasma-sprayed implants 8 and 16 weeks post-implantation in cancellous and cortical bone sites of goat tibiae and femora (Table 2.2). However, when compared on a pairwise basis, the plasma-sprayed implants yielded higher interface shear strengths than the porous-surfaced implants (by 18% to 57%) after 16 weeks of implantation in cancellous bone sites. Luckey et al. therefore concluded that the plasma-sprayed surface was more advantageous than the porous-surfaced design. However, the data to support this conclusion were based on results from only two

animals, and the conclusion ignores the differences observed in cortical bone sites, for which the porous-surfaced implants had shear strengths that were higher by 10% to 45%. In contrast to the results obtained by Luckey et al., Friedman et al. (1996) showed CoCr plasma-sprayed implants placed in the cancellous bone of rabbit femoral condyles to have significantly lower bone apposition and shear strengths than CoCr porous-surfaced implants 6 and 12 weeks post-implantation (Table 2.2).

Table 2.1. Summary of in vivo studies on the effect of the surface geometry of non-functional screw-shaped implants on tissue formation and mechanical stability.

Reference	Implant type	Animal model	Healing period	Surface geometry	Bone-implant apposition ¹ (%)	Removal torque ¹ (Ncm)	Estimated shear strength ^{1,2} (MPa)
Carlsson et al. (1988)	cpTi screw-shaped	Rabbit femoral condyle	6 weeks	Electropolished	60	17.2	1.73
				As machined	60	26.4	2.7
Wilke et al. (1990)	Ti screw-shaped	Sheep tibia	2 weeks / 9 weeks	Electropolished	-	70 / 32	1.83 / 0.83
				GB ³ (fine grit) + HF/HNO ₃	-	65 / 96	1.70 / 2.5
				Plasma-sprayed	-	84 / 171	2.2 / 4.5
				GB (med. grit) + HF/HNO ₃	-	74 / 55	1.91 / 1.44
				GB (large grit) + HF/HNO ₃	-	71 / 45	1.86 / 1.18
GB (large grit) + HCl/H ₂ SO ₄	-	88 / 216	2.3 / 5.7				
Buser et al. (1998)	cpTi screw-shaped	Miniature pig maxilla	4 / 8 / 12 weeks	GB (large grit) + HCl/H ₂ SO ₄	-	109.6 / 196.7 / 186.8	5.3 / 9.5 / 9.1
				Machined + HCl/H ₂ SO ₄	-	62.5 / 87.6 / 95.7	3.5 / 5.0 / 5.4
Wennerberg et al. (1996c)	cpTi screw-shaped	Rabbit tibia and femur	12 weeks	GB (25 µm particles)	17.6	40-44	3.1-3.5
				GB (75 µm particles)	24.5	47-53	3.7-4.2
Wennerberg et al. (1996b)	cpTi screw-shaped	Rabbit tibia and femur	12 weeks	As machined	19.1	-	-
				GB (25 µm particles)	36.7	26.5	2.4
				GB (75 µm particles)	38.4	-	-
Wennerberg et al. (1996a)	cpTi screw-shaped	Rabbit tibia and femur	4 weeks	GB (25 µm particles)	26.1	52	4.1
				GB (250 µm particles)	20.2	51	4.0
Wennerberg et al. (1997)	cpTi screw-shaped	Rabbit tibia and femur	52 weeks	As machined	50	58-62	4.6-4.9
				GB (25 µm particles)	62	71	5.9
				GB (250 µm particles)	-	74	5.8

Notes: ¹ In cases with multiple time periods, bone apposition and mechanical strength parameters for each period are given and separated by slashes

² The estimates of the interface shear strengths were based on the measured failure torques and estimates of the implant surface areas

³ GB = grit-blasted

Table 2.2. Summary of in vivo studies on the effect of the surface geometry of non-functional press-fit implants on tissue formation and mechanical stability.

Reference	Implant type	Animal model	Healing period	Surface geometry	Bone-implant apposition ¹ (%)	Estimated shear strength ^{1,2} (MPa)
Thomas and Cook (1985)	cpTi press-fit cylindrical	Dog femur	32 weeks	Polished GB ³	Fibrous tissue Bone	2-2.48 2.85-2.92
Buser et al. (1991)	cpTi press-fit cylindrical	Pig tibia and femur	3 weeks / 6 weeks	Electropolished GB (med. grit) + HF/HNO ₃ GB (large grit) GB (large grit) + HCl/H ₂ SO ₄ Ti plasma-sprayed	24.9 / 25.1 22.3 / 21.6 30.4 / 33.6 52.1 / 57.7 39.2 / 37.8	- - - - -
Cochran et al. (1998)	cpTi press-fit cylindrical	Dog mandible	3 months	GB (large grit) + HCl/H ₂ SO ₄ Ti plasma-sprayed	72 52	- -
Wong et al. (1995)	CpTi, Ti alloy press-fit cylindrical	Pig tibia and femur	12 weeks	Fine GB Rough GB Rough GB + HCl/H ₂ SO ₄	38.5 (mean for all geometries.)	1.78 3.74 5.81
Steinemann et al. (1986)	Disc	Monkey ulna	95 days / 210 days	GB Ti plasma-sprayed	- -	0 / 3.3 ⁴ 0 / 1.5 ⁴
Luckey et al. (1992)	CoCrMo press-fit cylindrical	Goat tibia and femur	8 weeks / 16 weeks	CoCrMo plasma-sprayed CoCrMo porous-surfaced	- -	4.5-5.5 / 7-9 ⁵ 6-7 / 7-15 ⁵
Friedman et al. (1996)	CoCr and Ti press-fit cylindrical	Rabbit femoral condyles	6 weeks / 12 weeks	1 layer CoCr porous-surface 3 layer CoCr porous-surface Ti arc deposited CrCo plasma-sprayed GB Ti	65 / 63 50 / 63 40 / 65 25 / 45 25 / 30	6 / 8 5.5 / 6.5 6 / 6.5 4 / 4.5 0.5 / 1.5

- Notes: ¹ In cases with multiple time periods, bone apposition and mechanical strength parameters for each period are given and separated by slashes
² The interface shear strength estimates for the press-fit implants were provided in the references, except for Wong et al., in which case the estimate was based on push-out forces and the implant geometry
³ GB = grit-blasted
⁴ Tear-off strengths (see text)
⁵ The range of values is due to differences between strengths in cortical and trabecular sites. See text for elaboration of results.

Studies of functional implants in vivo

Very few studies have compared tissue formation around implants with different surface designs under conditions of functional loading or controlled micromovement. Some micromovement studies, such as those by Søballe et al. (1992b), have compared implant surfaces with different geometry and chemistry, and therefore conclusions on the effect of surface geometry alone cannot be made based on their results.

Maniatopoulos et al. (1986) compared threaded and porous-surfaced endosseous endodontic implants subjected to early loading resulting in limited relative movement. The threaded implants displayed better initial stability as indicated by higher pull-out forces because of mechanical anchorage resulting from thread-bone interlock versus the initial frictional resistance with the press-fit porous-surfaced implants. After 3 and 6 months of function, however, the porous-surfaced implants displayed secure fixation because of bone ingrowth while the threaded implants progressively loosened as a thick fibrous tissue encapsulating layer developed (Table 2.3). Cochran et al. (1998) compared the bone response to functional titanium implants with sandblasted, acid-etched surfaces to those with plasma-sprayed coatings. The implants were allowed to heal for 3 months in the canine mandible, followed by functional loading for up to 12 months. They found 22% greater bone apposition to the sandblasted implants after 12 months of loading (Table 2.3). There was no significant difference in bone apposition between the two surface designs after 3 months of loading. The effect of loading in this study was likely limited to bone remodelling rather than initial tissue synthesis and mineralization, because loading was applied only after osseointegration had occurred (Cochran et al., 1998). Brunette and Chehroudi (1999) found that smooth implants that were stabilized in the rat skull had a higher frequency of mineralized tissue production than unstabilized smooth implants. For implants with micromachined grooved or pitted surfaces, the effect of stabilization was evident, but not as marked as with the smooth-surfaced implants. Vercaigne et al. (1998a) concluded that the similarities in bone contact they observed between titanium plasma-spray coated and grit-blasted implants (in contrast to previous studies) was due to mechanical factors, including micromovement and varying load transfer to the interface tissue, influencing the tissue formation.

Pilliar and his colleagues have examined the effect of implant surface geometry on bone formation for endosseous dental implants subjected to *controlled* loading shortly after implantation, before osseointegration has occurred. The details of the model are described in

Section 3.2.3. In pilot studies with just two animals, Pilliar and his colleagues studied the healing response around plasma-sprayed implants for comparison with the porous-surfaced design (Simmons and Pilliar, 2000). Initial torsional displacements of 75 μm were applied to the two implant designs. After a three-week period of imposed force-controlled relative movement, the porous-surfaced implant was anchored to the surrounding bone by ligament-like fibrous connective tissue, with the collagen fibres more or less obliquely oriented to the implant surface and intertwined with the three-dimensional open-pored structure. In contrast, bone appeared to form close up to the plasma-sprayed surface with many regions of bone ingrowth into the surface irregularities that characterize these implants. Thus, while the porous-surfaced implants subjected to 75 μm of initial relative movement achieved a ligamentous-like anchorage, the plasma-sprayed implants became “osseointegrated” for this level of initial relative movement. A hypothesis to explain the differential response of these two surface designs under conditions of imposed loading is proposed in Chapter 7 of this thesis.

Table 2.3. Summary of in vivo studies on the effect of the surface geometry of functional implants on tissue formation and mechanical stability.

Reference	Implant type	Animal model	Healing period	Surface geometry	Bone apposition (%)	Estimated shear strength ¹ (MPa)
Maniatopoulos et al. (1986)	Various CoCrMo	Dog mandible	0 months / 3 months / 6 months / 12 months ²	Threaded	39.2 / 34.8 / 9 / 1.33	10.58 / 7.51 / 1.56 / -
				Smooth	-	0.42 / 0.17 / 0.05 / -
				Porous-surfaced	0 / 41 / 57.2 / 53.3	0.45 / 5.39 / 7.20 / -
Cochran et al. (1998)	cpTi press-fit cylindrical	Dog mandible	3 months unloaded + 3 months loaded ³	GB ⁴ (large grit) + HCl/H ₂ SO ₄	68	-
				Ti plasma-sprayed	78	-
			3 months unloaded + 12 months loaded	GB (large grit) + HCl/H ₂ SO ₄	72	-
				Ti plasma-sprayed	59	-

Notes: ¹ The interface shear strength estimates for the implants in the study by Maniatopoulos et al. (1986) were provided in the paper

² The implants in the study by Maniatopoulos et al. (1986) were loaded functionally immediately post-implantation

³ The implants in the study by Cochran et al. (1998) were loaded functionally after 3 months of unloaded healing

⁴ GB = grit-blasted

2.2.4 In vitro studies

The evidence demonstrating that implant surface geometry influences peri-implant bone formation in vivo has motivated several researchers to investigate, primarily through cell culture studies, the mechanisms for the differential tissue response to various surface designs. The paradigm is that the roughness and topography of the implant surface may influence the recruitment, attachment, locomotion, and shape of mesenchymal cells (Brunette and Chehroudi, 1999), resulting in alterations in proliferation, metabolism, matrix synthesis, and differentiation (Schwartz and Boyan, 1994). These phenomena are not limited to mesenchymal cells, as discussed in the review paper by Curtis and Wilkinson (1997).

Generally, one would expect a surface with greater surface area to provide greater area for protein adsorption, and therefore more opportunities for cell attachment. However, fibroblasts have been shown to attach and spread equally well on many titanium surfaces, including machined, grit-blasted, plasma-sprayed, and sintered porous (Brunette, 1988). Osteoblast-like cells appear to do so as well, but demonstrate improved adhesion, spreading, and proliferation on rougher surfaces (Ahmad et al., 1999; Bowers et al., 1992; Degasne et al., 1999). Cell orientation and patterns of mineralization also appear to be guided by the surface topography (Brunette and Chehroudi, 1999; Chehroudi et al., 1997; Cooper et al., 1999; Gomi and Davies, 1993; Ong et al., 1996). Several investigators have observed interesting effects of structured surface on cell orientation. Inoue et al. (1987) and Lowenberg et al. (1987) compared the orientation of human gingival fibroblasts in multilayers adjacent to metal discs with smooth and sintered porous surfaces. They observed that the cell bridges between the implant and surrounding multilayer oriented parallel to circumferential grooves of the smooth disc, but perpendicular to the porous-surfaced disc. Cells cultured on very rough or structured surfaces have been shown to achieve multiple points of attachment, sometimes spanning depressions in the surface, or in the case of sintered porous surfaces, bridging between particles (Brunette, 1988; Groessner-Schreiber and Tuan, 1992). Not surprisingly, this phenomenon may also be influenced by surface composition (Shah et al., 1999). Despite recent insights on aspects of integrin function and cytoskeletal organization in cell-implant interactions (Ahmad et al., 1999; Shah et al., 1999), the specific implications of the effect of surface geometry on cell attachment, spreading, and shape in terms of cell function are generally unknown.

What is known, however, is that surface roughness and surface topography alter mesenchymal cell function. Several studies, particularly those by Boyan, Schwartz, and their

colleagues, have shown that surface roughness can alter: (1) osteoblast proliferation, differentiation, and matrix production (Lincks et al., 1998; Martin et al., 1995); (2) the local production of growth factors and cytokines by osteoblast-like cells (Kieswetter et al., 1996; Lincks et al., 1998); and (3) bone cell response to systemic hormones (Batzer et al., 1998; Boyan et al., 1998). Reviews of earlier studies by the Boyan and Schwartz group were provided in Schwartz et al. (1997), Boyan et al. (1996), and Schwartz and Boyan (1994). A possible mechanism for the influence of surface roughness on osteoblast function was recently proposed by Lohmann et al. (1999). In general, the studies by this group concluded a rougher surface is more favourable for bone formation. This finding is consistent with that observed in other cell culture studies (Ahmad et al., 1999; Gomi and Davies, 1993; Groessner-Schreiber and Tuan, 1992) and many in vivo studies.

It has also been suggested that surface texture may dictate the mechanism of osseointegration based on the stability of the fibrin scaffold that forms shortly after implantation (Davies, 1998; Dziedzic, 1995). This hypothesis states that a stable scaffold that is firmly attached to the implant surface will permit osteogenic cells to reach the implant surface where they can initiate bone formation (i.e., contact osteogenesis). Stable attachment of fibrin to the implant is assisted by a roughened surface that provides a greater surface area for protein adsorption and physical features with which the fibrin can become entangled.

The mechanisms by which surface geometry influences peri-implant tissue formation is likely dependent on the surface roughness, surface topology, and the size of the surface features relative to the size of the cells responsible for initial tissue formation. For surface textured implants, where the surface features are smaller than the size of the adherent cells, the modulation of cellular activity by the texture is a plausible explanation for the observed differences in bone formation. Differences in bone formation for *smooth* and *textured* surfaces may also be due to the stability of the fibrin scaffold as proposed by Davies (1998). However, differences in bone formation around implants with different surface structures (i.e., plasma-sprayed and porous-surfaced) have not been shown in vitro, with the only comparison being that by Brunette (1988), which showed similar cell morphology on titanium plasma-sprayed and sintered porous surfaces.

2.4 Summary

In vivo experimental results demonstrate clearly that bone formation is influenced by the implant surface geometry. However, the in vivo evidence to date has been based on observations made several weeks post-implantation after osseointegration and, in some cases, bone remodelling have occurred. The early healing response prior to osseointegration is also of interest, since it is during this period that cellular differentiation and tissue synthesis and mineralization leading to osseointegration are initiated. In vivo studies have focussed on the early healing response, but generally have been limited to comparison of various implant surface *textures* rather than surface *structures*. Furthermore, extrapolation of in vitro results to the in vivo situation is often difficult, particularly in cases where surface texture is not the only variable, as is inevitably the case. The issue of early healing response in vivo next to implants with different surface structures and the mechanical characterization of the repair/regeneration tissues formed within the implant-host bone interface zone has not been addressed fully. Implants with plasma-sprayed coatings and porous-surfaced structures are frequently used in orthopaedics and dentistry, and therefore a comparison of the tissue responses to implants with these surface designs will not only address a gap in the literature, but also has important clinical value.

Chapter 3

Mechanical regulation of tissue formation: Review of the literature

3.1 Introduction and scope

It is well recognized that mechanical forces can have a significant effect on the formation and remodelling of a variety of tissues, including mesenchymal tissues. Of particular relevance to this work are the numerous experimental studies that have demonstrated the importance of mechanical regulation of tissue formation around dental and orthopaedic implants. However, studies on fracture healing, distraction osteogenesis, and skeletal morphogenesis have also contributed significantly to our understanding of the role of mechanical stimuli in the formation of bone, cartilage, and other connective tissues. The first portion of this chapter reviews several experimental investigations of mechanically regulated tissue formation, with emphasis on bone formation. Frequently, however, measuring the local mechanical environment to which the developing tissue is exposed is difficult or impossible. Consequently, the finite element method and other computational modelling techniques have been used to predict the mechanical environment in developing tissue and to explore the relationship between mechanical parameters and tissue formation. The second part of this chapter reviews those computational efforts, with emphasis on the different modelling approaches and the outcomes of these analyses.

3.2 Experimental studies of mechanically regulated tissue formation

The influence of mechanical stimuli on tissue formation and maintenance is well recognized. The studies reviewed in this section have provided convincing evidence that mesenchymal tissue formation is regulated in part by mechanical factors. The effect of mechanical factors on tissue maintenance and remodelling is not addressed in this review, since the focus of this thesis is *initial* tissue formation (i.e., modelling) and the relationship between mechanically regulated tissue modelling and remodelling is not well established. Much of our knowledge on the mechanical regulation of mesenchymal tissue formation comes from studies and observations of fracture healing, distraction osteogenesis, and skeletal development. Studies

of tissue formation around implants subjected to early loading have also provided persuasive evidence of the important role of mechanical factors in achieving implant osseointegration.

3.2.1 Fracture healing and distraction osteogenesis

The influence on the healing process of the local mechanical environment at a fracture site has been well demonstrated clinically and experimentally. The principal aim of clinical treatments for fracture repair is to limit the relative movement of the fracture fragments so that bony union may be achieved. The degree of interfragmentary movement dictates in large part the course of fracture healing (Perren, 1979; Perren and Cordey, 1980). Rigid immobilization of a fractured bone, using fixation plates for instance, leads to primary healing in which no callus is formed and direct cortical union occurs. The other extreme, when interfragmentary movement is excessive, leads to nonunion and the formation of a pseudoarthrosis. Fracture fixation devices, such as casts, intramedullary rods, and external fixation frames result in some degree of motion and callus formation. Generally, the quantity and quality of callus tissue formed are correlated with the degree of interfragmentary motion (McKibbin, 1978). Chao and co-workers (1995; 1998) showed that rigid fixation with plates and screws facilitated more rapid healing than less rigid external fixators. Furthermore, differences in the rate and pattern of healing were observed between external fixators with different degrees of stiffness. Sarmiento et al. (1977) examined the effect of external loading on fracture healing by comparing healing in non-functional and immediately functional weight bearing rat femora in which the fracture was stabilized by an intramedullary rod. They showed that the fractures subjected to loading (and presumably greater interfragmentary movement) developed larger calluses with more cartilage. However, in contrast to the results of Chao et al., bone formation occurred earlier and more extensively in the weight-bearing cases, with a concomitant more rapid return of functional mechanical integrity. These results suggest that method of fixation, the applied loads, and the local mechanical environment play important roles in determining the course of healing. Furthermore, the results of Sarmiento et al. suggest that some degree of interfragmentary movement is conducive to more rapid fracture healing. This phenomenon was also demonstrated by Goodship and Kenwright (1985) who showed that controlled interfragmentary axial micromovements induced by a 360 N load applied at 0.5 Hz for 17 minutes per day for 10 weeks improved healing of tibial osteotomies in sheep compared with rigid fixation. Similar methods have been applied to repair human tibial fractures (Kenwright and Goodship, 1989; Kenwright et al., 1991) and recent

evidence suggests that the rate and degree of induced micromovement should be coordinated with the stage of fracture healing for greatest effectiveness (Goodship et al., 1998). Similar results were obtained by Wolf et al. (1981), who suggested that rapid fracture healing might require rigid immobilization during the initial stages of healing followed by intermittent compressive movement during the later stages.

Related to fracture healing is distraction osteogenesis, which is the generation of new bone by separation of osteotomized bone in a controlled fashion. The distraction osteogenesis process is therefore a fracture healing process under relatively extreme loading conditions. It has received growing acceptance not only for the treatment of several orthopaedic and craniofacial conditions, but also as a model to investigate the effects of mechanical forces on bone formation. Several researchers have attempted to determine the optimal distraction conditions for various limb or mandibular lengthening procedures. Distraction rates of 0.7 mm/day have been shown to be conducive to cell proliferation and tissue formation and preferable to lower rates of 0.3 mm/day (Li et al., 1997). In terms of uniaxial strain, distraction levels with physiological magnitudes ($<2\%$) have been shown to permit bone formation in a mandible model, whereas hyperphysiologic strain magnitudes ($>20\%$) led to fibrous tissue formation (Meyer et al., 1999). The stiffness of the distraction device (Goldstein et al., 1994; Richards et al., 1999a) and the angle of the osteotomy (Richards et al., 1998) also influence the structural characteristics of the newly formed bone. New bone formation under conditions of external loading has also been investigated using bone chambers (Guldborg et al., 1997; Tägil and Aspenberg, 1999). Using this model, Tägil and Aspenberg (1999) showed that application of 2 MPa of compressive stress (20 cycles at 0.17 Hz twice per day) to the developing tissue resulted in cartilage formation adjacent to loading piston, whereas bone formation occurred under unloaded conditions.

Although the studies reviewed above provide important information on the role of mechanical stimuli in fracture healing and distraction osteogenesis, the results are limited in their universal applicability because the local mechanical environment is poorly defined. Several researchers have attempted to resolve this limitation by correlating specific mechanical stimuli with patterns of tissue formation. Perren and co-workers proposed the interfragmentary strain hypothesis, which states that tissue can only be formed in the interfragmentary region if the local axial strain is less than the failure strain of the tissue (Perren, 1979; Perren and Cordey, 1980). Once a tissue has formed, it will contribute to the rigidity of the fracture site, and therefore alter the local mechanical environment, making possible the next stage of tissue formation. Although

this theory is valid in concept, it disregards the complex mechanical environment that results from structural and mechanical heterogeneity in the interfragmentary region. Based on earlier work by Roux, Pauwels (1980) developed general concepts relating tissue formation to specific mechanical stimuli that accounted for the multiaxial nature of tissue stresses and strains. His theory was based on observations from fracture healing, skeletal development, and tissue formation after corrective surgical procedures. He concluded that hydrostatic compression causes cartilage formation, whereas distortional stresses cause fibrous tissue formation. He believed there was no specific stimulus for bone formation. Carter and his associates have further developed the theories of Perren and Pauwels using computational models; their “Tissue Differentiation Hypothesis” and efforts by other investigators to relate patterns of tissue formation to the mechanical environment predicted by computational models are discussed in Section 3.3.

3.2.2 Skeletal development

The influence of mechanical forces on skeletal development has not been well established because the mechanical environment to which embryonic or fetal tissue is exposed is difficult to measure or manipulate experimentally. However, the coincidence of the timing of the first muscular contractions during skeletal morphogenesis and the process of endochondral ossification suggests that physical factors may influence skeletal development (Burger et al., 1991; Wong and Carter, 1990b). Additional evidence from in vitro studies supports the role of mechanical stimuli in skeletal development (reviewed in Carter and Wong, 1988a; Wong and Carter, 1990b). For instance, Klein-Nulend et al. (1986) studied the effect of intermittent hydrostatic pressure on the mineralization of fetal cartilaginous mouse metatarsals. They showed that the loaded metatarsals had a mineralized diaphyseal portion that was two to three times longer than that of unloaded controls, leading to the conclusion that the loading stimulated the mineralization process. This study has been the subject of subsequent biomechanical investigations and is discussed in further detail in Section 3.3.3.

3.2.3 Peri-implant tissue formation

The effect of mechanical stimuli on tissue formation around implants is well recognized by clinicians and scientists. Early loading of bone-interfacing implants can result in excessive movement of the implant relative to the host bone site, and several clinical and experimental studies have demonstrated that implants subjected to excessive early loading do not

osseointegrate. Based on those observations, dental and orthopaedic implant rehabilitation protocols, which limit the initiation and magnitude of loading, have been established. Reviews by Pilliar (1991) and by Szumukler-Moncler et al. (1998) have provided thorough summaries of a number of studies on the effect of implant micromovement on tissue formation. In this section, the current understanding of the effect of implant relative movement and mechanical factors on peri-implant tissue formation is summarized.

Currently, the accepted paradigm regarding implant relative movement is that loading of bone-interfacing implants during the early healing period is only detrimental to peri-implant bone formation if the loading results in "excessive" micromovement. Excessive micromovement results in formation of fibrous tissue around the implant, which provides non-rigid fixation and an unpredictable clinical outcome. Peri-implant fibrous tissue formation due to excessive relative movement has been demonstrated experimentally for porous-surfaced implants (Cameron et al., 1973; Pilliar et al., 1981; Pilliar et al., 1995; Pilliar et al., 1996), porous metal fibre coated implants (Bragdon et al., 1996; Ducheyne et al., 1977; Heck et al., 1986), plasma-sprayed implants (Hollis et al., 1992; Søballe et al., 1992b), blade implants (Brunski et al., 1979), threaded implants (Akagawa et al., 1986; Maniatopoulos et al., 1986), fixation screws (Uthoff and Germain, 1977), and in bone chambers (Aspenberg et al., 1992; Goodman et al., 1993). Conversely, a well-fixed implant that experiences minimal relative movements is able to osseointegrate. Furthermore, as was shown by Uthoff and Germain (1977) and Søballe et al. (1993), the fibrous tissue around an implant that was subjected to a period of excessive micromovement can be replaced by bone if the implant is immobilized.

Until fairly recently, however, the maximum level of implant relative movement for osseointegration was unknown. Early attempts to quantify the critical threshold level of relative movement for bone formation were based on retrospective analyses of studies for which the implant loading conditions were poorly defined. For instance, retrospective analyses of experiments with porous-surfaced implants (Maniatopoulos et al., 1986; Pilliar et al., 1981) indicated that relative movements above approximately 150 μm prevented bone ingrowth (Pilliar et al., 1986), whereas bone formation within the surface pores occurred for implant relative movements estimated to be as high as 21 μm (Pilliar et al., 1993).

More recently, experiments have been designed to apply better-defined loading conditions to determine tolerable levels of micromovement. In two of those experiments, the

relative movement of the implant was subjected to *displacement* control. The results of displacement-controlled experiments with plasma-sprayed implants suggested 200 μm of rotational displacement (i.e., arc length displacement of the implant interface) inhibits bone ingrowth (Hollis et al., 1992). Bragdon et al. (1996) showed that rotational displacements of 20 μm permitted bone growth into sintered titanium fibre mesh surfaces, but displacements of 150 μm prevented ingrowth. Intermediate displacements (e.g., 40 μm) resulted in a mixture of fibrous tissue and bone. However in the actual clinical situation, implant movement is subjected to *load* control, either by extraneous loading or muscle contraction. Søballe et al. (1992a; 1992b) investigated tissue formation around titanium and hydroxyapatite plasma-spray coated implants under load controlled movements. They implanted loading devices into the femoral condyles of dogs such that the test implants would be loaded during gait. The device limited the maximum relative movement of the test implants to a predetermined level. Using this experimental set-up, they demonstrated that maximum relative movements of 150 μm and 500 μm inhibited ingrowth of bone into titanium plasma-sprayed coatings, and that the surface chemistry influenced the response to implant movement. However, it is important to note that in those experiments as peri-implant tissue healing progressed and the tissue matured, the implant movements resulting from the applied loads would decrease. Therefore, the movement levels reported are maximum values; in order to determine the *history* of implant movement throughout the experiments, it would be necessary to estimate the applied loads and tissue properties (see Section 3.3.4). Hollister et al. (1996) used a device that applied cyclic loads of 35 N to porous-surfaced implants and found no significant difference in type-I procollagen synthesis between unloaded and loaded implants. The relative movement of the implants in those experiments was estimated immediately post-implantation to be less than 50 μm . However, as in the experiments by Søballe et al., the movement history of the implants was not measured.

Pilliar and his research group (1995; 1996) have examined the effect of implant surface geometry on bone formation for endosseous dental implants subjected to controlled loading shortly after implantation, before osseointegration has occurred. They developed a custom loading apparatus with which they were able to apply relative shear displacements at the implant-tissue interface under torsional *load* control (Pilliar et al., 1995). Using this apparatus and a canine mandible model, they initiated loading of the implants one week after implantation, before initial tissue mineralization had occurred. For the first seven days of loading, they used

displacement control and determined the average reaction torque. For the remaining 18 days of the experiment, the implants were subjected to this average torque and the reaction displacements were recorded. Thus, the torque-displacements characteristics were recorded throughout the history of the loading regime. As expected, in cases where tissue maturation leading to bone formation occurred, the relative displacements decreased in the first few days of torque-controlled movements. Using this experimental model and protocol, Pilliar et al. (1995; 1996) determined that bone ingrowth can occur for Ti6Al4V porous-surfaced implants subjected to initial relative displacements of up to 50 μm . Greater relative displacements of 75 μm resulted in implant anchorage by fibrous tissue forming and intertwining with the porous surface region. They have also used this animal model to study the healing response around plasma-sprayed implants for comparison with the porous-surfaced design (Simmons and Pilliar, 2000). The results of that pilot study indicated that the healing response under conditions of early loading might be dependent on implant surface design. The details of the experimental method and the results are provided in Section 2.3.1 and Chapter 7. The observation that peri-implant tissue formation under conditions of early loading may be influenced by the implant surface geometry is interesting and consistent with previous observations (Brunette and Chehroudi, 1999; Goodman et al., 1993; Hollis et al., 1992; Maniatopoulos et al., 1986; Vercaigne et al., 1998a). However, the relationship between implant surface geometry, peri-implant tissue formation, and mechanical factors remains largely unknown. Furthermore, all implant micromovement studies use implant *displacement* (torsional or axial) as the parameter that dictates tissue formation. Clearly, differences in implant shape, surface design, and implantation site will influence the threshold level of implant relative movement for bone formation. Therefore, a dimensionless parameter, such as local tissue strain, is necessary to provide a more universal criterion with which implant osseointegration potential can be assessed. However, as alluded to earlier, measuring the local mechanical environment in the healing peri-implant tissue is impossible with current technologies. As a result, investigators have estimated the local tissue stresses and strains using computational models in an effort to determine the relationship between tissue strain and tissue formation; those studies are discussed in Section 3.3.

It is interesting to note that low-amplitude mechanical stimulation may in fact be stimulatory to implant osseointegration. Rubin and McLeod (1994) showed that porous-surfaced implants stimulated 100 seconds per day for eight weeks with a sinusoidal strain stimulus (amplitude of 150 $\mu\epsilon$) had greater bone ingrowth (measured as area fraction) than non-stimulated

implants. Furthermore, the response was dependent on the frequency of the stimulation, with a 1 Hz stimulus producing 28% bone ingrowth and a 20 Hz stimulus producing 69% ingrowth. It is likely, however, that remodelling was responsible for at least part of the observed osseointegration response. It is not known whether mechanical stimulation has a positive effect on *initial* peri-implant bone formation and what role implant surface geometry may play in mediating the tissue response.

3.2.4 Cell culture studies

Although *in vitro* studies on the effect of mechanical stimuli on cell function have revealed important information concerning the mechanisms of mechanotransduction and mechanoregulation, those studies were intentionally not addressed in this review. One reason for not surveying those studies was to limit the scope of this review to tissue-level studies, since the current research focuses on tissue-level mechanics and biology. The other reason is that the relationship between tissue-level mechanical stimuli and cell-level mechanical signals is poorly understood. As a result, interpretation of many cell culture studies within the context of the *in vivo* situation is difficult. Significant efforts to understand the factors important to the relationship between tissue-level and cell-level mechanical stimuli are necessary before the bridge between tissue and cell mechanics can be made. Certainly, this should be an important area for research in the immediate future.

3.3 Computational studies of mechanically regulated tissue formation

Computational methods, particularly the finite element method, have been used in orthopaedic and dental biomechanics research for close to thirty years. A thorough review of the applications of finite element analysis (FEA) to biomechanics is beyond the scope of this chapter. Surveys of the application of FEA to orthopaedic biomechanics can be found in Huiskes and Chao (1983), Huiskes and Hollister (1993), and Beaupré and Carter (1992). Reviews of the application of FEA to dental biomechanics can be found in Kohn (1992) and Koriath and Versluis (1997). The use of FEA to design of orthopaedic, dental and cardiovascular biomaterials was reviewed in Vander Sloten et al. (1998).

Of primary interest for this thesis are those studies that use the finite element method or other computational techniques to explore the relationship between mechanical parameters and

tissue formation and healing. In particular, studies of tissue formation at fracture healing sites, during distraction osteogenesis and skeletal development, and at the implant interface are relevant and are reviewed in this section. Additionally, the theories used to relate mechanical parameters to tissue formation are reviewed within the context of the individual studies. The scope of this review is limited to studies of bone formation or modelling. The issue of bone remodelling has been the subject of numerous computational studies, with significant interest in remodelling around implants. Although the roles of mechanical stimuli in the modelling and remodelling processes may be similar, the relationship is not well established, and the two processes are usually considered separately. Reviews on bone remodelling can be found in the general FEA articles cited earlier, as well as in Cowin (1990) and Goldstein et al. (1990) for cortical and trabecular bone, respectively.

3.3.1 Fracture healing

Motivated by the observation that interfragmentary movement influences the course of healing of a fractured bone (Section 3.2.1), several researchers have attempted to correlate tissue formation in a fracture gap to the local mechanical environment using FEA. The first efforts in this regard were those of Carter and associates (Blenman et al., 1989; Carter et al., 1988). The basis of their studies was the “Tissue Differentiation Hypothesis”, a semi-quantitative theory relating mechanical parameters to the formation of mesenchymal tissue.

The tissue differentiation hypothesis proposed by Carter and co-workers has been applied to investigate the role of mechanical loading in skeletal tissue development (Carter et al., 1987; Carter and Wong, 1988a; Carter and Wong, 1988b; Wong and Carter, 1988; Wong and Carter, 1990a; Wong and Carter, 1990b), fracture healing (Blenman et al., 1989; Carter et al., 1988), and peri-implant tissue formation (Carter and Giori, 1991; Giori et al., 1995). A review of the theory, its applications, and its implications is provided in Carter (1987) and Carter et al. (1998). The hypothesis is formulated such that tissue formation is related to the mechanical state of the tissue, where the mechanical state is described in terms of two scalar invariants: the distortional (octahedral shear) stress (or strain) and the hydrostatic stress (or volumetric strain). The relationship between these mechanical parameters and tissue formation is based on experimental observations of others (as discussed in Section 3.2.1), and is summarized in Figure 3.1. It is important to note that the mechanical parameters are typically some function of the hydrostatic

and distortional stress histories, which are constructed based on intermittent loading of the tissue over a certain period of time for a variety of loading conditions.

According to Carter's tissue differentiation hypothesis, the proliferation and differentiation of the pluripotential mesenchymal cells responsible for tissue formation are influenced by the mechanical environment experienced by the tissue. Progenitor cells within developing mesenchymal tissues that experience a loading history of low distortional strain and low compressive hydrostatic stress are more likely to become osteogenic, assuming an adequate blood supply. In this case, bone formation will be intramembranous. However, if the developing tissue is exposed to excessive distortional strains, fibrogenesis will result. The demarcation between osteogenesis and fibrogenesis is indicated by the line labelled "tension" in Figure 3.1. The line labelled "vascularity" in Figure 3.1 separates the tissues requiring high vascularity (bone and fibrous tissue) from those that need only low oxygen tension and can form in a relatively avascular environment (cartilage and fibrocartilage). Thus, large, intermittent compressive hydrostatic stresses encourage cartilage or fibrocartilage formation. The effect of compressive hydrostatic stress on tissue formation may be two-fold: (a) cyclic compressive stresses may inhibit capillary blood flow, oxygen delivery, and angiogenesis; and (b) hydrostatic compression may act directly on cells to stimulate synthesis of biological factors that encourage chondrogenesis and cartilage maintenance.

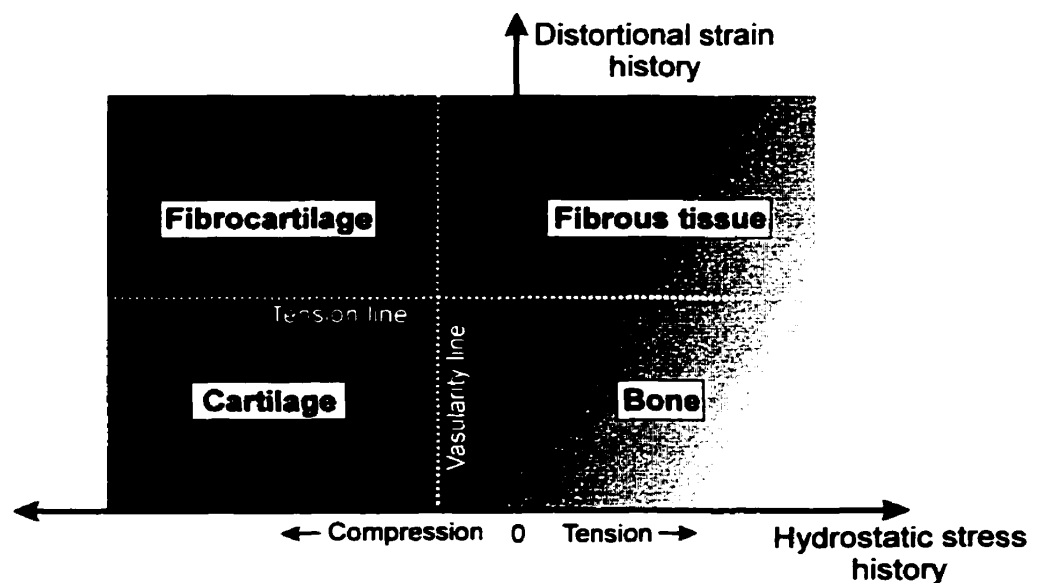


Figure 3.1. Schematic of Carter's tissue differentiation hypothesis (adapted from Carter et al., 1998).

The tension and vascularity lines indicated in Figure 3.1 are parallel to the axes, implying that there are distinct threshold values, there is no interaction between the two mechanical parameters, and hydrostatic tension will not cause fibrous tissue formation. Realistically, it is unlikely that the threshold values are so distinct. Furthermore, the exact nature of the relationship is unknown because of the lack of biological evidence. In modelling studies by Carter and co-workers, other formulations were successful at predicting patterns of tissue differentiation (Carter and Giori, 1991).

As indicated in Figure 3.1, minimal cyclic stresses and a good blood supply will result in direct or intramembranous bone formation. However, bone formation may also occur by endochondral ossification, as is often the case in skeletal development and fracture callus ossification. In the case where a cartilaginous anlage or chondroid-like tissue is present, the hypothesis states that intermittent distortional stresses encourage tissue proliferation and ossification, while intermittent compressive hydrostatic stresses inhibit ossification. The majority of work by Carter and co-workers has been on the process of endochondral ossification in the context of fracture callus healing or skeletal development.

Applied to fracture healing, the tissue differentiation hypothesis predicts the following sequence of events (Carter et al., 1988):

- (a) If minimal cyclic stresses are created and there is a good blood supply, bone forms directly with minimal callus formation. This type of healing (primary fracture healing) can be achieved with certain fracture fixation devices.
- (b) If there is poor vascularization of the early healing tissue, however, intramembranous bone formation will not occur and a small, fibrocartilaginous callus may result. Resolution of the callus will proceed as described in (d).
- (c) If the fracture is not fixed rigidly, relatively high stresses and strains may be created in the early healing tissue. In this case, the intermittent shear stresses resulting from relative motion of the fracture segments will cause tissue proliferation and callus formation. The characteristics of the tissue in different regions of the callus will be related to the stress history and blood supply. Avascularity and hydrostatic compression will encourage cartilage or fibrocartilage formation. Fibrous tissue, or possibly intramembranous bone, will form in other regions.
- (d) Once the callus is formed, intermittent shear stresses will encourage callus proliferation and eventually ossification by secondary fracture healing. Excessive

compressive hydrostatic stresses or a poor vascular supply may prevent ossification, leading to a non-union.

Carter and co-workers have focussed on the fracture healing process assuming an initial callus is present at the fracture site. Using 2D equivalent-thickness plane stress finite element models with isotropic, linear elastic material models, they have correlated mechanical parameters in the healing gap of a femoral midshaft osteotomy with the patterns and progression of healing for axial and bending loads (Blenman et al., 1989; Carter et al., 1988). Their predictions based on the tissue differentiation hypothesis were consistent with observed patterns of tissue formation, when they assumed that intermittent hydrostatic pressure played a dominant role in determining tissue synthesis in a fracture callus.

It is important to note that Carter's model focuses on regulation of tissue formation by mechanical factors only, and it does not incorporate explicitly the role of non-mechanical factors in its formulation. This is an important limitation, one that is common to many theories on mechanically regulated tissue formation and remodelling. Therefore, it is critical when applying these models to consider this limitation and realize that, while mechanical factors may influence tissue formation and remodelling, non-mechanical factors play a significant, if not dominant role as well.

Another criticism of the fracture healing studies by Carter and co-workers is that the loading conditions and histories applied in the models are arbitrary. More recently, other investigators have attempted to overcome this limitation by comparing predictions of local tissue stresses with tissue differentiation patterns observed from experiments with better defined loading conditions and histories. Cheal et al. (1991) examined tissue differentiation in 1 mm tibial osteotomies in sheep. The osteotomies were subjected to cyclic bending deformations, which created a gradient in tissue elongation of 10% to 100% across the diameter of the gap. Using a non-linear 3D finite element model of the interfragmentary gap tissue, stresses and strains were predicted and compared with histological observations. The authors found that ingrowth of vascular tissue and subsequent bone formation occurred earlier and to a greater degree in regions of low strain, whereas callus tissue proliferation was greatest in areas with higher strain. Bone resorption at the fracture fragment ends corresponded to areas with increased tissue strain and stress, although no consistent quantitative relationship between strain magnitude and volume of bone resorption could be determined. These observations are generally consistent with Carter's tissue differentiation hypothesis.

More recently, Gardner et al. (2000) examined the stresses in the callus of a diaphyseal tibial fracture at four stages of healing and, similar to Cheal et al. (1991), found bone formation occurred in regions that were strain protected. This study was unique because the geometric and loading parameters in the finite element model were based on reasonably accurate measurements made on a single patient throughout the healing period. Based on their analysis with typical loading conditions, the authors also found regions where the maximum principal tissue stresses exceeded the yield stresses, suggesting that tissue damage and partial structural failure of the callus would occur, and healing would be delayed.

Claes and Heigele (1999) proposed a new tissue differentiation theory based on their experimental and computational studies of interfragmentary movement of osteotomies of sheep metatarsals. The authors hypothesized that new bone formation occurs along fronts of existing bone or calcified tissue (i.e., appositional bone growth) and the type of bone healing (intramembranous or endochondral) depends on the magnitudes of the local stress and strain. Based on a comparison of histological observations with model predictions, they proposed the quantitative theory summarized in Figure 3.2. The theory differs significantly from Carter's in a few important aspects. First, it assumes that fracture healing proceeds primarily along existing fronts of calcified tissue. Second, instead of using an invariant such as distortional strain, Claes and Heigele used longitudinal and transverse strain components. Finally, the authors *quantified* the relationship between mechanical conditions and tissue formation. In a related study (Heigele and Claes, 1998), the same investigators applied their theory to predict tissue differentiation in a 3.5 mm drill hole defect. Based on their analysis, the theory predicted intramembranous bone formation, consistent with histological observations.

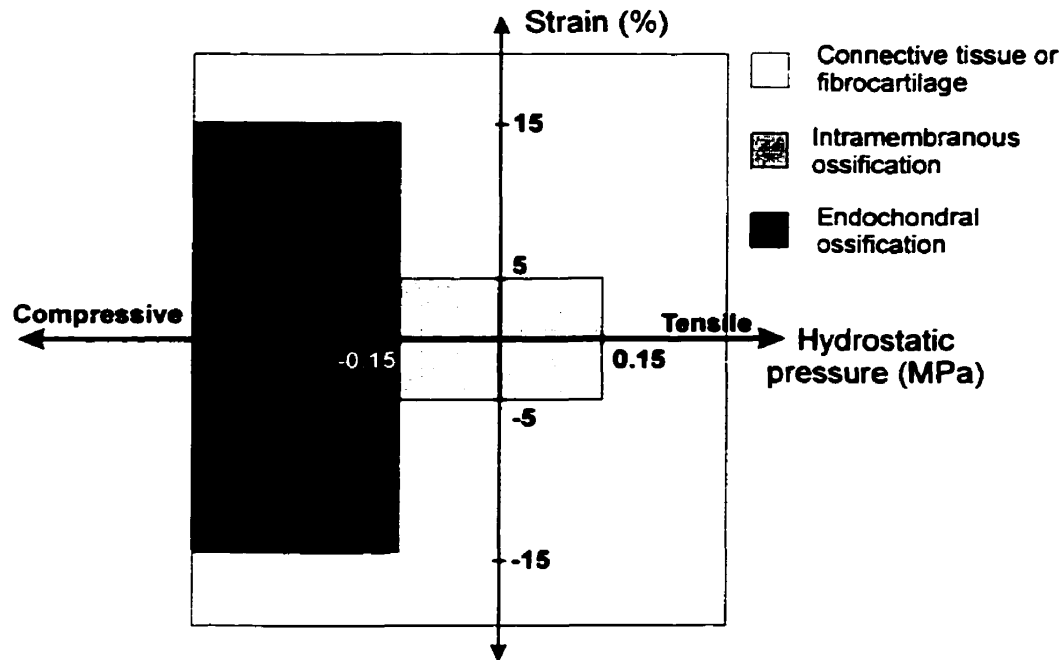


Figure 3.2. Schematic of the quantitative mechanoregulatory hypothesis proposed by Claes and Heigele (1999) for fracture healing (adapted from Claes and Heigele, 1999).

3.3.2 Distraction osteogenesis

Despite its clear relationship with fracture healing, it is only recently that distraction osteogenesis has been used experimentally to investigate the role of mechanical stimuli on bone formation (Section 3.2.1). The issue of mechanically regulated tissue formation is addressed particularly well with distraction osteogenesis models because the procedure produces large volumes of new tissue under well-controlled loading conditions. Because of its brief history, however, few groups have used computational models to investigate the correlation between tissue phenotype and the local mechanical environment in the distraction gap. Carter et al. (1998) used an axisymmetric finite element model with linear, elastic material properties to predict patterns of tensile strain and hydrostatic stress in the distraction tissue of a mouse tibia. As with the fracture healing studies, their predictions of the local mechanical environment were consistent with histologic and molecular observations from the distraction tissue, when interpreted in the context of their tissue differentiation hypothesis. Richards et al. (1998; 1999a; 1999b) have performed several experimental and computational studies with the overall goal of investigating the relationship between strain environment and bone regeneration. Using non-linear 3D finite element analysis, they predicted the local strain distribution in the distraction gap

and found decreased trabecular bone volume fraction and trabecular thickness with a decrease in average tissue strain. However, they did not report any correlation between local strain distribution and patterns of tissue formation.

3.3.3 Skeletal development

The role of external mechanical forces in skeletal development has not been well established, although there appears to be a relationship (Section 3.2.2). The most extensive efforts to correlate local mechanical environment with skeletal development are those of Carter and co-workers who have applied their tissue differentiation hypothesis to investigate the role of mechanical factors in endochondral ossification and skeletal development at various sites. Using 2D and 3D finite element models with linear elastic single-phase material properties, Carter and co-workers have investigated the role of mechanical loading history on the ossification pattern of prenatal and postnatal femora (Carter et al., 1987), the development of diarthroidal joints (Carter and Wong, 1988b), the ossification and architectural construction of long bones (Wong and Carter, 1990a), and the ossification of the chondroepiphysis (Carter and Wong, 1988a), the sternum (Wong and Carter, 1988), and in an organ culture system (Wong and Carter, 1990b). In all cases they were able to achieve patterns of ossification that were comparable to observed ossification patterns. The mechanical loading histories were based on plausible, but arbitrary, loading conditions.

The study on organ culture osteogenesis (Wong and Carter, 1990b) is of particular interest because it has been re-visited recently by another group (Tanck et al., 1999b). The organ culture system studied was that of Klein-Nulend et al. (1986), as discussed in Section 3.2.2. Wong and Carter (1990b) performed a finite element analysis of these experiments using a 3D finite element model, with the tissues modelled as linear elastic materials. Based on a comparison of their stress predictions with the pattern of mineralization observed in the experiments, they concluded that shear stresses at the interface of cartilage and mineralized tissue accelerated osteogenesis and hydrostatic pressure at the metatarsal ends maintained the cartilaginous tissue. These conclusions were consistent with their tissue differentiation hypothesis. Tanck et al. (1999b) have also used the finite element method to analyze the in vitro experiments by Klein-Nulend et al. The primary difference between this study and that by Wong and Carter (1990b) is that Tanck et al. used a poroelastic description of the fetal metatarsal tissue. This material description was selected since cartilage is a biphasic material consisting of

a solid phase (collagen and proteoglycans) and a fluid phase of interstitial water. Its deformation behaviour, therefore, is non-linear and time dependent (Mow et al., 1980), features that are not represented in a linear elastic analysis. Based on their poroelastic analysis, Tanck et al. concluded that fluid flow effects on the mineralization process were probably negligible given the small fluid pressure gradients in the tissue. The role of distortional strain in mineralization, however, was unclear. This was due to the sensitivity of the magnitude of the strain to the intrinsic compressible modulus of the solid phase of the cartilage, a quantity that is unknown for fetal cartilage. However, using a “realistic” value based on adult articular cartilage resulted in maximum distortional strain magnitudes of 2 μ strain, a level which the authors state is likely too low to alter cell function significantly. Therefore, the authors deduced that hydrostatic pressure was responsible for enhancing the mineralization process, possibly by altering the diffusion of ions across the cell membrane. While their predictions of distortional strain magnitude may be more realistic than those from linear elastic models, the paucity of data on the effects of well-defined mechanical stimuli on cell function and tissue formation limits their hypotheses on the mechanisms of mechanoregulation to speculation at best. Nonetheless, the incorporation of a more realistic material model and their consideration of chemical as well as mechanical stimuli are important contributions. The differences between the two approaches and the implications for the analyses were debated recently by Carter and Beaupré (1999) and Tanck et al. (1999a) without adequate resolution.

Lerner et al. (1998) also investigated the role of mechanical loading on skeletal development by comparing patterns of bone growth in the rabbit distal femur growth plate with patterns of mechanical stresses. Specifically, they tested the hypothesis that high compressive stresses were correlated with low rates of bone growth. To do so, they predicted local stress and strain parameters using 3D finite element models generated directly from micro-computed tomography images of the distal femora. Overall variations in bone growth were weakly correlated ($r^2 < 0.15$ by linear regression) with mechanical parameters. However, there was a significant correlation between high compressive stresses and reduced bone growth rates, particularly in the anterior frontal plane of 42 day old rabbits. Thus, the results of this study support the effect of hydrostatic pressure as described by Carter’s tissue differentiation hypothesis, although with a weak correlation. Distortional strain was not a predictive parameter for bone growth in this study. The authors identified uncertainties in loading conditions and inter-animal differences as the primary sources of variation in their results and suggested that

animal-specific finite element models may improve the correlation of bone growth with mechanical parameters.

3.3.4 Implant interface mechanics and tissue formation

As discussed in Section 3.2.3, experimental and clinical evidence indicates that mechanical factors play an important role in influencing peri-implant tissue formation. However, only a few studies have applied computational techniques to investigate the role of mechanical forces in initial peri-implant tissue formation (the bone growth or modelling process). These studies are reviewed in the next section.

Mechanical loading also influences the remodelling of bone around implants, and it is the issue of bone remodelling that has been the primary focus of computational studies to date (for a review, refer to Huiskes and Hollister (1993)). Of these studies, relatively few have incorporated the microstructural features of the implant interface into their modelling approach. Because a focus of this thesis is implant surface geometry, previous efforts to incorporate surface features in computational models will be reviewed. Particular attention is paid to the work of Hollister and co-workers, who have accounted for implant surface geometry in a systematic and efficient manner using homogenization theory.

Computational studies of peri-implant tissue formation

The similarities between fracture healing and healing around bone-interfacing implants led logically to the application of Carter's tissue differentiation hypothesis to peri-implant tissue formation, as first suggested and explained by Carter and Giori (1991). Giori et al. (1995) then performed a finite element study to investigate the influence of mechanical factors on tissue formation beneath cemented knee prostheses. Using a 2D finite element model with the interface tissue modelled as an isotropic, hyperelastic material, the investigators predicted hydrostatic stress and distortional strain patterns in the interface zone tissue for loading conditions typical of walking. Based on their analysis and comparison with observed patterns of tissue phenotype, the authors concluded that a frequently applied compressive hydrostatic stress of 0.7 MPa may be sufficient to stimulate fibrocartilage formation and a frequently applied distortional strain of 10% may be sufficient to simulate fibrous tissue formation. The correlation between high compressive hydrostatic stresses and high distortional strain with cartilage and fibrous tissue, respectively, was consistent with their tissue differentiation hypothesis. Although the authors provided quantitative threshold stresses and strains, they cautioned that the results

should be considered “semi-quantitative”, since several non-mechanical factors may influence tissue formation, and therefore unique values of threshold hydrostatic stress or distortional strain may not exist.

Prendergast, Huiskes and colleagues (Huiskes et al., 1997; Prendergast and Huiskes, 1996; Prendergast et al., 1997) also investigated peri-implant tissue formation using finite element analysis and compared their findings with those observed in animal experiments reported by Søballe et al. (1992a; 1992b). In these experiments, as discussed in Section 3.2.3, a range of tissue phenotypes were observed at the implant interface, including loose fibrous tissue, fibrocartilage and bone; the tissue types and resulting mechanical stability were dependent on the degree of micromovement and the implant surface characteristics.

Prendergast et al. (1997) analyzed these experiments by modelling the tissue as a biphasic material with solid and fluid constituents, similar to the approach used for cartilage (Mow et al., 1980) and by Tanck et al. (1999b) for fetal metatarsal tissue. The modulus of the interface tissue was determined from the push-out test data reported by Søballe et al. The permeability of interface zone tissue has not been determined previously, and therefore the authors estimated the permeability based on values reported for similar tissues. However, sensitivity analyses indicated that the permeability had a significant influence on certain mechanical parameters, and therefore the results of this study must be interpreted with caution. Using a simple axisymmetric implant geometry, they monitored the maximum cyclic pressure, fluid velocity, and strains in the interface tissue for a typical loading cycle for the micromovement device. It is important to note that although the implants in the experiments had surface features of significant size (the pore size was reported to be 200-1000 μm (Søballe et al., 1992a)), the finite element model did not incorporate these microstructural features; instead, the model had a simple linear interface with perfect bonding. Their analyses predicted that the movement of the implant device would change from being controlled by the maximum displacement allowed by the implant device (motion control) to the maximum available force (force control). This was a consequence of the maturation and mechanical changes that occurred in the interface tissue as healing progressed. The change to force-controlled motion caused the fluid velocity and pressure to decrease accompanied by a reduction in tissue strain. Based on their analyses, the authors proposed a “mechano-regulatory pathway” to describe the interaction between biophysical stimuli (shear strain in the solid phase and the relative velocity between the fluid and solid) and tissue phenotype (Figure 3.3). Thus, in the experiments by Søballe et al. the hypothesized switch to

force control resulted in decreased fluid velocity and tissue strains, which permitted ossification to occur, possibly through intermediate tissues (represented by the dotted line in Figure 3.3, which indicates a decrease in fluid velocity and strain with time). However, if motion control had been maintained, the authors predicted that the no bone would have formed due to a combination of high fluid velocity and tissue strains (solid line in Figure 3.3).

Huiskes et al. (1997) subsequently applied the hypothesized regulatory model to an iterative simulation of the experiment by Søballe et al. (1992a; 1992b). In the simulation, the properties of tissue elements were updated based on the values of maximal distortional strain and the relative fluid velocity. By applying the maximum available force cyclically, they were able to show a progression in the tissue phenotype from granulation tissue to fibrous tissue to fibrocartilage to bone. A similar pattern was observed experimentally by Søballe et al., thus supporting the proposed regulatory model.

Apparently, the regulatory hypothesis proposed by Prendergast et al. (1997) differs from the tissue differentiation hypothesis proposed by Carter. The main difference is the choice of mechanical parameters: Prendergast et al. suggested distortional strain and relative fluid velocity influence tissue formation, whereas Carter proposed distortional strain and hydrostatic stress as the controlling parameters. One reason for the difference in choice of mechanical parameters is the modelling approach adopted by the two groups: Prendergast et al. used a biphasic model, which can account for fluid movement, whereas Carter and co-workers have used single-phase material models. Prendergast and colleagues (1996; 1997) reasoned that fluid flow may alter the deformation of the solid phase or the deformation of the cells directly, and therefore must be considered as an important mechanical stimulus to tissue formation. The differences in approaches and implications have been discussed in the literature, without adequate resolution (Carter and Beaupré, 1999; Prendergast and Huiskes, 1996; Tanck et al., 1999a). Huiskes et al. (1997) have noted that high local gradients in fluid pressure can cause fluid flow, and therefore hydrostatic pressure and relative fluid velocity are not independent variables. This suggests that the elastic approach, while more simplistic, may be adequate in some cases.

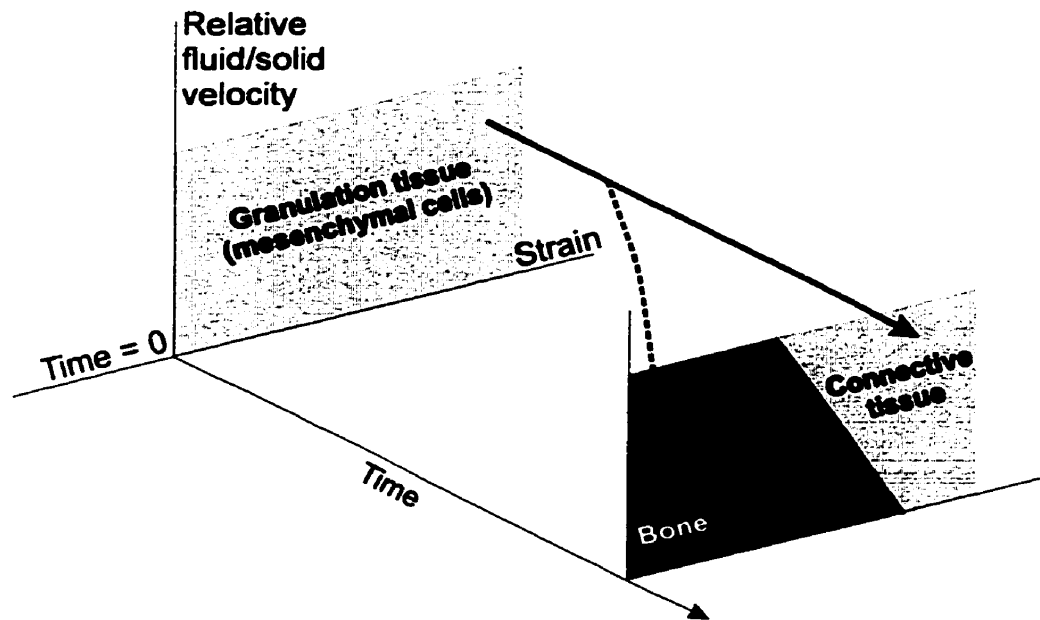


Figure 3.3. Schematic of the mechanoregulatory relationship proposed by Prendergast et al. (1997) (adapted from Prendergast et al., 1997).

A different approach was taken by Harrigan and Reuben (1997) to investigate the role of strain in initial mineralization of soft tissues. By incorporating mechanical energy due to time-varying loads into the thermodynamic description of the chemical process of mineralization, they were able to model the dependency of mineralization on tissue strain. Although their model predicts a maximum allowable strain exists for peri-implant tissue mineralization, they were unable to quantify the threshold value because the necessary chemical data are unknown. This approach is much more mechanistic than those discussed previously, and therefore may ultimately provide a better understanding of the mineralization process. However, the model does not account for cellular factors, which clearly are important, and therefore the model has limited applicability in its present form.

Computational studies incorporating implant surface geometry

Although several computational studies have examined bone formation and adaptation around implants, relatively few have incorporated the geometric characteristics of the implant interface into the model. More often, the implant surface geometry is neglected completely (Giori et al., 1995; Huiskes et al., 1997; Prendergast and Huiskes, 1996; Prendergast et al., 1997; Qin et al., 1996; Weinans et al., 1990; Weinans et al., 1993) or the surface structure is modelled

as a homogeneous material with effective properties (Ducheyne et al., 1978; Moyle et al., 1973). The latter approach, while recognizing that implant surface features exist, cannot account for the local geometry nor predict the local mechanical environment.

Efforts to incorporate implant surface geometry into studies of bone remodelling at the implant interface have been made by Sadegh et al. (1993) and Luo et al. (1999) using the boundary element method. In the study by Sadegh et al., implant surface features such as threads or pores were modelled and bone ingrowth patterns were predicted as a function of geometry and the applied load. However, the loads were applied locally, and the validity of the local loads and their relationship to the loads applied to the whole implant (global loading) was not investigated. Essentially, this approach failed to couple the microstructural (local) analysis with the whole implant (global) analysis. The same is true for the study by Luo et al.: loads were applied only locally, with no connection to the macro-scale loads on the implant or bone. Furthermore, Luo et al. accounted for implant surface roughness by modifying the contact condition between the bone and implant (i.e., perfect bonding or slip). This approach does not account for the influence of the implant surface features on the local stress field in the peri-implant tissue.

The modelling approach that seems best suited to incorporate implant microstructural features into a global model of the implant is the unit cell approach. This approach is applicable to spatially periodic structures, where the entire structure can be represented by a series of repeating unit cells. By coupling the stress analysis of the unit cell with that of the entire structure, one can model the implant microstructure within the context of the whole implant, thus overcoming the limitations of traditional global models (Ducheyne et al., 1978; Giori et al., 1995; Huiskes et al., 1997; Moyle et al., 1973; Prendergast and Huiskes, 1996; Prendergast et al., 1997; Qin et al., 1996; Weinans et al., 1990; Weinans et al., 1993) and local-only models (Luo et al., 1999; Sadegh et al., 1993).

Pedersen et al. (1991) used the unit cell approach to examine local stress distributions in bone ingrown wire mesh prosthesis coatings. They developed a 2D unit cell model comprised of the wire of the coating, the prosthesis substrate and the surrounding tissue. They then constructed a global model of a portion of the coating by repeating the unit cells and coupling them with truss elements to simulate the coupling between wires that occurs in the real mesh coating due to sintering. Using this approach, they were able to investigate load transmission through the mesh as well as local stress distributions around the individual wires. Their results demonstrated that peak bone stresses were several-fold greater than the "regional" or average

host bone stresses estimated by conventional global finite element stress analysis, indicating the importance of modelling microstructural features to predict accurately the local mechanical environment. This approach has limitations, however. Accurate local stress predictions require a relatively high finite element mesh density, and therefore unit cell models must have a large number of degrees of freedom. Since computational resources are limited, the size of a global model constructed from several repeating unit cell models is also limited. Pedersen et al. were able to model only 32 wires in their global model, clearly far fewer than would exist in the actual coating of an entire implant. This limitation is addressed by the homogenization methods used by Hollister and co-workers; their work is described in the next section.

Homogenization theory applied to implant interface mechanics

The mathematical details of asymptotic homogenization theory, as implemented by Hollister and co-workers, are provided in Chapter 5. Hollister, Ko and Kohn have applied this theory to investigate the micromechanics of the tissue-implant interface for threaded (Ko et al., 1992) and porous-surfaced (Ko et al., 1996) implants. They modelled the tissue-implant interface using a series of repeating unit cells (UC) that were geometrically representative of the interface zone. The 2D UC models were then analyzed using asymptotic homogenization theory (Section 5.3) to determine the local and effective properties of the tissue-implant interface zone. This method decouples the analysis of the interface zone into analyses at the local (microscopic) and global (macroscopic) levels. Thus, the microstructural features of the implant are incorporated into the model of the entire implant in a systematic and computationally efficient manner. Furthermore, the local and global level analyses are implicitly linked with this approach.

The general applicability and advantages of homogenization theory over standard unit cell approaches were investigated by Hollister and Kikuchi (1992). In brief, they found homogenization methods more accurate and efficient than standard mechanics approaches for unit cell-based methods. The details of their results and conclusions are discussed in Section 5.5. Analysis of threaded and porous-surfaced implants using the homogenization method has led to several conclusions regarding the utility of the method for this particular application. The most important are summarized below:

- (1) Local tissue strains predicted by homogenization theory are several times greater than those predicted by traditional global finite element analysis (Ko et al., 1992; Kohn et

al., 1993b), indicating the necessity to model the microstructural features to predict accurately the local mechanical environment. The same conclusion was reached by Pedersen et al. (1991) using a standard finite element approach.

- (2) In order to validate the effective properties predicted by homogenization theory for the porous-surfaced interface zone, Ko et al. (1996) measured experimentally the effective elastic constants for interface zones comprised of a titanium porous surface and epoxies. They reported no statistically significant differences between the experimentally measured moduli and those predicted by homogenization theory, confirming the validity of this method for predicting effective properties. This study is discussed in further detail in Section 5.8.1.
- (3) Although homogenization theory assumes that the microstructure is spatially periodic, the implant interface zone models were periodic in only one direction (i.e., parallel, but not normal, to the implant interface). Ko (1994) and Kohn et al. (1993a) investigated the error introduced by the unidirectional periodicity by comparing the local von Mises stresses in the bone predicted by homogenization theory to those predicted by the standard finite element method. For loads applied either parallel or perpendicular to the direction of periodicity, the difference was less than 4%. However, for shear and off-axis loads, the differences were as high as 122%, indicating that the homogenization method may not be applicable in such cases. The local stress predictions have not been validated experimentally, however.

3.4 Summary

It is clear from earlier studies that mesenchymal tissue formation can be regulated mechanically. This has been demonstrated clinically and experimentally at fracture healing sites, during distraction osteogenesis and skeletal development, and around implants. For peri-implant tissue formation, not only the applied load, but also the geometry of the implant surface may influence the tissue formation. However, the relationship between implant surface geometry, peri-implant tissue formation, and mechanical factors remains largely unknown. And although a threshold level of implant movement that permits osseointegration has been defined, the mechanical stimuli experienced locally by the tissue have not been determined experimentally. The same is true for the studies on fracture healing and distraction osteogenesis, for instance.

Thus, the role of mechanical factors in determining skeletal tissue formation has received significant interest from members of the biomechanics community, who have attempted to correlate patterns of tissue formation with estimates of the local mechanical environment predicted by computational models. The issue of tissue formation around implants presents its own particular complexities, many of which have not been addressed by the few studies published in this area. This may explain in part the inability of these studies to reach firm, quantitative conclusions. The most obvious deficiency of previous models (Giori et al., 1995; Huiskes et al., 1997; Prendergast and Huiskes, 1996; Prendergast et al., 1997) is that they did not account for the local implant geometry. As shown by Pedersen et al. (1991) and Ko et al. (1992), the implant microstructure influences the local mechanical environment significantly and must be incorporated into any computational model. The homogenization method appears to be well suited in this regard. However, the validity of the local properties predicted by this method, particularly for a composite with unidirectional periodicity, needs to be confirmed experimentally.

The issue of an appropriate material model for the interface tissue is an important one, but is complicated by the lack of experimental data describing the mechanical properties of the early healing interface tissue. Furthermore, the mechanical characteristics of the interface between the tissue and implant surface have not been well established. To date, most models have used a perfect bonding condition between the metal and tissue. The uncertainty related to the mechanical characteristics of the tissue-material interface requires that alternative interface conditions be considered.

Another challenge in studying implant interface mechanics is accurate quantification of the applied loads. Due to the nature of typical in vivo experiments, loads applied to implants or fracture fragments are not well characterized and are estimated based on gait analysis (Claes and Heigele, 1999; Gardner et al., 2000; Giori et al., 1995; Huiskes et al., 1997; Ko et al., 1995; Prendergast and Huiskes, 1996; Prendergast et al., 1997; Richards et al., 1999a). Clearly, the local mechanical environment is dependent on the loads applied to the implant or fracture fragments, and therefore accurate definition of the loading conditions is required to make quantitative conclusions.

The final challenge, which applies to all studies in the area of mechanoregulation of tissue formation, is defining the relationship between the mechanical stimuli and tissue formation. The tissue differentiation hypothesis and computational studies by Carter and co-

workers are the most significant contributions to this area. Although their contributions are important to a general understanding of how skeletal tissue formation is influenced by mechanical environment, the simplifications in geometry and material properties, arbitrary loading conditions, and lack of specific experimental validation of their analyses limit their conclusions to qualitative generalities. Unfortunately, but perhaps not too surprisingly given the complexity of the systems being studied, efforts to incorporate more realistic material models (Claes and Heigele, 1999; Gardner et al., 2000; Giori et al., 1995; Huiskes et al., 1997; Prendergast and Huiskes, 1996; Prendergast et al., 1997; Tanck et al., 1999b) or geometries (Lerner et al., 1998) have not been much more successful in determining a quantitative mechanical regulatory model for tissue formation. Further improvements to models, as discussed above, will help in this regard. However, the phenomenological approach of correlating predictions of local mechanical environment with local tissue formation may itself be somewhat limited. A primary limitation of almost all mechanoregulatory models is that they do not account for non-mechanical factors, which may be more important than mechanical factors in initial bone formation (Hollister et al., 1996). Furthermore, the computational tissue mechanics approaches typically do not consider extracellular matrix-cell interactions, which ultimately will dictate the mechanical signal sensed by the cells. Therefore, while significant information and hypotheses may be generated by computational studies that improve upon those reviewed in this chapter, it is important to realize that the specific details and mechanisms of the mechanoregulation of tissue formation will likely only be revealed by well-formulated cell and tissue culture studies. Furthermore, an essential feature of the most important studies will be an effort to relate tissue-level mechanical stimuli to cell-level mechanical signals.

Chapter 4

Animal model study of the influence of implant surface geometry on early post-implantation healing response

Summary

The osseointegration and long-term success of bone-interfacing implants are dependent on the mechanical stability of the implant relative to the host bone during the early healing period. The geometric design of an implant surface may play an important role in affecting early implant stabilization, possibly by influencing the dynamics of tissue healing. In this study, we compared the early tissue healing response and the resulting implant stability for two surface designs by characterizing the histological and mechanical properties of the healing tissue around Ti6Al4V sintered porous-surfaced and Ti plasma-sprayed implants. The implants were inserted transversely in rabbit femoral condyles and evaluated at 0, 4, 8, and 16 days post-implantation. Four and eight days after implantation, the early healing tissue (fibrin and collagenous matrix) was more extensively integrated with the three-dimensional interconnected structure of the sintered porous surface than with the irregular geometry of the plasma-sprayed coating. Additionally, histological examination and quantitative image analysis indicated that initial matrix mineralization leading to osseointegration occurred more rapidly with the porous-surfaced implants. The more extensive tissue integration and more rapid matrix mineralization with the porous-surfaced implants were reflected in the mechanical test data which demonstrated greater attachment strength and interfacial stiffness for the porous-surfaced implants four and eight days post-implantation ($p < 0.05$). Sixteen days after implantation, both implant designs were osseointegrated and had comparable attachment characteristics. These data demonstrate that appropriate surface design selection can improve early implant stability and induce an accelerated healing response, thereby improving the potential for implant osseointegration.

4.1 Introduction and motivation

The results of several experimental studies in vivo suggest that the quality of implant osseointegration and stability is dependent, in part, on the geometric surface design (Section 2.3). However, the observations from those experiments were made several weeks post-implantation

after osseointegration and, in some case, bone remodelling have occurred. The early healing response prior to osseointegration is also of interest, since it is during this period that cellular differentiation and tissue synthesis and mineralization leading to osseointegration are initiated. This is also the period when relative movement of the implant may prevent bone formation (Carter and Giori, 1991; Pilliar, 1991; Szmukler-Moncler et al., 1998), and therefore implant stability during this period is necessary for osseointegration to occur. While in vitro studies that have focussed on the early healing response have provided insights into the mechanisms by which *textured* implant surfaces may influence tissue formation, cell culture studies to date have not compared tissue formation for different surface *structures*. Furthermore, it is difficult to relate in vitro results to implant function in vivo, particularly for issues such as mechanical stability.

The early healing response in vivo next to implants with different surface structures and the mechanical characterization of the repair/regeneration tissues formed within the peri-implant region has not yet been addressed. Implants with plasma-sprayed coatings and porous-surfaced structures are frequently used in orthopaedics and dentistry, and therefore a comparison of the tissue responses to implants with these surface designs has important clinical value.

4.2 Specific research objectives

The objectives of this portion of the research were:

- (1) to investigate the histological characteristics and healing dynamics of the peri-implant tissues formed in the early post-implantation period; and
- (2) to determine the resulting early mechanical stability of different implant surface designs.

Our studies focussed on a comparison of two types of press-fit and cementless implant designs: (1) Ti6Al4V implants with a sintered Ti6Al4V porous surface region; and (2) Ti6Al4V implants with a Ti plasma-sprayed coating.

4.3 Materials and methods

4.3.1 Implants

The implants used in this study were similar in shape and appearance to an endosseous dental implant root component developed and studied by Deporter, Pilliar, and their colleagues (Deporter et al., 1997; Deporter et al., 1990; Deporter et al., 1992; Pilliar et al., 1991a). The implants were 9 mm long, had a truncated conical (tapered) shape having a taper angle of approximately 5° and a maximum coronal diameter of 4.1 mm, and had an internal thread (to which a cover screw and abutment can be attached when the implant is used clinically). The coronal 1 mm of the implants had a smooth machined surface (Figure 4.1).

The implants, as noted previously, were fabricated with one of two bone-interfacing surface geometries: a sintered porous-structured surface or a plasma-sprayed surface. The porous surface was created by sintering Ti6Al4V particles of 45-150 µm in diameter (-100/+325 mesh) to a machined Ti6Al4V substrate (Innova Corp., Toronto, ON). Sintering was achieved in a high vacuum furnace ($<10^{-5}$ torr) at a temperature of 1250°C for approximately one hour. The resulting porous structure had an average thickness of 225 µm and consisted of two to three particle layers bonded to each other and the substrate. This treatment produced pore sizes in the range of 50-200 µm, a volume porosity of 35-40%, and a surface region with a three-dimensional interconnected porosity (Figure 4.2A).

The plasma-sprayed implants were produced by application of a titanium plasma spray coating to a grit-blasted Ti6Al4V substrate (Hitemco Medical Applications, Inc., Old Bethpage, NY). The plasma-sprayed layer had an average thickness of 20-25 µm. This treatment produced a rough, irregular surface with approximately 5-10% volume porosity. Because of the surface irregularities, the coating thickness ranged from 10 µm to almost 50 µm. The pores within the layer were more or less isolated and did not form an interconnected network of pores and channels as observed with the sintered porous surface structure. However, the plasma-sprayed surface did possess regions with undercuts and intrusions that permitted interdigitation and mechanical interlock with tissue (Figure 4.2B).

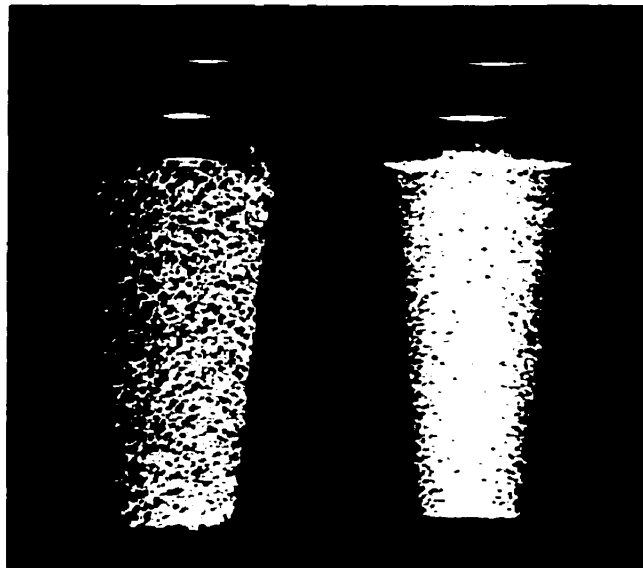


Figure 4.1. The implants used in this study were fabricated with a Ti6Al4V sintered porous surface (left) or a Ti plasma-sprayed surface (right).

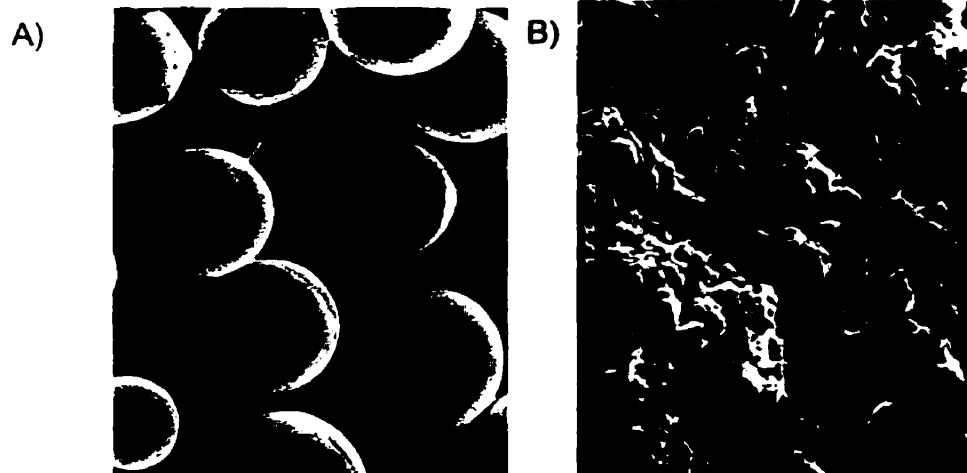


Figure 4.2. Scanning electron micrographs of the (A) Ti6Al4V sintered porous-structured surface and (B) the Ti plasma-sprayed surface. Original magnifications: (A) $\times 200$; (B) $\times 500$.

4.3.2 Surgical procedure

The appropriate guidelines for the care and use of laboratory animals were observed in this study (Canadian Council on Animal Care, 1993). The implants were placed transversely in the medial femoral condyles of mature (4 to 4.5 kg) New Zealand White rabbits. The rabbits were anesthetized by induction with ketamine HCl and xylazine, and then maintained with Halothane via inhalation.

The implants were placed in the flattest region of the medial surface, midway between the anterior and posterior surfaces of the condyle and distal to the growth plate (Figure 4.3). The implant site was prepared by drilling under sterile saline irrigation using a series of dental burs. The diameter of the final bur was slightly smaller than that of the implant, and the implants were inserted with an initial interference fit. The implantation site and procedure provided initial contact between cancellous bone and the porous-surfaced or plasma-sprayed region of the implants. Each rabbit received one porous-surfaced implant in one condyle and one plasma-sprayed implant in the contralateral condyle. The side (right or left) and order of placement of the implants were randomized. The rabbits were observed closely following surgery and were permitted normal ambulation. Buprenorphine HCl was administered as required to control post-operative discomfort.



Figure 4.3. Contact radiograph showing the implant location in rabbit femoral condyle.

Implants were placed in twenty-one rabbits. Seven rabbits were allotted to each of three groups: 4, 8, or 16 days of healing. Additionally, seven pairs of fresh frozen femurs from rabbits used in unrelated experiments were obtained and allotted to the immediate post-operative group (0 days of healing). This group was used to assess the initial press-fit condition of the two implant designs. Implants were placed in these femurs (after thawing) according to the procedure described above. The experimental design is summarized in Figure 4.4.

After the prescribed healing time, the rabbits were euthanized by T-61 euthanasia solution (Hoechst Canada, Inc., Regina, SK) and bone sections (femoral condyles with the implants intact) were harvested.

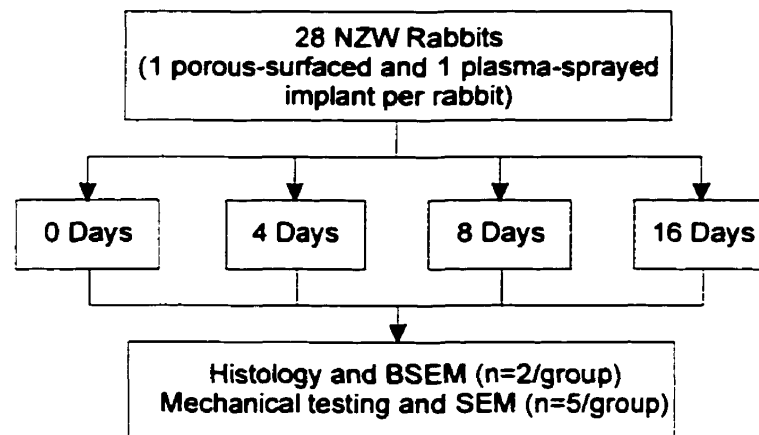


Figure 4.4. Summary of the experimental design for the rabbit study.

4.3.3 Histological examination

The bone sections from two of the seven rabbits in each group were stored in 10% formalin and assigned for histological examination. Ground non-demineralized sections were prepared from the implants using methods described previously (Deporter et al., 1990). The 30 μm sections were stained with a 1:1 mixture of 0.3% toluidine blue and 2% sodium borate, and then counterstained with Unna's variant of Van Gieson's stain. The sections were examined by light microscopy and back-scattered electron (BSE) microscopy (15 kV) to characterize the interface zone and detect mineralization of the tissue within the interface zone. At each time point, two to four sections per implant were examined histologically and with BSE microscopy.

The width of the interface zone and the extent of tissue mineralization were quantified by image analysis of the BSE micrographs using SigmaScan (SPSS Inc., Chicago, IL). The average interface zone width was determined from the Day 4 images by making several measurements along the length of the implants. To quantify the degree of mineralization at Days 4, 8, and 16, the BSE micrographs were first filtered and segmented based on grayscale values to identify bone (Figure 4.5). Then, the mineralized area fraction (MAF) within a specified region of interest (ROI) adjacent to implant interface was calculated as

$$MAF = \frac{\text{Area of mineralized tissue in ROI}}{\text{Area of all tissue in ROI}} \times 100\% \quad (4.1)$$

The width of the ROI for each implant design was equal to the average interface zone width measured from the Day 4 BSE images for that design. The distinction between the gray values of bone and the implant interface was not clear in some cases, and therefore a threshold artifact was introduced into the measurements of the MAF. Because of the artifact, the MAF for the Day 4 specimens was non-zero, although it was clear from the histological sections and SEM images that mineralization had not occurred four days post-implantation. Therefore, the Day 4 MAF results for each implant design were set as the baseline values, and the Day 8 and 16 MAF measurements were expressed relative to the baseline value for the particular implant design.

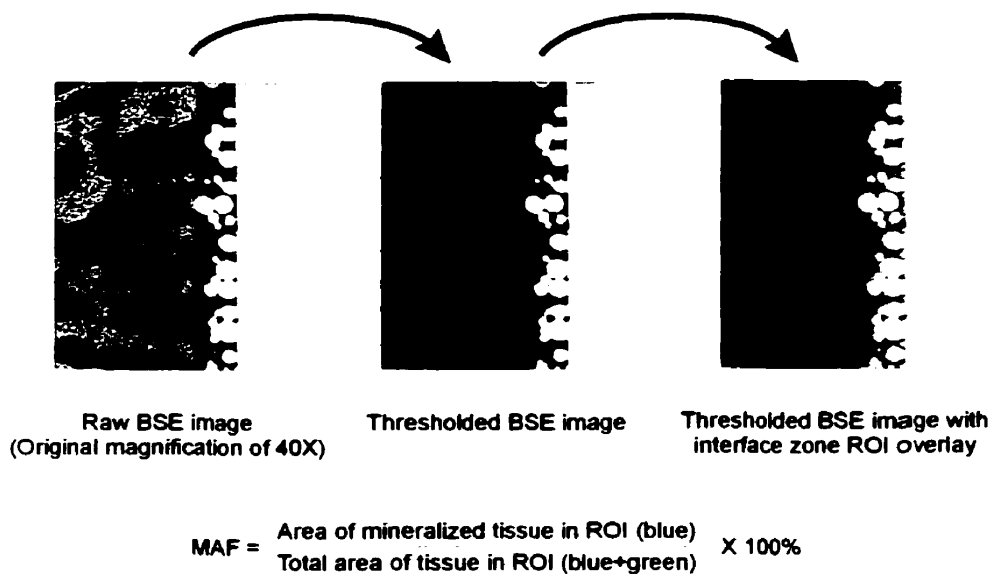


Figure 4.5. Method for quantifying the mineralized area fraction (MAF) of the interface zone tissue.

4.3.4 Mechanical testing

The bone sections from the remaining five rabbits in each group were assigned for mechanical testing and temporarily stored in saline. Pull-out tests were performed to determine characteristic load-deflection curves for the two implant designs at each of the time points. The tests were performed on fresh specimens (within two hours of harvesting) using a custom-made fixture attached to an Instron test machine under displacement control at a rate of 1 mm/min (Figure 4.6). The loading rod was attached to the implants by way of the internal threads. The fixture and specimen preparation ensured that the implant long axis was aligned with the Instron actuator. The precise alignment and tapered shape of the implants ensured that the load-deflection curve was characteristic of the properties of the tissue in the interface zone and the interaction of the tissue with the implant and host bone. The maximum pull-out force and maximum tangential stiffness were determined from the load-deflection curves; these parameters were used to indicate the quality of the attachment of the implants. Wilcoxon one-tailed paired-sample tests were performed at each time point to test the hypothesis that the porous-surfaced implants provided greater attachment strength and stiffness than the plasma-sprayed implants.

4.3.5 Scanning electron microscopy examination

Following pull-out, the extracted implants were temporarily stored in 10% formalin, and then dehydrated, critical-point dried, and coated with a thin platinum conducting layer for examination by scanning electron microscopy (Hitachi S2500). Several micrographs were examined along the entire length of each implant.

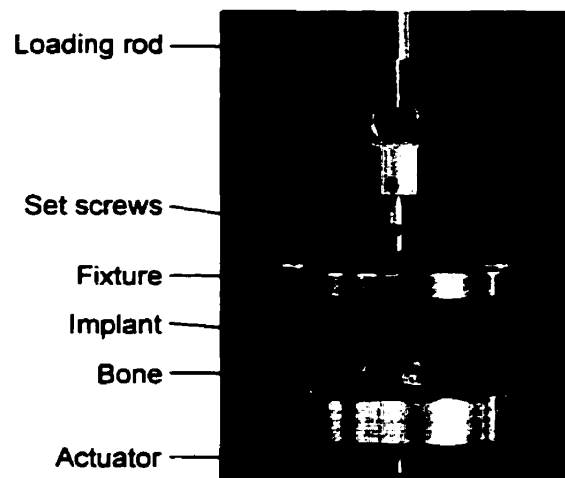


Figure 4.6. Mechanical test fixture used to perform the pull-out tests.

4.4 Results

4.4.1 Immediately post-implantation

For both implant designs, the back-scattered electron micrographs of the specimens retrieved immediately post-implantation demonstrated contact between the host bone and implant surface in many locations (Figure 4.7). Complete host bone-implant contact was not achieved along the entire length of the implants because of the porosity of the host bone and, in some cases, surgical damage. However, all implants were inserted with an interference fit and were judged to be stable at the time of implantation. Because of the tight initial interference fit of the implants, the mechanical properties of the interface zone were dominated by friction between the surface of the implants and the surrounding bone. The pull-out strength and maximum stiffness for the two implant designs were comparable at this time point (Figure 4.8; $p>0.5$).

Scanning electron microscopy was not performed on the implants retrieved at Day 0, since tissue healing and ingrowth could not have occurred with these specimens.

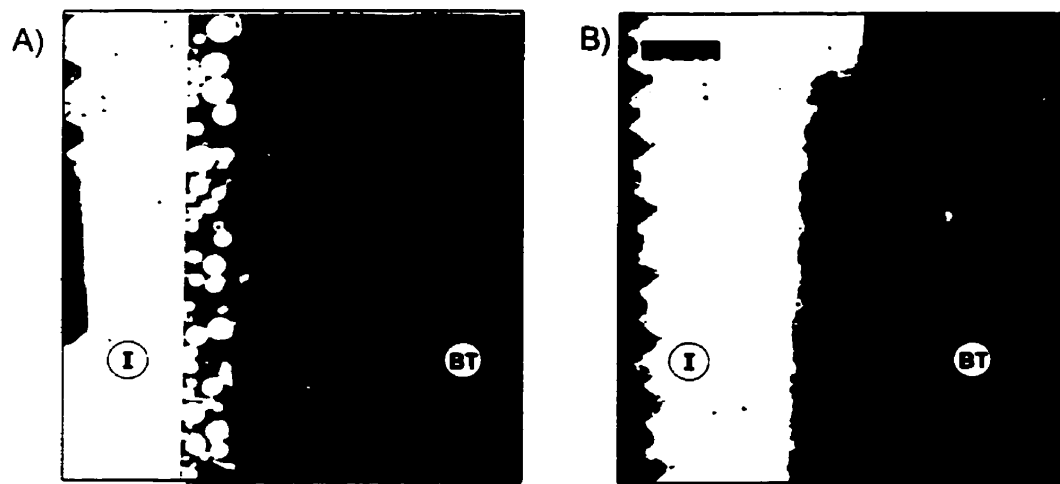


Figure 4.7. Back-scattered electron micrographs demonstrating contact between the bone (BT) and implant (I) immediately after surgery for the porous-surfaced (A) and plasma-sprayed (B) implants. Original magnifications: (A) $\times 40$; (B) $\times 40$.

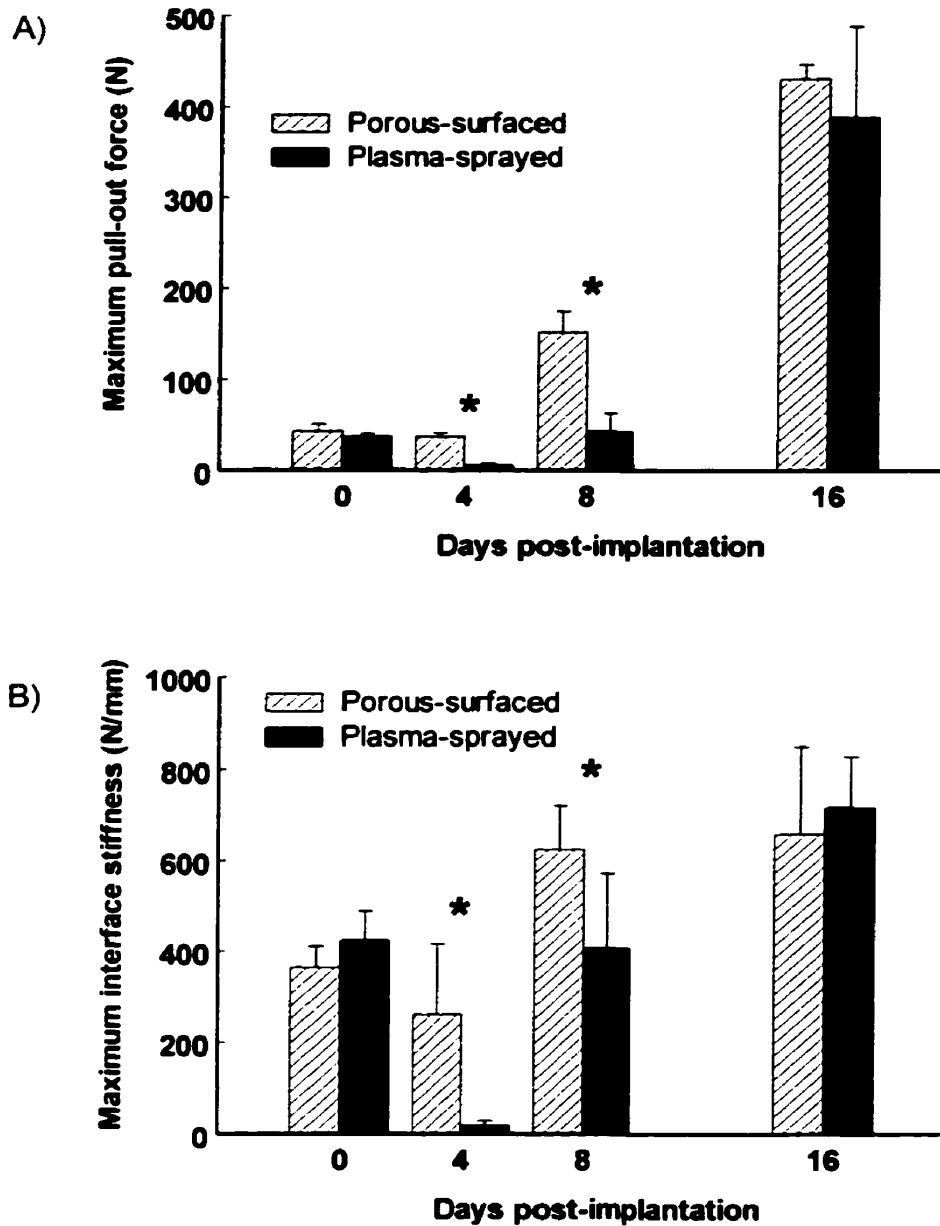


Figure 4.8. Pull-out strength (A) and maximum interface stiffness (B) measured for the two implant surface designs at each healing period. Data are presented as mean \pm standard error. An asterisk indicates a significant difference between implant designs ($p < 0.05$).

4.4.2 Four days post-implantation

Four days after implantation, the necrotic bone created during surgery had resorbed, and a well-defined interface zone had formed adjacent to both implant designs (Figure 4.9). The average widths of the interface zones (i.e., the distance from the host bone to the implant surface structure) were 82 μm and 71 μm for the porous-surfaced and plasma-sprayed implants, respectively. The histological sections indicated that the interface zones for both designs were filled with fibrin and loose fibrous extracellular matrix. The scanning electron micrographs demonstrated extensive interdigitation of the fibrin and collagen matrix with the three-dimensional interconnected structure of the porous surface regions (Figure 4.10A). The interaction of the healing tissue with the plasma-sprayed implants, however, was limited to isolated regions with recesses and undercuts (Figure 4.10B). The porous-surfaced implants also appeared qualitatively to have a greater percentage of their surface area covered with matrix.

The more extensive tissue integration and coverage observed for the porous-surfaced implants were reflected by significantly stronger and stiffer attachment with this implant design (Figure 4.8; $p < 0.05$). For both implant designs, the force-displacement curve was non-linear, with a toe region and increasing stiffness with increasing strain.

4.4.3 Eight days post-implantation

After eight days of healing, there was increased coverage and interdigitation of the healing tissue with the surface regions of both implants. However, the matrix around the porous-surfaced implants was more dense and extensive than that around the plasma-sprayed implants (Figure 4.11). In fact, in some areas of the porous surface regions, the fibres of the collagen matrix appeared to be “bonded” to the surface of the particles, thereby providing excellent tissue-implant attachment (Figure 4.11A). Additionally, the back-scattered electron micrographs demonstrated early evidence of mineralization in some areas of the porous-surfaced interface zones (Figure 4.12A), whereas the same degree of mineralization was not evident in the plasma-sprayed interface zones (Figure 4.12B). The quantitative analysis of the MAF in the interface zone confirmed these observations (Figure 4.13). Over 7% of the porous-surfaced interface zone was mineralized, whereas there was effectively no observable mineralization in the plasma-sprayed interface zone. Because there was no mineralized tissue observed in the interface zone at Day 4, the negative mean value for the plasma-sprayed MAF at Day 8 likely indicates that the change in MAF between Days 4 and 8 was below the detectable difference once variations due to thresholding and inter-animal variability were accounted for.

As a result of the better tissue integration and earlier mineralization, the attachment of the porous-surfaced implants was stiffer and stronger than that of the plasma-sprayed implants (Figure 4.8; $p < 0.05$).

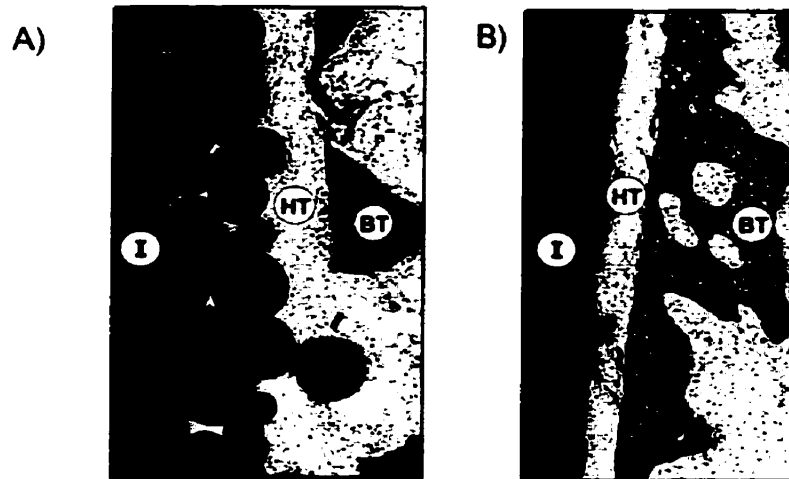


Figure 4.9. Histologic sections demonstrating a well-defined interface zone filled with healing tissue (HT) adjacent to both the porous-surfaced (A) and plasma-sprayed (B) implants after 4 days of healing. Original magnifications: (A) $\times 30$; (B) $\times 30$.

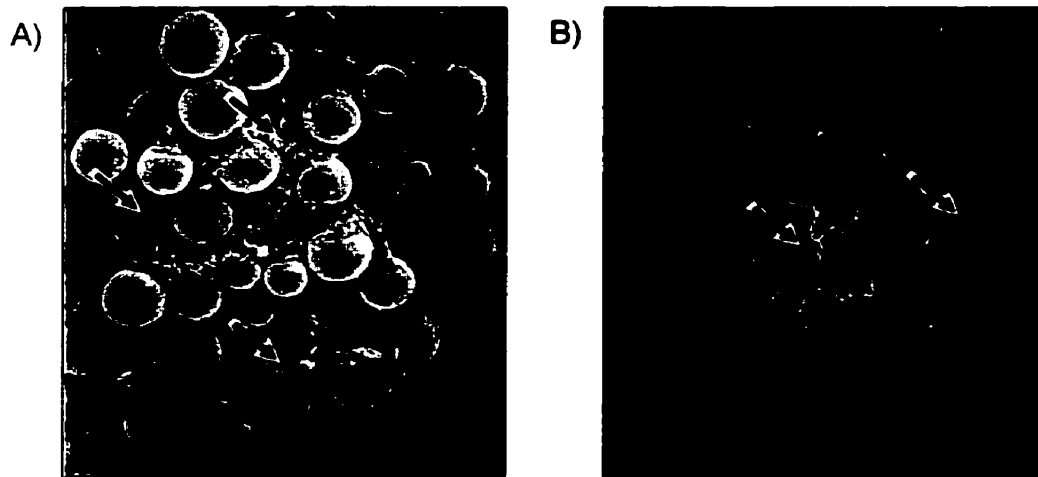


Figure 4.10. Scanning electron micrographs demonstrating more extensive coverage and interdigitation of the healing tissue matrix (indicated by arrows) with the sintered porous surface (A) than with the plasma-sprayed surface (B) four days post-implantation. Original magnifications: (A) $\times 100$; (B) $\times 100$.

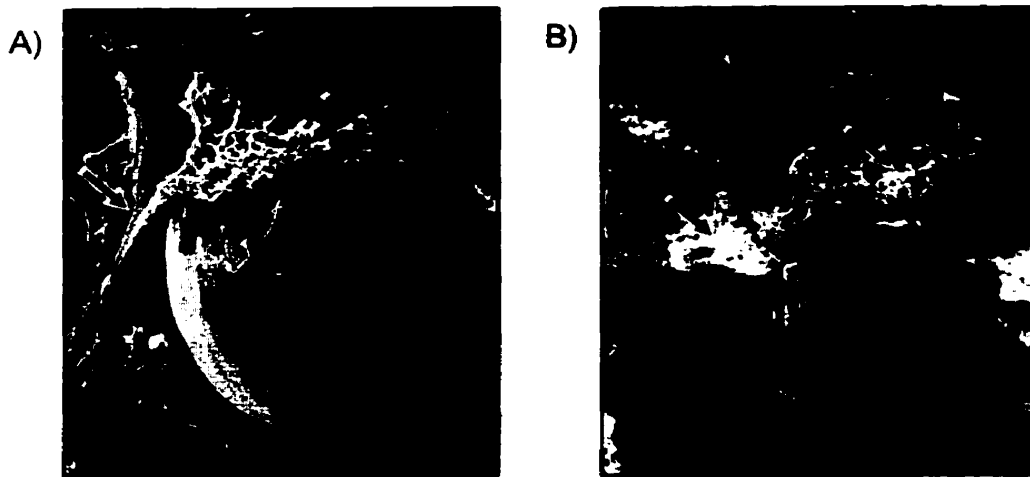


Figure 4.11. Scanning electron micrographs taken 8 days after implantation demonstrating more extensive tissue interdigitation and maturation (indicated by arrows) with the sintered porous surface (A) than with the plasma-sprayed surface (B). Original magnifications: (A) $\times 600$; (B) $\times 500$.

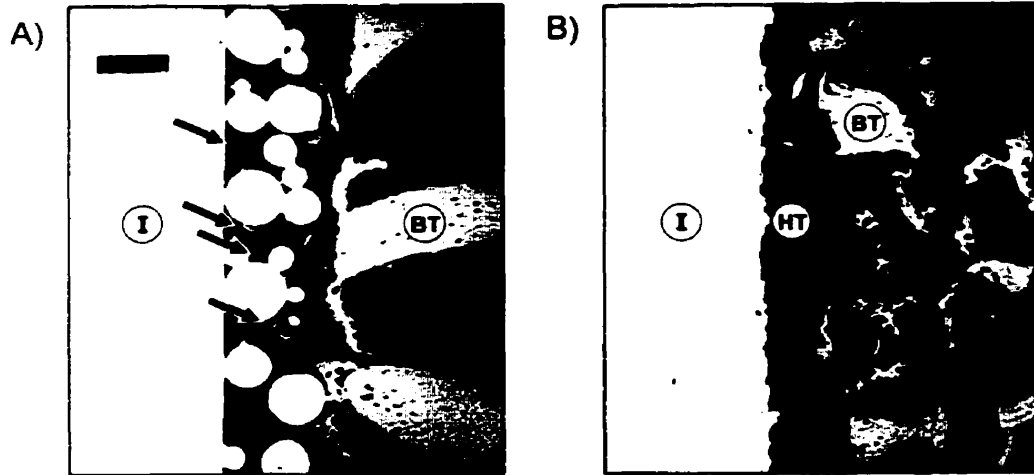


Figure 4.12. Back-scattered electron micrographs of the porous-surfaced (A) and plasma-sprayed (B) interface zones 8 days post-implantation. Areas with matrix mineralization (indicated by arrows) are evident throughout the porous-surfaced interface zone. The same degree of mineralization was not evident in the plasma-sprayed interface zone. Original magnifications: (A) $\times 40$; (B) $\times 40$.

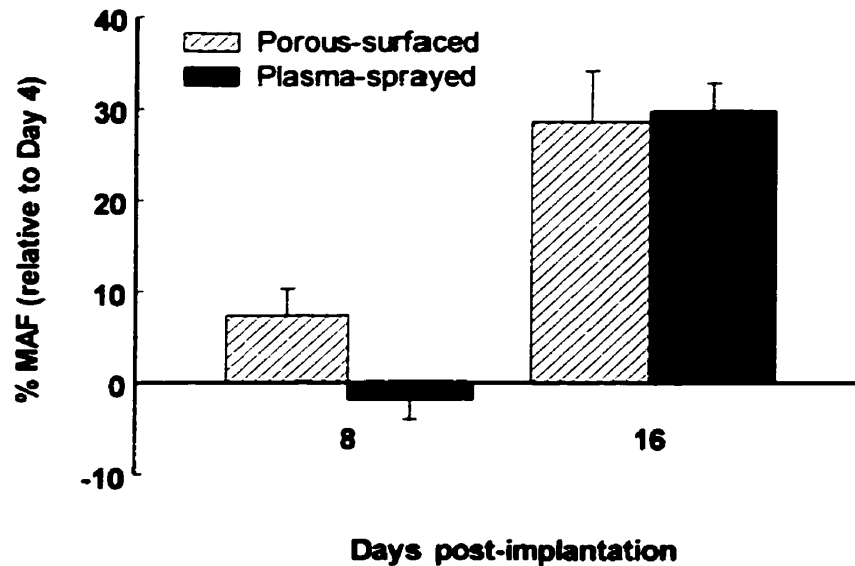


Figure 4.13. Mineralized area fraction (MAF) of the interface zone tissue at Days 8 and 16 post-implantation expressed relative to the average baseline value determined at Day 4 for each design. The data are presented as mean \pm standard error. Refer to the text for details on the Day 8 results.

4.4.4 Sixteen days post-implantation

After sixteen days of healing, both implant surfaces were well covered and extensively integrated with mineralized tissue, osteoid, and dense matrix. As well, scanning electron micrographs showed numerous active osteoblasts on both implant surfaces (Figure 4.14). It is likely the surface regions covered with osteoblasts were recessed, and therefore were protected from the shear forces generated during the pull-out tests. Back-scattered electron microscopy and quantitative analysis of the MAF revealed that the implant designs were equally osseointegrated by Day 16, with extensive mineralization of the interface zone tissues (Figure 4.13 and Figure 4.15).

At this time point, there were no significant differences in the strength and stiffness of attachment of the two implant designs (Figure 4.8; $p > 0.5$), consistent with the microscopy evidence.

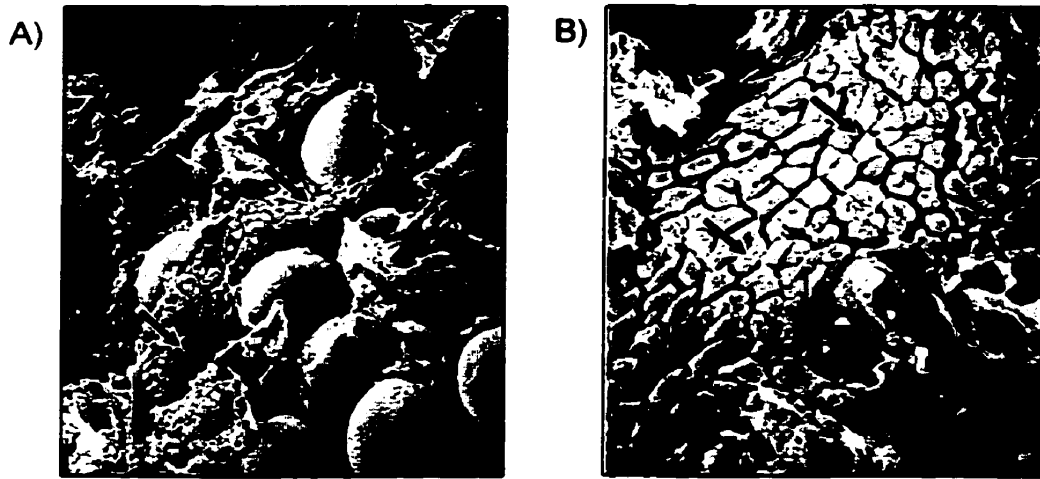


Figure 4.14. Scanning electron micrographs taken 16 days after implantation showing extensive coverage and interdigitation of the sintered porous (A) and plasma-sprayed (B) surfaces with mineralized tissue and dense matrix. Numerous active osteoblasts (indicated by arrows) were observed on both surfaces. Original magnifications: (A) $\times 200$; (B) $\times 500$.

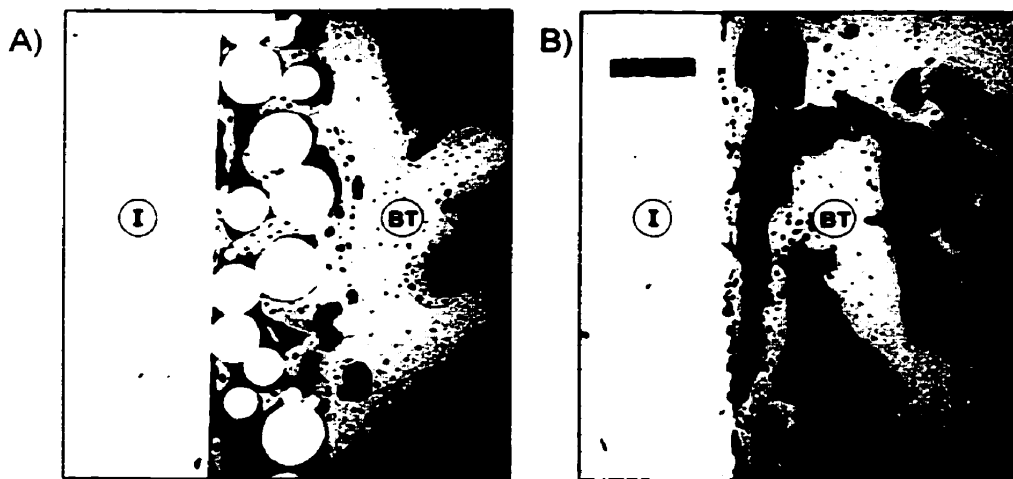


Figure 4.15. Back-scattered electron micrographs of the porous-surfaced (A) and plasma-sprayed (B) interface zones 16 days post-implantation. Both implant designs were osseointegrated by this point, with close apposition of bone to the implant surfaces. Original magnifications: (A) $\times 40$; (B) $\times 40$.

4.5 Discussion

The objective of this study was to determine whether the dynamics of early tissue healing and the stability of bone-interfacing implants were significantly influenced by the geometry of the implant surface for two designs currently used clinically in orthopaedic and dental implant systems. Based on histological analysis, back-scattered and scanning electron microscopy, quantitative image analysis, and mechanical testing, we found that the three-dimensional interconnected structure of the sintered Ti6Al4V porous surface was integrated with healing tissue more rapidly and more extensively than was the irregular geometry of the Ti plasma-sprayed coating. Additionally, the tissue in the porous-surfaced interface zone mineralized more rapidly than that in the plasma-sprayed interface zone. Consequently, the porous-surfaced implants developed stronger and stiffer early attachment. These data demonstrate that surface geometry strongly influences healing dynamics and as a result, the early mechanical stability of implants. Implant surface designs that provide better early stability are expected to improve the potential for osseointegration, particularly in situations in which early implant stability is difficult to achieve and maintain.

The more extensive matrix coverage and more rapid bone formation with the porous-surfaced implants suggests that osteogenic cells were able to initiate matrix formation and mineralization more effectively within the interface zone for this implant design. Although the primary difference between the two implant designs was the geometry of the surface region, the chemical composition of the surfaces also was different. Cell culture toxicity studies indicate that aluminum and vanadium ions released from Ti6Al4V implants can inhibit the differentiation and expression of osteoblasts and suppress the deposition of mineralized matrix (Thompson and Puleo, 1995; Thompson and Puleo, 1996). However, we observed more rapid mineralization in the Ti6Al4V porous-surfaced interface zone, suggesting that if surface chemistry was a factor, it was secondary to and superceded by surface geometry.

Comparisons of cell activity and matrix formation on plasma-sprayed and sintered porous surfaces in vitro have not been made, so it is difficult to determine whether the differences we observed in matrix formation in vivo were due to modulation of cell activity by the implant surfaces directly. The particles constituting the sintered porous structure in this study were characterized by submicron (0.1 μm) ridges that were the result of thermal etching during sintering (Smith et al., 1989) (Figure 2.3B). These regular topographical features may have modulated cell activity to accelerate bone formation. The plasma-sprayed surface was similar to

those considered in cell culture studies to be very rough and conducive to bone formation (see Section 2.3). Examination of the plasma-sprayed surfaces with SEM demonstrated certain regions that were devoid of submicron features. However, it is not known whether the differences in submicron-sized surface texture between the plasma-sprayed and sintered porous surfaces were sufficient to influence the healing dynamics to the degree observed in this study, particularly when taken in context of the significant differences in micron-sized surface geometry. The initial events of cell attachment and spreading appear to be similar for the two surface geometries (Brunette, 1988), but the implications in terms of cell function and subsequent tissue formation events are unknown.

The surface texture on the particles of the porous surface may have been responsible for the collagen fibre attachment that we observed with the Day 8 implants (Figure 4.11A). An initial event in the synthesis of matrix adjacent to an implant surface is the formation of an approximately 0.5 μm thick, collagen-free calcified tissue layer that juxtaposes the implant surface, but is not chemically bonded to it (Davies, 1996). This cement line-like layer is subsequently interdigitated with the collagen matrix of the healing interface zone tissue. Since chemical bonding did not occur at the implant surface, the attachment of the collagen fibres to the particles is apparently a striking example of mechanical interlock between the cement line-like layer and the submicron-sized thermal etch ridges. The integrity of this mechanical bond is substantial given that the attachment of the collagen fibres was evident even after the implants had been extracted during mechanical testing.

As discussed in Section 2.3.2, the surface texture may also dictate the mechanism of osseointegration based on the stability of the fibrin scaffold that forms shortly after implantation (Davies, 1998; Dziedzic, 1995). In this study, however, it is likely that both surfaces were sufficiently textured to provide adequate fibrin attachment. The presence of matrix on both implant surfaces after the pull-out tests indicates that the matrix-implant attachment strength exceeded that of the matrix, and therefore the matrix was sufficiently stable to support cell migration to both surfaces.

An alternative hypothesis to explain the accelerated osseointegration of the porous-surfaced implant is that the local mechanical environment around the porous surface may favour bone formation. Maniatopoulos et al. (1986) hypothesized that the differences they observed in tissue remodelling and implant stability of functionally loaded porous-surfaced and threaded implants were due to local mechanical conditions influencing tissue synthesis. The effect of mechanical stimuli on implant osseointegration has been demonstrated by numerous

experimental studies (reviewed in Section 3.2.3). Although the implants in this study were not functionally loaded, they were placed in a location that experiences mechanical forces. As discussed in Sections 3.2.3 and 3.3.4, the local mechanical environment in the healing peri-implant tissue may influence cell differentiation and expression, and consequently tissue formation. Since the mechanical environment in the interface tissue is dependent, in part, on the surface geometry of the implant, the tissue stresses and strains around a porous-surfaced implant may be more favourable for bone formation than those around a plasma-sprayed implant. This hypothesis is explored further in Chapter 6.

A unique aspect of this study was the characterization of the mechanical properties of the tissue attachment before the establishment of final osseointegration. Previous researchers have compared the attachment strength of implants with various surfaces, but typically only after osseointegration had occurred (as discussed in Section 2.3.1). We are unaware of any study that has characterized the mechanical properties of the attachment of a variety of implant designs by early healing tissue. The paucity of data can be attributed in part to the technical difficulties involved in measuring the mechanical properties of the tissue in the narrow interface zone. We were able to overcome these difficulties by using a test fixture that permitted accurate alignment of the implant and by using a tapered implant. The tapered shape of the implant ensured that once the pull-out test was initiated, the implant surface would not contact bone directly. Thus, only the properties of the interface zone tissue and its attachment to the implant and host bone were measured. The efficacy of the mechanical test was demonstrated by the detectable decrease in strength and stiffness between the tight friction fit at day 0 and the attachment by weak, compliant tissue at day 4 (Figure 4.8).

The decrease in mechanical stability observed for both implant types shortly after implantation is an interesting and important observation. The implants were inserted with an interference fit and were very stable at the time of surgery, as evidenced by the mechanical test parameters measured at Day 0 (Figure 4.8). However, four days after surgery, the stiffness and strength of attachment had decreased. The microscopic analyses revealed that the necrotic bone adjacent to the implant immediately after surgery had resorbed and was replaced by extracellular matrix, resulting in minimal bone-implant contact (Figure 4.9). Therefore, the mechanical stability during the early healing period was provided only by the healing tissue and its mechanical interaction with the implant surface region. This finding is consistent with the quantitative histomorphometric observations made by Dhert et al. (1998) for implants inserted in a cortical bone site. They found that osteoclastic resorption occurs following implantation,

resulting in reduced bone-implant contact compared with the immediate post-operative situation. With this study, we have demonstrated for the first time the mechanical consequences of this healing response: implant stability may be reduced in the period following surgery despite a tight initial interference fit.

Another clinically relevant finding is the early mechanical stability that was provided by the porous-surfaced implants. Early loading of dental and orthopaedic implants can result in excessive relative micromovement that will prevent bone formation and result in non-rigid fixation by fibrous tissue (Cameron et al., 1973; Maniatopoulos et al., 1986; Pilliar et al., 1995; Søballe et al., 1992b). Since the amount of micromovement is dependent on the stiffness of the implant attachment, an implant design that provides greater attachment stiffness during the early healing period will experience less micromovement. Furthermore, an implant that osseointegrates more rapidly will be less susceptible to the detrimental effects of micromovement and will require a shorter rehabilitation period. In this study, the porous-surfaced implants had stiffer and stronger attachment before bone formation and osseointegrated more rapidly than the plasma-sprayed implants. This suggests that, in a situation with early loading, porous-surfaced implants may be more resistant to the detrimental effects of micromovement, and therefore may have a greater potential for osseointegration than plasma-sprayed implants. This issue is considered further in Chapter 7.

Statistical analysis of our mechanical test results indicated differences in the mechanical parameters (interfacial stiffness and pull-out strength) at Days 4 and 8. We did not detect differences in the mechanical parameters at Days 0 and 16, possibly due to the limited power of our statistical tests. However, the mechanical data were supported by the microscopy analyses which demonstrated that the tissue integration and maturity were comparable for the two implant designs at Days 0 and 16. Therefore, the porous-surfaced and plasma-sprayed implants were similarly stable at the time of implantation and following osseointegration, which would be expected for nonfunctional implants placed in the site and species used in this study. Although osseointegration of both implant designs occurred within 16 days in the rabbits, the rates of tissue maturation and bone formation are slower in humans (Heikel, 1959). Thus in a clinical setting, the critical period during which an implant is susceptible to micromovement effects would be extended, and the differences in healing dynamics between the two implant designs investigated in this study may be exaggerated.

In this study, we focussed on the early healing period. Friedman et al. (1996) have demonstrated that CoCr porous-surfaced implants had greater bone apposition and shear strength

than CoCr plasma-sprayed implants 6 and 12 weeks after implantation in the femoral condyles of rabbits. Luckey et al. (1992) also found long-term differences in shear strength between CoCr porous-surfaced and plasma-sprayed implants, although their study had insufficient statistical power to demonstrate significance. In light of our finding that the two implant types have comparable stability once initial osseointegration occurs, the results obtained by Luckey et al. and Friedman et al. suggest that, as expected, the long-term success of an implant is also dependent on the bone remodelling that occurs after osseointegration.

4.6 Conclusions

In conclusion, we have demonstrated that surface geometry can influence the early healing dynamics around bone-interfacing implants with significant consequences in terms of early implant stability. Compared to plasma-sprayed implants, the more extensive tissue integration and more rapid matrix mineralization observed with the porous-surfaced implants suggests this surface design promotes an accelerated response in tissue formation and resulting mechanical stability. However, the reason for this differential response in the rate of osseointegration was unclear from the experimental studies. Nonetheless, these results suggest that appropriate selection of surface design can improve early implant stability and induce an accelerated healing response, thereby improving the potential for implant osseointegration.

Chapter 5

Development and validation of a computational model of the interface zone

Summary

Although previous studies have investigated the effect of the local mechanical environment on early peri-implant tissue formation using computational models, none have incorporated implant surface geometry into their analyses. To address this serious limitation, we implemented a homogenization technique that accounted for the microstructural features of the implant surface in a systematic and computationally efficient manner. Two-dimensional unit cell models with idealized geometries representing the sintered porous and plasma-sprayed surface designs were developed, and the effective and local properties of the interface zones were predicted using the computational model. The model predicted that the porous-surfaced interface zone was effectively stiffer than the plasma-sprayed interface zone. Furthermore, the sintered porous surface provided much larger regions locally where the tissue was strain-protected. These predictions were compared with data from mechanical tests, the Hashin-Shtrikman composite model, and photoelastic analysis for the purpose of validating the model. The validation studies indicated that the computational model provided reasonable initial estimates of the effective and local properties of the two interface zones. Finally, parametric studies were performed to investigate the implications of using unit cell models with idealized geometries. It was determined that although the idealized geometry models did not represent the full range in the properties of the geometrically irregular interface zones, they did predict effective and local properties that were within the range predicted with geometrically accurate models, and therefore are representative of the real implant surfaces.

5.1 Introduction and motivation

The role of mechanical forces in determining skeletal tissue formation is well recognized, particularly in the contexts of skeletal development, fracture healing, and peri-implant tissue formation (Section 3.2). The difficulties associated with measuring the local mechanical environment in healing tissue has led researchers to use computational modelling approaches to predict tissue stresses or strains, with the goal of correlating the mechanical environment with tissue formation (reviewed in Section 3.3). However, the issue of tissue formation around implants presents its own particular complexities, many of which have not been addressed by the few studies published in this area. This may explain in part the inability of these studies to reach firm, quantitative conclusions. The most obvious deficiency of previous models (Giori et al., 1995; Huiskes et al., 1997; Prendergast and Huiskes, 1996; Prendergast et al., 1997) is that they did not account for the local implant geometry. The results of previous *in vivo* studies and the animal model studies from this thesis (Chapter 4) demonstrate that implant surface geometry plays an important role in the dynamics of tissue formation. As shown by Pedersen et al. (1991) and Ko et al. (1992), the implant microstructure influences the local mechanical environment significantly, and therefore must be incorporated into any computational model that aims to investigate the effect of the local mechanical environment on tissue formation.

As discussed in Section 3.3.4, the approach that seems best suited to model the tissue-implant interface in a systematic and computationally efficient manner is a unit cell analysis using homogenization theory. The groundbreaking work by Hollister and his colleagues on the application of these techniques to biomechanics problems has established the homogenization method as an approach that is preferred for unit cell analysis (Hollister and Kikuchi, 1992) and that is appropriate for studying the mechanics of trabecular bone (Hollister et al., 1994; Hollister et al., 1991; Hollister and Kikuchi, 1994) and tissue-implant interfaces (Ko et al., 1992; Ko et al., 1996). Thus, the homogenization method was selected for the present study. However, a numerical implementation of the method was not readily available, and therefore had to be developed. Furthermore, the local properties predicted by the homogenization method, while similar to predictions using the standard finite element method (Ko, 1994; Kohn et al., 1993a), have not been confirmed experimentally. Finally, previous studies of the tissue-implant interface have been limited to investigations of porous-surfaced or threaded implants with idealized geometries (Ko et al., 1992; Ko et al., 1996); the implications of using unit cells with idealized geometries to model geometrically irregular surfaces (e.g., sintered porous and plasma-sprayed surfaces) have not been investigated.

5.2 Specific research objectives

The specific research objectives of this part of the work were:

- 1) to implement the homogenization technique numerically using the finite element method;
- 2) to develop unit cell models of the tissue-implant interface zone for the porous-surfaced and plasma-sprayed designs;
- 3) to validate the effective and local properties predicted for the porous-surfaced and plasma-sprayed interface zones;
- 4) to investigate implant surface design issues parametrically by determining the effect of pore size on the effective and local properties of the interface zones; and
- 5) to investigate the implications of using unit cells with idealized geometries to model the geometrically irregular sintered porous and plasma-sprayed surfaces considered in this study.

Several steps were taken in order to meet these objectives. The overall method of approach is illustrated in Figure 5.1.

5.3 Theoretical formulation of homogenization theory

This section provides an overview of the theoretical basis of homogenization theory without reference to our specific application, the tissue-implant interface zone. The theoretical derivation and much of the nomenclature in this chapter follows the derivation provided by Hollister and Kikuchi (1992) closely.

Homogenization theory was developed in the early to mid 1970's, primarily by applied mathematicians, to analyze the physical behaviour of microstructured materials (Bakhvalov and Panasenko, 1989). It has since been used in the engineering community to analyze composite material behaviour (e.g., Guedes and Kikuchi, 1990; Meguid and Kalamkarov, 1994; Meguid et al., 1996; Meguid et al., 1994; Suquet, 1985). Similar to other methods to analyze composites, the homogenization method is a unit cell (UC) approach.

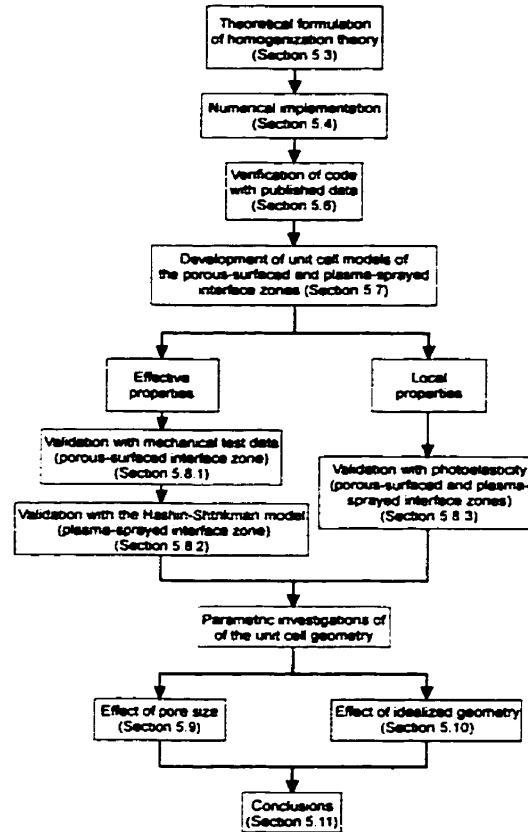


Figure 5.1. Schematic of the method of approach used in the development and validation of the computational model of the porous-surfaced and plasma-sprayed interface zones.

A unit cell (also known as a representative volume element (Hill, 1963)) is an element that is representative of the microscopic structure of a composite body, where the body is formed by spatial repetition of the unit cell (Figure 5.2). If the body is subjected to loading and boundary conditions, the resulting field variables (stresses and deformations) will vary from point to point on the macroscopic scale \mathbf{x} . Additionally, due to the heterogeneity in the microstructure, there will be rapid variations in the field variables in a small neighbourhood η of the macroscopic point \mathbf{x} . This corresponds to the microscopic scale, \mathbf{y} , where

$$\mathbf{y} = \frac{\mathbf{x}}{\eta}. \quad (5.1)$$

The parameter η , which is typically a very small positive number, is the ratio of the microstructural size to the total size of the analysis region. Thus, all field variables exhibit dependence on both length scales, i.e., for a general function g , $g^\eta = g(\mathbf{x}, \mathbf{y}) = g(\mathbf{x}, \mathbf{x}/\eta)$. Because of the periodicity of the structure, the dependence of a function on the microscopic variable, \mathbf{y} , is

also periodic. Equation (5.1) also implies a field variable on the local level varies $1/\eta$ more rapidly than the corresponding variable on the global level, again because of the microstructure.

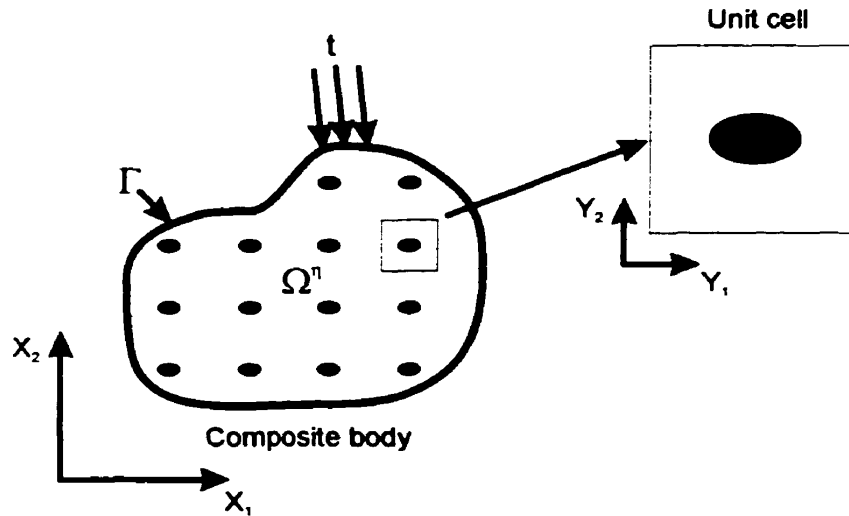


Figure 5.2. A composite body comprised of repeating unit cells, which are representative of the microstructure.

Solving such a problem using the standard finite element method, for instance, would be impractical, since the discretization necessary to represent the detailed microstructure would be enormous. The homogenization method overcomes this problem by reflecting the microstructure of a composite in the determination of the mechanical behaviour of the macroscopic body, without the need to consider the details of all material points in the body. This method also allows approximation of the microstructural mechanical behaviour based on the macroscopic stress analysis by a process known as localization.

The dependence of a field variable on both the macroscopic and microscopic levels makes it reasonable to assume the field variable can be approximated by an asymptotic expansion with respect to the parameter η , i.e.,

$$\mathbf{u}^\eta(\mathbf{x}) = \mathbf{u}^0(\mathbf{x}, \mathbf{y}) + \eta \mathbf{u}^1(\mathbf{x}, \mathbf{y}) + \eta^2 \mathbf{u}^2(\mathbf{x}, \mathbf{y}) + \dots, \quad (5.2)$$

where \mathbf{u}^η is the exact value of the field variable, \mathbf{u}^0 is the macroscopic or average value of the field variable, and \mathbf{u}^1 , \mathbf{u}^2 , etc. are the perturbations in the field variable due to the microstructural inhomogeneities. The perturbations are \mathbf{Y} -periodic, where \mathbf{Y} corresponds to the unit cell, and \mathbf{Y} -periodicity implies that the field variables take identical values on opposite sides of the unit cell.

For small deformation, the strain tensor is

$$\varepsilon_{ij}(\mathbf{u}^n) = \frac{1}{2} \left(\frac{\partial u_i^n}{\partial x_j} + \frac{\partial u_j^n}{\partial x_i} \right). \quad (5.3)$$

Applying the asymptotic expansion (5.2) to the displacement \mathbf{u}^n allows the strain tensor (after neglecting terms of $O(\varepsilon)$ and higher) to be written as

$$\varepsilon_{ij}^n = \bar{\varepsilon}_{ij} + \varepsilon_{ij}^\bullet, \quad (5.4)$$

where ε_{ij}^n is the local or microstructural strain tensor, $\bar{\varepsilon}_{ij}$ is the average or macrostructural strain tensor defined as

$$\bar{\varepsilon}_{ij} = \frac{1}{2} \left(\frac{\partial u_i^0}{\partial x_j} + \frac{\partial u_j^0}{\partial x_i} \right), \quad (5.5)$$

and ε_{ij}^\bullet is the fluctuating strain tensor which varies in a periodic manner and is defined as

$$\varepsilon_{ij}^\bullet = \frac{1}{2} \left(\frac{\partial u_i^1}{\partial x_j} + \frac{\partial u_j^1}{\partial x_i} \right). \quad (5.6)$$

Similarly, a virtual displacement \mathbf{v} and the virtual strain $\varepsilon_{ij}^n(\mathbf{v})$ can be expanded asymptotically as a function of \mathbf{x} and \mathbf{y} to give

$$\varepsilon_{ij}^n(\mathbf{v}) = \varepsilon_{ij}^0(\mathbf{v}) + \varepsilon_{ij}^1(\mathbf{v}), \quad (5.7)$$

where the average and fluctuating strain tensors are defined as for the displacement \mathbf{u}^n .

The expanded strain tensors (5.4) and (5.7) are substituted into the standard variational form of the equilibrium equations to yield

$$\int_{\Omega^n} C_{ijkl}^n (\varepsilon_{ij}^0(\mathbf{v}) + \varepsilon_{ij}^1(\mathbf{v})) (\bar{\varepsilon}_{kl}(\mathbf{u}^n) + \varepsilon_{kl}^\bullet(\mathbf{u}^n)) d\Omega^n = \int_{\Gamma} t_i v_i d\Gamma, \quad (5.8)$$

where C_{ijkl}^n is the local stiffness tensor, Ω^n represents the total macroscopic and microscopic domains, and t_i (and boundary displacements) are applied to the boundary, Γ , of the macroscopic region only.

Since \mathbf{v} is arbitrary, it can vary on the microscopic or macroscopic levels. Varying \mathbf{v} on the microscopic level yields

$$\int_{\Omega^n} C_{ijkl}^n \varepsilon_{ij}^1(\mathbf{v}) (\bar{\varepsilon}_{kl}(\mathbf{u}^n) + \varepsilon_{kl}^\bullet(\mathbf{u}^n)) d\Omega^n = 0, \quad (5.9)$$

which is a statement of equilibrium on the microscopic scale. Likewise, if \mathbf{v} varies on the macroscopic level only, then

$$\int_{\Omega^n} C_{ijkl}^n \varepsilon_{ij}^0(\mathbf{v}) (\bar{\varepsilon}_{kl}(\mathbf{u}^n) + \varepsilon_{kl}^\bullet(\mathbf{u}^n)) d\Omega^n = \int_{\Gamma} t_i v_i d\Gamma, \quad (5.10)$$

which is a statement of equilibrium on the macroscopic scale.

Since $\varepsilon_{kl}^{\bullet}$ varies periodically, the equilibrium equations (5.9) and (5.10) can be re-written, assuming $\eta \rightarrow 0$ in the limit, as

$$\int_{\Omega^n} \frac{1}{|V_{UC}|} \int_{V_{UC}} C_{ijkl}^n \varepsilon_{ij}^l(\mathbf{v})(\bar{\varepsilon}_{kl}(\mathbf{u}^n) + \varepsilon_{kl}^{\bullet}(\mathbf{u}^n)) dV_{UC} d\Omega^n = 0, \text{ and} \quad (5.11)$$

$$\int_{\Omega^n} \frac{1}{|V_{UC}|} \int_{V_{UC}} C_{ijkl}^n \varepsilon_{ij}^0(\mathbf{v})(\bar{\varepsilon}_{kl}(\mathbf{u}^n) + \varepsilon_{kl}^{\bullet}(\mathbf{u}^n)) dV_{UC} d\Omega^n = \int t_i v_i d\Gamma, \quad (5.12)$$

where V_{UC} is the volume of the unit cell.

The microscopic equilibrium equation (5.11) will be satisfied if the integral over the unit cell volume is equal to zero. Therefore, equation (5.11) can be re-written as

$$\int_{V_{UC}} C_{ijkl}^n \varepsilon_{ij}^l(\mathbf{v}) \varepsilon_{kl}^{\bullet}(\mathbf{u}^n) dV_{UC} = - \int_{V_{UC}} C_{ijkl}^n \varepsilon_{ij}^l(\mathbf{v}) \bar{\varepsilon}_{kl}(\mathbf{u}^n) dV_{UC}. \quad (5.13)$$

Equation (5.13) is a statement of equality of virtual work between the microscopic (left-hand side) and macroscopic (right-hand side) scales (Suquet, 1985). This equation is solved to determine the fluctuating component of the local strain tensor, $\varepsilon_{kl}^{\bullet}$. However, solving for $\varepsilon_{kl}^{\bullet}$ requires $\bar{\varepsilon}_{kl}$, which generally is not known beforehand. Equation (5.13) is a linear equation, however, and therefore $\bar{\varepsilon}_{kl}$ can be written as a linear combination of unit strains. For instance, in the two-dimensional case

$$\bar{\varepsilon}_{pm}^{11} = - \begin{bmatrix} 1 & 0 \\ 0 & 0 \end{bmatrix}, \bar{\varepsilon}_{pm}^{22} = - \begin{bmatrix} 0 & 0 \\ 0 & 1 \end{bmatrix}, \bar{\varepsilon}_{pm}^{12} = - \begin{bmatrix} 0 & 1 \\ 0 & 0 \end{bmatrix}, \bar{\varepsilon}_{pm}^{21} = - \begin{bmatrix} 0 & 0 \\ 1 & 0 \end{bmatrix}. \quad (5.14)$$

Substitution of the unit strains (5.14) into (5.13) gives

$$\int_{V_{UC}} C_{ijkl}^n \varepsilon_{ij}^l(\mathbf{v}) \varepsilon_{pm}^{\bullet kl}(\mathbf{u}^n) dV_{UC} = - \int_{V_{UC}} C_{ijkl}^n \varepsilon_{ij}^l(\mathbf{v}) \bar{\varepsilon}_{pm}^{kl}(\mathbf{u}^n) dV_{UC}, \quad (5.15)$$

which can be solved for $\varepsilon_{pm}^{\bullet kl}$ (using the finite element method, for instance). To ensure periodicity of $\varepsilon_{pm}^{\bullet kl}$, the displacements on opposite sides of the unit cell are constrained to be equal. Suquet (1985) has shown that periodic boundary conditions are preferable to uniform displacement or traction boundary conditions which over- and under-estimate the effective properties, respectively. The fluctuating local strain tensor can be recovered from the solution of $\varepsilon_{pm}^{\bullet kl}$ by

$$\varepsilon_{ij}^{\bullet} = - \varepsilon_{ij}^{\bullet kl} \bar{\varepsilon}_{kl}. \quad (5.16)$$

A local structure tensor, M_{ijkl} , is defined to relate the total microscopic strain to the average or macroscopic strain

$$\varepsilon_{ij}^n = \mathbf{M}_{ijkl} \bar{\varepsilon}_{kl} , \quad (5.17)$$

where the structure tensor is given by

$$\mathbf{M}_{ijkl} = \frac{1}{2}(\delta_{ik}\delta_{jl} - \delta_{il}\delta_{jk}) - \varepsilon_{ij}^{*kl} \quad (5.18)$$

(δ_{ij} is the Kronecker delta, and the first term on the right-hand side of the equation is the identity tensor).

Substituting equation (5.17) into the macroscopic equilibrium equation (5.12) gives

$$\int_{\Omega^n} \frac{1}{|V_{UC}|} \left(\int_{V_{UC}} C_{ijkl}^n M_{klpm} dV_{UC} \right) \varepsilon_{ij}^0(\mathbf{v}) \bar{\varepsilon}_{pm}(\mathbf{u}^n) d\Omega^n = \int \mathbf{t}_i v_i d\Gamma \quad (5.19)$$

since $\varepsilon_{ij}^0(\mathbf{v})$ and $\bar{\varepsilon}_{pm}(\mathbf{u}^n)$ are both constant over the unit cell volume. The effective stiffness tensor is then defined as

$$\bar{C}_{ijkl} = \frac{1}{|V_{UC}|} \int_{V_{UC}} C_{ijpm}^n M_{pmkl} dV_{UC} , \quad (5.20)$$

and the macroscopic equilibrium equation can be re-written as

$$\int_{\Omega^n} \bar{C}_{ijkl} \varepsilon_{ij}^0(\mathbf{v}) \bar{\varepsilon}_{kl}(\mathbf{u}^n) d\Omega^n = \int \mathbf{t}_i v_i d\Gamma . \quad (5.21)$$

This equation can be solved numerically (using, e.g., the finite element method) to determine the average (macroscopic) strains in the equivalent homogenized body.

5.4 Numerical implementation of homogenization theory

The finite element method can be used to solve the preceding formulation according to the implementation described in this section. The left-hand side of equation (5.15) is discretized in the standard manner (Bathe, 1982) to give the element stiffness matrix

$$\mathbf{K}^{(e)} = \int_{V^{(e)}} \mathbf{B}^T \mathbf{D} \mathbf{B} dV^{(e)} , \quad (5.22)$$

where \mathbf{B} is the strain-displacement matrix, \mathbf{D} is the element elasticity matrix, and $V^{(e)}$ is the volume of the element. The right-hand side of equation (5.15) can be discretized to give the element load vector for a given unit strain (i.e., $\bar{\varepsilon}^{11}$, $\bar{\varepsilon}^{22}$, or $\bar{\varepsilon}^{12}$ for the 2D case):

$$\mathbf{f}^{(e)kl} = \int_{V^{(e)}} \mathbf{B}^T \mathbf{D} \bar{\varepsilon}^{kl} dV^{(e)} . \quad (5.23)$$

A standard 2 x 2 Gauss integration scheme can be used to evaluate both the element stiffness matrix and the element load vector. The element stiffness matrix and load vector are then assembled in the standard manner to obtain the global stiffness matrix and load vector for the unit cell model.

Prior to solving for the nodal displacements, the displacements on opposite sides of the unit cell are constrained to be equal to ensure periodicity of the fluctuating strain component, ε_{pm}^{*kl} . The displacement constraint is imposed using the penalty method (Bathe, 1982), and thus the global stiffness matrix is modified such that

$$\mathbf{K}_{ii} = \mathbf{K}_{ii} + \lambda; \quad \mathbf{K}_{jj} = \mathbf{K}_{jj} + \lambda; \quad \mathbf{K}_{ij} = \mathbf{K}_{ij} + \lambda, \quad (5.24)$$

where i and j are the degrees of freedom on opposite sides of the unit cell that are constrained to displace equally and λ is the penalty parameter. The penalty parameter is selected to be a relatively large constant, i.e., $\lambda \gg \max(\mathbf{K}_{ii})$ (Bathe, 1982). For example, $\lambda = (1 \times 10^7)C_{1111}$, where C_{1111} is the constitutive tensor component of the stiffer material. To prevent rigid body modes, one node in the unit cell model is constrained not to displace. This is implemented by modifying the global stiffness matrix using the penalty method.

Once the global stiffness matrix is modified, the nodal displacements corresponding to the unit strain kl are determined by solving the finite element equation:

$$\mathbf{K} \mathbf{u}^{kl} = \mathbf{f}^{kl}. \quad (5.25)$$

The fluctuating strain components for unit strain kl are determined at the element centroids from the nodal displacements

$$\varepsilon^{*kl} = \mathbf{B} \mathbf{u}^{kl}, \quad (5.26)$$

where \mathbf{B} is evaluated at the element centroid.

This process is repeated for each unit strain (a total of three times for the 2D case). The fluctuating strain components determined by the finite element method are used to calculate the local structure tensor, M_{ijkl} , according to equation (5.18). Once the local structure tensor is determined, the effective stiffness tensor is calculated by discretizing equation (5.20):

$$\bar{\mathbf{C}} = \frac{1}{|V_{UC}|} \sum_{N^{(e)}} \mathbf{C}^n \mathbf{M} \mathbf{V}^{(e)}, \quad (5.27)$$

where $N^{(e)}$ is the number of elements in the unit cell model.

This formulation was implemented in a custom software package (HOMOG) written using MATLAB (The Mathworks, Inc., Natick, MA). This package was used in conjunction with a commercial finite element package (ANSYS v5.4, ANSYS, Inc., Canonsburg, PA), as outlined in Figure 5.3. The ANSYS pre-processor was used to develop finite element models of the unit cell and the global model. The unit cell finite element model was analyzed using HOMOG to generate the local structure tensor, M_{ijkl} , and the effective stiffness tensor, $\bar{\mathbf{C}}_{ijkl}$, of

the homogenized composite body. The effective stiffness tensor was incorporated into global model, which was then analyzed using ANSYS to obtain average (macroscopic) strain tensors for the homogenized composite (according to equation 5.21). Finally, the local (microscopic) strains in the composite were determined using the local structure matrix and the macroscopic strains obtained from the global analysis (according to equation 5.17).

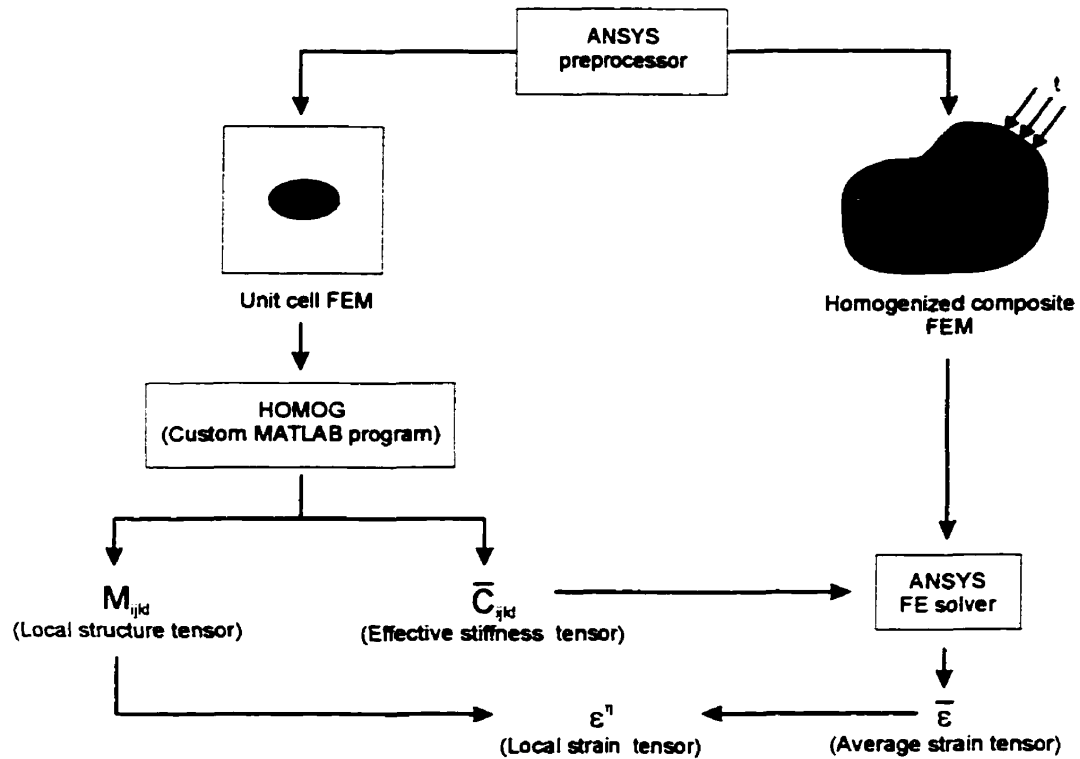


Figure 5.3. Numerical implementation of the homogenization method using custom software (HOMOG) and a commercial finite element package (ANSYS).

5.5 Additional comments on homogenization theory

The accuracy of homogenization theory has been shown to depend on η , the size of the unit cell relative to that of the macroscopic body (reviewed in Hollister and Kikuchi, 1992). Generally, the mechanical behaviour of the homogenized composite approaches that of the true composite material as η decreases, i.e.,

$$\lim_{\eta \rightarrow 0} \frac{\partial}{\partial x_i} \left[C_{ijkl}^{\eta} \frac{\partial u_k^{\eta}}{\partial x_l} \right] \rightarrow \frac{\partial}{\partial x_i} \left[\bar{C}_{ijkl} \frac{\partial u_k^0}{\partial x_l} \right]. \quad (5.28)$$

However, many composites have a finite η ; Hollister and Kikuchi (1992) considered this case by investigating the errors associated with standard mechanics and homogenization approaches to analyze unit cells with a finite η . Their findings relevant to this thesis include:

1. For periodic composites, where the ratio of the unit cell to the global structure is finite, the local strain energy predicted by homogenization analysis is more accurate than that predicted by standard mechanics approaches.
2. Homogenization analysis is more efficient computationally than standard mechanics approaches to unit cell analyses.
3. The local strain energy predicted by homogenization analysis was within 30% of that computed directly (by the finite element method) for most of the cases considered.
4. The largest errors with the homogenization method occurred at the traction and free boundaries of the composite, and at the boundary of dissimilar materials, but were confined to a relatively thin boundary layer. The inaccuracies result because the formulation applied here does not account for the large fluctuations in stress and strain that occur close to boundaries.

5.6 Verification of the code

In order to verify the code used to perform the homogenization analysis (HOMOG), predictions for the effective properties of three unit cell geometries were compared with published results, also determined using homogenization and finite element methods (Ghosh et al., 1995; Lukkassen et al., 1995).

5.6.1 Methods

The unit cell models used to verify the code had simple geometries representing unidirectional fibre-reinforced composites (Figure 5.4). Unit cells A and B represent longitudinal sections of short and long fibre composites, respectively. The finite element meshes for unit cells A and B were described by Ghosh et al. (1995), and were replicated identically for the verification experiments. Unit cell C represents a cross-section of a fibre-reinforced composite. The mesh for unit cell C was not provided by Lukkassen et al. (1995); for the verification experiments, a variety of mesh densities (192 to 1160 elements) were tested. The material properties of the constituents for each unit cell are provided in Table 5.1. For each unit cell, the components of the effective constitutive tensor predicted by HOMOG were compared to those reported in the literature.

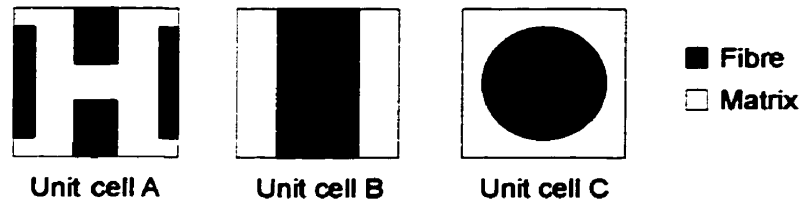


Figure 5.4. Unit cell models used to verify the homogenization code. (A) A longitudinal section of a short fibre composite; (B) a longitudinal section of a long fibre composite (from Ghosh et al., 1995); and (C) a cross-section of a fibre-reinforced composite (from Lukkassen et al., 1995).

Table 5.1. Elastic properties of the materials in the unit cell finite element models used to validate the code (from Ghosh et al., 1995; Lukkassen et al., 1995).

	Fibre			Matrix		
	Material	E (GPa)	ν	Material	E (GPa)	ν
Unit cell A	Boron	400	0.2	Aluminum	72.5	0.33
Unit cell B	Boron	400	0.2	Aluminum	72.5	0.33
Unit cell C	Glass	70	0.2	Epoxy	3.5	0.35

5.6.2 Results and discussion

The effective properties predicted using the custom code, HOMOG, were identical to those reported by Ghosh et al. (1995) for unit cells A and B (Table 5.2). For unit cell C, there was very good agreement between the predicted effective properties and those reported by Lukkassen et al. (1995) (Table 5.3). The small differences (maximal for the low-density mesh and less than 3.3% in all cases) are acceptable and expected, given that the finite element meshes were not identical. The agreement between the effective properties predicted by HOMOG and those reported in the literature verifies the code and the numerical implementation of the homogenization method.

Table 5.2. Comparison of the effective material properties predicted using HOMOG with those published by Ghosh et al. (1995) for unit cell models A and B.

	Unit Cell A		Unit Cell B	
	HOMOG	Ghosh	HOMOG	Ghosh
\bar{C}_{1111} (GPa)	122.4	122.4	136.1	136.1
\bar{C}_{2222} (GPa)	151.2	151.2	245.8	245.8
\bar{C}_{1212} (GPa)	42.10	42.10	46.85	46.85
\bar{C}_{1122} (GPa)	36.23	36.23	36.08	36.08

Table 5.3. Comparison of the effective material properties predicted using HOMOG with those published by Lukkassen et al. (1995) for unit cell model C.

	Unit Cell C				
	HOMOG 192	HOMOG 408	HOMOG 704	HOMOG 1160	Lukkassen
\bar{C}_{1111} (GPa)	11.75	11.74	11.74	11.73	11.7
\bar{C}_{2222} (GPa)	11.75	11.74	11.74	11.73	11.7
\bar{C}_{1212} (GPa)	2.480	2.467	2.461	2.457	2.4
\bar{C}_{1122} (GPa)	4.390	4.423	4.436	4.447	4.5

5.7 Idealized geometry unit cell models of the porous-surfaced and plasma-sprayed interface zones

The theory, numerical implementation, and code developed in the preceding sections were applied to model and analyze the interface zones for porous-surfaced and plasma-sprayed implants. The features of the models and the results of the analyses using the homogenization method are described in the following sections.

5.7.1 Features of the unit cell models

Baseline unit cell models were developed to represent the porous-surfaced and plasma-sprayed interface zones (Figure 5.5 and Figure 5.6, respectively). As a first approximation, the unit cells had idealized, two-dimensional geometries based on the characteristics of the actual interface zones, including volume porosity, pore size, interface zone width, and allowance for mechanical interlock between the tissue and implant surface features. These geometric characteristics were based on measurements made from back-scattered scanning electron micrographs of the implants used in the rabbit model study (Chapter 4). The idealized geometry approach provided initial models that were representative of the real surfaces, but were simplified for ease of analysis and for consistency between the governing parameters of the model and its predictions.

For the porous-surfaced interface zone model, the metal particles were constrained to one another using the penalty method, thus simulating the relative stiffness of the porous surface structure (Figure 5.5). This model is similar to one proposed by Ko (1994). The plasma-sprayed interface zone model had an undulating surface and isolated pores into which tissue could grow (Figure 5.6). The unit cells models represented the geometry of the interface as observed four days post-implantation in the animal model experiments (Section 4.4.2). After this short period of healing in the experiments, a well-defined interface zone filled with early repair tissue had formed adjacent to both implant designs, but without any evidence of mineralization. Convergence tests indicated that the mesh densities shown in Figure 5.5 and Figure 5.6 were appropriate.

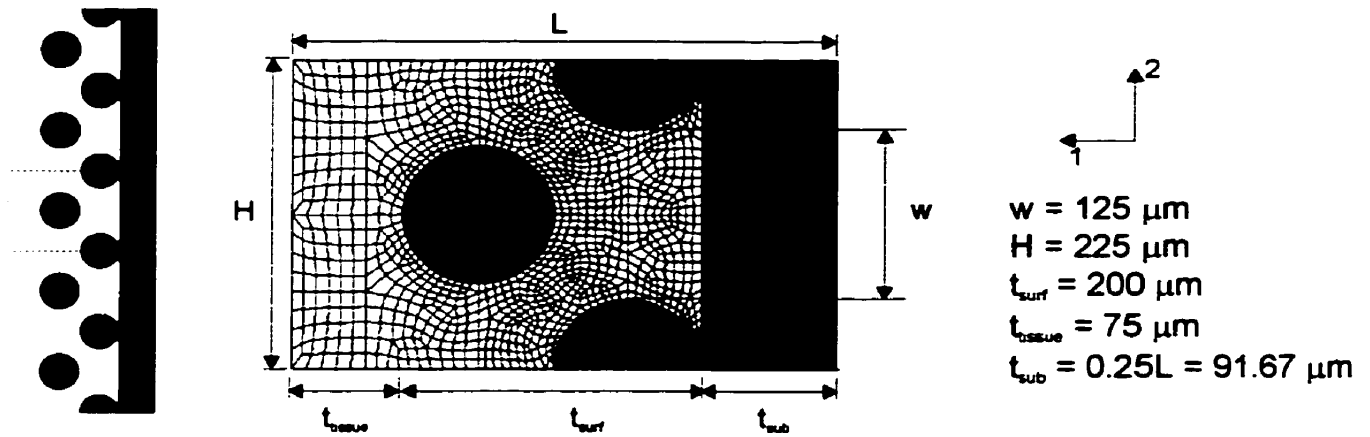


Figure 5.5. Idealized unit cell model of the porous-surfaced interface zone (baseline model). The displacements of the metal particles were constrained to one another in the model using the penalty method.

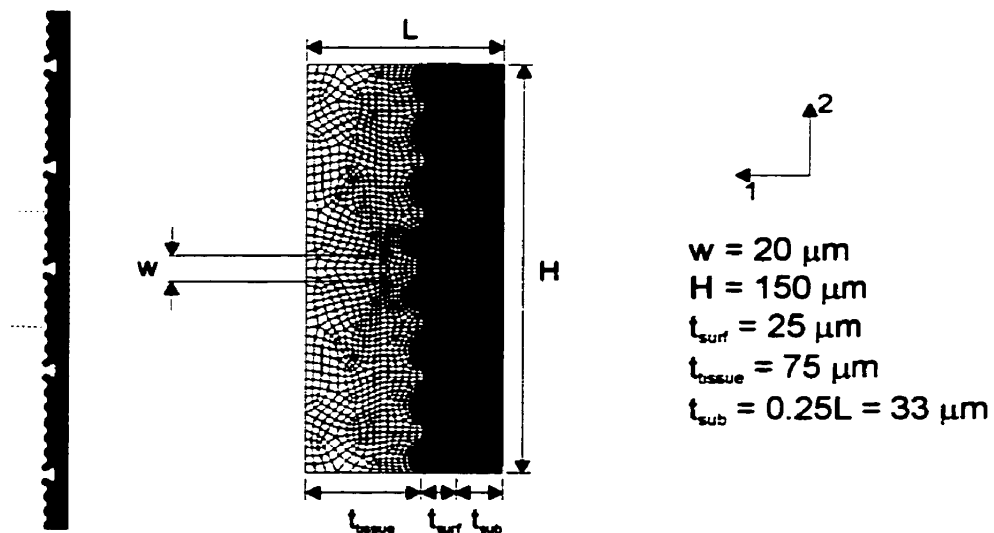


Figure 5.6. Idealized unit cell model of the plasma-sprayed interface zone (baseline model).

5.7.2 Effective and local properties of the idealized geometry unit cell models

Methods

The unit cell models were analyzed using the numerical implementation of the homogenization method described in Section 5.4. The implant material and ingrown tissue were modelled as homogeneous, linear elastic materials with the properties given in Table 5.4. The elastic properties of the interface zone tissue were similar to those of the initial tissues formed

during fracture healing (Carter et al., 1988; Cheal et al., 1991; Claes and Heigele, 1999). It was assumed the metal and tissue were perfectly bonded and the tissue infiltrated the porosity or irregularities of the implant surface structures fully.

Table 5.4. Elastic constants used in the unit cell finite element models

Material	E	ν	Reference
Titanium	100 GPa	0.33	-
Interface zone tissue	1 MPa	0.45	Based on Cheal et al., (1991), Claes and Heigele (1999), and Carter et al. (1988)

Results

The effective elastic constants predicted by the computational model for the homogenized interface zones were highly anisotropic. In the direction parallel to the long axis of the implant (the longitudinal direction), the modulus was dominated by the stiffness of the metal substrate and surface structure, whereas normal to the implant surface (the transverse direction) the modulus was dictated primarily by the compliance of the tissue component (Table 5.5). Comparison of the two surface designs indicated that the transverse and shear moduli for the porous-surfaced interface zone were over 36% larger than those for the plasma-sprayed interface zone. The longitudinal modulus of the porous-surfaced interface zone was 11% lower than that for the plasma-sprayed interface zone.

Due to the local surface geometry, the porous-surfaced interface zone had large regions that were “strain protected”, particularly for the transverse (M_{1111}) and shear (M_{1212}) components of the local structure tensor (Figure 5.7 and Figure 5.8). Although the tissue within the pores of the plasma-sprayed coating was similarly protected, this amount of tissue represented only a small fraction of the total tissue area; the majority of the tissue for the plasma-sprayed design had relatively high magnitudes for the local structure tensor components M_{1111} and M_{1212} . Conversely, the magnitudes of the longitudinal local structure component (M_{2222}) were generally lower in the plasma-sprayed interface zone than in the porous-surfaced interface zone.

The implications of the differences between the effective and local properties of the two surface designs are considered in Chapters 6 and 7.

Table 5.5. Effective elastic constants of the homogenized interface zones predicted by the computational model.

Constant	Porous surfaced	Plasma-sprayed
E_1 (MPa)	3.59	2.29
E_2 (GPa)	28.2	31.3
G_{12} (MPa)	1.18	0.663
ν_{12}	3.9×10^{-5}	2.5×10^{-5}
ν_{21}	0.306	0.348

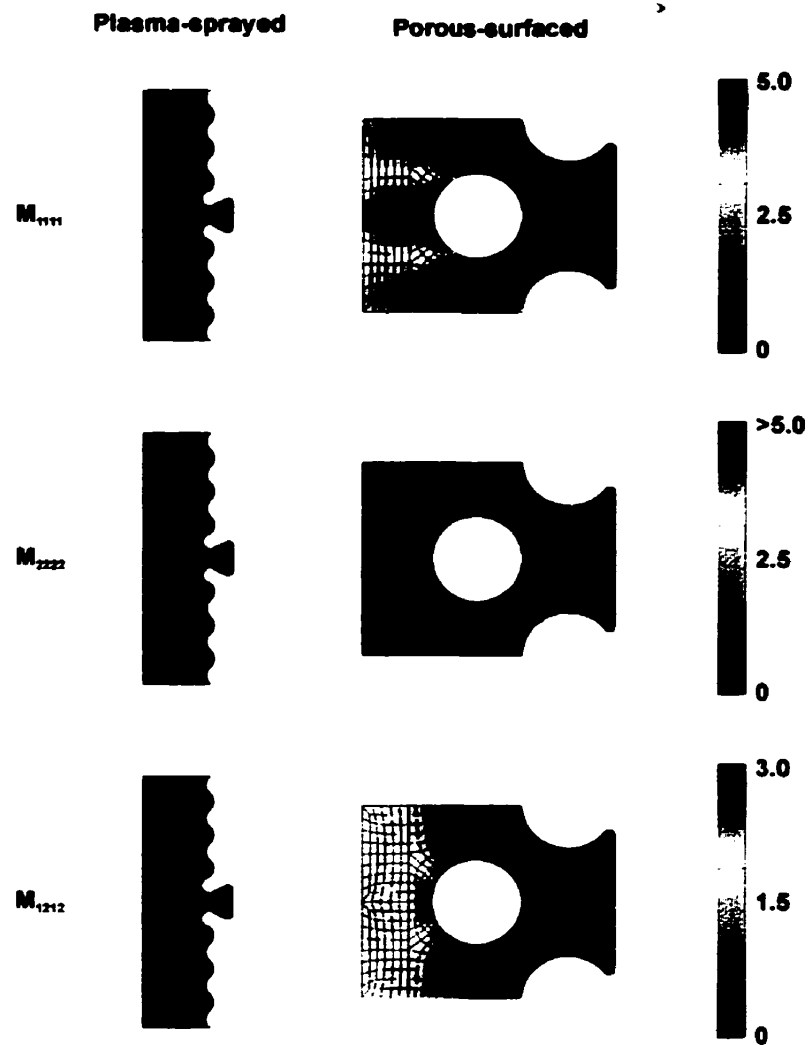


Figure 5.7. Field plots of the local structure tensor (M_{ijkl}) components for the plasma-sprayed interface zone tissue (left) and porous-surfaced interface zone tissue (right). Higher values of M_{ijkl} occur in regions with strain concentrations, whereas lower values of M_{ijkl} occur in strain-protected regions.

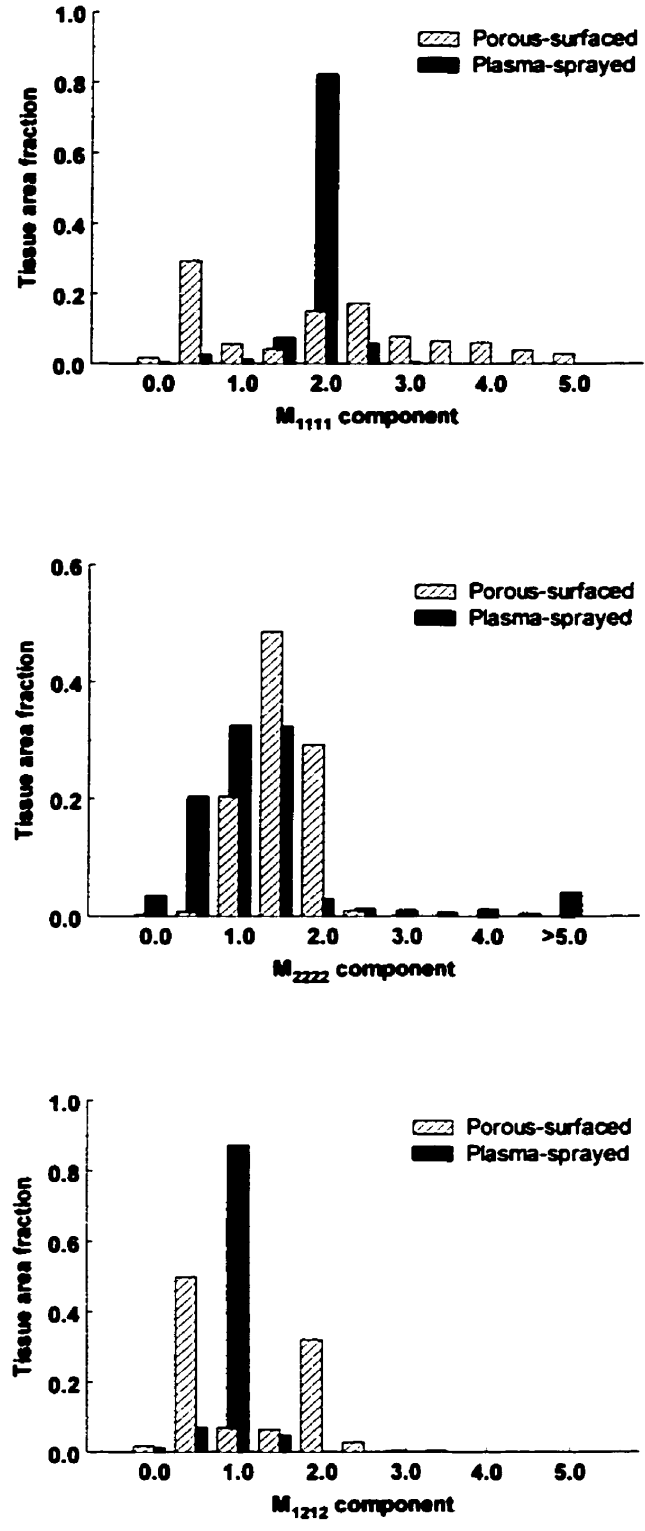


Figure 5.8. Histograms of the local structure tensor (M_{ijkl}) components for the porous-surfaced and plasma-sprayed interface zone tissues.

5.8 Validation of computational model

In order to validate the homogenization approach and the unit cell models for the two surface designs, the effective and local properties of the interface zones predicted by the computational models were compared to properties measured experimentally and to those predicted by another composite theory. Ko et al. (1996) have measured the effective elastic moduli of composites of titanium sintered porous surfaces and epoxies representing ingrown tissue. Their data were used to validate the effective properties of the porous-surfaced interface zone predicted by the homogenization method (Section 5.8.1). In order to validate the homogenization predictions for the effective properties of the plasma-sprayed interface zone, comparisons were made with the effective properties predicted by the Hashin-Shtrikman model (Hashin and Shtrikman, 1963) (Section 5.8.2). The local properties predicted by the homogenization method for a composite with unidirectional periodicity have not been validated experimentally. Therefore, we used the photoelastic method to determine the local stress field in test specimens representing the porous-surfaced and plasma-sprayed interface zones, and compared the experimental results with those predicted by homogenization theory (Section 5.8.3).

5.8.1 Validation of the effective properties of the porous-surfaced interface zone

Methods

Ko (1994) and Ko et al. (1996) have measured the effective elastic constants of composites of porous-surfaced titanium and epoxy (Figure 5.9). The specimens were developed to mimic the tissue-implant interface of a porous-surfaced implant. In their experiments, Ko et al. measured the effective elastic moduli of titanium-epoxy composites parallel to the implant interface, transverse to the implant interface, and in shear for two different epoxies. They used the data to validate the effective constants predicted by various composite theories, including homogenization (Ko et al., 1996).

In the present study, Ko's experimental data were used to validate the effective elastic constants of the porous-surfaced interface zone predicted by the homogenization method using the idealized unit cell described in Section 5.7. The dimensions of the model were modified to represent the geometry of Ko's experimental specimens (Figure 5.10). The elastic constants of the constituent materials considered (titanium and two epoxies) are given in Table 5.6. The

constants predicted by the model were compared to those obtained experimentally using a one-sample t-test with $\alpha=0.01$.

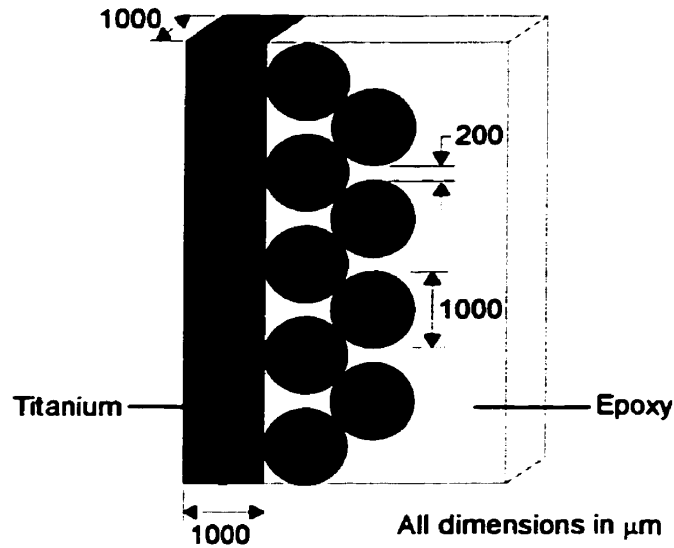


Figure 5.9. Schematic of the “tissue-implant” interface of the experimental test specimens used by Ko et al. (1996) to measure the effective elastic constants of a porous-surfaced titanium/epoxy composite (adapted from Ko et al., 1996).

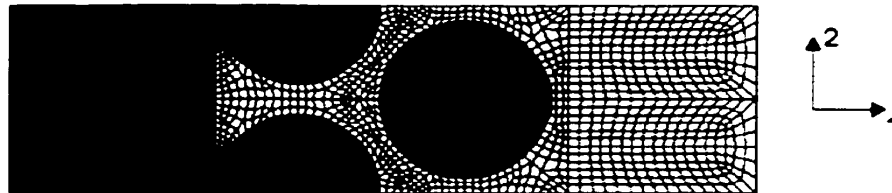


Figure 5.10. Idealized unit cell model used to predict the effective elastic constants of the porous-surfaced interface zone.

Table 5.6. Elastic constants of the constituent materials of the experimental test specimens (Ko et al., 1996).

Material	Volume fraction	E (GPa)	ν
Titanium	0.57	110	0.30
Epoxy I	0.43	0.2	0.42
Epoxy II	0.43	3.0	0.36

Results

The results predicted by the homogenization method for the idealized geometry unit cell model were very close to those obtained by Ko et al. (1996) using homogenization theory, but with a different unit cell model (Figure 5.11). The small differences are attributable to the possible differences between the unit cell models and the finite element models. The effective elastic constants predicted with the idealized geometry unit cell were also similar to those measured experimentally (Figure 5.11). There were no significant differences between the analytical and experimental values for the transverse (E_1) and shear (G_{12}) moduli for either epoxy. However, the longitudinal moduli (E_2) predicted by homogenization theory were less than those measured experimentally by 10 to 15% ($p < 0.01$). Ko et al. (1996) reported no significant differences between their experimental measurements and the effective moduli predicted by homogenization theory; however, analysis of the raw data from Ko's thesis (1994) indicates that their predictions for the longitudinal moduli are *different* from those measured experimentally ($p < 0.01$), in contrast to what was reported in their paper (Ko et al., 1996) but similar to the results obtained in the present study.

The differences between the predicted and measured moduli may have resulted from discrepancies between the experimental specimens and the unit cell model, which represented the sintered porous surface as a periodic structure with idealized geometry. Given the assumptions inherent in the homogenization method, the observed differences are quite reasonable and acceptable. Ko et al. (1996) showed that the method was more accurate than the rule of mixtures (Hill, 1963) and as accurate, but more versatile than the Hashin-Shtrikman approach (Hashin and Shtrikman, 1963) for estimating the effective elastic constants. Furthermore, Hashin-Shtrikman estimates become less accurate as the moduli of the constituent materials become more disparate (Hashin and Shtrikman, 1963), thus limiting the utility of this approach, particularly for the application proposed in this thesis.

In conclusion, the idealized geometry unit cell model and the homogenization approach were shown to predict accurately the effective transverse and shear moduli of the porous-surfaced interface zone. The homogenization approach predicted longitudinal moduli that were less than those measured experimentally by 10 to 15%; however homogenization theory has been shown to be more accurate and versatile than other composite theories. The implications of the modest difference between the experimental and analytical values for specific applications are considered in Chapters 6 and 7.

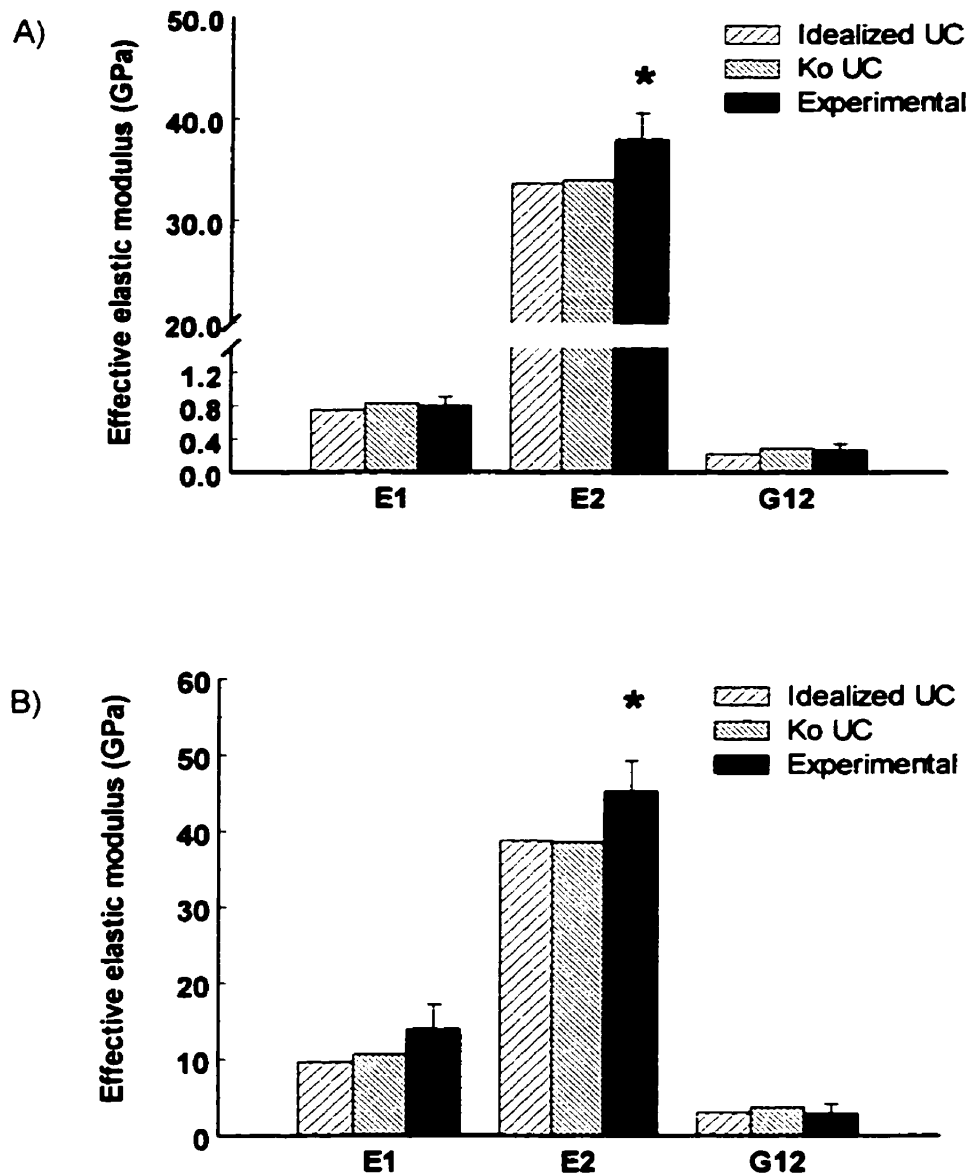


Figure 5.11. Effective elastic constants of the composite of porous-surfaced titanium and epoxy I (A) and epoxy II (B) predicted by the homogenization method for the current UC and the UC of Ko et al. (1996), and measured experimentally (Ko et al., 1996). The experimental data are presented as mean \pm standard deviation. An asterisk indicates a statistically significant difference between the theoretical and experimental values ($p < 0.01$).

5.8.2 Validation of the effective properties of the plasma-sprayed interface zone

Methods

The effective properties of the plasma-sprayed interface zone predicted by the homogenization method were compared with those predicted by the Hashin-Shtrikman model (Hashin and Shtrikman, 1963). This approach (i.e., validating the homogenization predictions by comparison with a standard composite theory) was pursued because the appropriate data necessary for experimental validation have not been obtained. The Hashin-Shtrikman model is a standard approach for analyzing composites and has been shown to predict values that are reasonably close to those determined experimentally (Ko et al., 1996). The baseline unit cell model of the plasma-sprayed interface zone (Figure 5.6) with the material properties described in Table 5.4 was used for the comparison.

Results

The effective properties predicted by the two theories were similar, with the homogenization method predicting effective transverse (E_1) and shear moduli (G_{12}) that were lower than the lower bounds predicted by the Hashin-Shtrikman model (by 14.5% and 29%, respectively). Conversely, the longitudinal modulus (E_2) predicted by the homogenization method was 17.1% greater than the upper bound predicted by the Hashin-Shtrikman model. In an earlier study with porous-surfaced implants, Ko et al. (1996) found that, although homogenization estimates were as much as 35% different from Hashin-Shtrikman estimates, there were no statistical differences between the values predicted by the two theories and those measured experimentally. This suggests that the differences observed here for the plasma-sprayed interface zone are reasonable and within the range that one would expect to measure experimentally. Therefore, in lieu of more conclusive experimental evidence, the comparison with Hashin-Shtrikman estimates provides initial support for the validity of the predictions of the effective properties of the plasma-sprayed interface zone using homogenization theory.

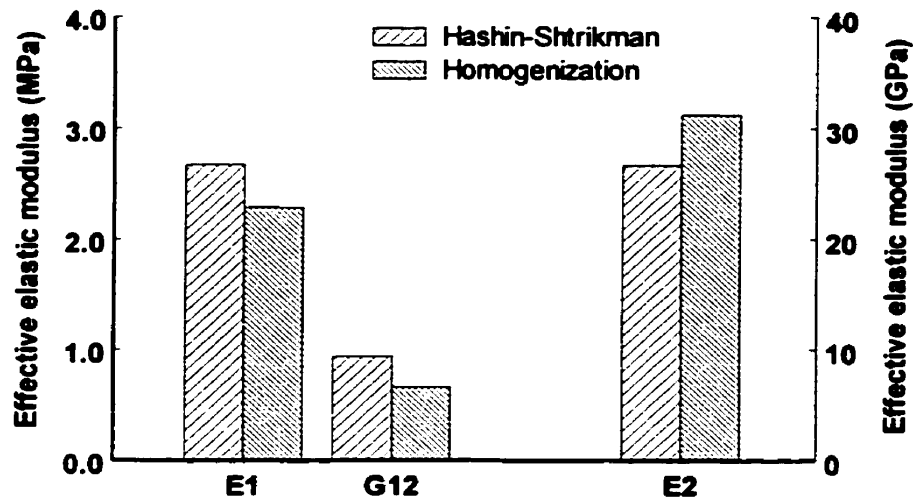


Figure 5.12. Effective elastic constants of the plasma-sprayed interface zone predicted by the Hashin-Shtrikman and homogenization methods for the baseline idealized unit cell model.

5.8.3 Validation of the local properties of the interface zones

Earlier studies by Ko (1994) and Kohn et al. (1993a), compared the local stresses around porous-surfaced implants predicted by the homogenization method with those predicted by the standard finite element method. They showed good agreement, with a maximum difference in the von Mises stresses of 15% for typical applied loads. However, the local field around porous-surfaced and plasma-sprayed implants has not been investigated experimentally. In order to validate the computational predictions for the local stress (strain) field experimentally, we compared the predictions using the homogenization method with those obtained using the photoelastic method.

Methods

In order to visualize the local strain field, we constructed large-scale two-dimensional models of the porous-surfaced and plasma-sprayed interface zones (Figure 5.13). The geometries of the two surfaces resembled those of the idealized unit cell models. The sintered porous surface was modelled with metal discs to represent the sintered particles; these discs were constrained to one another out of the plane of the model by 0.125 inch diameter steel bars that were inserted through channels in the discs, and then glued to the discs and the "substrate". This assembly mimicked the rigidity of the sintered porous surface structure. The geometry of the

plasma-sprayed model was simplified somewhat for ease of machining, but still replicated the undercut regions and irregular geometry of the plasma-sprayed surface.

Brass was used to represent the implant substrate and surface features, and birefringent polycarbonate sheets (PSM-1, Intertechnology, Inc., Toronto, ON) were used to represent the ingrown tissue. The mechanical and optical properties of the materials are provided in Table 5.7. This combination of materials was selected to mimic the disparity in material properties that exists at the tissue-implant interface. Two bonding conditions were investigated: (1) fully bonded, for which the metal and polycarbonate components were bonded with epoxy at all contacting surfaces; and (2) non-bonded, for which there was no adhesion between the metal and polycarbonate components, and the interaction between the two components was entirely via contact. Furthermore, two loading conditions were considered: (1) a tensile load applied parallel to the implant interface (the longitudinal direction); and (2) a tensile load applied normal to the implant interface (the transverse direction). In both cases, the distributed loads were applied to the edges of the test specimen by loading pins.

The photoelastic models were examined using a digital photoelasticity technique. This method uses a traditional diffuse light polariscope system (Series 060, Measurements Group, Inc., Raleigh, NC) with a load frame and a monochromator, which was used to acquire the isochromatic images. The applied load was measured directly using a load cell. Full field, isochromatic, and isoclinic images were obtained using a digital image analysis system, which included a standard CCD camera, an imaging board, an image processor, and a personal computer. The photoelastic images were captured with a spatial resolution of 640×480 pixels and 24-bit colour resolution. The digital isochromatic images were filtered (posterized) using image processing software (Corel PHOTO-PAINT Version 8, Corel Corporation, Ottawa, ON) to obtain fringe patterns that corresponded to the loci of points having the same difference in principal stress (or constant maximum shear stress).

Unit cell models were developed to replicate the geometry and dimensions of the photoelastic models. As with the unit cell models described in Section 5.7, full bonding was assumed between the materials, and the penalty method was used to constrain the metal particles of the sintered porous surface to the substrate (Section 5.4). Loading conditions representing the loads applied in the photoelastic experiments were applied to the unit cell models. The models were analyzed using the homogenization method to obtain contour plots of the difference in principal strains, and the results were compared qualitatively with the isochromatic fringe

patterns obtained with the fully bonded photoelastic models. Comparisons were also made between the photoelastic results obtained with the fully bonded and non-bonded models.

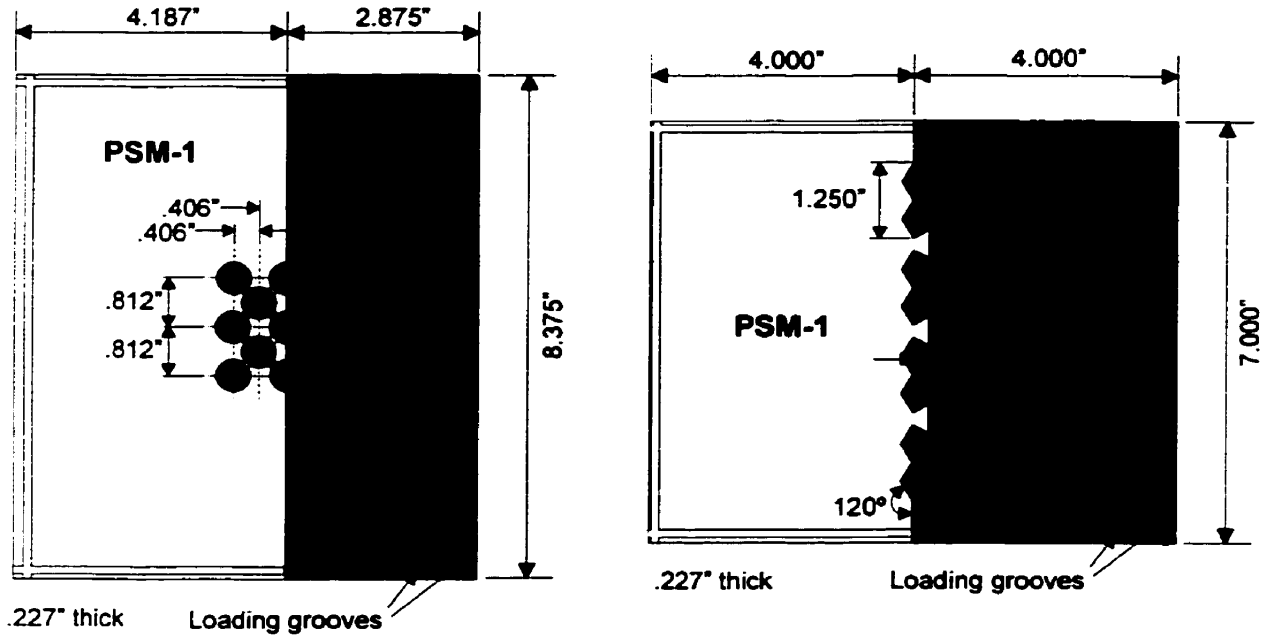


Figure 5.13. Schematics of the photoelastic test specimens used to model the porous-surfaced (left) and plasma-sprayed (right) interface zones.

Table 5.7. Mechanical and optical constants of the constituent materials of the photoelastic test specimens (provided by the supplier).

Material	E (GPa)	ν	f_G (kPa/fringe/m)
Brass	100	0.33	-
PSM-1	2.5	0.38	7.0

Results and discussion

Comparison between experimental and computational results: Although the photoelastic models were constructed with great care by experienced machinists, the machining and assembly of the models created significant residual stresses in the photoelastic material. This was particularly evident around the discs of the porous-surfaced model and around the undercut regions of the plasma-sprayed model. As a result, detailed comparisons of the stress field close to the surface features were not possible. Fortunately, the polycarbonate material in many of these regions of the fully bonded models was "shielded" by the rigid metal structures, and therefore one would expect negligible stresses in those regions. This was confirmed by comparing the full field image at full load with that obtained when the model was unloaded: in the shielded regions (i.e., within the sintered porous surface structure and within the recesses of the plasma-sprayed surface), the fringe pattern did not change markedly when the load was applied.

Despite the experimental errors resulting from the residual stresses, there was reasonable agreement between the isochromatic fringe patterns of the fully bonded photoelastic models with the computational model predictions for both interface zones (Figure 5.14 and Figure 5.15). For the porous-surfaced interface zone and a 454 N transverse load, both the experimental and computational models predicted a region of relatively low maximum shear stress (strain) within the surface structure (indicated by ① in Figure 5.14), a band of intermediate level stress extending from the particles into the tissue layer ②, and regions of relatively higher stress at the outer edge of the outermost particles ③. For the plasma-sprayed interface zone loaded transversely, the experimental and computational models predicted low maximum shear stresses (strains) within the recesses of the surface structure and extending out into the tissue (indicated by ① in Figure 5.15). Higher stresses were observed in the areas immediately adjacent to the pores ②. In the depressions in the implant surface, the stresses were relatively low in both the experimental and computational model ③.

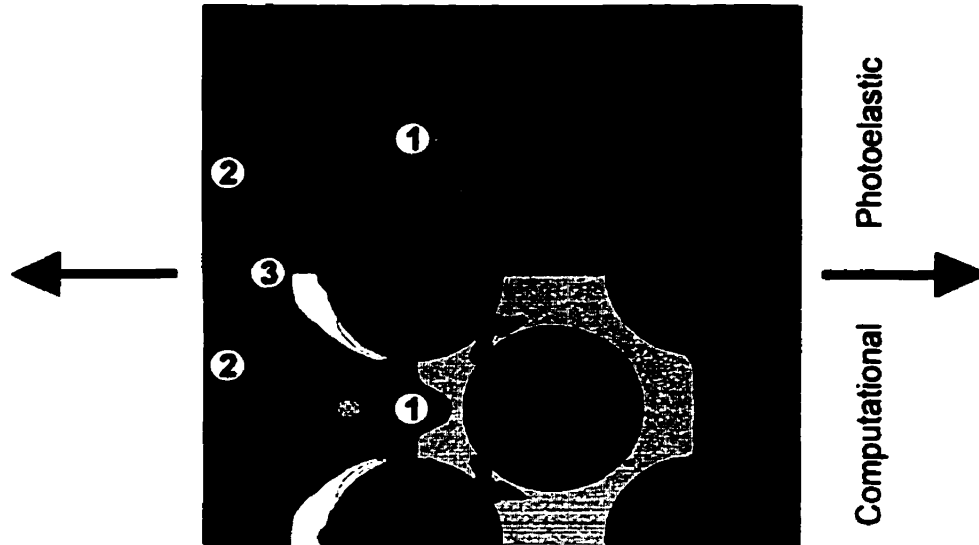


Figure 5.14. A comparison of the isochromatic fringe patterns obtained by the photoelastic method (top half) and the computational model (bottom half) for transverse loading of the porous-surfaced interface zone models. Numbers indicate corresponding regions in the two models (refer to text for an explanation).

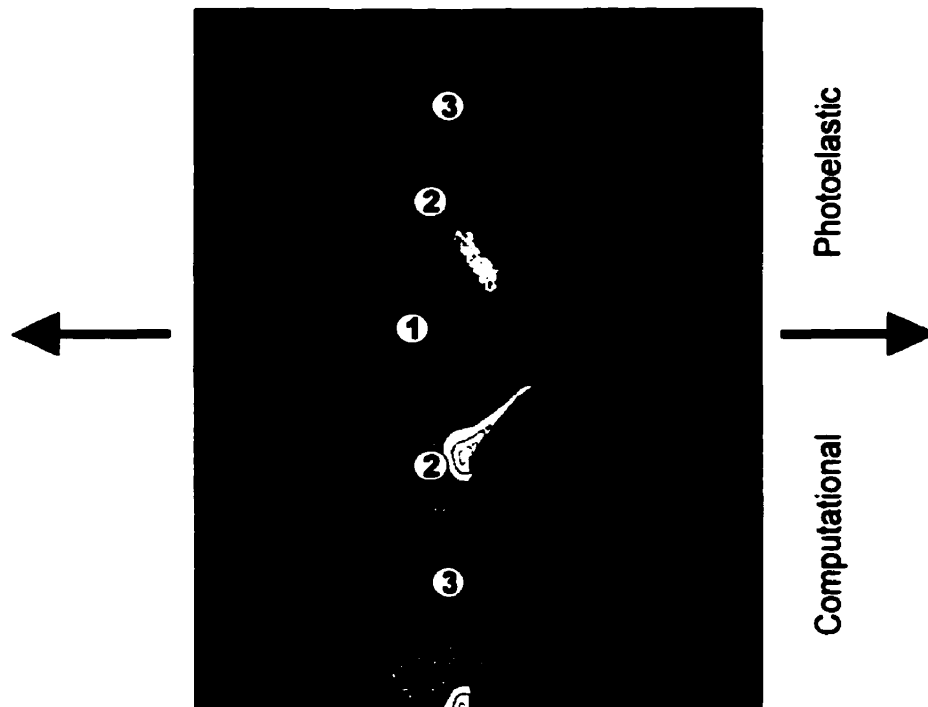


Figure 5.15. A comparison of the isochromatic fringe patterns obtained by the photoelastic method (top half) and the computational model (bottom half) for transverse loading of the plasma-sprayed interface zone models. Numbers indicate corresponding regions in the two models (refer to text for an explanation).

When the same load magnitudes were applied longitudinally (i.e., parallel to the implant interface), there was little change in the local stress field within the photoelastic material, since the majority of the load was carried by the stiffer metal component (the resin and metal were loaded essentially in parallel in this case). At much higher loads (1589 N), relatively uniform stresses developed in the photoelastic material outside the surface structures, consistent with the predictions of the computational model.

The discrepancies between the experimental results and the computational predictions can be attributed in most part to the residual stresses resulting from preparation of the photoelastic specimens. An additional likely source of discrepancy was inaccuracies in the computational model predictions, particularly at the interface of dissimilar materials and the free boundaries of the unit cells. For instance, the computational predictions of the maximum shear strains adjacent to the outer discs appear to be higher and distributed slightly differently than those measured experimentally (Figure 5.14). Kohn et al. (1993a) and Hollister and Kikuchi (1992) also observed that the greatest differences between homogenization and standard FE predictions occurred at material interfaces and the free boundaries of the unit cell. The homogenization formulation used here does not include non-linear boundary layer terms (Bakhvalov and Panasenko, 1989), and therefore cannot model accurately the high strain gradients that occur in certain regions. However, as shown by the photoelastic results, these inaccuracies appear to be limited to relatively small boundary regions, consistent with the findings of previous theoretical studies (Hollister and Kikuchi, 1992). Additionally, homogenization theory assumes that the homogenized material is spatially periodic. In the case of the tissue-implant interface zone, the periodicity is only in the longitudinal direction. Therefore, one would expect the uni-directional periodicity of the interface zone to limit the accuracy of the homogenization predictions of the local strain field. Despite the potential limitations of the homogenization method as implemented in this study, the local strain field predicted with the computational model was reasonably similar to that observed experimentally.

Comparison between fully bonded and non-bonded interface conditions: The metal-polycarbonate interface condition had a significant influence on the local stress field. For both the porous-surfaced and plasma-sprayed interface zone models, the local maximum shear stresses resulting from the surface features were significantly higher in the non-bonded models than in the fully bonded models (Figure 5.16). This was evident for both loading conditions, and

not only in the regions outside the surface structures, but also within the surface pores. In general, the disturbances in the local stress fields resulting from the surface features were more pronounced for the non-bonded models, extending further away from the substrate. Although the residual stresses in the photoelastic materials prevented a detailed comparison, it appeared qualitatively that changing the interface condition from fully to non-bonded had a comparable effect on the local stress field for the two implant surface geometries.

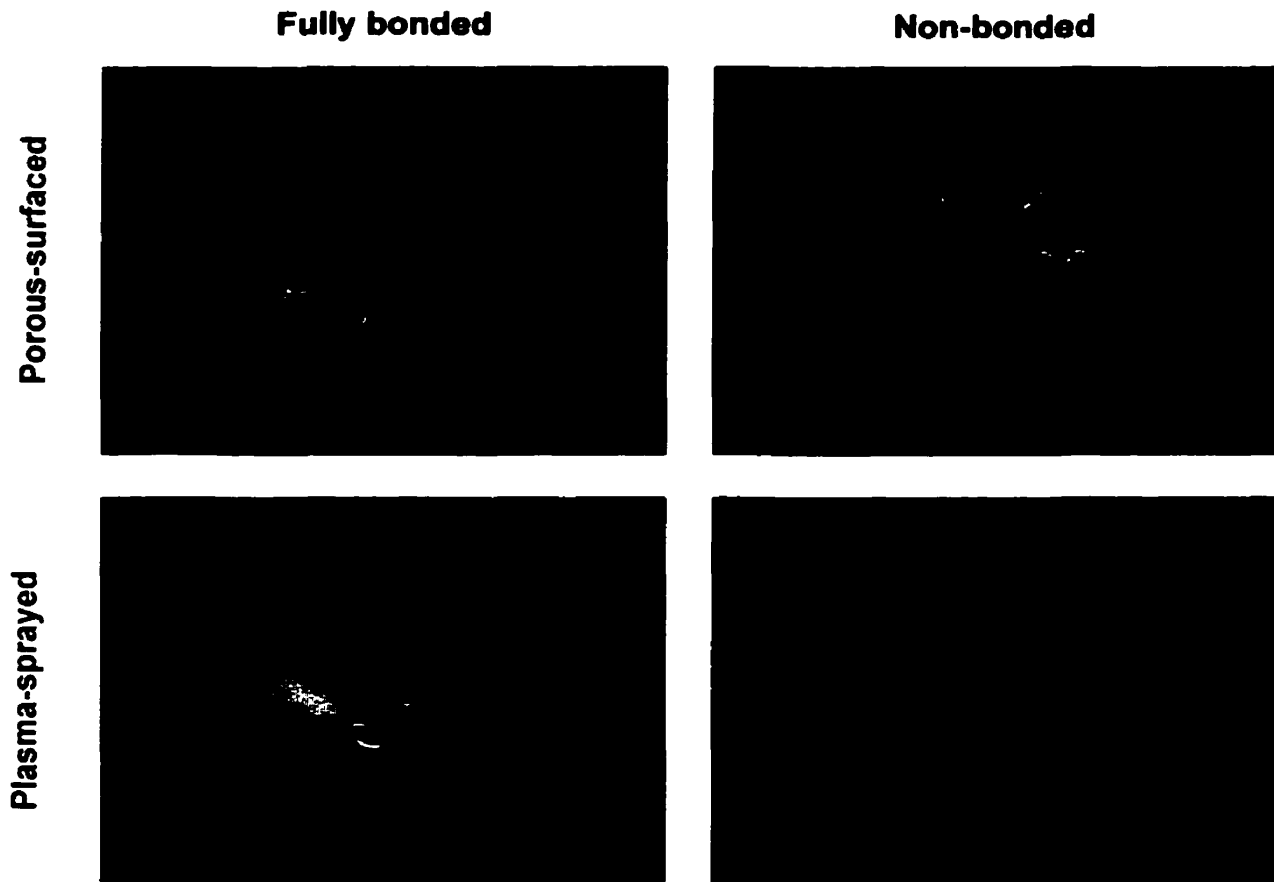


Figure 5.16. A comparison of the isochromatic fringe patterns for the two interface zone models, and the fully bonded and non-bonded interface conditions. A 454 N load was applied transverse to the interface in these cases.

5.9 Parametric investigations of implant surface pore size

The geometries of the baseline unit cell models developed in Section 5.7 (Figure 5.5 and Figure 5.6) were based on average values determined from the quantitative analysis of the BSE images. However, the geometries of the sintered porous and plasma-sprayed surfaces are very irregular. As a first step to understanding the effect of variations in surface geometry on the

effective and local mechanical properties of the interface zones, the pore sizes of the porous-surfaced and plasma-sprayed unit cell models were varied parametrically while keeping the volume porosities of the surface structures constant.

5.9.1 Methods

The pore sizes investigated for the sintered porous surface were 125 μm (baseline model), 50 μm , and 25 μm . Because the pore size of the porous surface is linearly related to the particle size and the volume porosity was kept constant, the width of the surface structure decreased with the pore size. For the plasma-sprayed surface, however, the coating thickness was kept constant and the pore sizes investigated were 50 μm , 20 μm (baseline), and 10 μm . To maintain the volume porosity, the inter-pore spacing in the plasma-sprayed coating was reduced as the pore size was reduced. In all cases, the width of the interface zone was 75 μm and the width of the substrate was $0.25L$, where L is the total width of the unit cell model. The dimensions of the UC models are given in Table 5.8.

The material properties of the UC models were the same as those used for the baseline UC models (Table 5.4). The UC models were analyzed using the homogenization method and the predicted effective and local properties for each model were compared to determine the effect of pore size on the properties of the interface zones.

Table 5.8. Dimensions (in μm) of unit cells used to investigate the effect of pore size (w) on the effective and local properties. Refer to Figure 5.5 and Figure 5.6 for definitions of dimension labels. An asterisk indicates baseline model geometry.

	w	H	t_{sub}	t_{surf}	t_{tissue}
Porous-surfaced 1 *	125	225	91.67	200	75
Porous-surfaced 2	50	90	51.67	80	75
Porous-surfaced 3	25	45	38.33	40	75
Plasma-sprayed 1	50	375	33	25	75
Plasma-sprayed 2 *	20	150	33	25	75
Plasma-sprayed 3	10	75	33	25	75

5.9.2 Results and discussion

The analyses revealed that the effective properties of the porous-surfaced design were dependent on the pore size, particularly in the transverse direction (Figure 5.17). A decrease in the pore size resulted in a decrease in the thickness of the porous surface structure. The decrease in the thickness of the surface layer, in conjunction with the width of the tissue region remaining constant, led to an increase in the volume fraction of the tissue component for the unit cell. Consequently, the effective transverse modulus (E_1), which is dominated by the compliant tissue layer, was reduced. The same dependency was not evident with the longitudinal modulus (E_2), since this modulus is dictated in large part by the metal component. For the plasma-sprayed design, the effective moduli were relatively insensitive to the variations in pore size (Figure 5.18). Again, the effective moduli are dictated in large part by the relative volume fractions of the metal and tissue components. The volume fraction and coating thickness were held constant for the plasma-sprayed models; thus, the relative volume fractions of the metal and tissue components, and therefore the effective moduli, remained essentially constant.

The local properties of the porous-surfaced interface zone, particularly the transverse (M_{1111}) and shear (M_{1212}) components of the local structure tensor, were also dependent on the pore size (Figure 5.19). Compared with the unit cells with small pore sizes, the distribution of the transverse and shear local structure components was wider for the unit cell with the 125 μm pore size, with greater volumes of tissue in strain protected and strain concentrated regions. With a smaller pore size, the amount of tissue that experienced extreme strain values decreased; this was because the size of the surface layer relative to the tissue layer was reduced as the pore size decreased, and therefore the effect of the surface features was limited to a smaller local region (on a tissue volume basis). For the plasma-sprayed interface zone, the local properties were relatively insensitive to variations in pore size (Figure 5.20), with only minor variations in the M_{2222} component. The implications of the sensitivity of the effective and local properties to pore size are considered further in Chapters 6 and 7.

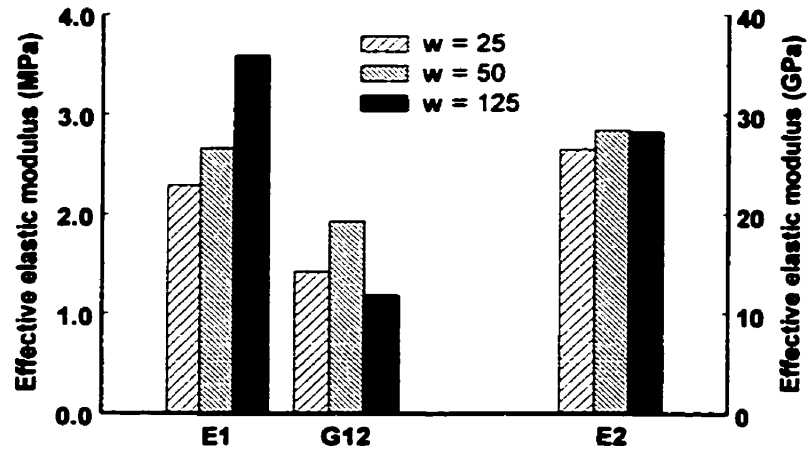


Figure 5.17. The effect of pore size (w , in μm) on the effective elastic moduli predicted by the homogenization method for the porous-surfaced interface zone.

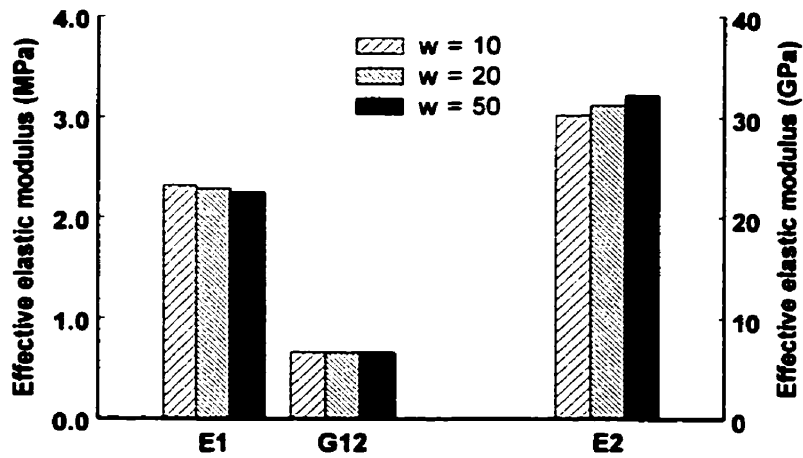


Figure 5.18. The effect of pore size (w , in μm) on the effective elastic moduli predicted by the homogenization method for the plasma-sprayed interface zone.

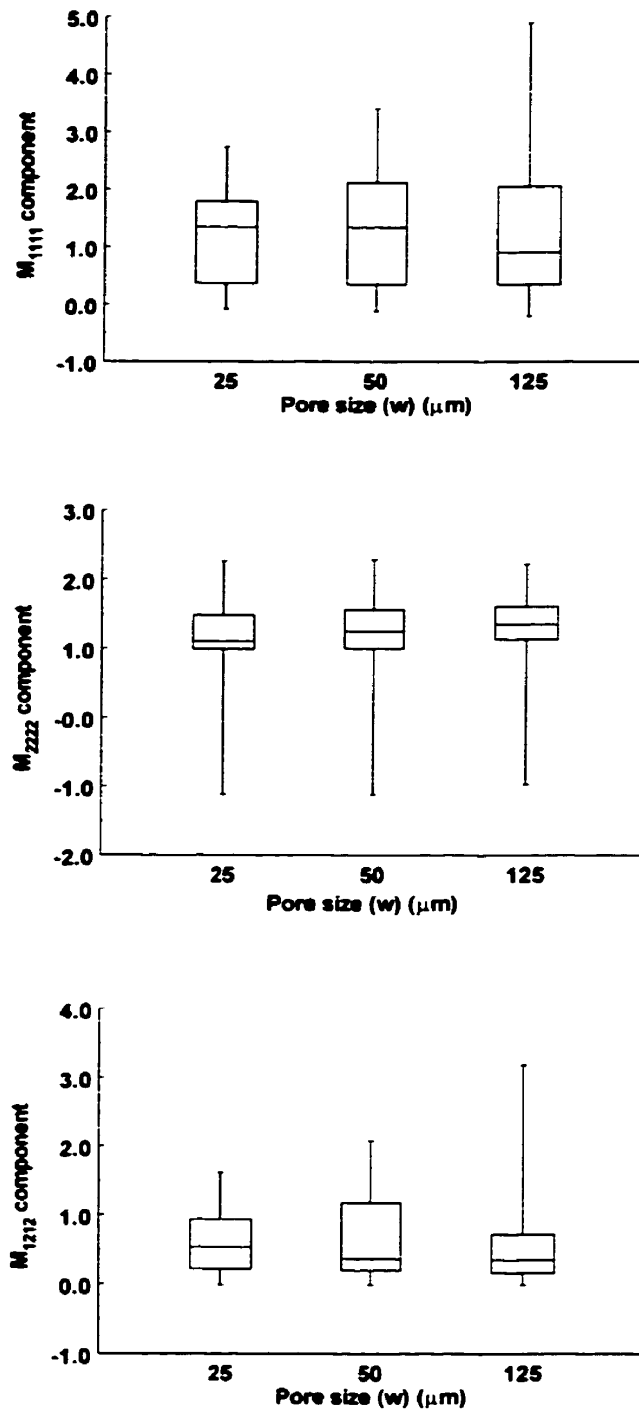


Figure 5.19. Box plots of the distributions of the local structure components for the porous-surfaced interface zone tissue for different implant surface pore sizes. The horizontal line within the box represents the median value, the upper and lower limits of the box represent the quartiles above and below the median, and the error bars indicate the full range of the local structure component.

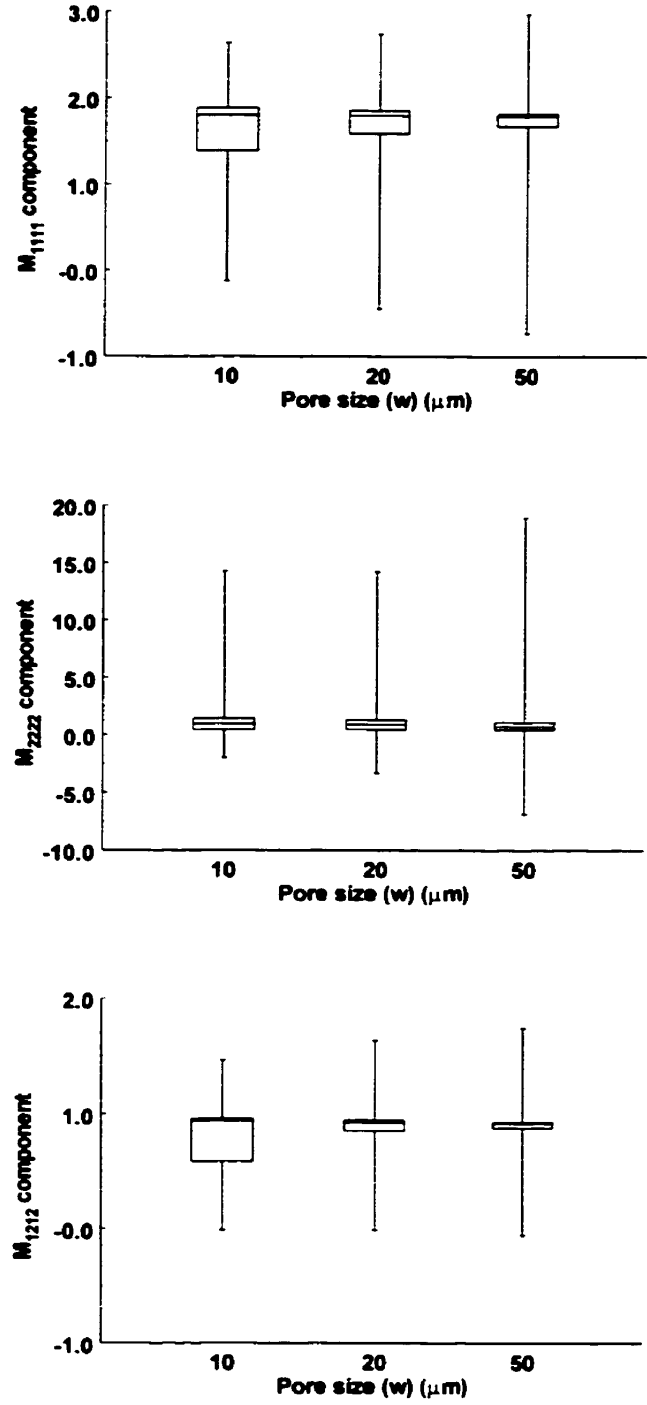


Figure 5.20. Box plots of the distributions of the local structure components for the plasma-sprayed interface zone tissue for different implant surface pore sizes.

5.10 Development and analysis of geometrically accurate unit cell models

In the investigations in Section 5.9, the effects of variations in pore size on the properties of the interface zones were investigated parametrically. In those investigations, however, the pore geometry was not varied. As mentioned previously, the sintered porous and plasma-sprayed surfaces have irregular geometries, a feature that cannot be represented by idealized unit cell models. In order to investigate the implications of using idealized geometry unit cells to model surfaces with irregular geometries, two-dimensional geometrically accurate unit cell (GAUC) models were developed, and the effective and local properties were compared with those for the idealized geometry models.

5.10.1 Methods

The 2D GAUC models were developed from digital back-scattered scanning electron (BSE) micrographs of the sintered porous and plasma-sprayed implant surfaces. Five representative regions for each surface design were selected at random from BSE digital micrographs for development into GAUC models. For the porous-surfaced implants, the substrate position and particle positions and dimensions in the selected regions were digitized manually using image analysis software (SigmaScan, SPSS, Inc., Chicago, IL). For the plasma-sprayed implants, the surface and particle contours in the selected regions were digitized manually, also using SigmaScan. Using custom software, the geometry data were converted into the ANSYS log file format so that the digital image geometry could be replicated as a solid model in the ANSYS preprocessor (Figure 5.21). For the porous-surfaced design, the particles were described as circular areas, and for the plasma-sprayed design, the surfaces were described by splines. Only the porosity of the plasma-sprayed surface that was contiguous with the implant surface was included in the unit cell model since it was assumed that the deeper porosity was not interconnected with the surface, and therefore was not accessible for tissue ingrowth.

Finite element models were created from the solid models using the ANSYS preprocessor. The models were meshed with 4-noded quadrilateral elements, with the number of elements ranging from 1462 for the simplest porous-surfaced GAUC to 20898 for the most complex plasma-sprayed GAUC. The width of the tissue layer in the GAUC models was 75 μm (as it was for the idealized geometry models), and the width of surface layer was determined directly from the BSE images. For the porous-surfaced GAUCs, the height of the UC was the same as for the idealized models (225 μm); for the plasma-sprayed GAUCs, the UC height was

determined directly from the BSE images. As with the idealized geometry models, the width of the substrate layer in the GAUCs was set to a quarter of the width of the entire UC. Components of the implant surface that were not contiguous with the implant substrate were constrained to the substrate using the penalty method. The material properties of the GAUC models were the same as those used for the idealized geometry unit cell models (Table 5.4).

The GAUC models were analyzed using the homogenization method, and comparisons were made between the properties predicted with the GAUC models and those predicted with the baseline idealized geometry models (Section 5.7.2). The effective properties predicted with the GAUC models were compared to those predicted with the idealized models using one-sample, one-tailed Wilcoxon tests. Analyses of variance were used to test for differences between the local properties predicted with the various GAUC models and the idealized model for each surface design. Pairwise comparisons were tested using the Fisher least significant difference test, with $\alpha=0.05$. All statistical analyses were performed using Minitab.

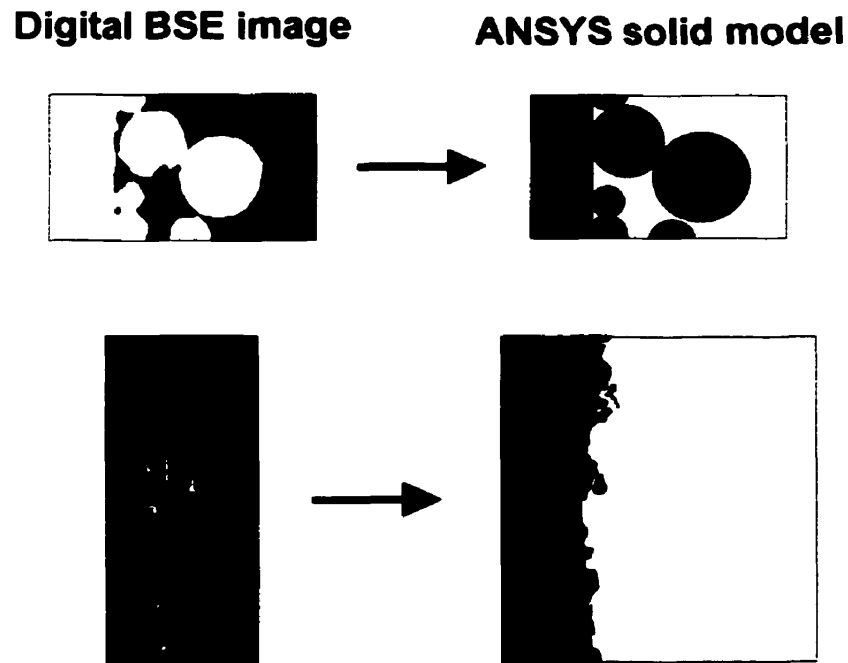


Figure 5.21. Examples of geometrically accurate unit cell solid models for the porous-surfaced (top) and plasma-sprayed (bottom) interface zones. The scales for the two models are different.

5.10.2 Results and discussion

The effective and local properties predicted with the GAUC models were quite variable, consistent with the geometric heterogeneity of these models. For the porous-surfaced interface zone, the mean effective transverse modulus (E_1) of the GAUCs was significantly greater than that predicted with the baseline idealized geometry model by 40% (Figure 5.22). The longitudinal (E_2) and shear (G_{12}) moduli were not statistically different from the predictions with the idealized model ($p>0.2$). For the plasma-sprayed interface zone, the effective transverse and longitudinal moduli of the GAUCs were significantly lower than those predicted with the idealized geometry model by 9% to 13% (Figure 5.23). There was no difference between the predictions with the GAUC and idealized models for the shear modulus ($p=0.3$). Therefore, compared with predictions based on models that are representative of the geometric irregularities of the implant surface, the idealized geometry model underestimated the effective transverse modulus of the porous-surfaced interface zone, but slightly overestimated the effective transverse and longitudinal moduli of the plasma-sprayed interface zone.

The effects of the irregularities in surface geometry were also apparent in the range of the local structure tensor components (M_{ijkl}). For both designs and all local structure components of the interface zone tissue, the predictions with the idealized geometry model were significantly different than the predictions with the GAUC models ($p=0$). However, it is important to note that in most cases there were significant differences between the local properties predicted with the individual GAUC models, and therefore the differences between the predictions with the idealized geometry model and the GAUC models are not surprising. Generally, the mean values of the local structure components predicted with the idealized model for the porous-surfaced interface zone tissue were lower than those predicted with the GAUCs (Figure 5.24). Conversely, the mean values of the local structure components predicted for the plasma-sprayed interface zone tissue with the idealized model were greater than those predicted with the GAUCs (Figure 5.25). For both surface designs, the range in the local structure components for the idealized models was generally smaller than it was for the heterogeneous GAUC models, although in all cases the ranges predicted with the idealized geometry models were within those predicted with the GAUC models. It is possible that some of the more extreme values obtained with the GAUC models may represent numerical inaccuracies due to insufficient mesh refinement around areas with stress concentrations in these models, and therefore the true range is narrower. Qualitatively, the spatial distributions of the local structure components within the GAUC models were consistent with those with the idealized models (Figure 5.26). The tissue

within pores of the sintered porous and plasma-sprayed surfaces was generally “strain protected”, as was observed with the idealized geometry models (Figure 5.7).

Therefore, the idealized models for the two surface designs provided estimates of the local properties that were within the range of properties predicted by the GAUC models. Furthermore, the general spatial distributions of the local properties predicted by the idealized geometry models are representative of the distributions observed with the GAUC models. The greatest discrepancy observed was for the predictions of the effective transverse modulus of the porous-surfaced interface zone. The underestimation of this modulus with the idealized model unit cell is consistent with the experimental validation studies, which showed that the homogenization method tended to underestimate the effective transverse modulus for this surface design (although not with statistical significance) (Figure 5.11). The implications of the limitations of the idealized geometry models at representing the irregular geometries of the actual implant surfaces are considered in Chapters 6 and 7.

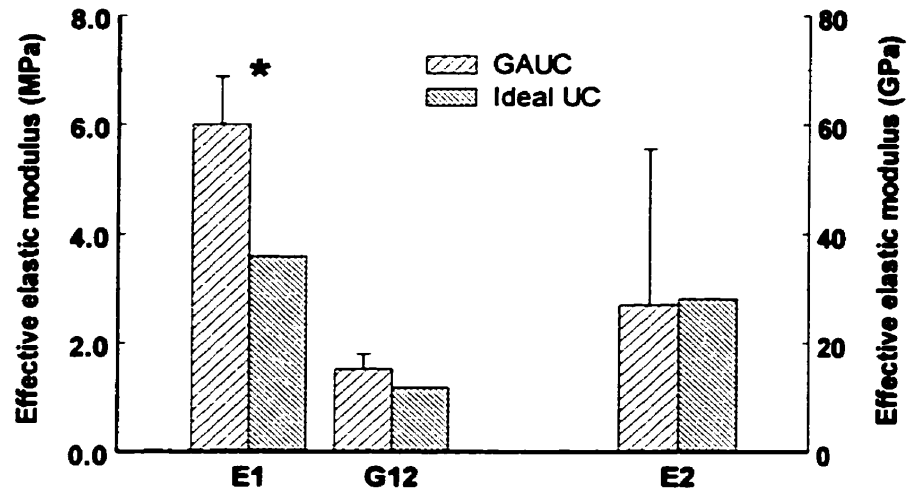


Figure 5.22. The effective moduli predicted by homogenization theory for the porous-surfaced geometrically accurate (GAUC) and idealized geometry unit cell models. The GAUC data are presented as mean \pm standard error of the mean. An asterisk indicates a statistically significant difference between the GAUC and idealized geometry values ($p < 0.05$).

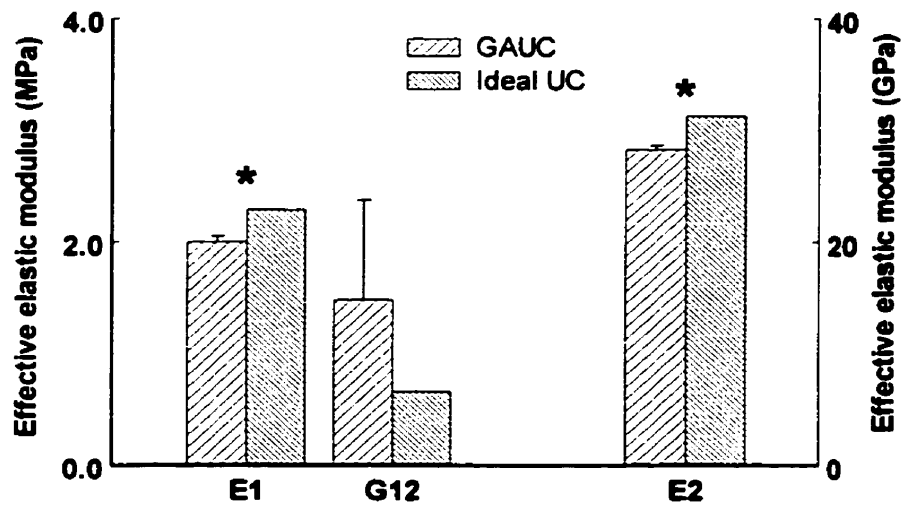


Figure 5.23. The effective moduli predicted by homogenization theory for the plasma-sprayed geometrically accurate (GAUC) and idealized geometry unit cell models. The GAUC data are presented as mean \pm standard error of the mean. An asterisk indicates a statistically significant difference between the GAUC and idealized geometry values ($p < 0.05$).

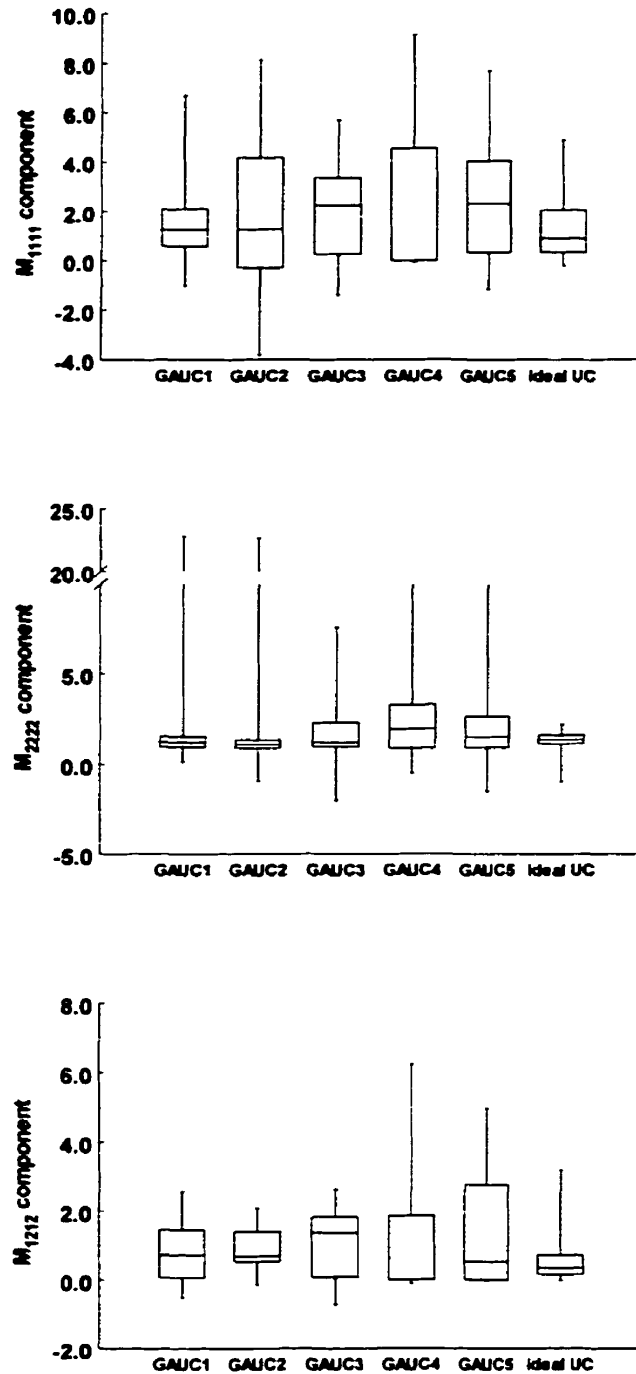


Figure 5.24. Box plots of the distributions of the local structure components for the porous-surfaced interface zone tissue predicted with the geometrically accurate (GAUC) and idealized geometry unit cell models. The horizontal line within the box represents the median value, the upper and lower limits of the box represent the quartiles above and below the median, and the error bars indicate the full range of the local structure component.

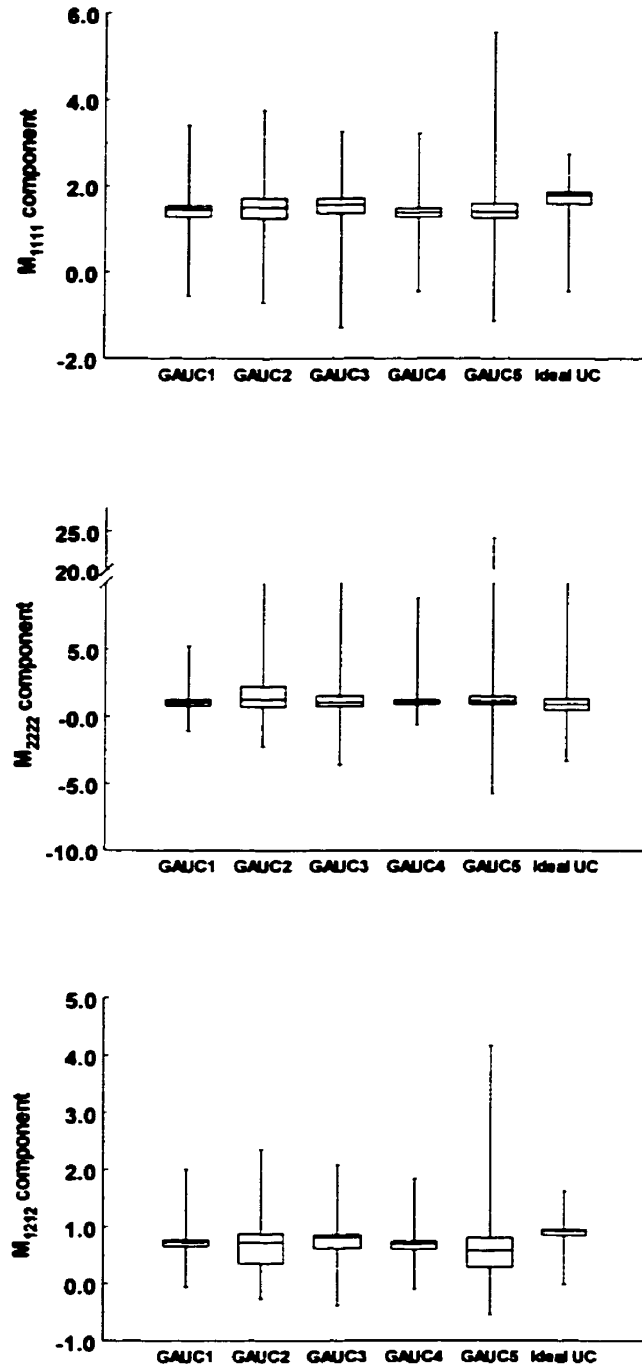


Figure 5.25. Box plots of the distributions of the local structure components for the plasma-sprayed interface zone tissue predicted with the geometrically accurate (GAUC) and idealized geometry unit cell models.

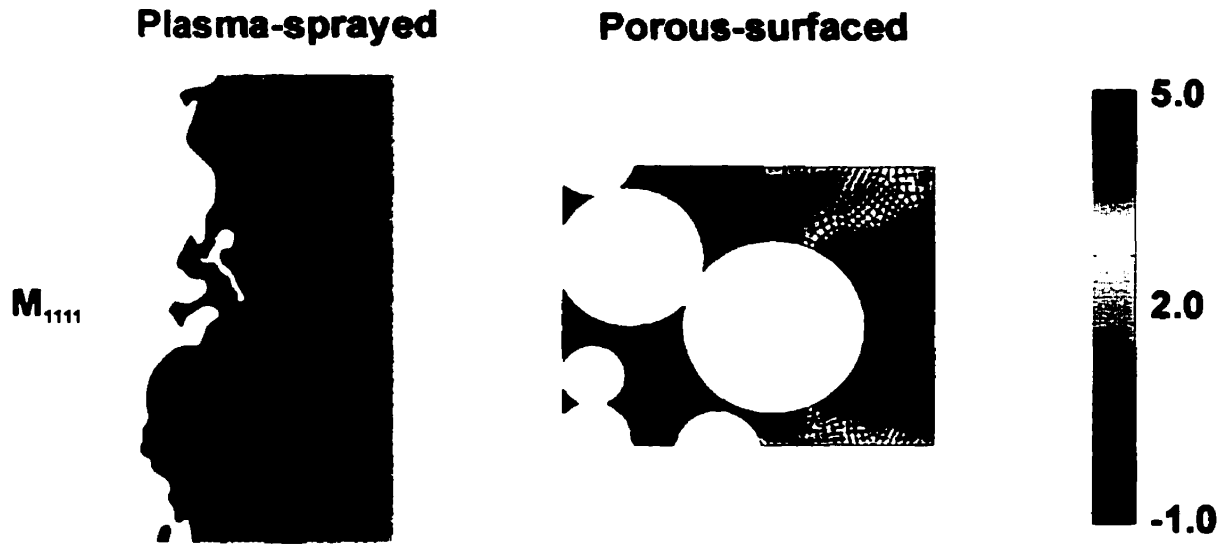


Figure 5.26. Transverse local structure components (M_{1111}) of the interface zone tissue for portions of typical geometrically accurate unit cell models of the plasma-sprayed and sintered porous surfaces. The scales for the two models are different.

5.11 Conclusions regarding the computational model

Based on the investigations described in this chapter, the following conclusions regarding the computational model can be made:

- (1) Based on homogenization analysis of unit cell models with idealized geometries, the effective transverse and shear moduli of the porous-surfaced interface zone are greater than those of the plasma-sprayed interface zone.
- (2) The porous-surfaced interface zone provides regions where a large fraction of the interface zone tissue is strain protected. The tissue within the pores of the plasma-sprayed surface is protected similarly, but this amount of tissue represents only a small fraction of the total interface zone tissue.
- (3) The effective transverse and shear moduli predicted for the porous-surfaced interface zone are comparable to those determined experimentally. The computational model predicts a longitudinal modulus that is 10% to 15% lower than that measured experimentally.

- (4) The effective properties predicted for the plasma-sprayed interface zone using the computational model differ from those predicted using the Hashin-Shtrikman model by up to 29%. However, previous studies have shown differences of this magnitude are within the range one would expect to measure experimentally, suggesting the computational model predictions are acceptably accurate.
- (5) The local stress field predicted by computational model for the porous-surfaced and plasma-sprayed interface zones are similar to those measured experimentally using photoelasticity. The greatest discrepancies occurred at the boundaries of dissimilar materials.
- (6) The photoelastic results demonstrated that the tissue-metal interface condition has a significant effect on the local stress field, with higher tissue stresses occurring when there is no bonding between the tissue and implant. The changes with bonding condition appear to be similar for the two implant surface designs.
- (7) The effective and local properties of the plasma-sprayed interface zone are relatively insensitive to variations in the size of the surface pores. The effect of changing only the pore size on the properties of the porous-surfaced interface zone cannot be determined, since the porous-surfaced pore size cannot be varied independently of the relative volume fractions of the constituent materials.
- (8) Idealized geometry unit cell models are not capable of representing the full range in effective and local properties of the geometrically irregular interface zones. However, the idealized unit cell models do predict properties that are within the range predicted by geometrically accurate unit cell models, and therefore the idealized models can be considered representative samples.

Overall, the computational model using idealized unit cell geometries provides reasonably accurate initial predictions of the effective and local properties of the porous-surfaced and plasma-sprayed interface zones. Furthermore, the model addresses many of the limitations of earlier efforts. As such, the model is adequate to provide initial insights into the role of surface geometry and mechanical factors in peri-implant tissue formation. The implications of the strengths and limitations of the computational model are considered for specific applications in Chapters 6 and 7. Suggestions for future enhancements to the model are provided in Chapter 8.

Chapter 6

Biomechanical analysis of the effect of implant surface geometry on early peri-implant tissue formation

Summary

Experimental evidence indicates that the surface geometry of bone-interfacing implants influences the nature and rate of tissues formed during healing around implants. In the animal model study reported in Chapter 4, it was shown that press-fit porous-surfaced implants placed in rabbit femoral condyle sites osseointegrated more rapidly than plasma-sprayed implants. We hypothesized that the accelerated osseointegration observed with the porous-surfaced design was the result of this design providing a local mechanical environment that is more favourable for bone formation. In the present study, we tested this hypothesis using finite element analysis and homogenization methods to predict the local strains in the pre-mineralized tissues formed around porous-surfaced and plasma-sprayed implants. We found that for loading perpendicular to the implant interface, the tissue in the region around the porous-surfaced implants experienced significantly lower distortional and volumetric strains than the tissue around the plasma-sprayed implants ($p = 0$). This difference was apparent for a variety of unit cell geometries, representing a range of pore sizes and shapes. Low distortional and volumetric strains are believed to favour bone formation, and therefore the model results provide initial support for our hypothesis that the porous-surfaced geometry provides a local mechanical environment that favours more rapid bone formation in certain situations.

6.1 Introduction and motivation

Previous studies *in vivo* have identified implant surface geometry as a design variable that significantly influences long-term implant performance (Section 2.3). In Chapter 4, we demonstrated that implant surface geometry also influences the initial healing and mineralization of the tissue in the peri-implant region. Specifically, we studied the early healing dynamics of the repair/regeneration tissues adjacent to non-functional implants with different surface geometries and demonstrated that implants formed with a sintered Ti6Al4V porous surface layer

osseointegrated more rapidly than Ti plasma-sprayed implants. However, the reason for this differential response in the rate of osseointegration was unclear from the experimental studies.

The formation and mineralization of peri-implant tissue is dependent on several factors, including the local mechanical environment. As discussed in Section 3.3, the proliferation and differentiation of the pluripotential mesenchymal cells responsible for tissue formation in the interface zone may be regulated by the local mechanical environment according to the tissue differentiation hypothesis proposed by Carter and his colleagues for skeletal regeneration. According to Carter's theory, progenitor cells within developing mesenchymal tissues that experience a loading history of low distortional strain and low compressive hydrostatic stress are more likely to become osteogenic, assuming an adequate blood supply. However, if the healing tissue is exposed to excessive distortional strains, fibrogenesis will result. Significant compressive hydrostatic stresses and poor vascularity will result in cartilage or fibrocartilage formation. Based on this hypothesis, one would expect more rapid implant osseointegration when the interface zone tissue experiences minimal distortional strain and hydrostatic stress, as is the case with a stable implant.

The local mechanical environment around an implant is dependent on the forces imposed and the surface geometry of the implant (Ko et al., 1992; Kohn et al., 1993b; Pedersen et al., 1991). Therefore, certain surface designs may promote osseointegration by providing a more favourable local mechanical environment for bone formation. Based on this reasoning, we hypothesized that the accelerated osseointegration observed in the animal model study with non-functional porous-surfaced implants compared with plasma spray-coated implants was the result of the porous-surfaced design providing a local mechanical environment in the healing tissue that was more favourable for bone formation.

The relationship between implant surface geometry, local mechanical environment, and interface tissue formation has not been addressed to date. While previous studies have correlated patterns of tissue formation in the interface zone with local mechanical parameters predicted by the finite element method (Giori et al., 1995; Huiskes et al., 1997; Prendergast and Huiskes, 1996; Prendergast et al., 1997), the models used in those studies did not incorporate the microstructural features of the implant surface, and therefore could not account for its influence on the local mechanical environment.

6.2 Specific research objectives

The aim of this part of the study was to investigate the effect of implant surface geometry in influencing mechanically regulated tissue formation adjacent to bone-interfacing implants. Specifically, our objectives were:

- 1) to predict the local strains in the pre-mineralized interface zone tissue around the porous-surfaced and plasma-sprayed implants used in the animal model study (Chapter 4);
- 2) to examine the influence of pore size and geometry on the local strains in the two interface zones; and,
- 3) to test the hypothesis that, within the context of Carter's theory for tissue differentiation, the local mechanical environment around the porous-surfaced implants was more conducive to early bone formation compared with the plasma-sprayed implants.

6.3 Methods

The unit cell models developed in Section 5.7 were used as the baseline models in this study (Figures 5.4 and 5.5). These unit cell models represented the porous-surfaced and plasma-sprayed interface zones (composites of the implant surface features and loosely organized granulation tissue) four days post-implantation, before mineralization was evident in the animal model study. The unit cells (UC) had idealized geometries that were based on the characteristics of the two surface designs used in the experiments. The implant material and ingrown tissue were modelled as homogeneous linear elastic materials with the properties given in Table 6.1. It was assumed the metal and tissue were perfectly bonded and the tissue infiltrated the porosity or irregularities of the implant surface structures fully.

Two-dimensional plane stress global finite element models were developed to represent the tapered implant placed transversely in the trabecular bone of the rabbit femoral condyle (Figure 6.1). The implant material, interface zone, and trabecular bone were modelled as homogeneous, linear elastic materials (Table 6.1). The global models for the two implant surface designs were identical, except for the width of the homogenized interface zone, which was 367 μm for the porous-surfaced implant and 133 μm for the plasma-sprayed implant. The global models were discretized with 2401 and 2399 quadrilateral elements for the porous-surfaced and plasma-sprayed implants, respectively. Although the implants were not loaded during the experiment, the rabbits ambulated shortly after implantation, thereby loading their

femoral condyles and consequently, the implants and concomitant interface zone tissues. Uniform compressive pressure loads with an arbitrary magnitude of 1 MPa were applied normal to each condylar surface; this loading direction is representative of the largest loading component experienced in vivo (Lerner, 1998) and the unit magnitude facilitated comparison of the two implant designs.

Based on the finite element and homogenization analyses, the effective elastic constants (\bar{C}_{ijkl}) and local structure tensor (M_{ijkl}) were determined for each surface design. The effective elastic constants were used to describe the properties of the homogenized interface zone, and the average tissue strain tensors ($\bar{\epsilon}_{kl}$) were determined at a mid-length location (indicated in Figure 6.1) for each design by finite element analysis of the global model. The local tissue strains within the unit cells (ϵ_{ij}) at this location were then determined from the average tissue strains and the local structure tensors according to equation (5.17). The local tissue strains were expressed as the distortional (octahedral) tissue strain,

$$\epsilon_{\text{dist}} = \frac{1}{3} \left[(\epsilon_1 - \epsilon_2)^2 + (\epsilon_2 - \epsilon_3)^2 + (\epsilon_3 - \epsilon_1)^2 \right]^{1/2}, \quad (6.1)$$

and the volumetric tissue strain (related to the hydrostatic stress),

$$\epsilon_{\text{vol}} = \frac{1}{3} (\epsilon_1 + \epsilon_2 + \epsilon_3), \quad (6.2)$$

where ϵ_1 , ϵ_2 , and ϵ_3 are the principal strains. Comparisons were made between the two implant surface designs and interpreted with the aid of Carter's tissue differentiation hypothesis (Carter et al., 1998). To compare the tissue strains around the two designs, a nonparametric one-tailed Mann-Whitney test was used with the alternate hypothesis being that the magnitude of the local strain invariants were lower in the porous-surfaced interface zone than in the plasma-sprayed interface zone. The statistical analysis, with appropriate adjustments for tied ranks, was performed using Minitab (Minitab Inc., State College, PA).

Additional studies were performed to determine the influence of the unit cell geometries on the comparison of the two surface designs. In order to determine the influence of pore size on the local tissue strains around the two implant surfaces, the analyses were repeated with the unit cell models described in Section 5.9. The analyses were also repeated with the geometrically accurate unit cell models described in Section 5.10 to investigate the implications of using idealized geometry models to represent the heterogeneous geometry of the implant surfaces. For these investigations, the mean effective properties from all the GAUC models were used in the global finite element model. The local tissue strains for each surface design were determined

using the GAUC model for which the local properties were most different from the idealized geometry models, thereby providing a rigorous test of the conclusions. The geometry of these models is shown in Figure 5.21.

Table 6.1. Elastic properties used in the finite element models.

Material	E	ν	Reference
Titanium	100 GPa	0.33	-
Trabecular bone	500 MPa	0.4	Keaveny and Hayes (1993)
Interface zone tissue	1 MPa	0.45	Based on Cheal et al., (1991), Claes and Heigele (1999), and Carter et al. (1988)
Homogeneous interface zone	Determined by homogenization analysis		-

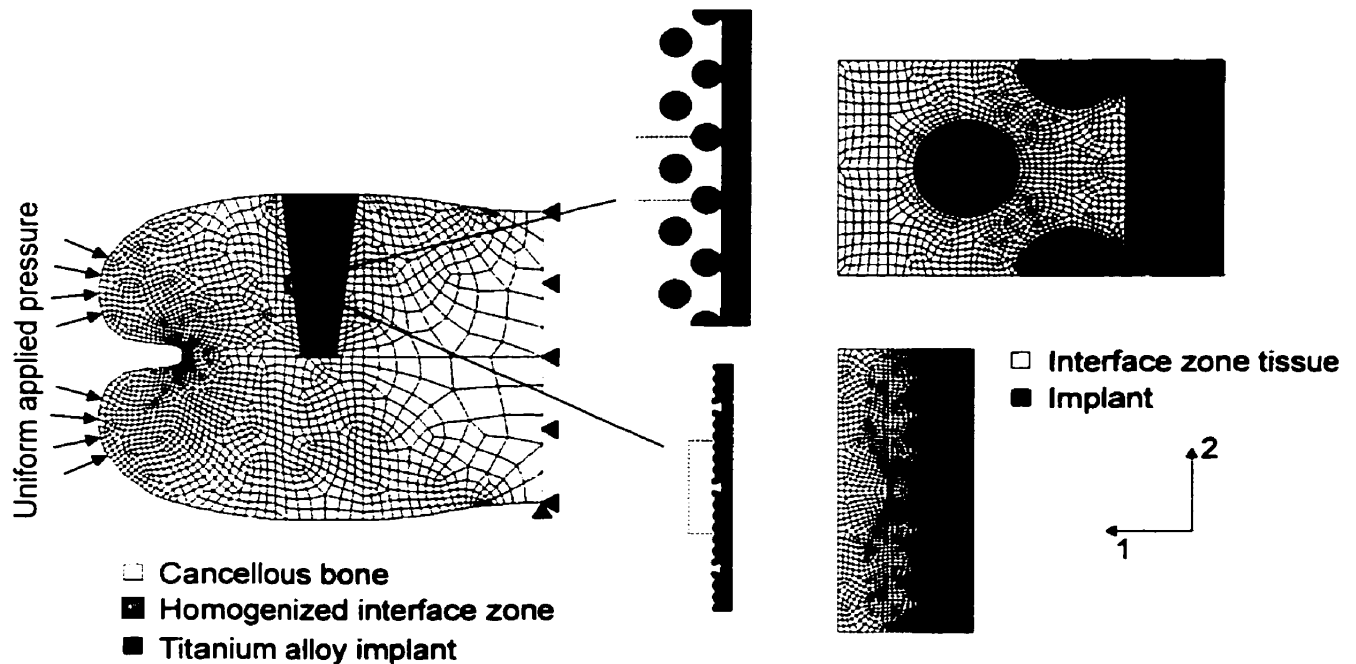


Figure 6.1. Two-dimensional plane stress finite element models of the implant and baseline unit cells with idealized geometries representing the porous-surfaced (top) and plasma-sprayed (bottom) designs.

6.4 Results

As described in Section 5.7.2, the effective elastic constants of the homogenized interface zones were highly anisotropic (Table 5.5). Comparison of the two surface designs (modelled with the baseline unit cell models) indicated that the moduli normal to the implant interface and in shear were over 36% larger for the porous-surfaced interface zone than for the plasma-sprayed interface zone. The modulus of the porous-surfaced interface zone parallel to the implant interface was 11% lower than that for the plasma-sprayed interface zone. Locally, the porous-surfaced interface zone had large regions that were “strain protected” (i.e., low local strains), particularly for the components of the local structure tensor normal to the implant interface (M_{1111}) and in shear (M_{1212}) (Figures 5.7 and 5.8). Load transfer to the implant interface during the animal experiments was primarily perpendicular to the implant interface, and therefore the effective and local properties normal to the interface and in shear would be expected to dominate the local mechanical environment.

Due to the stiffer effective properties in the primary direction of loading, the average (global) strains in the porous-surfaced interface zone tissue were lower than those in the plasma-sprayed interface zone tissue (Figure 6.2). The global strains were not uniform along the length of the implant, obtaining their maximum value at a mid-length location for both surface designs. Therefore, although local strain calculations were limited to only the mid-length location, one would expect similar relative differences between the two implant surface designs given that the spatial distribution of the global strains were similar.

The combination of the stiffer effective properties in the primary direction of loading and the locally “strain shielded” regions resulted in generally lower distortional and volumetric local strains for the porous-surfaced interface zone tissue (Figure 6.3). For instance, 85% of the tissue in the porous-surfaced interface zone experienced distortional strains lower than the median distortional strain in the plasma-sprayed interface zone tissue (Figure 6.4). Similarly, the volumetric strain magnitude in over 99% of the porous-surfaced interface zone tissue was lower than the median value for the plasma-sprayed interface zone tissue. For both the distortional and volumetric strain invariants, the magnitudes were significantly lower in the porous-surfaced interface zone tissue than in the plasma-sprayed interface zone tissue ($p=0$).

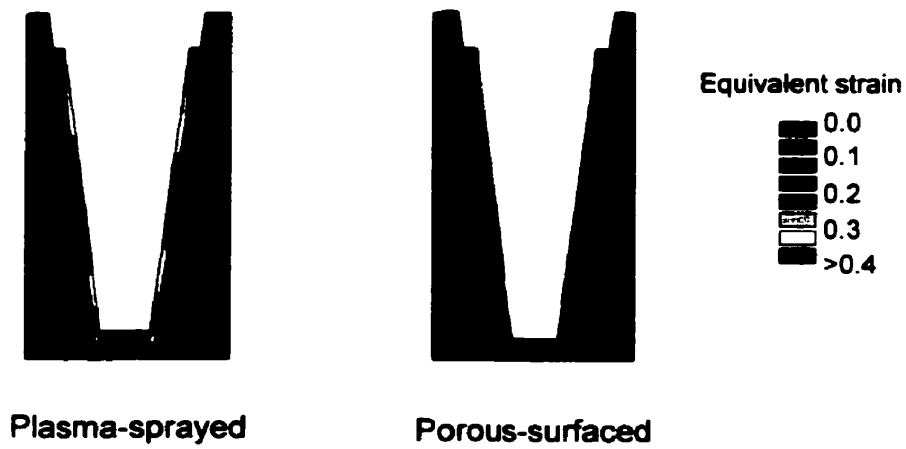


Figure 6.2. Field plots of the global equivalent interface zone strains for the two surface geometries.

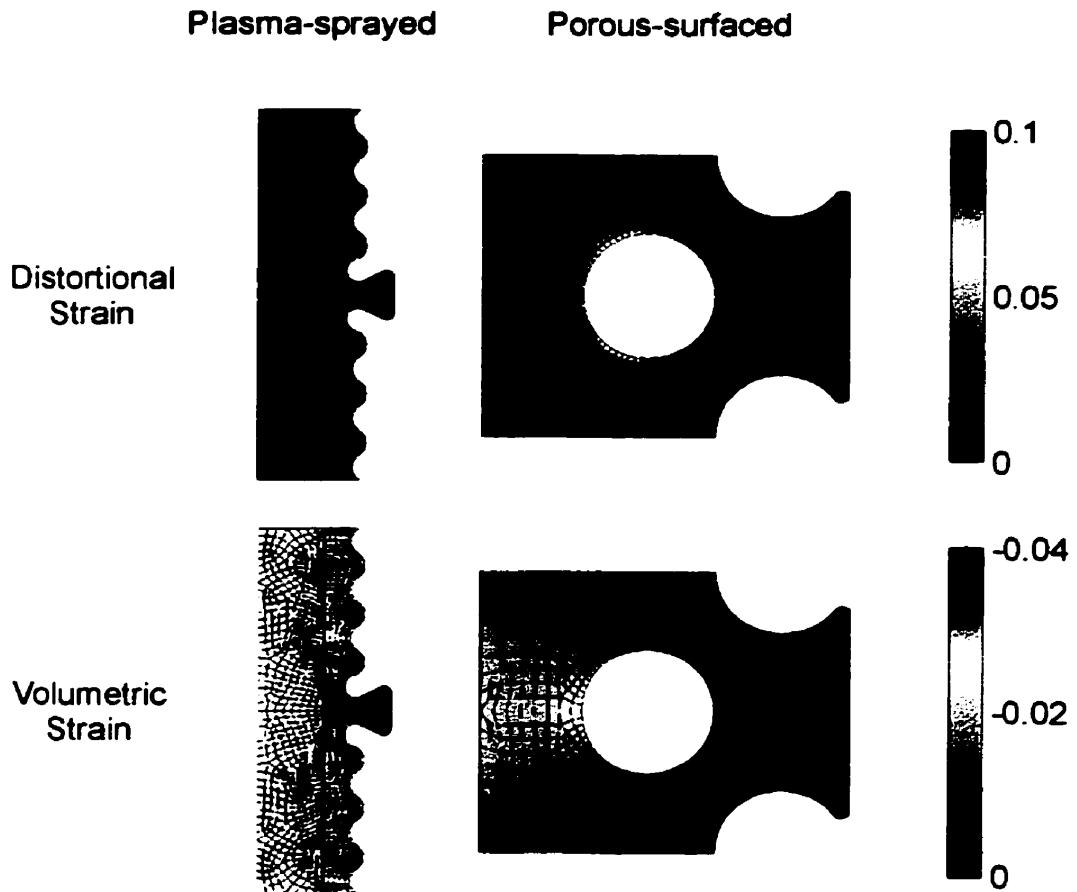


Figure 6.3. Field plots of the local distortional and volumetric tissue strains for the two surface geometries at a mid-length location on the implants.

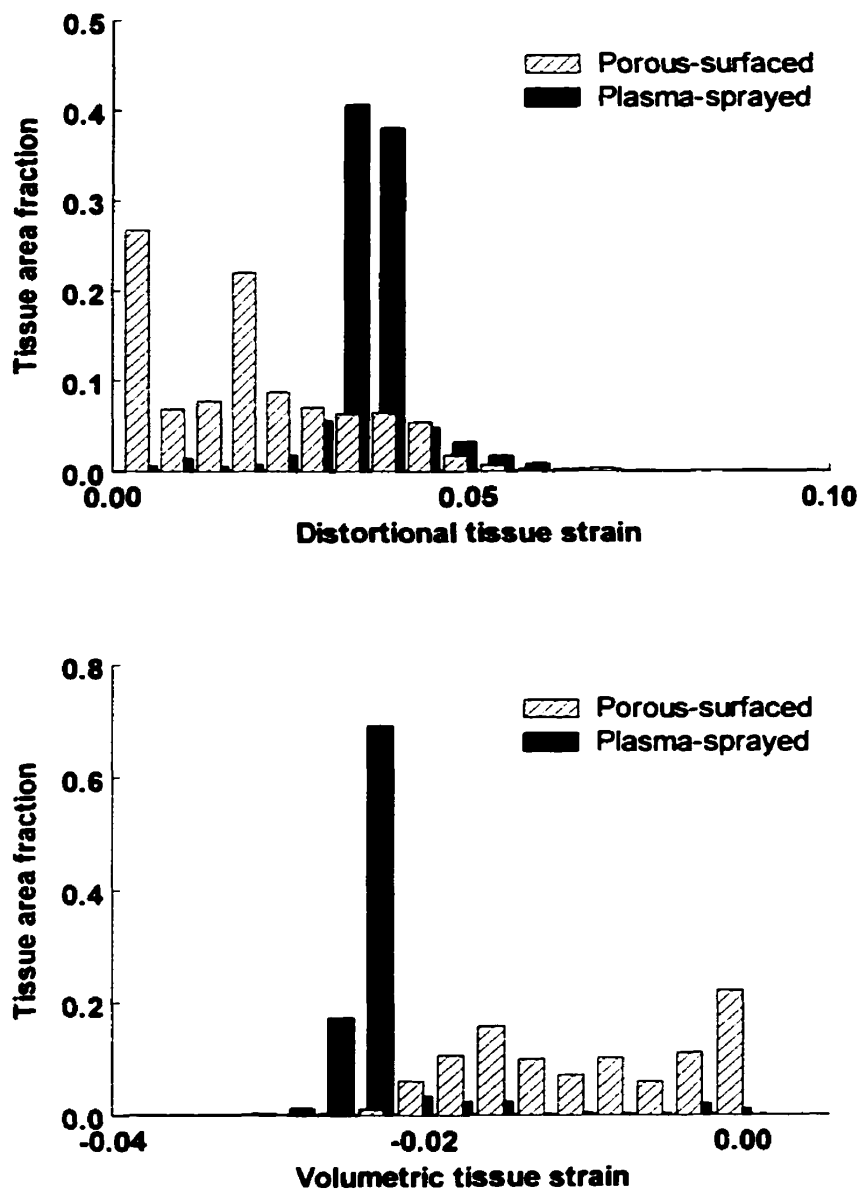


Figure 6.4. Histograms of the area fraction of tissue experiencing various levels of distortional and volumetric strain for the two implant surface designs at a mid-length location on the implants.

When the analyses were repeated with different pore sizes, the results were similar. Consistent with the findings in Section 5.9, decreasing the pore size for the porous-surfaced implant resulted in less extreme values of distortional and volumetric strain, but little change in

the median value (Figure 6.5). Similarly, varying the plasma-sprayed surface pore size had a slight effect on the strain distribution, but little effect on the median distortional and volumetric strain values (Figure 6.6). In all cases, the magnitudes of the distortional and volumetric strain invariants in the porous-surfaced interface zone tissue were significantly lower than those in the plasma-sprayed interface zone tissue ($p=0$). The analyses with the GAUC models resulted in the same conclusion: the magnitudes of both strain invariants were significantly lower in the porous-surfaced interface zone tissue than in the plasma-sprayed interface zone tissue ($p=0$) (Figure 6.7).

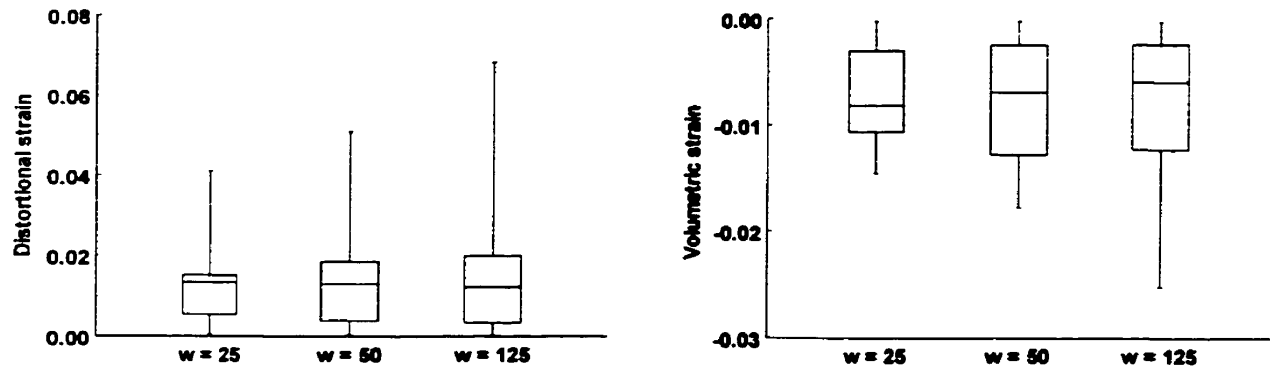


Figure 6.5. Box plots of the distortional and volumetric tissue strains for porous-surfaced implants with different pore sizes. The horizontal line within the box represents the median strain value, the upper and lower limits of the box represent the quartiles above and below the median, and the error bars indicate the full range of the strain data.

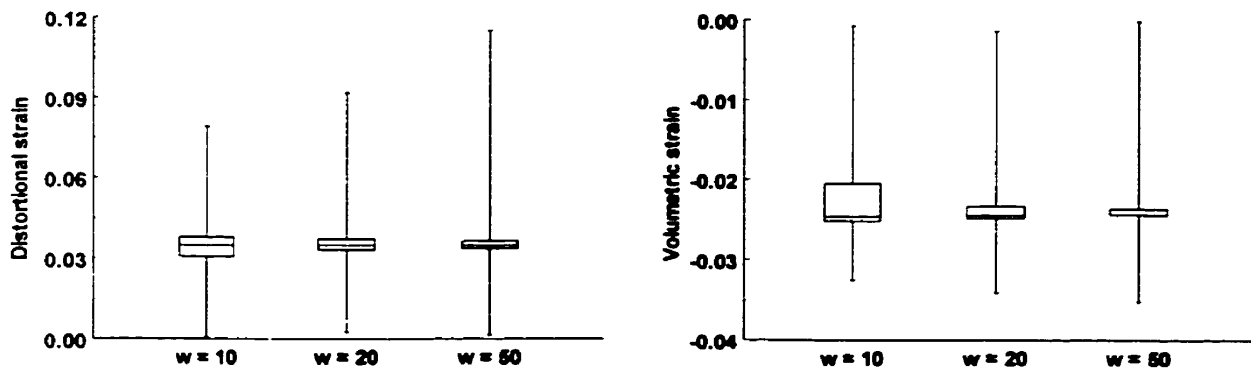


Figure 6.6. Box plots of the distortional and volumetric tissue strains for plasma-sprayed implants with different pore sizes.

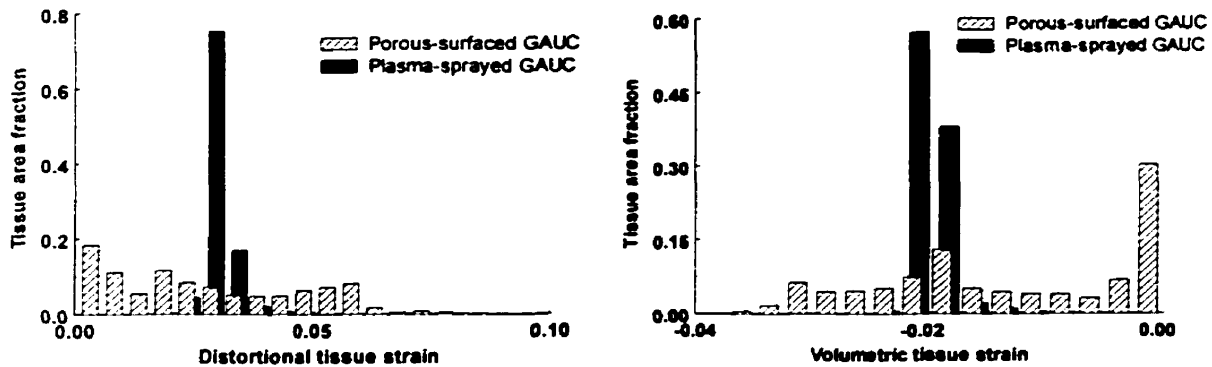


Figure 6.7. Histograms of the area fraction of tissue experiencing various levels of distortional and volumetric strain for the geometrically accurate unit cell models of the two surface designs at a mid-length location on the implants.

6.5 Discussion

In the animal model study (Chapter 4), we observed more rapid mineralization of the interface tissue around non-functional porous-surfaced implants compared with plasma-sprayed implants. We hypothesized that this differential response was because the surface geometry of the porous-surfaced implants provided a local mechanical environment that was more favourable for bone formation. The objective of the current study was to test this hypothesis using finite element analysis and homogenization theory to predict the local tissue strains before mineralization around the two implant surface designs used in the animal experiments. For loading perpendicular to the implant interface, we found that, compared with the plasma-sprayed coating, the porous surface structure provided an interface zone with stiffer effective properties and more local “strain protection”. As a result, the distortional and volumetric tissue strains in the porous-surfaced interface zone were generally lower than those in the plasma-sprayed interface zone. Lower distortional and volumetric tissue strains favour bone formation according to Carter’s tissue differentiation theory. Therefore, the modelling results provide initial support for our hypothesis that, for implants placed transversely in the femur and loaded primarily with major forces acting normal to the interface, the porous-surfaced geometry provides a local mechanical environment that is favourable for more rapid bone formation.

6.5.1 Significance and implications of the results

Previous finite element studies have examined the relationship between mechanical stimuli and peri-implant tissue formation at the tissue-implant (Huiskes et al., 1997; Prendergast and Huiskes, 1996; Prendergast et al., 1997) and tissue-cement interfaces (Giori et al., 1995). These studies used standard continuum analyses, and therefore did not account for the geometric features of the implant surface. In this study, we used homogenization theory and a unit cell approach to incorporate the geometric characteristics of the implant surfaces into global models of the implants in a systematic and computationally efficient manner. The significant influence of the surface geometry on the local mechanical environment was evident from the model predictions. The local level analyses revealed that the interface zone tissue experiences a range of strain magnitudes due to the microstructural surface features. For instance, the magnitudes of the local distortional strains in the porous-surfaced interface zone ranged from 5 to 807% of the magnitude of the global distortional strain at the same location. The surface geometry also influenced the spatial distribution of the local tissue strains; the interconnected pores and relative stiffness of the porous-surfaced structure provided large regions that were “strain protected”, whereas only the small amount of tissue in the isolated pores of the plasma-sprayed coating was shielded similarly.

Our analysis considered a single time point, representing the period prior to tissue mineralization (i.e., day 4 in the animal experiments). In order to simulate the bone formation process dynamically, a quantitative regulatory model relating the mechanical parameters to tissue synthesis would need to be implemented. Huiskes et al. (1997) have proposed such a model for peri-implant tissue formation; however, their finite element models did not incorporate the implant surface geometry and the applied loads in their finite element analyses were estimated from gait analysis (Prendergast et al., 1997), thereby limiting the accuracy of their finite element predictions and the regulatory model. Development of a reliable quantitative regulatory model requires experimental data relating well-defined loading conditions with tissue formation. However, a qualitative description of the tissue formation process and its relationship to the local mechanical environment can be postulated from our analyses. Assuming that low distortional and volumetric strains favour bone formation, the model results predict more localized bone formation in the porous-surfaced interface zone. With mineralization of the porous-surfaced interface zone tissue, the effective stiffness of the interface zone would increase and more regions may become strain protected. Thus, assuming the applied loads did not change, the local mechanical environment would become more favourable for further bone formation, resulting in

an increased rate of mineralization until the implant is osseointegrated. The plasma-sprayed interface zone starts with a less favourable environment for bone formation (fewer regions of low distortional and volumetric strains). However, as mineralization occurred at some preferred sites, the local strains would decrease. This change in local strain magnitudes would develop slowly at first and more rapidly as tissue mineralization and stiffening progressed. Thus, the tissues within the porous-surfaced interface zone would mineralize rapidly from the start, whereas the rate of mineralization in the plasma-sprayed interface zone would be slow initially, but would accelerate as mineralization occurred. This pattern of healing is consistent with that observed in our rabbit model experiments (Chapter 4) and is similar to that proposed by Perren et al. (1980) for fracture healing and by Prendergast et al. (1997) for peri-implant tissue formation. Clearly, if the applied loads changed during the healing period, then so would the local mechanical environment in the interface zone tissue. Thus, a regulatory model should also consider the loading history. For our purposes and research objectives, however, using a typical quasi-static load case was sufficient to elucidate basic differences between the implant surface designs.

6.5.2 Assumptions in the analysis

Although the homogenization approach was necessary to incorporate implant surface geometry into the models, the approach required several assumptions to be made. These assumptions and others are discussed in this section.

Unit cell model

Two key conditions in homogenization theory are that the microstructure (i.e., surface structure) is spatially periodic and can be represented by repeating idealized unit cells. Clearly, neither condition is met completely by the tissue-implant interface zone. The interface zone, as modelled in this study, is spatially periodic in the direction parallel, but not normal, to the implant interface. As discussed in Section 3.3.4, Ko (1994) and Kohn et al. (1993a) investigated the error introduced by unidirectional periodicity. For loads applied either parallel or perpendicular to the direction of periodicity (as was the case in this study), the difference was less than 4%, indicating that the homogenization method is adequate in these cases despite the unidirectional periodicity of the interface zone.

The unit cell models we developed for the two implant surface designs were based on key characteristics of the actual surfaces, but clearly do not represent accurately the real surface

geometries, which are heterogeneous and therefore not readily modelled by a single representative unit cell. The idealization of the geometries would likely limit the accuracy with which predictions can be made, particularly for the absolute magnitudes and spatial distributions of the local tissue strains. Nonetheless, the unit cell geometries capture the essential features of the surface designs, and therefore are sufficient for a first order understanding of the relative differences between the designs. The analyses with different pore sizes and with geometrically accurate unit cell models produced the same conclusions as with the idealized unit cell models, supporting the use of the idealized models. Furthermore, the correlation between the regions with the lowest predicted distortional and volumetric strains and the regions where initial bone formation was observed in the rabbit experiments supports the general validity of the models and approach.

As shown in Section 5.8.1, the homogenization method underestimates the effective longitudinal modulus of the porous-surfaced interface zone by 10-15%, but is accurate in its estimation of the transverse and shear moduli. In the analysis in this chapter, the global strain invariants for both implant designs were dominated by the transverse and shear components of the strain tensor. Thus, a 10-15% error in the longitudinal modulus, and therefore the strain tensor component in the longitudinal direction, would have a negligible effect on the global and local strain invariants. Therefore, for the case considered in this study, the model predictions for local strain invariants are insensitive to errors in the longitudinal stiffness.

The photoelastic analyses in Section 5.8.3 suggested that there were small, localized errors in the homogenization predictions of the local strain field. Although these errors may have affected the absolute difference between the two surface designs, it is unlikely they would have changed the final conclusions, which were based on statistically significant differences and supported by observations from the animal experiments. The photoelastic analyses also demonstrated that the local stress field was dependent on the interface condition (fully-bonded or non-bonded) between the “tissue” and “implant”. However, the photoelastic tests showed similar changes for both implant surface geometries, suggesting that the relative difference between the two implant designs does not change with alternate interface conditions. This is an important issue, however, and modelling studies in the future should investigate the influence of alternate interface conditions on the local mechanical environment.

Material model

In addition to the assumptions on the unit cell geometry, we made assumptions on the mechanical behaviour of the tissue. For all materials, we used single-phase, isotropic, linear elastic material models. While this is appropriate for the metal and trabecular bone in the global level analysis, a poroelastic (Prendergast et al., 1997), hyperelastic (Giori et al., 1995), or hyperporoelastic material model may be more appropriate for the early interface zone tissue. However, the mechanical behaviour of early interface zone tissue is poorly characterized, and therefore it is difficult to determine the most appropriate material description. The elastic properties we used for the interface tissue were similar to those of the initial tissues formed during fracture healing (Carter et al., 1988; Cheal et al., 1991; Claes and Heigele, 1999; Gardner et al., 2000). We were also limited in our selection of material model by the homogenization method, which is most readily implemented numerically with linear elastic material descriptions for the composite components. Because our primary research objective was to investigate surface geometry effects, we used a modelling approach that considered local geometry effects at the expense of a more accurate material model. Nonetheless, we would expect similar differences between the two designs had the tissue been modelled as a poroelastic or hyperelastic material. Recently, Wu et al. (1999) incorporated biphasic material descriptions into homogenization schemes to study cartilage mechanics; this work provides a theoretical basis for the development of biphasic micromechanical models of the tissue-implant interface.

Tissue-metal interface condition

The other assumption we made regarding the interface zone tissue was that it was rigidly bonded to the metal surfaces of the implant interface. As with the material properties of the interface tissue, the mechanical characteristics of the interface between the tissue and implant surface are not well characterized. Histologic and microscopic examination of the tissue-implant interface indicates that one of the first events in the healing process is the formation of a collagen-free calcified tissue layer at the implant interface (Davies, 1996). This layer is not chemically bonded to the titanium alloy surface, but is likely attached mechanically by interdigitation with submicron features on the surface (e.g., ridges due to machining or thermal etching lines formed during sintering of Ti alloy particles (Pilliar, 1987)). Therefore, a weak interface bond may exist at the tissue-implant interface, consistent with our model assumption. Currently, numerical implementation of the homogenization method is limited to bonded or slip

interface conditions (Ko et al., 1996), and therefore our model cannot account for debonding of the tissue from the interface, which may occur in vivo.

Applied loads

In this analysis, only a single quasi-static loading condition, representing the largest loading component experienced in vivo (Lerner, 1998), was considered. It is likely that, despite limited activity by the rabbits, a range of dynamic loads and loading directions were applied to the rabbit femoral condyles post-implantation. Thus, the computational model did not account fully for the loading history experienced in vivo. Despite this limitation, it is likely that the differences in the local tissue strains observed for the loading case considered here would occur for other applied loads, given the relative differences in the local and effective properties of the two surface designs. Thus, for the purpose of comparing the relative osseointegration potential of the two surfaces designs, our approach was adequate. However, a dynamic simulation of the bone formation process, in which the computational model was updated iteratively to reflect tissue formation and mineralization, would need to consider the range of loads applied in vivo.

Mechanoregulatory hypothesis for tissue formation

We interpreted our results in terms of the tissue differentiation hypothesis proposed by Carter and co-workers (1998), in which the mechanical parameters controlling tissue formation are distortional and volumetric strain (or hydrostatic stress). This model is well-suited for analyses with single-phase materials. We have taken some liberties in our interpretation of the model by suggesting the *rate* of tissue formation is dependent on the strain invariants. This seems reasonable, since it is unlikely that the formation of various skeletal tissues is delimited by distinct threshold strain values. Prendergast et al. (1997) proposed a different model in which peri-implant tissue formation was dictated by distortional tissue strain and the velocity of the fluid within the tissue relative to the solid phase. In order to incorporate fluid and solid components, a biphasic material model was used for the interface zone tissue. We were limited to a single-phase material model for the tissue, since incorporating a biphasic model into the homogenization scheme was not feasible, and therefore we interpreted our results using Carter's tissue differentiation hypothesis. The appropriateness of a single-phase versus a biphasic material model and the implications to the various tissue differentiation theories were recently debated (Carter and Beaupré, 1999; Tanck et al., 1999a). However, until the specific details and mechanisms of mechanical regulation of tissue formation are revealed by well-formulated cell

and tissue culture studies, arguments regarding the most appropriate model for tissue formation are based on speculation and circumstantial evidence. Despite possible limitations to Carter's model, the success with which it has been applied previously suggests that it is adequate for at least a general understanding of how skeletal tissue formation is influenced by mechanical stimuli.

6.6 Conclusions

Our computational analyses suggested that in cases where loading is perpendicular to the implant interface, the porous-surface geometry provided a local mechanical environment that was more favourable for bone formation than that provided by the plasma-sprayed surface design. Although this conclusion was reached initially using idealized geometry models of the implant surfaces, parametric analyses, which considered pore size and geometry, confirmed that the sintered porous surface geometry offers a mechanical advantage for more rapid bone formation. This is the first study, to our knowledge, that considered the effect of implant surface geometry on peri-implant tissue formation around non-functional implants. Our conclusions are consistent with our experimental observations in the rabbit model experiments (Chapter 4), and the model results provide an explanation for the accelerated osseointegration we observed previously with porous-surfaced implants.

Chapter 7

Biomechanical investigation of implant micromovement and mechanically regulated peri-implant tissue formation

Summary

Experimental evidence suggests that there is a threshold level of implant displacement relative to the host bone above which bone formation is inhibited. The tolerable level of implant displacement is dependent on several factors, including the implant surface design, and therefore is a poor criterion with which to evaluate the osseointegration potential of orthopaedic and dental implants subjected to early loading. The local mechanical environment in the peri-implant tissue is likely a better predictor of bone formation, but efforts to quantify the relationship between peri-implant tissue formation and the local tissue strains have been relatively unsuccessful due to limitations in the computational analyses, including failure to account for the implant surface geometry. In this study, we developed a non-linear computational model that accounts for the implant surface geometry, thereby addressing a primary deficiency of earlier studies. Based on a computational analysis of experiments in which the critical threshold for implant movement was determined, we predicted local tissue strain thresholds for localized and appositional bone formation. We also used the model to predict differences in local tissue strains around porous-surfaced and plasma-sprayed implants subjected to small relative shear displacements. From these analyses, we proposed a quantitative model for the mechanical regulation of peri-implant tissue formation. Although several simplifying assumptions were required in our computational analyses, the mechanoregulatory model predictions are consistent with experimental evidence for porous-surfaced and plasma-sprayed implants subjected to early loading. This preliminary model provides criteria by which the osseointegration potential of a variety of bone-interfacing implant surface designs may be evaluated, and may also be applicable to evaluate the effects of mechanical loading on fracture healing and on engineered skeletal tissue formation.

7.1 Introduction and motivation

The effects of mechanical forces on tissue formation have been demonstrated by numerous experimental studies (Section 3.2). Hypotheses relating the effects of specific mechanical stimuli on tissue formation, such as those by Pauwels (1980), Perren (1979; 1980), Carter (1998), Prendergast and Huiskes (1997) and Claes and Heigele (1999), have contributed significantly to our understanding of the general relationship between mechanical parameters and tissue formation. However, efforts to *quantify* the relationship between mechanical parameters and tissue formation have been largely unsuccessful. In experimental studies, the difficulties associated with measuring the local mechanical environment in the healing tissue have prevented an accurate description of the local tissue stresses and strains. By necessity, the mechanical stimuli are described by the applied loading conditions, such as interfragmentary movement or implant relative displacement. However, the local mechanical environment experienced by the healing tissue in a fracture gap or around an implant is dependent on many factors other than the loads applied globally. For bone-interfacing implants, these factors include the shape of the implant, the geometry of the implant surface, the mechanical interaction between the tissue and implant, and the site of implantation. As a result of these additional variables, it has been impossible to define, based solely on the experimental data, a relationship between mechanical parameters and peri-implant tissue formation that is applicable to a variety of implant designs and applications.

In an effort to determine the relationship between tissue strain and tissue formation, several investigators have estimated the local mechanical environment in healing tissue using computational models. However, as discussed in Sections 3.3 and 3.4, several of those studies had significant limitations, including rough estimates of the applied loads from gait analysis data (Claes and Heigele, 1999; Gardner et al., 2000; Giori et al., 1995; Huiskes et al., 1997; Ko et al., 1995; Lerner et al., 1998; Prendergast and Huiskes, 1996; Prendergast et al., 1997; Richards et al., 1999a), poorly characterized tissue material properties (Claes and Heigele, 1999; Giori et al., 1995), and in the case of peri-implant tissue formation, failure to account for the implant surface geometry (Giori et al., 1995; Huiskes et al., 1997; Prendergast and Huiskes, 1996; Prendergast et al., 1997).

In this chapter, we report investigations on the quantitative relationship between tissue strain and tissue formation for implants with sintered porous and plasma-sprayed surfaces. We addressed the primary deficiencies of earlier studies by using: (1) a unit cell modelling approach

that accounts for implant surface geometry (similar to that developed in Chapter 5); (2) tissue material properties that were estimated from the mechanical test data obtained in our rabbit experiments (Chapter 4); and (3) the experimental data obtained from studies in which the loads applied to implants were well-characterized.

The latter set of experimental data was from studies performed by Pilliar and his associates (Pilliar et al., 1995; Pilliar et al., 1996; Simmons and Pilliar, 2000). In those studies, described below in Section 8.3, they determined that relative shear displacements at the tissue-implant interface below 50 μm permitted substantive osseointegration of porous-surfaced implants, whereas only minimal osseointegration was generally observed when the relative displacement was greater than 75 μm . For plasma-sprayed implants, however, implant osseointegration was achieved even for initial relative displacements of 75 μm . These data suggest that: (1) for porous-surfaced implants, 50 μm of relative shear displacement is the critical threshold above which bone formation is inhibited; and (2) the formation of tissues around implants subjected to direct loading is dependent on implant surface geometry (consistent with the studies reviewed in Section 2.3.1). However, micromovement is a poor criterion for evaluating the osseointegration potential of an implant because it is likely implant-specific, surface geometry-specific, and site-specific. A more universal criterion, such as local tissue strain, is necessary to determine orthopaedic and dental implant designs and rehabilitation protocols that promote more rapid and reliable osseointegration. Furthermore, identifying the relationship between tissue strain and tissue formation has important implications to the design of fracture repair devices and engineered skeletal tissues.

7.2 Specific research objectives

The aim of this study was to determine a quantitative relationship between local tissue strains and peri-implant tissue formation that accounted for implant surface geometry. Specifically, our objectives were:

- (1) to predict the elastic properties of the pre-mineralized interface zone tissue based on the experimental data from the rabbit experiments (Chapter 4);
- (2) to predict the local tissue strains around a porous-surfaced implant subjected to shear displacements near the critical threshold above which bone formation is inhibited (Pilliar et al., 1995; Pilliar et al., 1996);

- (3) to compare the predicted local tissue strains around porous-surfaced and plasma-sprayed implants subjected to the same shear displacement; and,
- (4) to use the model predictions to propose a quantitative model that relates peri-implant tissue formation and the local tissue strains around implants with different surface geometries.

7.3 Methods

7.3.1 Review of the canine micromovement experiments

The experiments by Pilliar and his associates (Pilliar et al., 1995; Pilliar et al., 1996; Simmons and Pilliar, 2000) were discussed in Section 3.2.3. Briefly, they developed a custom loading apparatus with which they were able to apply relative shear displacements at the tissue-implant interface under torsional load or rotational displacement control. Using this apparatus and a canine mandible model, they initiated loading of test implants one week after implantation, before mineralization had occurred. For the first week of loading, displacement control was used and the average reaction torques were recorded. For the remaining 18 days of the experiments, load control was used and the implants were subjected to the average torque recorded in the first week of loading. In all cases, 30 cycles of loading were applied at a frequency of approximately 1 Hz every other day.

Pilliar and his colleagues have tested several implant surface designs and levels of initial relative shear displacement using this experimental model. The magnitude of the shear displacement refers to the path length through which a point on the implant surface displaces relative to the host bone. For instance, for an implant with a radius of 1.54 mm, an angular displacement of 1.86° (0.0325 radians) would result in a 50 μm relative shear displacement at the implant-tissue interface. The porous-surfaced implants used in the experiments were cylindrical, with a diameter of 3.08 mm (Pilliar et al., 1995). The implants were prepared with a Ti6Al4V sintered porous surface or a Ti plasma-sprayed surface using processes similar to those described in Section 4.3.1. The resulting surface structures covered 3.6 mm of the length of the implants, and had characteristics similar to those described in Section 4.3.1.

The results from several experiments by Pilliar and his colleagues most relevant to this study are:

- (1) The degree of bone ingrowth into porous-surfaced implants was dependent on the level of applied relative shear displacement (Pilliar et al., 1995; Pilliar et al., 1996). Although the data are quite variable, as would be expected in a biological system, there appeared to be a critical threshold shear displacement level of 50 μm above which bone formation around porous-surfaced implants was inhibited (Figure 7.1).
- (2) The degree of bone ingrowth decreased from the outer regions of the sintered porous surface structure towards to the inner regions, adjacent to the implant substrate (Pilliar et al., 1996) (Figure 7.1).
- (3) In a comparison of porous-surfaced and plasma-sprayed implants with initial applied shear displacements of 75 μm , bone was observed to form close up to the plasma-sprayed implants, whereas the porous-surfaced implants were anchored to the surrounding bone by ligament-like fibrous connective tissue, with the collagen fibres more or less obliquely oriented to the implant surface and intertwined with the three-dimensional open-pored structure (Simmons and Pilliar, 2000).

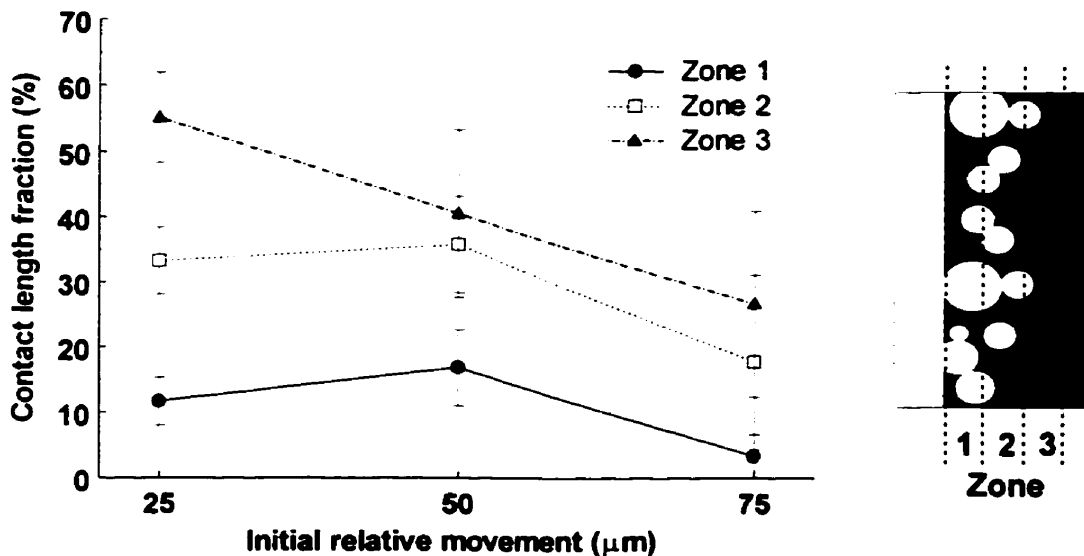


Figure 7.1. Bone ingrowth (quantified as contact length fraction) into the mesial aspect of the surface structure of porous-surfaced implants for various levels of applied shear displacement (data from Pilliar et al., 1996). Data are presented as mean \pm standard error.

7.3.2 Estimation of the early interface zone tissue material properties

Determination of the local tissue strains in the peri-implant region required an accurate description of the interface zone tissue properties. In order to estimate the material properties of the pre-mineralized tissue in the porous-surfaced interface zone, the pull-out tests conducted in the rabbit experiments (Section 4.3.4) were simulated using the computational model (assuming a linear elastic single-phase material model and small deformation), and the tissue properties in the model were varied parametrically to obtain agreement between the predicted pull-out stiffness and the stiffness determined experimentally. Because we were interested in the period prior to mineralization, we simulated the pull-out tests conducted four days post-implantation with the porous-surfaced implant. At this time point in the experiment, the average initial stiffness calculated from the force-displacement curves (for a displacement of 0.05 mm) was 247.2 N/mm.

The baseline idealized geometry unit cell model of the sintered porous surface was used in the computational simulation (Figure 5.4). The material properties of the implant and the tissue are given in Table 7.1. A range of Young's moduli and Poisson's ratios were considered for the tissue. The homogenized effective properties of the porous-surfaced interface zone were determined by varying one of the two elastic properties of the tissue (E or ν) while holding the other constant at its baseline value. The baseline values for the Young's modulus and Poisson's ratio were 1 MPa and 0.45, respectively.

A two-dimensional, plane stress global finite element model, similar to that described in Chapter 6 (Figure 6.1), was developed to represent the implant in the bone block. The implant material, interface zone, and trabecular bone were modelled as homogeneous, linear elastic materials (Table 6.1). As discussed previously, the elastic properties of the interface zone, which were determined by the homogenization method, varied with the tissue properties. A point displacement of 0.05 mm was applied normal to the top surface of the implant (simulating the pull-out test) and the reaction force was determined. The predicted pull-out stiffness was defined as the ratio of the reaction force to the applied displacement.

Table 7.1. Elastic properties used in the unit cell model. An asterisk indicates the baseline tissue material property.

Material	E	ν
Titanium	100 GPa	0.33
Interface zone tissue	0.1, 0.5, 1*, 5, 10, 100 MPa	0.35, 0.4, 0.43, 0.45*, 0.47, 0.49

7.3.3 Computational modelling of the micromovement experiments

A two-dimensional, plane strain global finite element model was developed to represent a test implant placed in the canine mandible in cross-section (Figure 7.2). The dimensions of the implant were based on the actual dimensions of the implants used by Pilliar et al. (1995) in their experiments, and the widths of the interface zones were based on observations of BSE micrographs from the same micromovement experiments. The implant material, interface zone, and surrounding bone bed were modelled as homogeneous, linear elastic materials (Table 7.2). Full bonding was assumed between all materials. Since the implants in the canine experiments were adjacent to bone of varying density and quality, we repeated our analyses for a variety of bone properties representing a range of trabecular bone and cortical bone (Keaveny and Hayes, 1993).

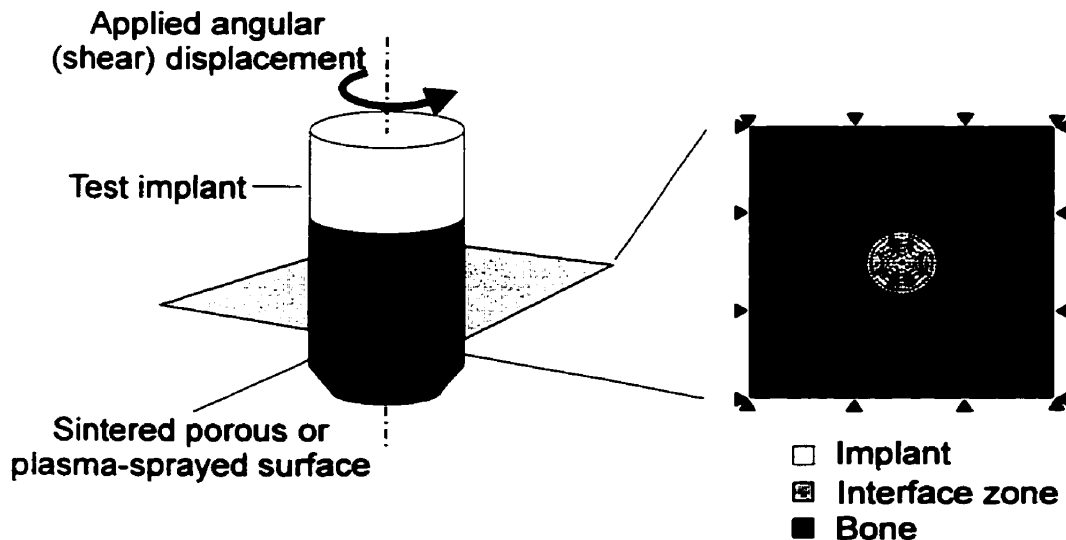


Figure 7.2. The global finite element model representing the transverse cross-section of the test implants used in the canine micromovement experiments (Pilliar et al., 1995).

Table 7.2. Linear elastic properties used in the global finite element model. An asterisk indicates the baseline Young's modulus for bone.

Material	E	ν
Titanium	100 GPa	0.33
Bone	10 GPa, 500 MPa*, 100 MPa	0.4
Interface zone tissue	Determined by homogenization analysis	

Both porous-surfaced and plasma-sprayed interface zones were considered. The effective properties of the porous-surfaced and plasma-sprayed interface zones were determined by homogenization analysis of the baseline idealized geometry unit cell models (Figure 5.4 and Figure 5.5). Although this unit cell model was developed to represent a longitudinal section of the surface structures, the geometries of the sintered porous and plasma-sprayed structures are similar in the longitudinal and transverse planes. Thus, the interface zones are transversely isotropic, with the properties in the 2-direction (i.e., parallel to the implant interface) equivalent to those in the 3-direction (i.e., tangential to the implant interface), and therefore the unit cell models can be used to model the surface structures in cross-section. The material properties of the titanium component of the unit cell model were the same as those given in Table 7.1. The tissue material properties of the unit cell model were determined by the pull-out test simulation (Section 7.3.2). The tissue and metal components were assumed to be fully bonded in both unit cell models.

Nodal displacements were applied tangential to the implant interface in the global finite element model to simulate the applied loading conditions in the canine micromovement experiments. The global strains in the interface zone were determined using a non-linear finite element analysis that accounted for large rotations and finite strains. Because of the geometry and applied loading conditions, the strains in the interface were not constant, but varied significantly and, in some cases, were large (see Section 7.4.2). The homogenization method described in Chapter 5 assumes a constant, infinitesimal strain within the homogenized body in its prediction of the local strains (equation 5.17), and therefore was inappropriate for this application. Instead, the local tissue strains were determined using a cut-boundary displacement method (ANSYS Inc., 1997) and a non-linear finite element analysis. In this analysis, the unit

cell model represented a region of the global model (the interface zone in this case), and the boundary of the unit cell model represented a cut through the global model. The displacements predicted by the global model along the cut boundary were interpolated for each node on the unit cell boundary using the element shape functions, and then applied as boundary conditions in the unit cell model. The unit cell model was then analyzed using a non-linear finite element analysis to determine the local strains. Therefore, this technique accounted for non-uniform, finite strains within the global interface zone and the unit cell.

Two related studies were performed using this computational model:

- (1) In the first study, our goal was to determine the threshold local tissue strains that permit bone formation around porous-surfaced implants. To do this, we applied a displacement to the global finite element model that was equivalent to 45 μm and determined the local tissue strains around the sintered porous-surface. This displacement level is just below the threshold level above which bone formation was inhibited experimentally (Pilliar et al., 1995; Pilliar et al., 1996),
- (2) In the second study, our goal was to compare the local tissue strains around porous-surfaced implants with those around plasma-sprayed implants, when the implants were subjected to applied relative shear displacements. In this case, we applied a displacement to the global finite element model that was equivalent to 10 μm . This relatively low level was selected because we were primarily interested in a comparison of the two implant surface designs and because convergent solutions were attained readily with this loading condition. Furthermore, this analysis provided insight into the local mechanical environment around nonfunctional and minimally loaded implants. We determined the local tissue strains and made comparisons between the two implant surface designs.

In interpreting the local tissue strains, we considered two theories that relate local tissue strains to tissue formation. The first was Carter's tissue differentiation hypothesis (Carter et al., 1998), which relates the distortional and volumetric tissue strains (equations (6.1) and (6.2), respectively) to the tissue formation (Section 3.3.1). Since this hypothesis is based on tissue (matrix) deformation, we considered it to be predictive primarily of local osteogenesis, i.e., within the bulk of the tissue. This differs from the hypothesis of Claes and Heigele (1999),

which limits bone formation to existing bony surfaces (Section 3.3.1). Therefore, we also interpreted our predicted tissue strains according to the theory of Claes and Heigele, which, in the context of peri-implant tissue formation, is relevant to appositional bone growth from the bone bed towards the implant surface. According to Claes and Heigele, the magnitude of the longitudinal and transverse local strain components, and the hydrostatic pressure acting at a bone surface will dictate tissue formation. Therefore, in addition to calculating the distortional and volumetric strains within the tissue matrix, we determined the transverse and longitudinal strain components and hydrostatic pressure at nodes along the tissue-bone interface in the unit cell models (Figure 7.3).

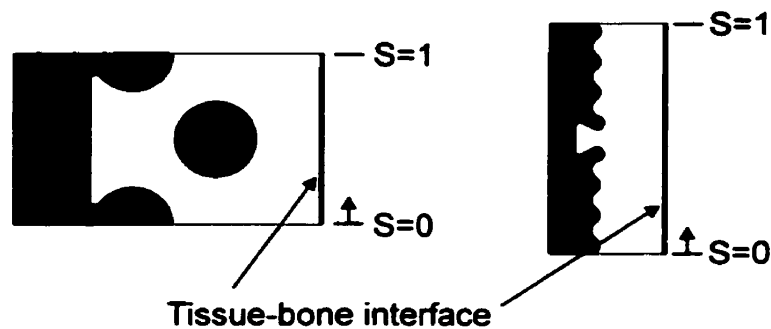


Figure 7.3. The local strain components and hydrostatic stress were calculated along the tissue-bone interface, with the normalized path length, s , originating at the bottom of the unit cell.

7.4 Results

7.4.1 Estimation of early, pre-mineralized tissue material properties

The pull-out stiffnesses predicted by finite element analysis and homogenization theory were shown to be strongly dependent on the Young's modulus of the tissue (Figure 7.4). Conversely, the pull-out stiffnesses changed less than 1% when the Poisson ratio of the tissue was increased 40% (Figure 7.4). The optimal tissue properties, which minimized the difference between the predicted and measured pull-out stiffnesses to less than 1%, were $E = 1$ MPa and $\nu = 0.47$. These tissue properties, corresponding to the tissues formed four days post-implantation in the rabbit model, were used as the reference properties in the subsequent analyses.

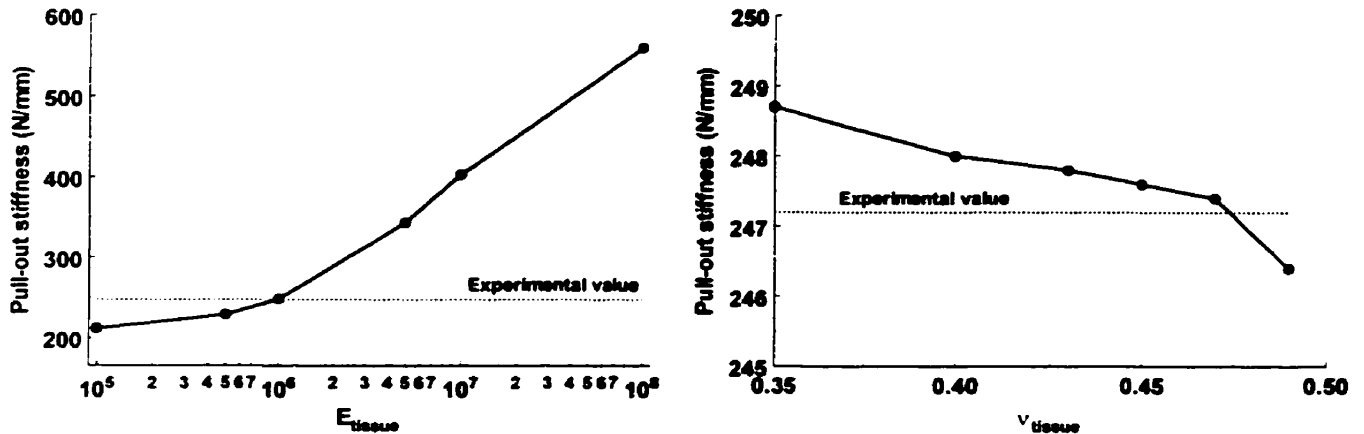


Figure 7.4. Pull-out stiffnesses predicted by the finite element simulation for various values of the Young's modulus and the Poisson's ratio of the early, pre-mineralized interface zone tissue (i.e., four days post-implantation in the rabbit model).

7.4.2 Prediction of local tissue strains due to implant micromovement

Porous-surfaced implant with 45 μm shear displacement

For the porous-surfaced implant with the baseline pre-mineralized tissue properties and an applied shear displacement of 45 μm , the global equivalent strain varied non-linearly across the interface zone (Figure 7.5). The equivalent strain was lowest near the implant surface (6.7%) and the tissue-bone interface (6.6%), and highest near the middle of the interface zone (12.7%).

However, due to the structural features of the interface zone, a wide range of local distortional and volumetric tissue strains was predicted (Figure 7.6). Furthermore, the spatial distribution of the local tissue strains was altered significantly from that predicted by the global model (Figure 7.7). For the 45 μm applied displacement, the median distortional tissue strain was 17.0%. The distortional strain magnitudes ranged from a low of 0.85% within the pores of the sintered porous surface to high levels of 45% adjacent to the implant substrate and 78% at the interface of the outer particle and the neighbouring tissue (Figure 7.7). At the tissue-bone interface, the distortional tissue strain ranged from 9% to 17%.

The magnitudes of the volumetric tissue strains were lower than those of the distortional tissue strains (Figure 7.6). For instance, for the porous-surfaced implant subjected to 45 μm of

relative displacement, the median volumetric tissue strain was 0.4%, and 87% of the tissue experienced volumetric tissue strains between -5% and $+5\%$. Due to the rotational movement of the implant, both tensile and compressive volumetric strains were predicted within the interface zone tissue (Figure 7.7).

We also calculated the local longitudinal and transverse strain components and the local hydrostatic pressure at the tissue-bone interface, as described by Claes and Heigele (Claes and Heigele, 1999). For the porous-surfaced implant and an applied shear displacement of $45\ \mu\text{m}$, the transverse strains varied between -8% and $+2\%$ and the longitudinal strains were less than 1% along the bony surface (Figure 7.8). The hydrostatic pressure fluctuated along the bony surface, with a maximum value of $-0.13\ \text{MPa}$ (compression) (Figure 7.8).

Finally, we repeated the analyses for bone properties representing cortical bone ($E = 10\ \text{GPa}$) and poor quality trabecular bone ($E = 100\ \text{MPa}$). Increasing the bone modulus in the global finite element model from $500\ \text{MPa}$ to $10\ \text{GPa}$ had a minimal effect on all of the global and local strain measures. Decreasing the bone modulus from $500\ \text{MPa}$ to $100\ \text{MPa}$ had a more significant effect on the predicted strains. Generally, lower magnitudes were predicted for all strain measures when the bone modulus was $100\ \text{MPa}$. This was expected, since decreasing the modulus caused increased deformation of the bone relative to the interface zone. However, even in this extreme case (representing porous trabecular bone), the median distortional tissue strain was 14.7% and the maximum magnitude of the transverse strain along the bony surface was 5.9% , values that were not markedly different from the baseline case.

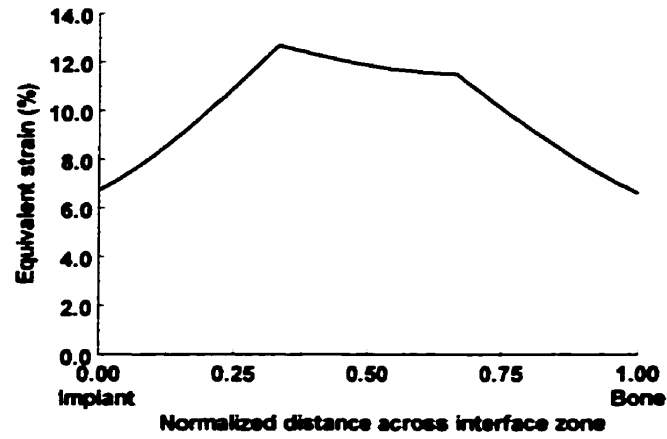


Figure 7.5. Equivalent strain across the porous-surfaced interface zone with an applied shear displacement of 45 μm .

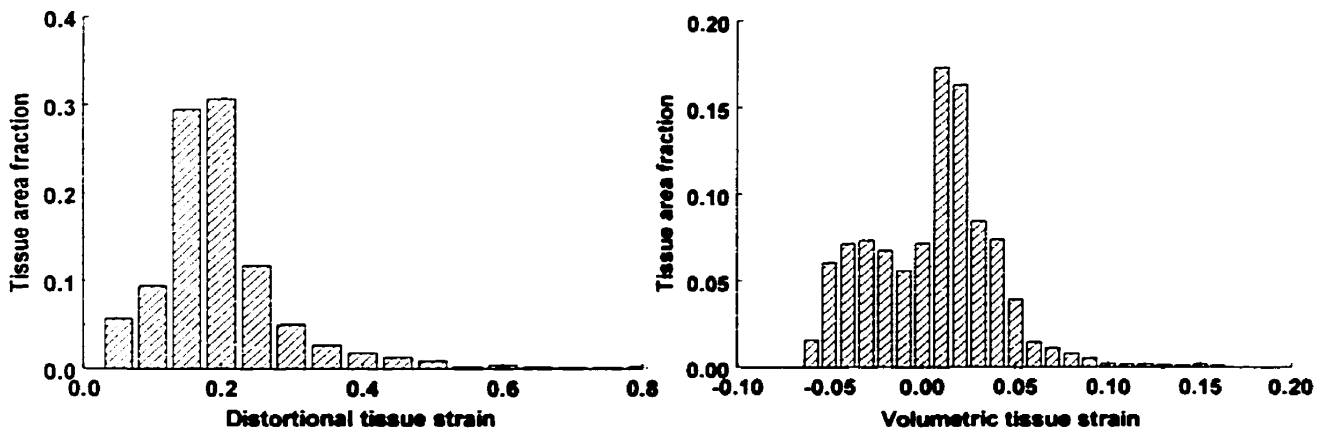


Figure 7.6. Histograms of the local distortional and volumetric tissue strains in the porous-surfaced interface zone for an applied shear displacement of 45 μm .

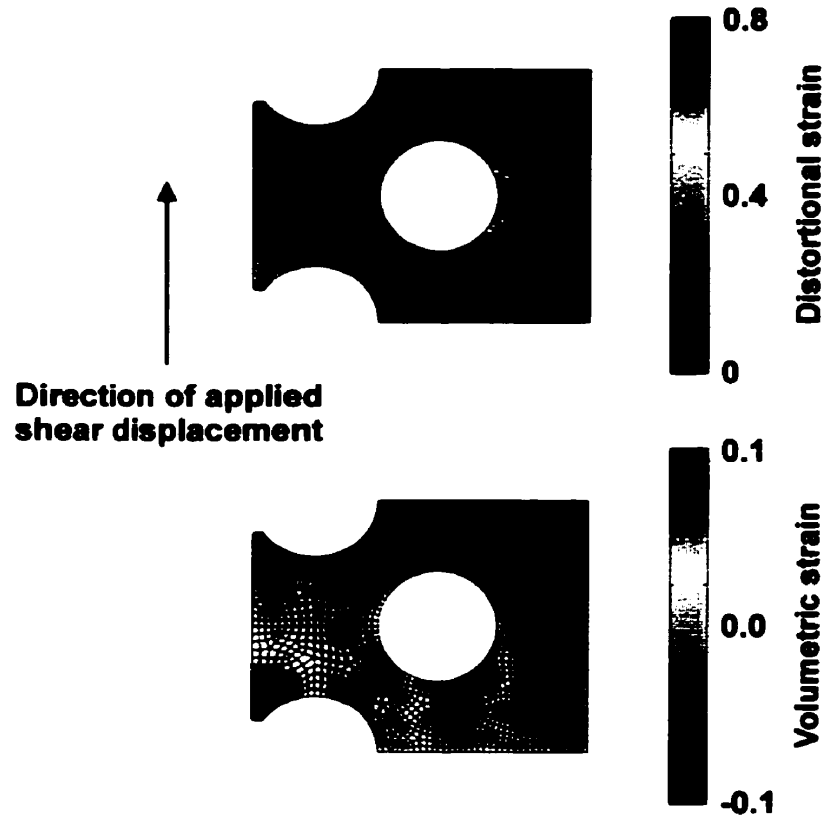


Figure 7.7. Field plots of the local distortional and volumetric tissue strains in the porous-surfaced interface zone for an applied shear displacement of $45\ \mu\text{m}$.

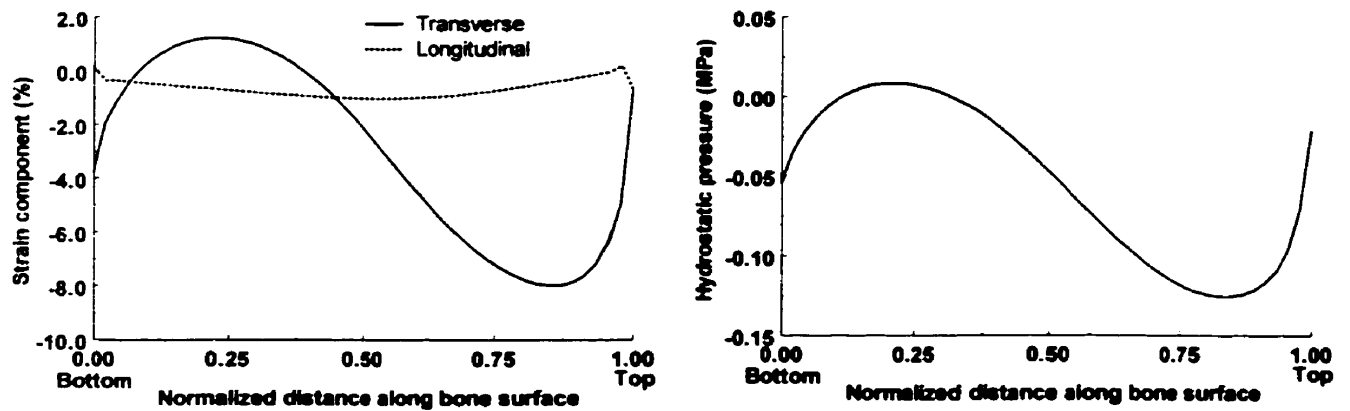


Figure 7.8. Local transverse strain, longitudinal strain, and hydrostatic pressure at the tissue-bone interface for a porous-surfaced implant with an applied shear displacement of $45\ \mu\text{m}$. The distance along the bone surface was measured from the bottom to the top of the unit cell (refer to Figure 7.3).

Porous-surfaced and plasma-sprayed implants with 10 μm shear displacement

For an applied shear displacement of 10 μm and the baseline early, pre-mineralized tissue properties, the global equivalent strains across the porous-surfaced and plasma-sprayed interface zones varied non-linearly, with the equivalent strain being as much as three times greater in the plasma-sprayed interface zone (Figure 7.9). The difference in strain magnitudes between the two interface zones was likely due to the differences in the width of gap and the differences in the effective properties for the two designs. In both cases, the equivalent strain was highest near the middle of the interface zone and lowest at the edges.

Due to the microstructural features of the two implant surface designs, a wide range of local distortional and volumetric tissue strains were predicted (Figure 7.10), and the spatial distributions of the local tissue strains were altered significantly from those predicted by the global model (Figure 7.11). As with the global strains, the local distortional tissue strains were generally higher in the plasma-sprayed interface zone than in the porous-surfaced interface zone (Figure 7.10). For instance, the median distortional tissue strains were 3.7% and 6.9% for the porous-surfaced and plasma-sprayed implants, respectively. The volumetric tissue strains were similar for the two designs (Figure 7.10). At the tissue-bone interface, there was less difference between the two surface designs. The transverse and longitudinal strain components were similar in magnitude and distribution for the two designs (Figure 7.12), with magnitudes generally slightly higher for the plasma-sprayed surface, but less than 2% in all cases. Small hydrostatic pressures ($< \pm 0.015$ MPa) were predicted along the bony surface for the porous-surfaced implant (Figure 7.13). For the plasma-sprayed implant, the hydrostatic pressure along the entire bony surface was approximately zero.

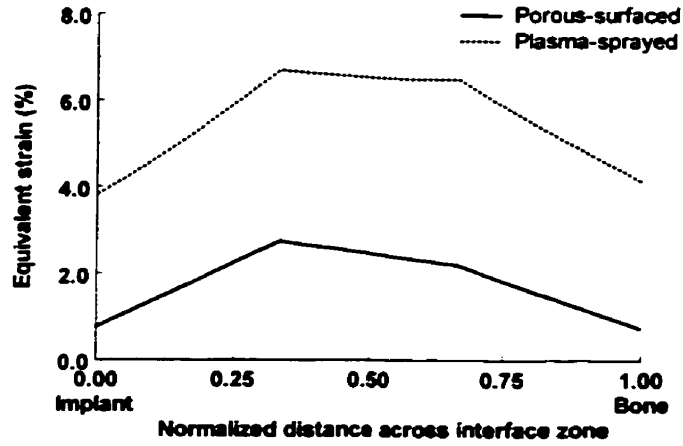


Figure 7.9. Equivalent strain across the porous-surfaced and plasma-sprayed interface zones with an applied shear displacement of 10 mm.

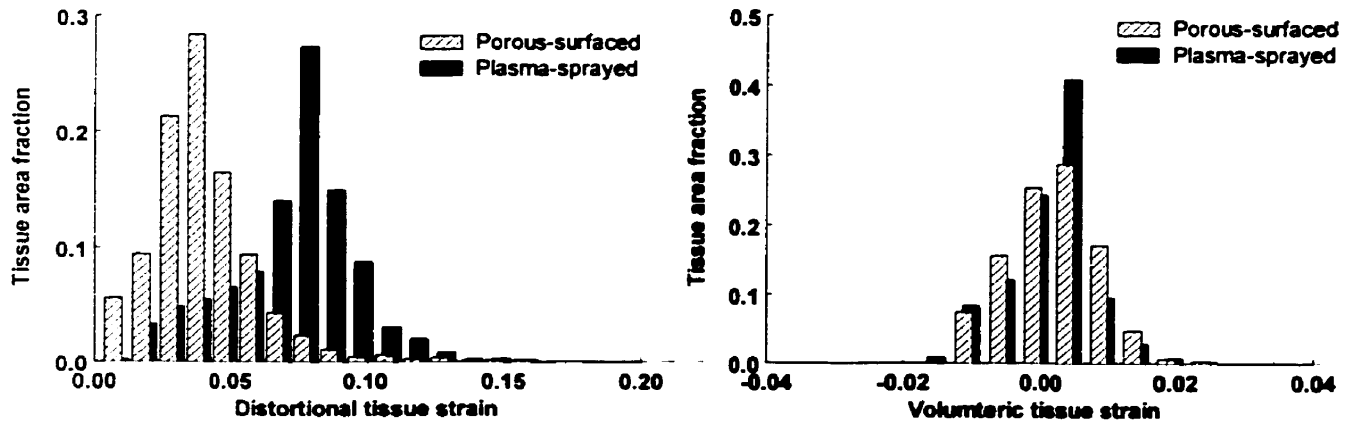


Figure 7.10. Local distortional and volumetric tissue strains in the porous-surfaced and plasma-sprayed interface zones for an applied shear displacement of 10 μm .

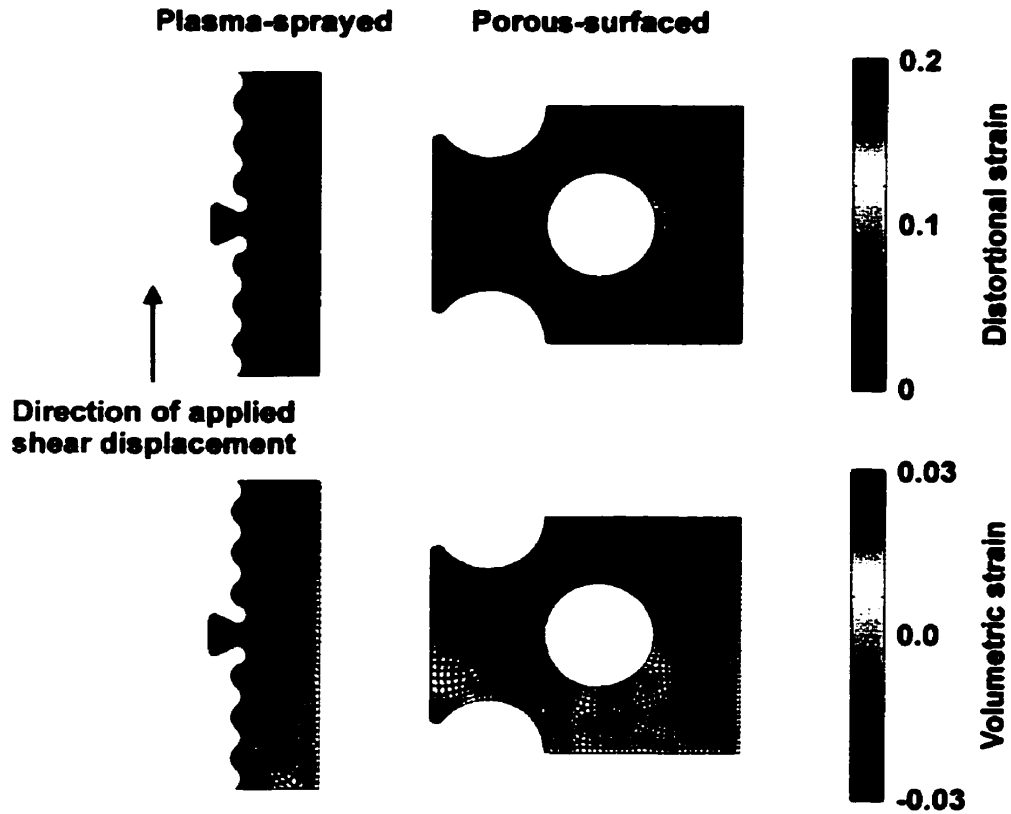


Figure 7.11. Field plots of the local distortional and volumetric tissue strains in the porous-surfaced and plasma-sprayed interface zones for an applied shear displacement of $10\ \mu\text{m}$.

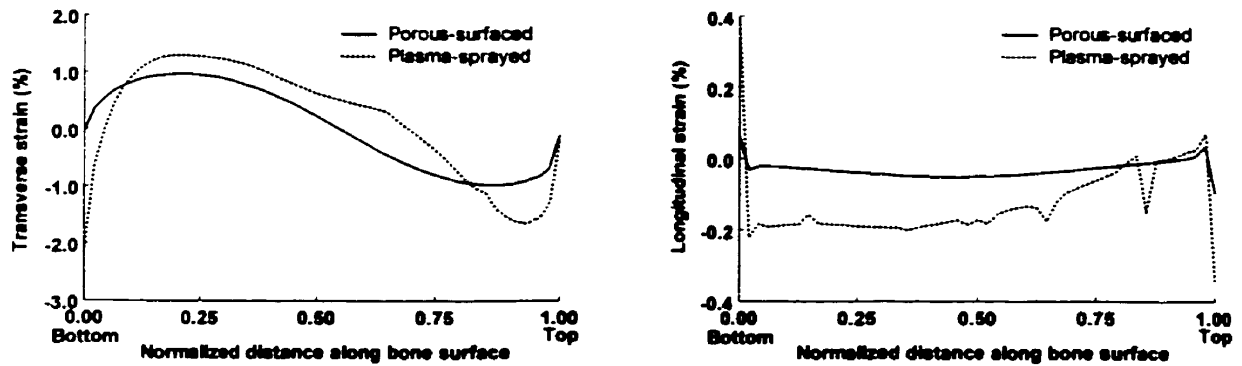


Figure 7.12. Local transverse and longitudinal strain components at the tissue-bone interface for porous-surfaced and plasma-sprayed implants with an applied shear displacement of $10\ \mu\text{m}$.

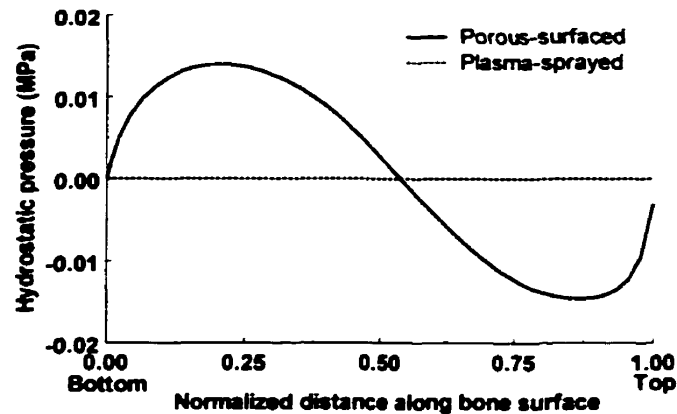


Figure 7.13. Local hydrostatic pressure at the tissue-bone interface for porous-surfaced and plasma-sprayed implants with an applied shear displacement of 10 μm .

7.5 Discussion

The objective of this portion of the thesis was to investigate the effect of implant surface geometry and applied relative movement on peri-implant tissue formation by simulating the canine micromovement experiments. Using a non-linear computational model and the unit cell approach, we determined the local mechanical environment in the peri-implant tissue for applied displacements near the critical threshold for bone formation (Pilliar et al., 1995; Pilliar et al., 1996). We also investigated the relative differences between porous-surfaced and plasma-sprayed implants, since previous experimental evidence has demonstrated that the tissue response to implant relative movement is dependent on the surface geometry (Simmons and Pilliar, 2000). The interpretation, significance, and limitations of these analyses are discussed in the sections that follow.

7.5.1 Threshold tissue strain for bone formation

As discussed previously, implant relative movement is a poor criterion for evaluating the osseointegration potential of implants, since the tissue response to applied loading is implant-specific, surface geometry-specific, and site-specific. A more universal criterion, such as local tissue strain, is necessary to evaluate orthopaedic and dental implant designs, and rehabilitation protocols that promote more rapid and reliable osseointegration. Furthermore, identifying the relationship between tissue strain and tissue formation has important implications to the design

of fracture repair devices and engineered skeletal tissues. Thus, our motivation for predicting the local tissue strains around a porous-surfaced implant subjected to an applied shear displacement near the critical threshold for bone formation was to determine a relationship between peri-implant tissue strains and tissue formation that could be used more universally for the evaluation of not only osseointegration potential, but also *osteogenesis* potential.

Earlier studies using computational, *in vitro*, and *in vivo* models have provided estimates of the critical level of strain above which bone formation is inhibited and of the critical level of hydrostatic stress above which cartilage formation is stimulated. Generally, the critical tissue or matrix strain level above which bone formation is inhibited or osteoblasts de-differentiate to fibroblast-like cells has been estimated to be on the order of 1% to 10% (quantified using a variety of strain measures) (Claes and Heigele, 1999; Giori et al., 1995; Huiskes et al., 1997; Jones et al., 1991; Meyer et al., 1999; Tägil and Aspenberg, 1999). The critical compressive hydrostatic stress magnitude above which cartilage formation is stimulated has been estimated to be between 0.15 MPa and 2 MPa (Claes and Heigele, 1999; Giori et al., 1995; Tägil and Aspenberg, 1999). As discussed in Chapter 3, several hypotheses relating these mechanical parameters to tissue formation have been proposed, and some of the critical level estimates have been based on application of these theories (Claes and Heigele, 1999; Giori et al., 1995; Huiskes et al., 1997).

Our approach to determine the critical strain threshold for bone formation was to estimate the local strains around a porous-surfaced implant subjected to an applied shear displacement near the critical displacement threshold determined experimentally (Pilliar et al., 1995; Pilliar et al., 1996). We first quantified the local tissue strains within the porous-surfaced interface zone using strain invariants, as proposed by Carter et al. (1998). Since this hypothesis is based on tissue (matrix) deformation, we considered it to be predictive primarily of local osteogenesis, *i.e.*, within the bulk of the tissue. For an applied shear displacement of 45 μm , the computational model predicted that over 84% of the tissue around the porous-surfaced implant experienced local distortional strains greater than 10%. Based on previous estimates of the critical strain level, these results suggest that localized bone formation within the interface zone tissue would be largely inhibited. The experimental data with porous-surfaced implants subjected to 50 μm of shear displacement support this conclusion. Less bone ingrowth was observed deep within the porous surface structure than just outside surface structure (Figure 7.1), suggesting that bone

formation for this applied load is primarily appositional, from the bone bed towards the implant, with much less localized bone formation within the porous surface structure.

We also quantified the local longitudinal and transverse strain components at the tissue-bone interface (i.e., the edge of the bone bed). Based on observations of fracture healing, Claes and Heigele (1999) hypothesized that the formation of new bone occurs along existing bony surfaces and is regulated in part by the local strain components. In the context of peri-implant tissue formation, this is analogous to appositional bone growth. For an applied displacement of 45 μm , just below the critical threshold for bone formation, the computational model predicted local strain magnitudes along the bone bed surface between -8% and 2% . This range of strains is generally consistent with the threshold levels estimated from previous computational, in vivo, and in vitro studies. Therefore, the model predicted strain levels at the existing bone surface that would permit appositional bone growth, again consistent with the experimental observations.

The model predictions were also consistent with the experimental observations with regard to the volumetric (hydrostatic) strain and stress parameters. Since shear loading was applied to the implants, the majority of the tissue within the interface zone experienced volumetric strains of less than 5% ; for the interface zone tissue, this is equivalent to a hydrostatic stress of less than 0.05 MPa . Similarly, the magnitude of the hydrostatic pressure acting at the tissue-bone interface was less than 0.13 MPa . These hydrostatic stress values are well below the upper threshold reported in the literature, suggesting that cartilage formation would not occur for this loading condition. This conclusion is supported by the canine micromovement experiments, in which cartilage formation has never been reported around porous-surfaced implants, even for applied shear displacements as large as $100\text{ }\mu\text{m}$ (Pilliar et al., 1995; Pilliar et al., 1996).

The model predictions for the porous-surfaced implant with $10\text{ }\mu\text{m}$ applied shear displacement are also relevant to this discussion. An applied displacement of $10\text{ }\mu\text{m}$ is very low, and likely approximates the deformations experienced by unloaded implants (due to bone deformation, for instance). In this case, the model predictions for the local distortional strain within the interface zone tissue were quite low, with over 81% of the tissue experiencing less than 5% distortional strain. The local strain magnitudes at the tissue-bone interface were also minimal ($<1\%$). Thus, based on previous estimates of the critical strain threshold, the model would predict both localized bone formation within the sintered porous surface and appositional bone growth towards the implant. Experimental data describing the bone ingrowth mechanism

for this level of applied displacement are not available. However, in our rabbit model experiments (Chapter 4), we observed localized osteogenesis within the sintered porous surface of unloaded implants eight days post-implantation. Although the loading conditions applied to the interface zone tissue around the implants in the rabbit study were different from those applied in this study, one would expect low tissue deformations in both cases. Therefore, the observations of localized and appositional bone growth in the rabbit model experiments add further support for the computational model predictions at low applied displacement levels.

7.5.2 Effect of implant surface geometry on local tissue strains

The impetus for our comparison of the local tissue strains around porous-surfaced and plasma-sprayed implants subjected to applied displacements was the observation that plasma-sprayed implants with applied displacements above the threshold displacement level (determined with porous-surfaced implants) were able to osseointegrate (Simmons and Pilliar, 2000). One explanation for this observation is that the critical threshold displacement level is higher for the plasma-sprayed design than for the porous-surfaced design. If this were the case, then the local tissue strains in the plasma-sprayed interface zone would have to be lower than those in the porous-surfaced interface zone for the same loading condition. This hypothesis assumes that the properties and the response to mechanical stimulation of the early healing peri-implant tissue around the two implant designs are similar, which is a reasonable assumption. The hypothesis also assumes that in both cases the tissue remains fully bonded to the implant and to the bone, an assumption that will be discussed below in more detail.

The computational model predictions for the two implant surface designs do not support the hypothesis that the local tissue strains around the plasma-sprayed surface are lower than those around the sintered porous surface for the same applied shear displacement. For an applied displacement of 10 μm , the model predicted significantly higher distortional strains within the plasma-sprayed interface zone tissue, and slightly higher longitudinal and transverse strains at the tissue-bone interface for the plasma-sprayed implant. Although we did not compute the strain parameters for the critical displacement level (convergent solutions were difficult to attain readily for large applied displacements), parametric investigations suggested that the strain magnitudes scale proportionately with the applied displacement for both surface designs. As a result, one would expect similar differences between the two surface designs at higher levels of applied displacement. Therefore, at the critical level of applied displacement (50 μm), the local

strains in the plasma-sprayed interface zone would be higher than those in the porous-surfaced interface zone. Based on the discussion in the previous section, localized bone formation could not occur in the plasma-sprayed interface zone at these strain levels. Furthermore, assuming the strain magnitudes predicted for the porous-surfaced implant along the bone interface are threshold values, then the model predictions for the plasma-sprayed implant would suggest appositional bone formation could not occur either. Therefore, the model would predict a *lower* threshold level of applied displacement for bone formation around plasma-sprayed implants, apparently in contradiction to the experimental evidence.

An alternate hypothesis to explain the experimental observation is that the tissue attachment to the plasma-sprayed implant is disrupted at relatively high levels of displacement. If this were to happen, there would be minimal mechanical interaction between the interface zone tissue and the implant, resulting in negligible distortional strains in the interface zone tissue and low strains at the bone interface. Therefore, both localized and appositional bone formation would be possible, despite the large applied shear displacement. We did not incorporate a mechanism for debonding at the implant-tissue interface in the computational model, and therefore could not predict this situation. However, this hypothesis is supported by the mechanical test results from our rabbit model experiments (Chapter 4). Before mineralization of the interface zone tissue in the rabbit model experiments (Day 4), the plasma-sprayed implants provided little attachment strength compared with the porous-surfaced implants (Figure 4.8). The early healing tissue in the rabbit model at this time point is likely similar to the tissue around the plasma-sprayed implants in the canine mandible at the point when loading was initiated in the micromovement experiments. Given the weak attachment strength provided by the plasma-sprayed implants, an applied displacement of 75 μm would be sufficient to damage the tissue-implant interface bone, resulting in unloading of the interface zone tissue and a low strain mechanical environment conducive to bone formation. The tissue around porous-surfaced implants is attached much more strongly, and therefore is able to maintain its interaction with the implant surface. As a result, for applied displacements above the critical threshold level for bone formation but still low enough to maintain the tissue-implant bond (such as 75 μm), the porous-surfaced interface zone tissue would experience excessive strains, resulting in fibrous tissue formation.

7.5.3 Assumptions in the analysis

Although our computational model addressed the main deficiencies of earlier studies, our analysis must be considered preliminary since several assumptions were made. These assumptions and their implications are discussed in this section. Despite the assumptions and potential limitations of the current model, its predictions are consistent with data from several in vivo and in vitro experimental studies, thus supporting the initial validity of the model and the analysis.

Tissue and bone material properties

A limitation of many earlier studies on bone formation was that the material properties of the initial healing tissues were based on the properties of similar tissues rather than experimental characterization. We attempted to address this limitation by estimating the material properties of the initial interface zone tissues based on simulation of the mechanical tests in the rabbit model experiments using finite element analysis and the homogenization method. The tissue properties we determined ($E = 1 \text{ MPa}$, $\nu = 0.47$) were similar to those of comparable tissues, suggesting that our estimates were accurate. Although more rigorous experimental characterization of the early interface zone tissue properties would be desirable, doing so is difficult because tissue samples of adequate size are unavailable typically. If our estimates of the material constants were slightly inaccurate, the implications would be minor for this study. Since the implant was rotated under displacement control, the deformation of the interface zone was dependent primarily on the elastic properties of the interface zone relative to those of the bone and implant, rather than the absolute properties. The bone and implant were much stiffer than the interface zone, and therefore small changes in the tissue properties would have little effect on the predicted interface zone strains.

In this initial analysis, we assumed the tissue was an isotropic, single-phase, linear elastic material. Although this is clearly a simplification of the real material behaviour, it was a necessary assumption in order to implement the homogenization method (as discussed in Section 6.5.2). Again, because one of our primary research objectives was to investigate surface geometry effects, we used a modelling approach that incorporated the local geometry at the expense of a more accurate material model. In one instance, the computational model predicted strains as high as 78%, which is clearly incompatible with a linear elastic material model. This implies that the model predictions in regions with high strains are inaccurate. Furthermore, the

difficulties we had in obtaining convergent solutions in some cases may have stemmed from the inconsistency between the large predicted strains and the linear elastic material model (which is strictly valid only for infinitesimal strains). To obtain more accurate strain predictions, the initial interface zone tissue could be modelled as a hyperelastic material, as was done by Giori et al. (1995) and Claes and Heigele (1999). Because of the non-linear stress-strain characteristics of biological tissues (their stiffness increases the more they are deformed), the upper strain limit predicted with a more accurate material model would be lower than that predicted with the linear elastic model. However, we were not primarily interested in the regions with high strains; instead, our interest was the regions with low strains, since these regions are conducive to bone formation. Thus, it is likely that inaccuracies in the large strain predictions would have a minor effect on threshold strain levels determined with the linear material model.

We were unable to consider the effects of fluid flow in our analysis, since we modelled the tissue as a single-phase material. This may have consequences not only to the predicted tissue strains, but also to the mechanoregulatory model (discussed below). It is difficult to predict how the tissue strain predictions may have changed had a poroelastic or biphasic material model been implemented, and the literature provides conflicting opinions (Carter and Beaupré, 1999; Prendergast and Huiskes, 1996; Tanck et al., 1999a). Fluid flow-induced shear stresses may be an important mechanoregulatory signal, and therefore future modelling efforts should incorporate biphasic material models. Wu et al. (1999) recently incorporated biphasic material descriptions into a homogenization method to study cartilage mechanics. This formulation provides a theoretical basis for the development of biphasic micromechanical models of the tissue-implant interface.

The computational model predictions for the interface zone strains were relatively insensitive to the modulus of the bone bed. This was true particularly for moduli above the baseline value of 500 MPa. At lower moduli, the strains decreased slightly, suggesting an increased potential for bone formation. However, trabecular bone with an apparent modulus of 100 MPa represents a pathological condition, with low density, osteoporotic bone (Sugita et al., 1999). It is likely that in this extreme case, biological factors play a more important role in dictating bone formation than do mechanical factors.

Computational modelling approach

This study is the first we are aware of to consider the effect of implant surface geometry on the mechanical regulation of peri-implant tissue formation. Previous computational models have not accounted for the implant surface features (Giori et al., 1995; Huiskes et al., 1997; Prendergast and Huiskes, 1996; Prendergast et al., 1997). Based on our results using a unit cell approach and non-linear finite element analysis, the local tissue strains within the interface zone differ substantially from those predicted by a global analysis alone, thus emphasizing the importance of incorporating implant surface geometry into the computational model.

As in the previous chapters, we used a unit cell approach to model the implant surface geometry in a systematic and efficient manner. We used idealized geometry unit cell models to represent the sintered porous and plasma-sprayed surfaces, recognizing that they do not represent the full range in effective and local properties of the structurally heterogeneous interface zones, but they do provide reasonably accurate first-order predictions of the effective and local properties of the interface zones (as discussed in Chapter 5). We modified our approach slightly for the current study, because the homogenization method developed in Chapter 5 assumes small deformations. Since the global strains within the interface zone were not constant and were as high as 12.7%, we conducted a geometrically non-linear finite element analysis of the global model, and used a cut-boundary displacement method (ANSYS Inc., 1997) and a non-linear finite element analysis to determine the local strains in the unit cell model. Unit cell analyses with applied displacement boundary conditions tend to over predict the apparent stiffness of the unit cell (Hollister and Kikuchi, 1992; Suquet, 1985), and therefore the local strain predictions using the cut-boundary displacement method are conservative estimates. However, it is difficult to determine how different the predicted strains are from the real values without experimental validation.

We assumed full bonding between the tissue and implant in the computational model. As discussed in Section 7.5.2, the model predictions for the plasma-sprayed implant were inconsistent with the experimental observations because of this assumption. Furthermore, the photoelastic tests demonstrated that the tissue-metal interface condition has a significant effect on the predicted local stress field. Therefore, subsequent modelling efforts should incorporate alternate interface conditions, such as contact and the ability for the interface to fail. The

difficulty in doing so is that mechanical characteristics of the tissue-metal interface are poorly characterized and difficult to determine experimentally.

Applied loads

Earlier efforts to quantify the local mechanical environment in peri-implant tissue have relied on gait analysis to estimate the loads applied to the implants (Claes and Heigele, 1999; Gardner et al., 2000; Giori et al., 1995; Huiskes et al., 1997; Ko et al., 1995; Lerner et al., 1998; Prendergast and Huiskes, 1996; Prendergast et al., 1997; Richards et al., 1999a). This approach can provide, at best, only very rough estimates of implant loading. Our computational analysis was based on experimental studies in which implant loading was applied in a controlled manner (Pilliar et al., 1995; Pilliar et al., 1996). Therefore, the loading conditions in our model were significantly more accurate than those applied in earlier studies. We applied the rotational shear displacement as a quasi-static load. This approach was consistent with our linear, elastic material model, but is not completely representative of the dynamic loading that was applied in the experiments. With the implementation of a more accurate dynamic material model, such as viscoelastic or poroelastic, the time-dependency of the local tissue strains, and its potential biological effect, could be investigated.

Mechanoregulatory model

We interpreted the computational model results using two theories that have been proposed to relate tissue strains and tissue formation. These theories were selected because: (i) they were compatible with the material model assumed in the current analysis, and (ii) in the context of peri-implant tissue formation, they are applicable to different bone formation mechanisms. We applied Carter's tissue differentiation hypothesis (Carter et al., 1998) as a predictor of localized bone formation, within the bulk of the tissue, and we applied Claes and Heigele's bone formation hypothesis (Claes and Heigele, 1999) as a predictor of appositional bone formation at the tissue-bone interface. These theories differ not only in that Carter's allows for bone formation anywhere within the healing tissue, whereas Claes and Heigele's permits bone formation only along existing bony surfaces, but also in the mechanical parameters they use to predict tissue formation. The inconsistency in parameters results from the fact that both these theories, and in fact all studies of this sort (the current one included), are phenomenological. The particular strain or stress parameters have been selected because their spatial distribution

correlates with observed patterns of tissue formation. This approach is limited in that it cannot elucidate the specific details and mechanisms that regulate tissue formation mechanically. However, the phenomenological approach can provide valuable insights into the process of tissue formation and can suggest avenues for future basic research. Furthermore, the results from these analyses may have practical, clinical value.

Since our model did not incorporate a biphasic material model, we did not apply the theory proposed by Prendergast et al. (1997) and Huiskes et al. (1997), in which the distortional strain and relative fluid velocity are the regulatory parameters. Fluid flow-induced shear stresses have been shown to influence a variety of bone cell activities (Ajubi et al., 1999; Smalt et al., 1997). Therefore, fluid flow may play an important role in peri-implant tissue formation and should be considered in future modelling studies.

It is important to note that the tissue differentiation hypotheses reviewed here and the analyses undertaken in the current study account only for the mechanical regulation of tissue formation and neglect non-mechanical factors, although they are clearly important. The poor clinical results with cementless implants in elderly patients suggest that hormonal and age-related factors play an important role in determining osseointegration potential. An adequate blood supply is “probably the most absolute requirement for new bone formation” (Aronson, 1994). Limited bone ingrowth into porous-surfaced implants with small pore sizes may be the result of poor vascularization within the porous surface structure (Bobyne et al., 1980). Although Carter’s hypothesis accounts for the inhibition of angiogenesis by excessive hydrostatic pressure, other non-mechanical anti-angiogenic factors are not accounted for in any of the theories. The implication of this caveat is that it is likely that there is not a single critical strain threshold for peri-implant bone formation, but there is a range of strains that is dependent on several non-mechanical factors, including age, health status, and implantation site. The variability in the data from micromovement experiments supports this conclusion (Figure 7.1).

7.6 A quantitative mechanoregulatory model of peri-implant tissue formation

Based on the computational analyses, the results from the rabbit model experiments, and the discussion presented in the previous sections, we have formulated a preliminary quantitative model that relates the local mechanical environment to bone formation around porous-surfaced and plasma-sprayed implants. We considered a single time point in our computational analyses,

representing the point at which loading was initiated in the canine micromovement experiments and no bone formation had occurred. Although the strain thresholds predicted in this study could be used to implement a dynamic simulation of the bone growth process, this was beyond the scope of the current study. However, a qualitative description of the process can be postulated from our investigations and is incorporated in our mechanoregulatory model.

7.6.1 Description of the model

The mechanoregulatory model is summarized in Figure 7.14. Following the theories proposed by Carter (1998) and Claes and Heigele (1999), we use distortional tissue strain as a predictor of localized bone formation within the interface zone tissue and the magnitude of the longitudinal and transverse strain components at the tissue-bone interface (referred to as bone interface strains) as a predictor of appositional bone growth. Because our analyses did not consider all loading conditions and the mechanical properties of the tissue-metal interface are not well characterized, we were unable to define the quantitative aspects of the model completely. Where possible, however, threshold strain values based on the computational model predictions are provided, with the qualifications that these are initial estimates based on our preliminary computational model and it is likely that a range of strain thresholds exists. The model accounts only for bone or fibrous tissue formation, since those were the only tissue types observed in the micromovement experiments. If large compressive hydrostatic stresses cause cartilage formation (as proposed by Carter et al. (1998) and Claes and Heigele (1999)), then based on the computational model predictions, the magnitude of the hydrostatic stress threshold is greater than 0.15 MPa.

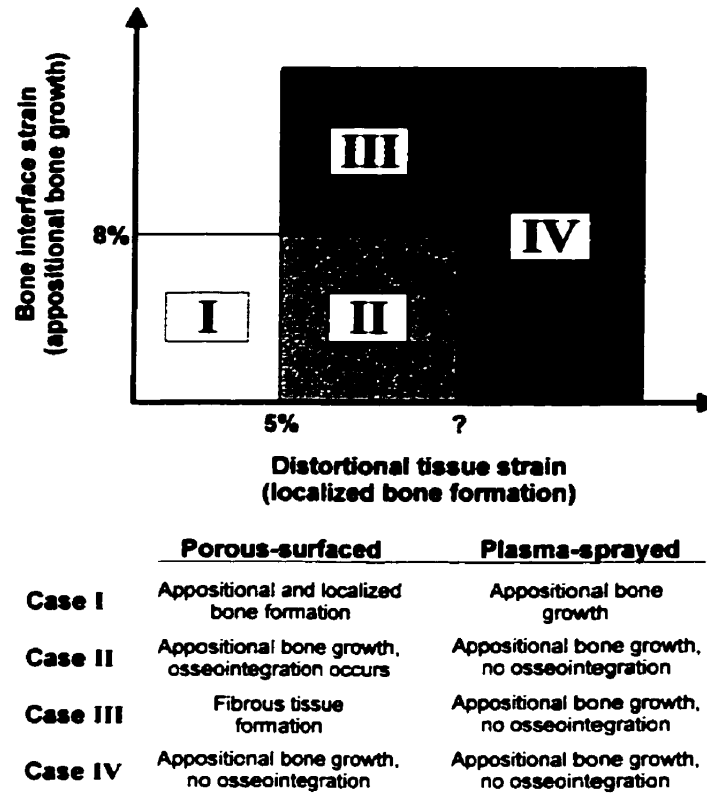


Figure 7.14. Model proposed to describe the mechanical regulation of peri-implant tissue formation around porous-surfaced and plasma-sprayed implants.

There are four cases in the mechanoregulatory model, representing different combinations of strain parameters and as a result, different tissue formation process that are dependent on the implant surface design (Figure 7.14).

Case I

In Case I, the interface zone tissue experiences distortional strains below approximately 5% and the magnitudes of the strain components at the tissue-bone interface are less than 8%. For this case, both appositional and localized bone formation can occur. For porous-surfaced implants, this represents unloaded or minimally loaded conditions (resulting in less than approximately 20 μm of relative shear displacement) and would result in osseointegration. Based on the computational model predictions for a plasma-sprayed implant with an applied displacement of 10 μm , distortional tissue strains below 5% can only occur around a plasma-

sprayed implant when it is unloaded almost completely. Since load transfer through the bone surrounding an implant to the interface zone tissue is inevitable, it is unlikely that this case would ever occur for a plasma-sprayed implant. However, if tissue attachment to the plasma-sprayed implant was maintained, and the bone interface strains remained below the threshold value of 8%, then appositional bone growth could occur. That case represents a non-functional plasma-sprayed implant.

Case II

In Case II, much of the interface zone tissue experiences strains above the 5% threshold for localized bone formation, and the bone interface strains are below the 8% threshold for appositional bone growth. The high distortional strains prevent localized bone formation within most of the interface zone. As a result, bone formation around porous-surfaced implants would be primarily appositional, possibly with some localized mineralization in strain-protected regions of the surface structure. As healing progressed, the maturation and spotty mineralization of the interface zone tissue would result in decreased interface zone strains, assuming the implant movement was load-controlled, which is the clinically relevant situation. The stiffening of the interface zone would result in lower distortional tissue strains, leading to more rapid localized bone formation (Case I). This situation represents a porous-surfaced implant subjected to sub-threshold levels of applied displacement (i.e., between 20 μm and 50 μm).

For plasma-sprayed implants and the strain levels for Case II, bone formation would be primarily appositional, similar to the situation for porous-surfaced implants (assuming tissue attachment was maintained). However, if the tissue deformation caused failure at the implant-tissue interface (the probable occurrence) then the interface zone tissue would be essentially unloaded and bone formation could progress as in Case I, with localized and appositional bone formation in the interface zone tissue. It is unclear what level of applied displacement this case would represent for a plasma-sprayed implant, but 75 μm is likely well above the threshold. The progression of bone formation is difficult to predict in this case, although the experimental evidence indicates that osseointegration does occur (Simmons and Pilliar, 2000). At some point, the implant and surrounding tissue must become coupled for ingrowth to occur. However, as the unstrained interface zone tissue mineralized, the interface zone gap narrowed, and tissue ingrowth occurred, one would expect large tissue strains, which would prevent osseointegration, resulting in fibrous tissue attachment or encapsulation. This assumes that the loading of the

implant continues during the healing process at a level comparable to that that caused the initial disruption of the tissue-implant interface. This is a realistic and clinically relevant situation, and this pattern of tissue formation is supported by clinical experience with loose implants. In the canine micromovement experiments, however, the loads applied during the load-control phase were based on the average reaction torques measured during the first week of displacement-controlled loading. If the interface zone tissue was damaged and became detached during the first week of loading, then little resistance to torquing would be measured. Consequently, the torque applied during the load-control phase would be very low, and the interface zone tissue deformation would be comparable to that of a nonfunctional implant, allowing bone formation to occur as in Case I.

Case III

In this case, assuming tissue attachment to the implant, neither localized or appositional bone formation is possible since the distortional and bone interface strains are above the threshold levels for bone formation. For porous-surfaced implants, this is the case for applied displacements above the critical threshold (i.e., $> 50 \mu\text{m}$). The implant would become attached by fibrous tissue initially, reducing the chances for osseointegration, although with time the tissue may mature sufficiently to limit deformation to levels that would encourage bone formation. For plasma-sprayed implants, tissue attachment to the implant would likely be disrupted at these levels, and tissue formation, but not osseointegration would occur (as in Case II).

Case IV

Presumably, excessively high tissue strains would result in disruption of the tissue-implant interface for any implant surface design. The threshold strains for failure of the tissue-implant interface are currently not known (indicated by “?” in Figure 7.14). Assuming interface failure, tissue formation would occur for porous-surfaced and plasma-sprayed implants as it does for plasma-sprayed implants in Case II.

7.6.2 Clinical implications

Some clinically relevant implications can be postulated from the mechanoregulatory model. In the case of nonfunctional implants, osseointegration of both porous-surfaced and plasma-sprayed surface designs would be expected. However, because localized bone formation

is encouraged in the porous-surfaced interface zone, more rapid osseointegration would be expected with this design. We observed this to be the case in the rabbit experiments. The model predicts that the porous-surfaced design not only osseointegrates more rapidly, but also can tolerate higher levels of micromovement. As discussed in Section 4.5, an implant that integrates more rapidly will be less susceptible to the detrimental effects of micromovement. Furthermore, an implant with a higher tolerance for micromovement will be less vulnerable to adverse loads, and will require a shorter rehabilitation period. Thus, for the shear loading condition considered in this study, porous-surfaced implants have a greater potential for osseointegration, particularly in situations in which osseointegration is difficult to achieve.

7.7 Conclusions

The objective of this study was to investigate the effect of implant surface geometry and applied relative movement on peri-implant tissue formation by simulating the canine micromovement experiments. Based on non-linear finite element analyses, we developed a quantitative model to describe the mechanical regulation of peri-implant tissue formation for porous-surfaced and plasma-sprayed implants. Although several assumptions were made in our initial computational analysis, the mechanoregulatory model predicts localized and appositional bone formation patterns that are consistent with experimental observations for a range of loading conditions. Furthermore, our analyses predicted critical stress and strain thresholds similar to those determined previously in computational, in vitro, and in vivo studies. This is the first study we are aware of that considered the effect of implant surface geometry on peri-implant tissue formation around functional implants. The mechanoregulatory model we proposed provides initial criteria by which the osseointegration potential of a variety of bone-interfacing implant surface designs may be evaluated. The model may also be applicable to evaluate the effects of mechanical loading on fracture healing and on engineered skeletal tissue formation.

Chapter 8

Conclusions and recommendations for future work

8.1 Motivation

The demand for orthopaedic and dental implants, which are used to restore function to diseased or damaged joints and edentulous jaws, has grown dramatically in recent years, and is expected continue to rise. Although the use of implants is an effective treatment strategy in many cases, there are several clinical situations in which failure rates are unacceptably high. Therefore, the challenge in orthopaedic and dental implantology is to establish implant designs, surgical procedures, and rehabilitation protocols that will restore function to patients more reliably and rapidly.

Experimental evidence indicates that functional osseointegration, and therefore the clinical success of an implant, depends on the geometric features of the implant surface. However, there is considerable debate whether certain surface geometries are preferable to others in terms of the rate and reliability of osseointegration. It has been suggested that implant surface geometry may influence the mechanical environment in the peri-implant tissue, which in turn regulates tissue formation. However, the relationship between implant surface geometry and the local mechanical environment, and its role in regulating early peri-implant tissue formation have not been investigated previously.

Identifying implant surface designs that promote more rapid and reliable osseointegration will improve the design and use of orthopaedic and dental implants, resulting in improvements in patient care and reductions in health care expenditures. Furthermore, identifying the mechanisms by which implant surface geometry influences peri-implant tissue formation has important implications not only to implant design, but also to the design of fracture repair devices and engineered skeletal tissues.

8.2 Research objectives and conclusions

Based on the motivation provided above, we identified several research objectives, with the overall aim of investigating the relationship between implant surface geometry, the local

mechanical environment, and early peri-implant tissue formation. The research objectives and the conclusions resulting from the related investigations are summarized below.

Objective 1: To investigate the effect of implant surface geometry on early tissue formation by determining the histological and mechanical characteristics of the tissue-implant interface zone for porous-surfaced and plasma-sprayed implants, two designs that are used clinically in orthopaedic and dental implant systems.

Conclusions: We placed nonfunctional porous-surfaced and plasma-sprayed implants in the femoral condyles of rabbits and evaluated the implants at early times post-implantation. Based on histological analysis, back-scattered and scanning electron microscopy, quantitative image analysis, and mechanical testing, we found that the three-dimensional interconnected structure of the sintered Ti6Al4V porous surface was integrated with healing tissue more rapidly and more extensively than was the irregular geometry of the Ti plasma-sprayed coating. Additionally, the tissue in the porous-surfaced interface zone mineralized more rapidly than that in the plasma-sprayed interface zone. Consequently, the porous-surfaced implants developed stronger and stiffer early attachment. These data demonstrate that surface geometry strongly influences early healing dynamics and as a result, the early mechanical stability of implants.

Objectives 2 and 3: To develop a computational micromechanical model to describe accurately the effective and local properties of the porous-surfaced and plasma-sprayed interface zones, and to validate the numerical model experimentally and analytically.

Conclusions: Using a unit cell approach, we developed a two-dimensional computational model based on homogenization methods to describe the effective and local properties of the porous-surfaced and plasma-sprayed interface zones. The model predictions indicated that the porous-surfaced interface zone was effectively stiffer than the plasma-sprayed interface zone, and also provided large local regions in which the tissue was strain-protected. The validation studies, using mechanical test data, the Hashin-Shtrikman composite model, and photoelastic analysis, suggested that, although there were discrepancies between the homogenization predictions and the validation data, the computational model provided reasonable initial predictions of the effective and local properties of the two interface zones. The model was therefore judged to be adequate for preliminary investigations on the role of surface geometry and mechanical factors in peri-implant tissue formation.

Objective 4a: To apply the model to investigate the effect of surface geometry and local mechanical environment on peri-implant tissue formation.

Conclusions: Using the computational model, we tested the hypothesis that the accelerated osseointegration we observed with porous-surfaced implants was the result of this design providing a local mechanical environment that was favourable for bone formation. We found that, in cases where the implants were nonfunctional or minimally loaded, the tissue in the region around porous-surfaced implants experienced significantly lower distortional and volumetric strains than the tissue around plasma-sprayed implants. Low distortional and volumetric tissue strains are believed to favour localized bone formation, and therefore the model supports the hypothesis that the porous-surfaced geometry provides a local mechanical environment that favours more rapid, localized bone formation. For nonfunctional or minimally loaded conditions, the local strain components at the tissue-bone interface were conducive to appositional bone formation for both porous-surfaced and plasma-sprayed implants. These model predictions were consistent with our experimental observations of early tissue formation in the rabbit model experiments.

Objective 4b: To apply the model to propose a quantitative model of mechanical regulation of peri-implant tissue formation.

Conclusions: Using experimental data from earlier studies and a non-linear finite element analysis that accounted for implant surface geometry, we predicted the local strain thresholds for localized and appositional bone formation. Based on the computational analyses, the results from the rabbit model experiments, and the data from earlier experimental studies, we proposed a quantitative model for the mechanical regulation of peri-implant tissue formation. Despite several simplifying assumptions in our analyses, the mechanoregulatory model predictions were consistent with experimental observations of tissue formation around porous-surfaced and plasma-sprayed implants subjected to early loading.

In addition to these objective-specific conclusions, clinically relevant and practical conclusions can be inferred from this research, including:

- (1) Porous-surfaced implants have greater initial stability and induce an accelerated healing response compared with plasma-sprayed implants, in cases where the

implants are nonfunctional or minimally loaded. This suggests that porous-surfaced implants have a greater potential for osseointegration, and therefore may be the preferred design.

- (2) The local mechanical environment and tissue formation are significantly influenced by the implant surface geometry, and therefore future modelling studies should account for the effects of surface geometry.
- (3) The mechanoregulatory model provides the foundation for the development of a method to evaluate the osseointegration potential of other implant surface designs, thereby potentially reducing the need for costly, time-consuming, and inhumane animal experimentation at the early stages of implant development.
- (4) The results of this study with bone-interfacing implants have implications to other osteogenic processes, such as bone engineering. For instance, just as implant surface geometry influences the local mechanical environment and tissue formation, so too may the pore geometry and stiffness of synthetic scaffolds for tissue regeneration. These factors are likely to be particularly important when engineered tissues and their matrices are subjected to functional loads in vivo or applied loads in vitro. Certainly, serious consideration must be given to the role of physical stimuli in the formation of engineered tissues.

8.3 Contributions of this research

Several novel contributions have resulted from this research, including:

- (1) The characterization of the initial tissue formation process and of the mechanical characteristics of the early interface zone tissues around porous-surfaced and plasma-sprayed implants.
- (2) The development, implementation, and initial validation of a computational model of the interface zones of porous-surfaced and plasma-sprayed implants.
- (3) The first evidence that we are aware of that supports the hypothesis that implant surface geometry influences the rate of osseointegration by mechanical regulation of peri-implant tissue formation.
- (4) The first quantitative mechanoregulatory model for peri-implant tissue formation that considers implant surface geometry and is supported by experimental evidence.

8.4 Recommendations for future work

Based on the overall goal of improving implant designs and understanding how mechanical forces regulate tissue formation, the following areas of research merit further consideration.

Improvements to the computational model

Several simplifying assumptions were made in the computational model developed in this study, and therefore the model must be considered preliminary. By addressing the limitations of the current model, the accuracy of the predictions of the local peri-implant mechanical environment would be improved. The primary areas of focus should be:

- (1) The implementation of a more realistic material model, such as hyperelastic, viscoelastic, poroelastic, or hyperporoelastic.
- (2) The implementation of a more realistic tissue-metal interface condition that allows debonding and contact at the interface.
- (3) Development of three-dimensional unit cell models that represent the implant surface geometry more accurately.
- (4) More rigorous and complete experimental validation of the improved computational model accounting for the three-dimensional, non-linear characteristics of the tissue-implant interface zone.

Experimental investigations with other implant surface designs

We considered only porous-surfaced and plasma-sprayed surface designs in this thesis. The animal model and related experimental protocol that we established could be used to evaluate other implant surface geometries that are available commercially, including grit-blasted and acid-etched surfaces. Furthermore, additional implant surface design variables, such as implant surface chemistry, could be evaluated using the experimental model. The data from these experiments could be used to define ability of the mechanoregulatory model to predict osseointegration potential for a variety of implant designs.

Refinement of the mechanoregulatory model

In the mechanoregulatory model we proposed in Chapter 7, we provided estimates of the critical strain thresholds for cases where experimental data were available. The accuracy of the

critical strain thresholds will be improved by enhancing the computational model. However, additional micromovement experiments are required to define the quantitative aspects of the model completely. For instance, the displacement level at which the tissue-implant interface fails for porous-surfaced implants is unknown. Additionally, we were required to postulate the progression of tissue formation in some cases. Experiments in which the time course of tissue formation around loaded implants is observed would provide valuable data for the refinement and the validation of the mechanoregulatory model.

In vitro studies on the mechanical regulation of tissue formation

Although the investigations in this thesis provided significant insights into the effects of implant surface geometry and mechanical forces on early peri-implant tissue formation, the phenomenological approach we used is limited in that it cannot elucidate the specific details and mechanisms by which tissue formation is regulated mechanically. The specific mechanical signals and regulatory pathways responsible for cellular responses to physical stimulation will only be revealed by well-formulated cell and tissue culture studies. For instance, synthetic scaffolds developed for tissue engineering applications could be used as three-dimensional model matrix systems that could be manipulated appropriately to investigate mechanical regulation of gene expression and cell function. An improved understanding of the role of mechanical signals in cellular function and tissue development is important not only to implant design and tissue engineering, but also to developmental biology, wound healing, and other biological processes.

References

- Adell, R., Lekholm, U., Rockler, B., and Branemark, P. (1981) A 15-year study of osseointegrated implants in the treatment of the edentulous jaw. *International Journal of Oral Surgery*, **10**(6): 387-416.
- Ahmad, M., Gawronski, D., Blum, J., Goldberg, J., and Gronowicz, G. (1999) Differential response of human osteoblast-like cells to commercially pure (cp) titanium grades 1 and 4. *Journal of Biomedical Materials Research*, **46**: 121-131.
- Ajubi, N. E., Klein-Nulend, J., Alblas, M. J., Burger, E. H., and Nijweide, P. J. (1999) Signal transduction pathways involved in fluid flow-induced PGE₂ production by cultured osteocytes. *American Journal of Physiology*, **276**: E171-E178.
- Akagawa, Y., Hashimoto, M., Kondo, N., Satomi, K., Takata, T., and Tsuru, H. (1986) Initial bone-implant interfaces of submergible and supramergible endosseous single-crystal sapphire implants. *Journal of Prosthetic Dentistry*, **55**(1): 96-100.
- American Association of Oral and Maxillofacial Surgeons (1999) Dental Implants, American Association of Oral and Maxillofacial Surgeons, Rosemont, IL.
- ANSYS Inc. (1997) Submodeling. In: ANSYS Advanced Analysis Techniques, SAS IP, Inc., Canonsburg, PA.
- Aronson, J. (1994) Experimental assessment of bone regenerate quality during distraction osteogenesis. In: Bone Formation and Repair, C. T. Brighton, G. Friedlaender, and J. M. Lane, eds., American Academy of Orthopaedic Surgeons, Rosemont, IL, 441-463.
- Aspenberg, P., Goodman, S., Toksvig-Larsen, S., Ryd, L., and Albrektsson, T. (1992) Intermittent micromotion inhibits bone ingrowth: Titanium implants in rabbits. *Acta Orthopaedica Scandinavica*, **63**(2): 141-145.
- Bakhvalov, N., and Panasenko, G. (1989) Homogenisation: Averaging Processes in Periodic Media, Kluwer Academic Publishers, Boston.

- Bathe, K.-J. (1982) Finite element procedures in engineering analysis, Prentice-Hall, Inc., Englewood Cliffs, NJ.
- Batzer, R., Liu, Y., Cochran, D. L., Szmuckler-Moncler, S., Dean, D. D., Boyan, B. D., and Schwartz, Z. (1998) Prostaglandins mediate the effects of titanium surface roughness on MG63 osteoblast-like cells and alter cell responsiveness to $1\alpha,25\text{-(OH)}_2\text{D}_3$. *Journal of Biomedical Materials Research*, **41**: 489-496.
- Beaupré, G. S., and Carter, D. R. (1992) Finite element analysis in biomechanics. In: Biomechanics - Structures and Systems, A. A. Biewener, ed., Oxford University Press, New York, 149-174.
- Blenman, P. R., Carter, D. R., and Beaupré, G. S. (1989) Role of mechanical loading in the progressive ossification of a fracture callus. *Journal of Orthopaedic Research*, **7**: 398-407.
- Bobyn, J. D., Pilliar, R. M., Cameron, H. U., and Weatherly, G. C. (1980) The optimum pore size for the fixation of porous-surfaced metal implants by ingrowth of bone. *Clinical Orthopaedics and Related Research*, **150**: 263-270.
- Bowers, K. T., Keller, J. C., Randolph, B. A., Wick, D. G., and Michaels, C. M. (1992) Optimization of surface micromorphology for enhanced osteoblast responses in vitro. *International Journal of Oral & Maxillofacial Implants*, **7**(3): 302-310.
- Boyan, B. D., Batzer, R., Kieswetter, K., Liu, Y., Cochran, D. L., Szmuckler-Moncler, S., Dean, D. D., and Schwartz, Z. (1998) Titanium surface roughness alters responsiveness of MG63 osteoblast-like cells to $1\alpha,25\text{-(OH)}_2\text{D}_3$. *Journal of Biomedical Materials Research*, **39**: 77-85.
- Boyan, B. D., Hummert, T. W., Dean, D. D., and Schwartz, Z. (1996) Role of material surfaces in regulating bone and cartilage cell response. *Biomaterials*, **17**: 137-146.

- Bragdon, C. R., Burke, D. W., Lowenstein, J. D., O'Connor, D. O., Ramamurti, B., Jasty, M., and Harris, W. H. (1996) Differences in stiffness of the interface between a cementless porous implant and cancellous bone in vivo in dogs due to varying amounts of implant motion. *The Journal of Arthroplasty*, **11**(8): 945-951.
- Brunette, D. M. (1988) The effects of implant surface topography on the behavior of cells. *International Journal of Oral & Maxillofacial Implants*, **3**: 231-246.
- Brunette, D. M., and Chehroudi, B. (1999) The effects of the surface topography of micromachined titanium substrata on cell behavior in vitro and in vivo. *Journal of Biomechanical Engineering*, **121**: 49-57.
- Brunski, J. B., Moccia Jr., A. F., Pollack, S. R., Korostoff, E., and Trachtenberg, D. I. (1979) The influence of functional use of endosseous dental implants on the tissue-implant interface. I. Histological aspects. *Journal of Dental Research*, **58**(10): 1953-1969.
- Bryant, S. R. (1998) The effects of age, jaw site, and bone condition on oral implant outcomes. *International Journal of Prosthodontics*, **11**(5): 470-490.
- Burger, E. H., Klein-Nulend, J., and Veldhuijzen, J. P. (1991) Modulation of osteogenesis in fetal bone rudiments by mechanical stress in vitro. *Journal of Biomechanics*, **24 Suppl 1**: 101-109.
- Buser, D., Nydegger, T., Hirt, H. P., Cochran, D. L., and Nolte, L.-P. (1998) Removal torque values of titanium implants in the maxilla of miniature pigs. *International Journal of Oral & Maxillofacial Implants*, **13**: 611-619.
- Buser, D., Schenk, R. K., Steinemann, S., Fiorellini, J. P., Fox, C. H., and Stich, H. (1991) Influence of surface characteristics on bone integration of titanium implants. A histomorphometric study in miniature pigs. *Journal of Biomedical Materials Research*, **25**: 889-902.
- Cameron, H. U., Pilliar, R. M., and MacNab, I. (1973) The effect of movement on the bonding of porous metal to bone. *Journal of Biomedical Materials Research*, **7**(4): 301-311.

- Canadian Council on Animal Care (1993) CCAC Guide to the Care and Use of Experimental Animals, Canadian Council on Animal Care, Ottawa.
- Canadian Institute for Health Information (1999) Canadian Joint Replacement Registry (CJRR) Development. <www.cihi.ca/Roadmap/CJRR/start.htm> Accessed February 25, 2000.
- Carlsson, L., Röstlund, T., Albrektsson, B., and Albrektsson, T. (1988) Removal torques for polished and rough titanium implants. *International Journal of Oral & Maxillofacial Implants*, **3**: 21-24.
- Carter, D. R. (1987) Mechanical loading and skeletal biology. *Journal of Biomechanics*, **20**(11/12): 1095-1109.
- Carter, D. R., and Beaupré, G. S. (1999) Linear elastic and poroelastic models of cartilage can produce comparable stress results: a comment on Tanck et al. (J Biomech 32:153-161,1999). *Journal of Biomechanics*, **32**: 1255-56.
- Carter, D. R., Beaupre, G. S., Giori, N. J., and Helms, J. A. (1998) Mechanobiology of skeletal regeneration. *Clinical Orthopaedics and Related Research*, **355 Suppl**: S41-55.
- Carter, D. R., Blenman, P. R., and Beaupré, G. S. (1988) Correlations between mechanical stress history and tissue differentiation in initial fracture healing. *Journal of Orthopaedic Research*, **6**: 736-748.
- Carter, D. R., and Giori, N. J. (1991) Effect of mechanical stress on tissue differentiation in the bony implant bed. In: The Bone-Biomaterial Interface, J. E. Davies, ed., University of Toronto Press, Toronto, 367-379.
- Carter, D. R., Orr, T. E., Fyhrie, D. P., and Schurman, D. J. (1987) Influences of mechanical stress on prenatal and postnatal skeletal development. *Clinical Orthopaedics and Related Research*, **219**: 237-250.
- Carter, D. R., and Wong, M. (1988a) Mechanical stresses and endochondral ossification in chondroepiphysis. *Journal of Orthopaedic Research*, **6**: 148-154.

- Carter, D. R., and Wong, M. (1988b) The role of mechanical loading histories in the development of diarthrodial joints. *Journal of Orthopaedic Research*, **6**: 804-816.
- Chao, E. Y. S., Aro, H. T., and Inoue, N. (1995) Engineering principles in bone fracture fixation and repair. In: Biomedical Applications of Synthetic Biodegradable Polymers, J. O. Hollinger, ed., CRC Press, Boca Raton, 145-172.
- Chao, E. Y. S., Aro, H. T., and Inoue, N. (1998) Enhancement of fracture healing by mechanical and surgical intervention. *Clinical Orthopaedics and Related Research*, **355S**: S163-S178.
- Cheal, E. J., Mansmann, K. A., DiGioia, A. M., Hayes, W. C., and Perren, S. M. (1991) Role of interfragmentary strain in fracture healing: Ovine model of a healing osetotomy. *Journal of Orthopaedic Research*, **9**: 131-142.
- Chehroudi, B., McDonnell, D., and Brunette, D. M. (1997) The effects of micromachined surfaces on formation of bonelike tissue on subcutaneous implants as assessed by radiography and computer image processing. *Journal of Biomedical Materials Research*, **34**: 279-290.
- Claes, L. E., and Heigele, C. A. (1999) Magnitudes of local stress and strain along bony surfaces predict the course and type of fracture healing. *Journal of Biomechanics*, **32**: 255-266.
- Cochran, D. L., Schenk, R. K., Lussi, A., Higginbottom, F. L., and Buser, D. (1998) Bone response to unloaded and loaded titanium implants with a sandblasted and acid-etched surface: A histometric study in the canine mandible. *Journal of Biomedical Materials Research*, **40**: 1-11.
- Cooper, L. F., Masuda, T., Whitson, S. W., Yliheikkilä, P. K., and Felton, D. A. (1999) Formation of mineralizing osteoblast cultures on machined, titanium oxide grit-blasted and plasma-sprayed titanium surfaces. *International Journal of Oral & Maxillofacial Implants*, **14**: 37-47.

- Cooper, L. F., Masuda, T., Yliheikkilä, P. K., and Felton, D. A. (1998) Generalizations regarding the process and phenomenon of osseointegration. Part II. In vitro studies. *International Journal of Oral & Maxillofacial Implants*, **13**: 163-174.
- Cowin, S. C. (1990) Properties of cortical bone and theory of bone remodeling. In: Biomechanics of Diarthroidal Joints, V. C. Mow, A. Radcliffe, and S. L.-Y. Woo, eds., Springer-Verlag, New York, 119-153.
- Curtis, A., and Wilkinson, C. (1997) Topographical control of cells. *Biomaterials*, **18**: 1573-1583.
- Davies, J. E. (1996) In vitro modeling of the bone/implant interface. *The Anatomical Record*, **25**: 426-445.
- Davies, J. E. (1998) Mechanisms of endosseous integration. *International Journal of Prosthodontics*, **11**(5): 391-402.
- de Groot, K., Geesink, R., Klein, C. P. A. T., and Serekian, P. (1987) Plasma sprayed coatings of hydroxylapatite. *Journal of Biomedical Materials Research*, **21**: 1375-1381.
- Degasne, I., Baslé, M. F., Demais, V., Huré, G., Lesourd, M., Grolleau, B., Mercier, L., and Chappard, D. (1999) Effects of roughness, fibronectin, and vitronectin on attachment, spreading, and proliferation of human osteoblast-like cells (Saos-2) on titanium surfaces. *Calcified Tissue International*, **64**: 499-507.
- Deporter, D. A., Watson, P. A., Heller, A., Heller, R., and Pilliar, R. M. (1997) Use of the Endopore dental implant. Technique and 5-year clinical trial results using a mandibular overdenture. *Implantologie*, **25**: 15-27.
- Deporter, D. A., Watson, P. A., Pilliar, R. M., Chipman, M. L., and Valiquette, N. (1990) A histological comparison in the dog of porous-coated vs. threaded dental implants. *Journal of Dental Research*, **69**(5): 1138-1145.

- Deporter, D. A., Watson, P. A., Pilliar, R. M., Pharoah, M., Chipman, M., and Smith, D. C. (1992) A clinical trial of a partially porous-coated endosseous dental implant in humans: protocol and 6-month results. In: Tissue Integration in Oral, Orthopedic, and Maxillofacial Reconstruction, W. R. Laney and D. E. Tolman, eds., Quintessence Publishing Co., Inc., Chicago, 250-258.
- Dhert, W. J. A., Thomsen, P., Blomgren, A. K., Esposito, M., Ericson, L. E., and Verbout, A. J. (1998) Integration of press-fit implants in cortical bone. A study on interface kinetics. *Journal of Biomedical Materials Research*, **41**: 574-583.
- Ducheyne, P., Aernoudt, E., de Meester, P., Martens, M., Mulier, J. C., and van Leeuwen, D. (1978) Factors governing the mechanical behavior of the implant-porous coating-trabecular bone interface. *Journal of Biomechanics*, **11**: 297-307.
- Ducheyne, P., de Meester, P., Aernoudt, E., Martens, M., and Mulier, J. C. (1977) Influence of a functional dynamic loading on bone ingrowth into surface pores of orthopedic implants. *Journal of Biomedical Materials Research*, **11**: 811-838.
- Dziedzic, D. S. M. (1995). Effects of implant surface topography on osteoconduction, M.Sc. Thesis, University of Toronto, Toronto.
- Filiaggi, M. J., Coombs, N. A., and Pilliar, R. M. (1991) Characterization of the interface in the plasma-sprayed HA coating/Ti-6Al-4V implant system. *Journal of Biomedical Materials Research*, **25**: 1211-1229.
- Friedman, R. J., An, Y. H., Ming, J., Draughn, R. A., and Bauer, T. W. (1996) Influence of biomaterial surface texture on bone ingrowth in the rabbit femur. *Journal of Orthopaedic Research*, **14**(3): 455-464.
- Gardner, T. N., Stoll, T., Marks, L., Mishra, S., and Knothe Tate, M. (2000) The influence of mechanical stimulus on the pattern of tissue differentiation in a long bone fracture - an FEM study. *Journal of Biomechanics*, **33**: 415-425.

- Ghosh, S., Lee, K., and Moorthy, S. (1995) Multiple scale analysis of heterogeneous elastic structures using homogenization theory and Voronoi cell finite element method. *International Journal of Solids and Structures*, **32**(1): 27-62.
- Giori, N. J., Ryd, L., and Carter, D. R. (1995) Mechanical influences on tissue differentiation at bone-cement interfaces. *The Journal of Arthroplasty*, **10**(4): 514-522.
- Glantz, P.-O. (1998) The choice of alloplastic materials for oral implants: Does it really matter? *International Journal of Prosthodontics*, **11**(5): 402-407.
- Goldstein, S. A., Hollister, S. J., Kuhn, J. L., and Kikuchi, N. (1990) The mechanical and remodeling properties of trabecular bone. In: Biomechanics of Diarthroidal Joints, V. C. Mow, A. Radcliffe, and S. L.-Y. Woo, eds., Springer-Verlag, New York, 61-81.
- Goldstein, S. A., Waanders, N., Guldberg, R., Steen, H., Senunas, L., Goulet, J. A., and Bonadio, J. (1994) Stress morphology relationships during distraction osteogenesis: Linkages between mechanical and architectural factors in molecular regulation. In: Bone Formation and Repair, C. T. Brighton, G. Friedlaender, and J. M. Lane, eds., American Academy of Orthopaedic Surgeons, Rosemont, IL, 405-419.
- Gomi, K., and Davies, J. E. (1993) Guided bone tissue elaboration by osteogenic cells in vitro. *Journal of Biomedical Materials Research*, **27**: 429-431.
- Goodman, S., Toksvig-Larsen, S., and Aspenberg, P. (1993) Ingrowth of bone into pores in titanium chambers implanted in rabbits: Effect of pore cross-sectional shape in the presence of dynamic shear. *Journal of Biomedical Materials Research*, **27**: 247-253.
- Goodship, A. E., Cunningham, J. L., and Kenwright, J. (1998) Strain rate and timing of stimulation in mechanical modulation of fracture healing. *Clinical Orthopaedics and Related Research*, **355S**: S105-S115.
- Goodship, A. E., and Kenwright, J. (1985) The influence of induced micromovement upon the healing of experimental tibial fractures. *Journal of Bone and Joint Surgery [Br]*, **67-B**(4): 650-655.

- Groessner-Schreiber, B., and Tuan, R. S. (1992) Enhanced extracellular matrix production and mineralization by osteoblasts cultured on titanium surfaces in vitro. *Journal of Cell Science*, **101**: 209-217.
- Guedes, J. M., and Kikuchi, N. (1990) Preprocessing and postprocessing for materials based on the homogenization method with adaptive finite element methods. *Computer Methods in Applied Mechanics and Engineering*, **83**: 143-198.
- Guldberg, R. E., Caldwell, N. J., Guo, X. E., Goulet, R. W., Hollister, S. J., and Goldstein, S. A. (1997) Mechanical stimulation of tissue repair in the hydraulic bone chamber. *Journal of Bone and Mineral Research*, **12**(8): 1295-1302.
- Harrigan, T. P., and Reuben, J. D. (1997) Mechanical model for critical strain in mineralizing biological tissues: application to bone formation in biomaterials. *Biomaterials*, **18**: 877-883.
- Hashin, Z., and Shtrikman, S. (1963) A variational approach to the theory of the elastic behaviour of multiphase materials. *Journal of the Mechanics and Physics of Solids*, **11**: 127-140.
- Heck, D. A., Nakajima, I., Kelly, P. J., and Chao, E. Y. (1986) The effect of load alteration on the biological and biomechanical performance of a titanium fiber-metal segmental prosthesis. *Journal of Bone and Joint Surgery*, **68-A**(1): 118-126.
- Heigele, C. A., and Claes, L. E. (1998) Finite element analysis of the local strains and hydrostatic pressure in drill hole defects. *Journal of Biomechanics*, **Suppl. 1**: 12.
- Heikel, H. V. A. (1959) On ossification and growth of certain bones of the rabbit; with a comparison of the skeletal age in the rabbit and in man. *Acta Orthopaedica Scandinavica*, **29**(3): 171-184.
- Hill, R. (1963) Elastic properties of reinforced solids: Some theoretical principles. *Journal of the Mechanics and Physics of Solids*, **11**: 357-372.

- Hollis, J. M., Hoffman, O. E., Stewart, C. L., Flahiff, C. M., and Nelson, C. (1992) Effect of micromotion on ingrowth into porous coated implants using a transcortical model. *Fourth World Biomaterials Congress*, Berlin, Germany, 258.
- Hollister, S. J., Brennan, J. M., and Kikuchi, N. (1994) A homogenization sampling procedure for calculating trabecular bone effective stiffness and tissue level stress. *Journal of Biomechanics*, **27**(4): 433-444.
- Hollister, S. J., Fyhrie, D. P., Jepsen, K. J., and Goldstein, S. A. (1991) Application of homogenization theory to the study of trabecular bone mechanics. *Journal of Biomechanics*, **24**(9): 825-839.
- Hollister, S. J., Guldborg, R. E., Kuelske, C. L., Caldwell, N. J., Richards, M., and Goldstein, S. A. (1996) Relative effects of wound healing and mechanical stimulus on early bone response to porous-coated implants. *Journal of Orthopaedic Research*, **14**: 654-662.
- Hollister, S. J., and Kikuchi, N. (1992) A comparison of homogenization and standard mechanics analyses for periodic porous composites. *Computational Mechanics*, **10**: 73-95.
- Hollister, S. J., and Kikuchi, N. (1994) Homogenization theory and digital imaging: A basis for studying the mechanics and design principles of bone tissue. *Biotechnology and Bioengineering*, **43**: 586-596.
- Huiskes, R., and Chao, E. Y. S. (1983) A survey of finite element analysis in orthopedic biomechanics: The first decade. *Journal of Biomechanics*, **16**(6): 385-409.
- Huiskes, R., Driel, W. D. V., Prendergast, P. J., and Søballe, K. (1997) A biomechanical regulatory model for periprosthetic fibrous-tissue differentiation. *Journal of Materials Science: Materials in Medicine*, **8**: 785-788.
- Huiskes, R., and Hollister, S. J. (1993) From structure to process, from organ to cell: Recent developments of FE-analysis in orthopaedic biomechanics. *Journal of Biomechanical Engineering*, **115**: 520-527.

- Inoue, T., Cox, J. E., Pilliar, R. M., and Melcher, A. H. (1987) Effect of the surface geometry of smooth and porous-coated titanium alloy on the orientation of fibroblasts in vitro. *Journal of Biomedical Materials Research*, **21**: 107-126.
- Jaffin, R. A., and Berman, C. L. (1991) The excessive loss of Branemark fixtures in Type IV bone: A 5-year analysis. *Journal of Periodontology*, **62**: 2-4.
- Jemt, T. (1993) Implant treatment in resorbed edentulous upper jaws: A three-year follow-up study on 70 patients. *Clinical Oral Implant Research*, **4**: 187-194.
- Jones, D. B., Nolte, H., Scholübbbers, J.-G., Turner, E., and Veltel, D. (1991) Biochemical signal transduction of mechanical strain in osteoblast-like cells. *Biomaterials*, **12**: 101-110.
- Keaveny, T. M., and Hayes, W. C. (1993) Mechanical properties of cortical and trabecular bone. In: *Bone*, B. K. Hall, ed., CRC Press, Boca Raton, 285-344.
- Kenwright, J., and Goodship, A. E. (1989) Controlled mechanical stimulation in the treatment of tibial fractures. *Clinical Orthopaedics and Related Research*, **241**: 36-47.
- Kenwright, J., Richardson, J. B., Cunningham, J. L., White, S. H., Goodship, A. E., Adams, M. A., Magnussen, P. A., and Newman, J. H. (1991) Axial movement and tibial fractures. A controlled randomised trial of treatment. *Journal of Bone and Joint Surgery [Br]*, **73-B**(4): 654-659.
- Kieswetter, K., Schwartz, Z., Hummert, T. W., Cochran, D. L., Simpson, J., and Boyan, B. D. (1996) Surface roughness modulates the local production of growth factors and cytokines by osteoblast-like MG-63 cells. *Journal of Biomedical Materials Research*, **32**: 55-63.
- Klein-Nulend, J., Veldhuijzen, J. P., and Burger, E. H. (1986) Increased calcification of growth plate cartilage as a result of compressive force in vitro. *Arthritis Rheumatics*, **29**: 1002-1009.
- Ko, C.-C. (1994). Mechanical Characteristics of Implant/Tissue Interphases, Ph.D. Thesis, University of Michigan, Ann Arbor.

- Ko, C. C., Kohn, D. H., and Hollister, S. J. (1992) Micromechanics of implant/tissue interfaces. *Journal of Oral Implantology*, **18**(3): 220-230.
- Ko, C.-C., Kohn, D. H., and Hollister, S. J. (1996) Effective anisotropic elastic constants of bimaterial interphases: comparison between experimental and analytical techniques. *Journal of Materials Science: Materials in Medicine*, **7**: 109-117.
- Ko, C.-C., Kohn, D. H., Hollister, S. J., and Goldstein, S. A. (1995) Ingrowth rule: A relationship between tissue strain and osseointegration for porous coated implants. *ASME Bioengineering Conference*, 481-482.
- Kobayashi, S., Takaoka, K., Saito, N., and Hisa, K. (1997) Factors affecting aseptic failure of fixation after primary Charnley total hip arthroplasty: Multivariate survival analysis. *Journal of Bone and Joint Surgery*, **79A**(11): 1618-1627.
- Kohn, D. H. (1992) Overview of factors important in implant design. *Journal of Oral Implantology*, **18**(3): 204-219.
- Kohn, D. H., Ko, C.-C., and Hollister, S. J. (1993a) Coupled global/local modeling of porous coated implants: Error estimates for different loading conditions. *Orthopaedic Research Society*, San Francisco, California, 469.
- Kohn, D. H., Ko, C.-C., and Hollister, S. J. (1993b) Effect of tissue modulus, symmetry and fibrous tissue on the local properties of a porous coating/tissue interfacial zone. *Orthopaedic Research Society*, San Francisco, California, 223.
- Korioth, T. W. P., and Versluis, A. (1997) Modeling the mechanical behavior of the jaws and their related structures by finite element (FE) analysis. *Critical Reviews in Oral Biology and Medicine*, **8**(1): 90-104.
- Lerner, A. (1998). Influence of Mechanical Stresses on Normal Bone Growth in the Developing Femur, Ph.D. Thesis, University of Michigan, Ann Arbor.
- Lerner, A. L., Kuhn, J. L., and Hollister, S. J. (1998) Are regional variations in bone growth related to mechanical stress and strain parameters? *Journal of Biomechanics*, **31**: 327-335.

- Li, G., Simpson, A. H. R. W., Kenwright, J., and Triffitt, J. T. (1997) Assessment of cell proliferation in regenerating bone during distraction osteogenesis at different distraction rates. *Journal of Orthopaedic Research*, **15**: 765-772.
- Lincks, J., Boyan, B. D., Blanchard, C. R., Lohmann, C. H., Liu, Y., Cochran, D. L., Dean, D. D., and Schwartz, Z. (1998) Response of MG63 osteoblast-like cells to titanium and titanium alloy is dependent on surface roughness and composition. *Biomaterials*, **19**: 2219-2232.
- Lohmann, C. H., Sagun, R., Jr., Sylvia, V. L., Cochran, D. L., Dean, D. D., Boyan, B. D., and Schwartz, Z. (1999) Surface roughness modulates the response of MG63 osteoblast-like cells to 1,25-(OH)₂D₃ through regulation of phospholipase A₂ activity and activation of protein kinase A. *Journal of Biomedical Materials Research*, **47**(2): 139-151.
- Lowenberg, B. F., Pilliar, R. M., Aubin, J. E., Fernie, G. R., and Melcher, A. H. (1987) Migration, attachment, and orientation of human gingival fibroblasts to root slices, naked and porous-surfaced titanium alloy discs, and zircalloy 2 discs in vitro. *Journal of Dental Research*, **66**(5): 1000-1005.
- Luckey, H. A., Lamprecht, E. G., and Walt, M. J. (1992) Bone apposition to plasma-sprayed cobalt-chromium alloy. *Journal of Biomedical Materials Research*, **26**: 557-575.
- Lukkassen, D., Persson, L.-E., and Wall, P. (1995) Some engineering and mathematical aspects of the homogenization method. *Composites Engineering*, **5**(5): 519-531.
- Luo, G., Sadegh, A. M., Alexander, H., Jaffe, W., Scott, D., and Cowin, S. C. (1999) The effect of surface roughness on the stress adaptation of trabecular architecture around a cylindrical implant. *Journal of Biomechanics*, **32**: 275-284.
- Maniatopoulos, C., Pilliar, R. M., and Smith, D. C. (1986) Threaded versus porous-surfaced designs for implant stabilization in bone-endodontic implant model. *Journal of Biomedical Materials Research*, **20**: 1309-1333.

- Martin, J. Y., Schwartz, Z., Hummert, T. W., Schraub, D. M., Simpson, J., Lankford, J., Jr., Dean, D. D., Cochran, D. L., and Boyan, B. D. (1995) Effect of titanium surface roughness on proliferation, differentiation, and protein synthesis of human osteoblast-like cells (MG63). *Journal of Biomedical Materials Research*, **29**: 389-401.
- Masuda, T., Yliheikkilä, P. K., Felton, D. A., and Cooper, L. F. (1998) Generalizations regarding the process and phenomenon of osseointegration. Part I. In vivo studies. *International Journal of Oral & Maxillofacial Implants*, **13**: 17-29.
- McKibbin, B. (1978) The biology of fracture healing in long bones. *Journal of Bone and Joint Surgery [Br]*, **60-B(2)**: 150-162.
- Meguid, S. A., and Kalamkarov, A. L. (1994) Asymptotic homogenization of elastic composite materials with a regular structure. *International Journal of Solids and Structures*, **31(3)**: 303-316.
- Meguid, S. A., Kalamkarov, A. L., Tao, J., and Zougas, A. (1996) Analytical, numerical, and experimental studies of effective elastic properties of periodically perforated materials. *Journal of Engineering Materials and Technology*, **118**: 43-48.
- Meguid, S. A., Kalamkarov, A. L., and Zougas, A. (1994) Analysis of local and effective elastic properties of fibre-reinforced materials. *Composites Engineering*, **4(5)**: 525-535.
- Meyer, U., Wiesmann, H. P., Kruse-Lösler, B., Handschel, J., Stratmann, U., and Joos, U. (1999) Strain-related bone remodeling in distraction osteogenesis of the mandible. *Plastic and Reconstructive Surgery*, **103(3)**: 800-807.
- Mow, V. C., Kuei, S. C., Lai, W. M., and Armstrong, C. G. (1980) Biphasic creep and stress relaxation of articular cartilage in compression: Theory and experiments. *Journal of Biomechanical Engineering*, **102**: 73-84.
- Moyle, D. D., Klawitter, J. J., and Hulbert, S. F. (1973) Mechanical properties of the bone-porous biomaterial interface: elastic behavior. *Journal of Biomedical Materials Research*, **7(3)**: 363-82.

- National Institutes of Health (1988) Dental Implants. *NIH Consensus Statement Online 1988 Jun 13-15 [cited 2000 01 10]*, 1-22.
- National Institutes of Health (1994) Total Hip Replacement. *NIH Consensus Statement Online 1994 September 12-14 [cited 2000 01 10]*, 1-31.
- Ong, J. L., Prince, C. W., Raikar, G. N., and Lucas, L. C. (1996) Effect of surface topography of titanium on surface chemistry and cellular response. *Implant Dentistry*, **5**: 83-88.
- Pauwels, F. (1980) Biomechanics of the Locomotor Apparatus, Maquet, P., Furlong, R., translator, Springer-Verlag, Berlin.
- Pedersen, D. R., Brown, T. D., and Brand, R. A. (1991) Interstitial bone stress distributions accompanying ingrowth of a screen-like prosthesis anchorage layer. *Journal of Biomechanics*, **24**(12): 1131-1142.
- Perren, S. M. (1979) Physical and biological aspects of fracture healing with special reference to internal fixation. *Clinical Orthopaedics and Related Research*, **138**: 175-196.
- Perren, S. M., and Cordey, J. (1980) The concept of interfragmentary strain. In: Current Concepts of Internal Fixation of Fractures, H. K. Uthoff, ed., Springer-Verlag, New York, NY, 63-77.
- Pilliar, R. M. (1987) Porous-surface metallic implants for orthopaedic applications. *Journal of Biomedical Materials Research*, **21**(A1 Suppl): 1-33.
- Pilliar, R. M. (1991) Quantitative evaluation of the effect of movement at a porous coated implant-bone interface. In: The Bone-Biomaterial Interface, J. E. Davies, ed., University of Toronto Press, Toronto, 380-387.
- Pilliar, R. M. (1998) An overview of surface variability of metallic endosseous dental implants: Textured and porous surface-structured designs. *Implant Dentistry*, **7**(4): 305-314.
- Pilliar, R. M., Cameron, H. U., Welsh, R. P., and Binnington, A. G. (1981) Radiographic and morphologic studies of load-bearing porous surface structured implants. *Clinical Orthopaedics and Related Research*, **156**: 249-256.

- Pilliar, R. M., Deporter, D. A., and Watson, P. (1995) Tissue-implant interface: Micromovement effects. In: Material in Clinical Applications, P. Vincenzini, ed., Techna, Faenza, 569-579.
- Pilliar, R. M., Deporter, D. A., Watson, P. A., Abdulla, D., Valiquette, N., and Lindsay, D. (1996) Quantitative determination of relative movement effects on bone ingrowth with porous-coated implants. *Fifth World Biomaterials Congress*, Toronto, 261.
- Pilliar, R. M., Deporter, D. A., Watson, P. A., Pharoah, M., Chipman, M., Valiquette, N., Carter, S., and Groot, K. D. (1991a) The effect of partial coating with hydroxyapatite on bone remodeling in relation to porous-coated titanium alloy dental implants in the dog. *Journal of Dental Research*, **70**: 1338-1345.
- Pilliar, R. M., Deporter, D. A., Watson, P. A., and Valiquette, N. (1991b) Dental implant design - Effect on bone remodeling. *Journal of Biomedical Materials Research*, **25**: 467-483.
- Pilliar, R. M., Lee, J. M., and Davies, J. E. (1993) Interface zone: Factors influencing its structure for cementless implants. In: Biological, Material, and Mechanical Considerations of Joint Replacement, B. F. Morrey, ed., Raven Press, Ltd., New York, 225-235.
- Pilliar, R. M., Lee, J. M., and Maniopoulos, C. (1986) Observations on the effect of movement on bone ingrowth into porous-surfaced implants. *Clinical Orthopaedics and Related Research*, **208**: 108-113.
- Prendergast, P. J., and Huiskes, R. (1996) Finite element analysis of fibrous tissue morphogenesis - A study of the osteogenic index with a biphasic approach. *Mechanics of Composite Materials*, **32**(2): 144-150.
- Prendergast, P. J., Huiskes, R., and Søballe, K. (1997) Biophysical stimuli on cells during tissue differentiation at implant interfaces. *Journal of Biomechanics*, **30**(6): 539-548.
- Qin, Y.-X., McLeod, K. J., Guilak, F., Chiang, F.-P., and Rubin, C. T. (1996) Correlation of bony ingrowth to the distribution of stress and strain parameters surrounding a porous-coated implant. *Journal of Orthopaedic Research*, **14**: 862-870.

- Richards, M., Goulet, J. A., Weiss, J. A., Waanders, N. A., Schaffler, M. B., and Goldstein, S. A. (1998) Bone regeneration and fracture healing. Experience with distraction osteogenesis model. *Clinical Orthopaedics & Related Research*, **355 Suppl**: S191-204.
- Richards, M., Waanders, N. A., Weiss, J. A., Bhatia, V., Senunas, L. E., Schaffler, M. B., Goldstein, S. A., and Goulet, J. A. (1999a) Reduced gap strains induce changes in bone regeneration during distraction. *Journal of Biomechanical Engineering*, **121**: 348-355.
- Richards, M., Wineman, A. S., Alsberg, E., Goulet, J. A., and Goldstein, S. A. (1999b) Viscoelastic characterization of mesenchymal gap tissue and consequences for tension accumulation during distraction. *Journal of Biomechanical Engineering*, **121**(1): 116-23.
- Rieger, M. R., Adams, W. K., and Kinzel, G. L. (1990) A finite element survey of eleven endosseous implants. *The Journal of Prosthetic Dentistry*, **63**: 457-65.
- Rubin, C. T., and McLeod, K. J. (1994) Promotion of bony ingrowth by frequency-specific, low-amplitude mechanical strain. *Clinical Orthopaedics and Related Research*, **298**: 165-174.
- Sadegh, A. M., Luo, G. M., and Cowin, S. C. (1993) Bone ingrowth: An application of the boundary element method to bone remodeling at the implant interface. *Journal of Biomechanics*, **26**(2): 167-182.
- Sarmiento, A., Schaeffer, J. F., Beckerman, L., Latta, L. L., and Enis, J. E. (1977) Fracture healing in rat femora as affected by functional weight-bearing. *Journal of Bone and Joint Surgery*, **59-A**(3): 369-375.
- Schwartz, Z., and Boyan, B. D. (1994) Underlying mechanisms at the bone-biomaterial interface. *Journal of Cellular Biochemistry*, **56**: 340-347.
- Schwartz, Z., Kieswetter, K., Dean, D. D., and Boyan, B. D. (1997) Underlying mechanisms at the bone-surface interface during regeneration. *Journal of Periodontal Research*, **32**: 166-171.
- Sennerby, L., and Roos, J. (1998) Surgical determinants of clinical success of osseointegrated oral implants: A review of the literature. *International Journal of Prosthodontics*, **11**(5): 408-420.

- Shah, A. K., Sinha, R. K., Hickok, N. J., and Tuan, R. S. (1999) High-resolution morphometric analysis of human osteoblastic cell adhesion on clinically relevant orthopaedic alloys. *Bone*, **24**(5): 499-506.
- Simmons, C. A., and Pilliar, R. M. (2000) A biomechanical study of early tissue formation around bone-interfacing implants - The effect of implant surface geometry. In: Bone Engineering, J. E. Davies, ed., EM squared, Toronto.
- Smalt, R., Mitchell, F. T., Howard, R. L., and Chambers, T. J. (1997) Induction of NO and prostaglandin E₂ in osteoblasts by wall-shear stress but not mechanical strain. *American Journal of Physiology*, **273**: E751-758.
- Smith, D. C., Pilliar, R. M., and McIntyre, N. S. (1989) Surface characteristics of dental implant materials. In: Oral Implantology and Biomaterials, H. Kawahara, ed., Elsevier Science Publishers B.V., Amsterdam, 185-192.
- Søballe, K., Brockstedt-Rasmussen, H., Hansen, E. S., and Bünger, C. (1992a) Hydroxyapatite coating modifies implant membrane formation. *Acta Orthopaedica Scandinavica*, **63**(2): 128-140.
- Søballe, K., Hansen, E. S., Brockstedt-Rasmussen, H., Jørgensen, P. H., and Bünger, C. (1992b) Tissue ingrowth into titanium and hydroxyapatite-coated implants during stable and unstable conditions. *Journal of Orthopaedic Research*, **10**: 285-299.
- Søballe, K., Hansen, E. S., Brockstedt-Rasmussen, H., and Bünger, C. (1993) Hydroxyapatite coating converts fibrous tissue to bone around loaded implants. *Journal of Bone and Joint Surgery [Br]*, **75-B**(2): 270-278.
- Steinemann, S. G., Eulenberger, J., Maesuli, P.-A., and Schroeder, A. (1986) Adhesion of bone to titanium. In: Biological and Biomechanical Performance of Biomaterials, P. Christel, A. Meunier, and A. J. C. Lee, eds., Elsevier Science Publishers B.V., Amsterdam, 409-414.
- Sugita, H., Oka, M., Toguchida, J., Nakamura, T., Ueo, T., and Hayami, T. (1999) Anisotropy of osteoporotic cancellous bone. *Bone*, **24**(5): 513-516.

- Suquet, P. M. (1985) Elements of homogenization for inelastic solid mechanics. In: Homogenization Techniques for Composite Media, E. Sanchez-Palencia and A. Zaoui, eds., Springer-Verlag, New York, 194-278.
- Szmukler-Moncler, S., Salama, H., Reingewirtz, Y., and Dubruille, J. H. (1998) Timing of loading and effect of micromotion on bone-dental implant interface: Review of experimental literature. *Journal of Biomedical Materials Research (Applied Biomaterials)*, **43**: 192-203.
- Tägil, M., and Aspenberg, P. (1999) Cartilage induction by controlled mechanical stimulation in vivo. *Journal of Orthopaedic Research*, **17**: 200-204.
- Tanck, E., van Driel, W. D., Blankevoort, L., Huiskes, R., Hagen, J. W., and Burger, E. H. (1999a) Response to Beaupré and Carter. *Journal of Biomechanics*, **32**: 1257.
- Tanck, E., van Driel, W. D., Hagen, J. W., Burger, E. H., Blankevoort, L., and Huiskes, R. (1999b) Why does intermittent hydrostatic pressure enhance the mineralization process in fetal cartilage? *Journal of Biomechanics*, **32**: 153-161.
- Thomas, K. A., and Cook, S. D. (1985) An evaluation of variables influencing implant fixation by direct bone apposition. *Journal of Biomedical Materials Research*, **19**: 875-901.
- Thompson, G. J., and Puleo, D. A. (1995) Effects of sublethal metal ion concentrations on osteogenic cells derived from bone marrow stromal cells. *Journal of Applied Biomaterials*, **6(4)**: 249-258.
- Thompson, G. J., and Puleo, D. A. (1996) Ti-6Al-4V ion solution inhibition of osteogenic cell phenotype as a function of differentiation timecourse in vitro. *Biomaterials*, **17(20)**: 1949-1954.
- Uthoff, H. K., and Germain, J.-P. (1977) The reversal of tissue differentiation around screws. *Clinical Orthopaedics and Related Research*, **123**: 248-252.
- Vander Sloten, J., Hobatho, M.-C., and Verdonck, P. (1998) Applications of computer modelling for the design of orthopaedic, dental and cardiovascular biomaterials. *Proceedings of the Institution of Mechanical Engineers, Part H*, **212**: 489-500.

- Vercaigne, S., Wolke, J. G. C., Naert, I., and Jansen, J. A. (1998a) The effect of titanium plasma-sprayed implants on trabecular bone healing in the goat. *Biomaterials*, **19**: 1093-1099.
- Vercaigne, S., Wolke, J. G. C., Naert, I., and Jansen, J. A. (1998b) Histomorphometrical and mechanical evaluation of titanium plasma-spray-coated implants placed in the cortical bone of goats. *Journal of Biomedical Materials Research*, **41**: 41-48.
- Weinans, H., Huiskes, R., and Grootenboer, H. J. (1990) Trends of mechanical consequences and modeling of a fibrous membrane around femoral hip prostheses. *Journal of Biomechanics*, **23**(10): 991-1000.
- Weinans, H., Huiskes, R., and Grootenboer, H. J. (1993) Quantitative analysis of bone reactions to relative motions at implant-bone interfaces. *Journal of Biomechanics*, **26**(11): 1271-1281.
- Wen, X., Wang, X., and Zhang, N. (1996) Microrough surface of metallic biomaterials: a literature review. *Bio-Medical Materials and Engineering*, **6**: 173-189.
- Wennerberg, A., Albrektsson, T., and Andersson, B. (1993) Design and surface characteristics of 13 commercially available oral implant systems. *The International Journal of Oral & Maxillofacial Implants*, **8**(6): 622-633.
- Wennerberg, A., Albrektsson, T., and Andersson, B. (1996a) Bone tissue response to commercially pure titanium implants blasted with fine and coarse particles of aluminum oxide. *International Journal of Oral & Maxillofacial Implants*, **11**(1): 38-45.
- Wennerberg, A., Albrektsson, T., Johansson, C., and Andersson, B. (1996b) Experimental study of turned and grit-blasted screw-shaped implants with special emphasis on effects of blasting material and surface topography. *Biomaterials*, **17**: 15-22.
- Wennerberg, A., Albrektsson, T., and Lausmaa, J. (1996c) Torque and histomorphometric evaluation of c.p. titanium screws blasted with 25- and 75- μm -sized particles of Al_2O_3 . *Journal of Biomedical Materials Research*, **30**: 251-260.

- Wennerberg, A., Ektessabi, A., Albrektsson, T., Johansson, C., and Andersson, B. (1997) A 1-year follow-up of implants of differing surface roughness placed in rabbit bone. *International Journal of Oral & Maxillofacial Implants*, **12**(4): 486-494.
- Wilke, H.-J., Claes, L., and Steinemann, S. (1990) The influence of various titanium surfaces on the interface shear strength between implants and bone. In: *Clinical Implant Materials*, G. Heimke, U. Soltész, and A. J. C. Lee, eds., Elsevier Science Publishers B.V., Amsterdam, 309-314.
- Wolf, J. W., White, A. A., Panjabi, M. M., and Southwick, W. O. (1981) Comparison of cyclic loading versus constant compression in the treatment of long-bone fractures in rabbits. *Journal of Bone and Joint Surgery*, **63-A**(5): 805-810.
- Wong, M., and Carter, D. R. (1988) Mechanical stress and morphogenetic endochondral ossification of the sternum. *Journal of Bone and Joint Surgery*, **70A**: 992-1000.
- Wong, M., and Carter, D. R. (1990a) A theoretical model of endochondral ossification and bone architecture construction in long bone ontogeny. *Anatomy and Embryology*, **181**: 523-532.
- Wong, M., and Carter, D. R. (1990b) Theoretical stress analysis of organ culture osteogenesis. *Bone*, **11**: 127-131.
- Wong, M., Eulenberger, J., Schenk, R., and Hunziker, E. (1995) Effect of surface topology on the osseointegration of implant materials in trabecular bone. *Journal of Biomedical Materials Research*, **29**: 1567-75.
- Wu, J. Z., Herzog, W., and Epstein, M. (1999) Modelling of location- and time-dependent deformation of chondrocytes during cartilage loading. *Journal of Biomechanics*, **32**: 563-572.